# Origin and geochemical evolution of the metamorphosed SEDEX Zn-Pb deposit at Kayad, western India: constraints from texture, hydrothermal alteration, major and trace element geochemistry and stable isotope systematics

Submitted in fulfillment of the requirements for the degree of
Doctor of Philosophy (Science)

by

**Eileena Das**

CSIR-SRF (09/096(0986)/2019-EMR-I)

Index No.: 56/19/Geol.Sc./26

Registration No.: SOGEO1105619

**Department of Geological Sciences**

**Jadavpur University**

Kolkata-700032, India

September, 2024

যাদবপুর বিশ্ববিদ্যালয়
কলকাতা - ৭০০০৩২, ভারত

JADAVPUR UNIVERSITY
KOLKATA-700 032, INDIA

FACULTY OF SCIENCE : DEPARTMENT OF GEOLOGICAL SCIENCES

## CERTIFICATE FROM THE SUPERVISOR

This is to certify that the thesis entitled "***Origin and geochemical evolution of the metamorphosed SEDEX Zn-Pb deposit at Kayad, western India: constraints from texture, hydrothermal alteration, major and trace element geochemistry and stable isotope systematics***" submitted by ***Smt. Eileena Das*** who got her name registered on 30.08.2019 for the award of **Ph. D. (Science)** Degree of Jadavpur University, is absolutely based upon her own work under the supervision of Prof. Dipak C Pal and that neither this thesis nor any part of it has been submitted for either any degree / diploma or any other academic award anywhere before.

**Date:** 25.09.2024

**Place:** Jadavpur, Kolkata, India

.....

**Dr. Dipak C Pal** (Supervisor)
Professor
Department of Geological Sciences
Jadavpur University
Kolkata 700032, WB, INDIA

Dr. Dipak C. Pal
Professor
Dept. of Geological Sciences
Jadavpur University
Kolkata-700 072

Website : www.jaduniv.edu.in
E-mail : hod.geology@jadavpuruniversity.in

HOD Phone : 033 2457 2719
Office : 033 2457 2268

*Dedicated to my parents and to all women scientists and researchers*

# ACKNOWLEDGEMENTS

This thesis is the embodiment of not just my own efforts, but rather it stands on the shoulders of all the people who have guided, helped, encouraged and motivated me for these precious years. It is finally time for me to reflect on this journey and express my sincere most words of gratitude to all who have propelled me towards this success.

This string of acknowledgements cannot begin without a heartfelt thanks to my doctoral supervisor, Prof. Dipak Chandra Pal, without whose vast knowledge, advice, direction, and kind encouragement, this thesis would not have been possible. I extend my deepest gratitude to him for being my academic compass and a sounding board to help me turn scattered ideas into coherent pieces of research. His unwavering support and patience helped me calmly navigate through all the challenging moments in my entire PhD journey. I will forever cherish the invaluable lessons I have learned from him, not only in the realm of research but also in matters of work and life, that have shaped both my academic and personal growth.

I extend my profound gratitude to Hindustan Zinc Limited for their assistance with fieldwork, including facilitating an underground mine visit and allowing us to collect samples, and for sponsoring our stay in Ajmer, Rajasthan. Special thanks to Atree Bandyopadhyay for providing us with an insightful tour of the operations and guidance in the field. His expertise and contributions have greatly helped shape our understanding of the deposit geology and ore disposition.

I owe my earnest appreciation to all the laboratories where I conducted my sample analyses. I am especially grateful to Prof. Dewashish Upadhyay and all the members of his ICPMS lab at IIT-Kharagpur for their invaluable support. My sincere thanks go to Rupashree Saha for her assistance and constant presence whenever I needed guidance in the lab. I also wish to acknowledge Prof. Biswajit Mishra along with the members and lab assistants of the SEM and EPMA lab at IIT-Kharagpur, and Prof. N.V. Chalapathi Rao at Banaras Hindu University for granting me the freedom to utilize their facilities. Additionally, I extend my gratitude to Dr. Bin Fu at the Australian National University and Dr. Nurul Absar in Pondicherry University for their efforts in conducting the geochemical analyses. Their insights and analytical expertise have been integral in generating data that constitutes a significant and essential part of my research.

My heartfelt thanks to my collaborators Prof. Dewashish Upadhyay, Dr. Bin Fu, and Dr. Nurul Absar for their scientific contributions and expertise; Aparajita Tripathi for her analytical support; and Vijendra Kashyap and Kastoor Meena from HZL for their industrial perspective and suggestions. I ow my immense gratitude to the journal editors and reviewers for their critical review that enhanced the quality of my research work.

# *Acknowledgements*

My warmest thanks go to all my lab-mates with whom I have had the opportunity of working during my tenure. My seniors, Dr. Abu Saeed Baidya and Dr. Subhadip Adak deserve special mention for their intellectual inputs which have been indispensable for refining my ideas and approach towards the subject matter. Their support, whether through addressing my uncertainties during my nascent years as a scholar, or offering constructive and honest feedback, combined with their spirit of camaraderie, made my PhD journey both enriching and enjoyable. I am also thankful to my colleagues and juniors; Sayantan De, Sohini Chatterjee, Debarima Pal and Rishabh Maity for their insightful discussions and assistance with analyses, as well as to all the other members of the lab who contributed to an enriching environment for learning.

My deepest gratitude goes to my Mom and Dad, for their understanding and unwavering belief in my abilities, and for patting my back for every little achievement that helped me persevere and reach this milestone. I am also thankful to my friends and classmates, who have shared in my joys and also stood by me through challenging times. A special note of gratitude goes to Dr. Arnab Roy, whose love and encouragement has been a constant source of strength throughout this experience. Thank you for giving me courage when I doubted myself, and for always applauding the loudest at my success. Your belief in me and ability to keep me grounded made a world of difference.

My humble gratitude goes to the academic faculty and staff of Dept. of Geological Sciences, Jadavpur University, who have played a role in fostering a nurturing academic environment that has significantly contributed to my development as a scholar.

Finally, I extend my gratitude to CSIR, India for their generous support in providing the Junior and Senior Research Fellowships during my doctoral tenure. Their financial assistance has been instrumental in ensuring the smooth and uninterrupted progress of my research, even during the trying times of the COVID-19 pandemic. I would also take this opportunity to thank AGU and DST-SERB for funding my participation in annual international conferences by providing travel grants. The analytical cost for sulfide analysis was partially met from “Departmental support towards upgradation in research” to Prof. Dipak Chandra Pal through JU RUSA 2.0 of the University Grants Commission, Government of India for which it is thus acknowledged.

Eileena Das

# ABSTRACT

Sedimentary exhalative (SEDEX) deposits belong to an intriguing and important class of sediment-hosted zinc and lead deposits that contribute approximately 50% of the world's zinc and lead resources. These stratiform to stratabound deposits are known to be formed through the exhalation of hot, metalliferous fluid from submarine vents onto the seafloor contemporaneously during sedimentation. Despite the apparently straightforward definition of its genesis, SEDEX deposits are observed to have varied mechanisms of formation in terms of source of metals and fluids, physicochemical conditions of the mineralizing fluid, and timing of mineralization with respect to the host sediments. Most SEDEX deposits are metamorphosed and deformed which variably alters the tell-a-tale geological, mineralogical and geochemical signature of the deposits and thereby pose challenges in interpreting their origins. The present work integrates field relations, mineralogy, texture, sulfide geochemistry, and sulfur and boron isotope systematics to address some of the key issues of SEDEX mineralization, using Kayad Zn-Pb deposit in Aravalli Delhi fold belt (ADFB), western India as a case study.

The ADFB is home to some of the oldest and richest Pb-Zn deposits in the world that are confined in the Bhilwara belt (Rajpura-Dariba, Rampura-Agucha etc.) and in the Aravalli belt (Zawar). The Kayad Zn-Pb deposit near Ajmer in Rajasthan is a part of the Ghugra-Kayad mineralized belt of the North Delhi fold belt. Based on morphology, mineralogy and textural attributes, three different styles of sulfide mineralization are recognized: i) a *laminated/disseminated* type where sphalerite and pyrrhotite, with minor galena and chalcopyrite occur as lamina/bands parallel to the schistosity of quartz mica schist, and as disseminations in quartzite, ii) a *massive* type consisting of sphalerite, galena, pyrrhotite, chalcopyrite and arsenopyrite which occur in large masses disrupting and replacing the general foliation of the schists and accumulating primarily at the fold hinge, iii) a *vein-hosted* type represented by pyrrhotite + chalcopyrite ± sphalerite ± galena in pegmatites, and sphalerite + galena ± chalcopyrite ± pyrrhotite in K-feldspar and quartz veins.

Based on mode of occurrence and mineralogy, the laminated/disseminated sulfide ores are interpreted to represent the original syn-sedimentary/diagenetic SEDEX mineralization in the area. On the other hand, several lines of evidences suggest that the massive high-grade ores and the vein-hosted ores are the products of remobilization of the existing SEDEX ores. Presence of durchbewegung texture, accumulation and attenuation of ores at the fold hinge and the limb respectively, and piercement veins suggest that syn-metamorphic plastic flow played important role in the formation of massive ores. Furthermore, very low dihedral angles between sphalerite and galena wherein galena displays cusps and carries texture in tandem with locally preserved re-equilibrated melt textures indicate remobilization through sulfide melting also played significant role in the formation of massive ores. The massive ores are enriched in low melting chalcophile elements (LMCEs) such as Ag, Sb, As, Bi, Tl, and Se, evidenced by ubiquitous intergrowths of sulfides with sulfosalts such as Ag-bearing tetrahedrite, gudmundite, pyrargyrite, breithauptite, inclusions and exsolutions of sulfosalts in sulfides and high concentrations of LMCEs in the sulfide minerals. The LMCEs facilitated sulfide melting by lowering the melting temperature and in turn were fractionated in the massive ores. The Fe-Cu dominant mineralization associated with pegmatite show pervasive replacement of pegmatitic plagioclase and muscovite by albite + orthoclase + chamosite + biotite ± clinochlore suggesting

a K + Na + Fe metasomatism. On the other hand, microcline in Zn-Pb dominated K-feldspar rich veins is replaced by prehnite + pumpellyite + clinochlore ± fluorite suggesting overprinting of K-metasomatism by a later Na + Ca metasomatism.

Major and trace element compositions of tourmaline (dravitic composition, oxydravite compositional trends, enrichment in Ti, V, Cr, depletion in granitophile elements, and strongly positive Eu anomaly), negative $\delta^{11}B$ of tourmaline (-13‰ to -10.7‰; avg. -11.8±0.7 ‰) in conjunction with highly positive $\delta^{34}S$ (+4.3 ‰ to 11.3‰) of sulfide precludes involvement of marine fluids and suggests fluids derived from continental evaporite were responsible for the SEDEX mineralization. Sulfide precipitation occurred via thermochemical sulfate reduction of sulfate as suggested by positive $\delta^{34}S$ and minor deviation of $\Delta^{33}S$ and $\Delta^{36}S$ from mass dependent fractionation line. Similarity of $\delta^{34}S$ values of massive and vein-hosted ore with the laminated SEDEX ore implies that the sulfur from the original SEDEX mineralization was recycled and remobilized to form the massive and the vein-type ores. Tourmalines associated with pegmatite-hosted Fe-Cu mineralization, connote magmatic/magmatic-hydrothermal origin based on its Fe-rich schorl nature, Al-Fe-Mg composition and lightest $\delta^{11}B$ value of -13.1‰ to -15.2 ‰. Tourmaline associated with K-feldspar vein-hosted Zn-Pb mineralization occurs as outsized clots of dravite having major and trace element compositions similar to SEDEX tourmaline and boron isotope compositions intermediate between SEDEX tourmaline and pegmatitic tourmaline. Based on these observations and similar alteration types of pegmatite-hosted Fe-Cu and K-feldspar vein-hosted Zn-Pb mineralization, it is proposed that the magmatic fluid responsible for pegmatite-hosted Fe-Cu mineralization also recycled boron, sulfur and metals from existing SEDEX mineralization and locally formed fluid-mediated remobilized Zn-Pb mineralization. In summary, the Kayad laminated/disseminated Zn-Pb deposit initially formed by thermochemical reduction of sulfate-rich fluids derived from the dissolution of continental evaporites in euxinic basins in the North Delhi fold belt. During regional deformation and metamorphism, the Zn-Pb ores were remobilized primarily via mechanical transport and partial melting and subordinately by hydrothermal fluids forming the massive mineable ore lodes. The mobilizing fluids were derived from a magmatic source that recycled ore constituents from existing SEDEX ores to form vein-type mineralization associated with hydrothermal alteration.

# LIST OF FIGURES

# LIST OF TABLES

# LIST OF APPENDICES

# *List of Appendices*

# CONTENTS

# CHAPTER 1: Introduction

## 1.1 Introduction

Sedimentary exhalative (SEDEX) Pb-Zn (-Ag-Cu) deposits, alongside Volcanogenic Massive Sulfide (VMS) and Mississippi Valley Type (MVT) deposits, rank among the world's most significant sources of lead and zinc. SEDEX deposits account for 25% of the world's Pb and Zn production (Goodfellow 2004) and are estimated to host 31% Zn, 36% Pb and 9.9% Ag of the world (Singer 1995; Wilkinson 2014). SEDEX, coined by Carne and Cathro (1982), refers to deposits that are a product of dewatering and metamorphism of thick piles of ocean basin sediments, with no genetic connection to magmatic activities. Hence the 'Sed' denotes the sedimentary origin, while 'Ex' stands for "Exhalative" which pertains to the geological process of venting hot, saline, metalliferous hydrothermal fluids onto the ocean floor during ongoing basin-floor sedimentation, resulting in syngenetic and stratabound mineralization. Since its inception, this style of mineralization has variably been described as sediment-hosted lead-zinc deposits (Badham 1981), sediment-hosted stratiform lead-zinc deposits (Lydon 1983), syngenetic and diagenetic lead-zinc deposits in shales and carbonates (Edwards and Atkinson 1986), and sediment-hosted massive sulfide deposits (Misra 2000). SEDEX share similarities with other sediment-hosted deposits such as MVT and stratiform copper deposits in terms of host rocks, which are primarily clastic sedimentary rocks and carbonates. But, unlike the other sediment-hosted deposits, SEDEX formations are at places massive rather than stratiform, containing approximately 50% sulfides, therefore it is also often characterized as a "massive sulfide".

Lead and zinc are indispensable metals in the modern world, each contributing significantly to various industries and high-tech applications. Lead, primarily used in lead-acid batteries, is a cornerstone of the automotive industry, and is also vital in providing

radiation shielding for medical and industrial purposes. On the other hand, zinc is essential for galvanization, thereby extending the lifespan of infrastructure and construction materials. Moreover, zinc is a crucial component in the production of alloys such as brass and bronze, used in a long range of products from musical instruments to plumbing fixtures. Its role in human health is equally important, as zinc-supplements help prevent deficiency-related diseases and boost the immune system. In other words, lead and zinc together are pivotal in advancing technology, healthcare, and infrastructure. The ever-increasing demand for these metals in the society necessitates a deeper understanding of the geological processes that drive the genetic mechanisms of Pb-Zn deposits. This understanding is pivotal for ensuring the resilience of the supply-and-demand chain through improved prediction, exploration, and extraction of ores, and for the development of sustainable mining strategies for the future. From an academic perspective, gaining a comprehensive understanding of these deposits is essential for uncovering the factors that govern ore formation, distribution, and quality. Such insights not only enhance our ability to locate and efficiently extract valuable minerals but also enable us to minimize environmental impacts, optimize resource use, and contribute to the advancement of geoscientific knowledge.

## 1.2 Sedimentary Exhalative Systems: Character, Major Developments and Lacuna

The definition of SEDEX deposits given by Carne and Cathro has widened over time to include and explain various similar stratiform and stratabound Zn-Pb mineralization, and direct evidence of an exhalite component in the ore is no longer a prerequisite to classify a deposit as SEDEX type. Currently, various processes such as synsedimentary exhalation, diagenesis, epigenetic replacement, and low-grade metamorphism are believed to play a role in metal precipitation in these deposits (Leach et al. 2010). Since an unequivocal classification

scheme for SEDEX is lacking, several sub-classes exist based on genetic character of the deposit. Sangster (2002) classified these deposits based on proximity to feeder vents and associated alterations. To be classified as a vent proximal deposit, there must be evidence of a vent zone with related alterations occurring just below the stratiform mineralization. On the other hand, vent distal deposits are stratiform and concordant with no spatial connection with feeder zones. According to Sangster and Hillary (1998), almost 80% of the known SEDEX deposits are of vent-distal type (Leach et al. 2005). However, SEDEX deposits are highly vulnerable to intense metamorphism and deformation which results in ambiguous identification of a vent zone. Thus, the practical application of this classification meets with uncertainty. Cooke et al. (2000) suggested a sub-classification based on brine-type. Cool, oxidized and near-neutral brines form 'McArthur type' deposit while hot, reduced and acidic brines form the 'Selwyn type' deposits. Emsbo (2000) based his categorization on the deposit's base metal, barite and gold content. However, all these classifications are not without exceptions therefore, it is often broadly classified on the basis of host rock type, whether carbonate-, coarse clastic- or shale-hosted.

### 1.2.1 Tectonic Setting and Distribution through Time

The tectonic setup of the region hosting SEDEX deposit plays an extremely important role in determining the nature of the deposit (host-rock type, temperature and pressure at deposition site) and its eventual fate during tectonic recycling (Leach et al. 2005). Most SEDEX deposits occur in continental rifts, passive margins, extensional arc settings or continental sag basins. All of these setups have the following factors in common:

1. A basin or a part of the basin is **devoid of direct magmatic activity**. Intra-continental rifts accumulate coarse, immature clastics eroded from the highlands which are deposited along the extensional growth faults at rift-flanks. Sedimentation along rift

axis may be marine or non-marine, however, it is more common for deep water environments to develop, which form perfect spots for clastic-dominated Pb-Zn mineralization. For rifts, that proceed to completion and are followed by the creation of a mid-oceanic ridge, SEDEX systems occur at passive margins where thermal subsidence ensues due to cooling as the plates move away from the ridge axis. At higher latitudes, mature sandstones and siltstones characterize the shelf environments whereas at low latitudes, platform carbonates are the dominant assemblage at passive margins. Fine grained silt and shale deposited offshore on the continental slope are eligible to host syngenetic or diagenetic clastic-dominated Pb-Zn deposits (Leach et al. 2010).

2. **Gradually subsiding basin** so that a laterally extensive, thick basin sequence is created that can provide enough metal for the circulating hydrothermal brines to leach. Hoggard et al. (2020) established a remarkable correlation between occurrence of giant Pb-Zn deposits and lithospheric edge thickness. Greater thickness of lithosphere renders higher cratonic edge stability, abundant ore forming ingredients for extensive periods of time, low basal heat (since oxidation–reduction reactions that drive the metal precipitation in sediment hosted deposits become ineffective at brine temperatures above ~250 °C; Huston et al., 2016), and higher preservation potential compared to deposits that occur on thin lithosphere or are related to magmatic activity such as porphyry deposits.
3. **Basin anoxia and low clastic sediment supply** that can allow accumulation of organic matter to create a reducing environment for efficient sulfur trapping. Largest size and tonnage of lead and zinc is observed in carbonaceous shale-hosted deposits which indicates that the presence of organic matter amplifies metal precipitation and therefore is vital in the formation of economic grade SEDEX deposits. This is further

corroborated by the excellent correlation shown by the temporal distribution of SEDEX deposits with global oceanic anoxia (Goodfellow et al., 1993; Goodfellow, 2004; Turner, 1992).

4. **Deep syn-sedimentary faults** in the extensional zones that can act as conduits for down welling brines and ascent of buoyant metal-rich hydrothermal fluids. In some cases, mineralization occurs at the hanging wall of fault zones while in others they simply act as feeder pipes that provide pathways for fluids to pass onto permeable host sediments (Goodfellow et al., 1993). Due to ensuing extensional processes resulting in faults and sub-basin formation, that play important role as a trap for brines resulting in brine pools that may give rise to mineralizing ore fluids.

The Proterozoic deposits of Australia and India mainly represent the intracontinental rift setting while passive margin settings are depicted by Paleozoic systems like Selwyn and Kuna basins (Wilkinson 2014). Both Proterozoic and Phanerozoic basins are comprised of extensional sub-basins filled with rift and sag sequences of coarse clastics and minor volcanics, overlain by fine reduced silts, carbonates and shale.

The temporal and spatial distribution of mineral deposits can offer clues to the geological processes driving ore formation and can guide future exploration endeavors (Leach et al. 2010). The current distribution of ore deposits on Earth's surface is intricately linked to the evolution of tectonic processes, changes in atmospheric and hydrospheric oxygen levels, rapid biological evolution, and ongoing tectonic recycling that can lead to the destruction or alteration of ore bodies. The distribution of SEDEX deposits varies significantly across geological time. They first appeared during the Proterozoic era around 2.02 billion years ago, marking the earliest known occurrences of Pb-Zn deposits. Subsequently, between 1.85 and 1.58 billion years ago, a notable surge in SEDEX mineralization occurred in Australia (Mt Isa,

HYC, Century and Broken Hill Pb-Zn-Ag deposits), India (Delhi-Aravalli fold belt deposits), and Canada (Sullivan Zn-Pb-Fe deposits). This timeframe coincides with the Great Oxygenation Event (GOE) that lasted from approximately 2.4 to 1.8 Ga, a pivotal period during which Earth's atmosphere transitioned from a reduced state to an oxygenated environment due to the emergence of $O_2$-producing microbes. The GOE facilitated the oxidation of Earth's hydrosphere, through oxygen dissolution into the upper parts of the oceans and receiving sulfate-rich riverine drainage, effects of which were more pronounced in shallow marginal seas and shelf environments. The added presence of sulfate reducing bacteria in deep marine basins led to massive production of reduced sulfur thereby creating anoxic environments that kick-started the production of SEDEX deposits.

Another cluster of SEDEX deposits emerged during the Late Paleozoic era, such as Tom and Jason Zn-Pb-Ag-barite and Howard's Pass Zn-Pb deposit in Canada, Rammelsberg Zn-Pb-Cu deposit in Germany, and Red Dog and Anarraaq Zn-Pb-Ag deposits in Alaska. This period coincided with global oceanic anoxia driven by high organic productivity and phosphate reflux, creating favorable conditions for SEDEX formation. The absence of SEDEX deposits during the Archean era can be attributed to low sulfate concentrations in seawater with limited oxygen, which hindered the formation of evaporites or basinal brines necessary for SEDEX mineralization (Knauth 2005).

### 1.2.2 Mineralization, Element Zoning and Alteration

Primary minerals in SEDEX include sulfides, sulfosalts, phosphates, chert, barite and carbonates but their proportions vary, for example, barite is seen to be more common in Phanerozoic deposits while pyrrhotite exceeds pyrite abundance in most Proterozoic deposits (Leach et al. 2005). The main ore minerals are sphalerite and galena. Most SEDEX deposits have higher Zn content than Pb with Zn/(Zn+Pb) ratio of 0.7 though deposits like Mt Isa and

Sullivan have near equal amount of Zn and Pb (Large et al., 2005). The ore bodies occur as laminated, wedge-, or lens-shaped, with generally low aspect ratios. The lenses can range up to hundreds or thousands of meters in lateral extent with typical widths of tens of meters (Wilkinson 2014). The dominant iron-sulfide species varies with deposit, for example, in Red Dog and Howards Pass deposits, pyrite is minor to dominant whereas pyrrhotite is ubiquitous in Mt Isa and Sullivan (Leach et al. 2005). Marcasite is common in Duddar deposit (Jankovic 1986) while in others arsenopyrite may also be present. Sulfosalts such as freibergite, boulangerite, tetrahedrite etc. can be minor to ubiquitous component whereas chalcopyrite is enriched in shale hosted deposits (Leach et al. 2005).

Both lateral and vertical mineralogical zoning is common. For example, in Selwyn deposit, there is an increase in oxidized facies, such as barites and iron-oxides, compared to reduced facies, such as sulfides, away from the vent complex (Goodfellow, 2004; Lydon, 2004). This is manifested by decrease in Zn/Ba, Zn/Mn, Cu/(Zn+Pb), Pb/Ag, $SiO_2$/Zn ratios and increase in Zn/Pb ratio away from feeder zone (Leach et al., 2005 and references therein). Vertically upwards, a general decrease in Zn/Pb ratio (Large et al., 2005) and increase in Zn/Fe ratio (Kelley et al. 2004) have been observed in many Australian deposits.

Depending on the characteristics of host sediments and stratigraphic control, alteration haloes in most SEDEX systems are rather laterally extensive than intensive. Broadly, two types of haloes are observed around such deposits; i) *Fe-Mn alteration haloes* occur in dolomitic-siltstones of northern Australian deposits (like Lady-Loretta and HYC) and have Mn-siderite, Mn-ankerite, ferroan dolomite to dolomite zonation, with the Fe and Mn contents gradually decreasing away from the ore (Chapman, 2004; Large et al., 2001; Large & McGoldrick, 1998), and ii) *Silicate alteration haloes* are found in siliciclastic dominated SEDEX systems like Sullivan which exhibit chlorite-pyrrhotite/chlorite-pyrite-albite/tourmaline alteration enveloped by muscovite/sericite alteration on the hanging wall

side accompanied by an overall silicification. Carbonate alteration also occurs at the transition between vent complex and laminated sulfides. In addition to these, lithogeochemical haloes manifested by trace elements like Mn, Tl, As, Ba, Sb, P, REEs (Goodfellow et al., 1990; Large et al., 2001; Slack, 2004) serve as good indicators to ore accumulation and fluid pathways (Leach et al. 2005).

### 1.2.3 Nature and Source of Ore Fluids

To develop a robust genetic model of a hydrothermal deposit, it is essential to address fundamental questions such as the sources of metals and fluids, the physicochemical characteristics of the ore-forming fluid (including temperature, salinity, and $fO_2$), and the mechanism of metal transport by and metal precipitation from the fluid. A direct window to the SEDEX ore fluid properties such as temperature, composition and salinity is provided by fluid inclusion studies; however, high-quality fluid inclusion data is limited due to post-ore modification caused by overprinting deformation and metamorphism of ores in older deposits. Fluid inclusion studies on Proterozoic deposits are best available from Century deposit, Australia where inclusions in sphalerite yielded salinities of 8.9 to 23.3 wt.% NaCl equivalent and temperatures in the range 63 - 180 °C (Polito et al. 2006). Temperature and salinity determined from fluid inclusion studies in the Sullivan deposit span a wide range, up to 400 °C and 45 wt.% NaCl equivalent respectively (Leitch and Lydon 2000). However, a complex fluid flow history and uncertainties on vein genesis hinders data usage and interpretations. Selwyn and Red Dog deposits provide the most reliable data for the Paleozoic group. Salinity and temperature ranges of 4.1 to 18.3 wt.% NaCl equivalent and 194 - 282°C have been recorded for fluid inclusions in gangue minerals such as ankerite, quartz and carbonates from the Tom and Jason deposits (Gardner and Hutcheon 1985; Ansdell et al. 1989). Similar values were recorded by Leach et al., (2004) for inclusions in sphalerite from

Red Dog deposit. Although limitations exist, the fluid inclusion data shows that most of the SEDEX-forming ore fluids are highly saline and low to moderate in temperature. Fluids circulating in the basin sub-surface can be heated by some deep-seated magmatic body (e.g. Sullivan deposit) or simply by elevated geothermal gradient due to rifting. However, evidence of plutonic bodies in the vicinity of ore zones has not been found for most deposits (Lydon 2004a; Leach et al. 2005). High salinity can be explained by the involvement of subsurface evaporitic beds (Land & Macpherson, 1992) or evaporitic brine pools (Lydon 2004b; Leach et al. 2004) giving rise to the basin hugging brine model by Sangster (2002). In systems where direct evidence of evaporites has not been found, strong evaporation of seawater is considered to have contributed to the ore-fluid salinity. According to Cooke et al. (2000), variable concentrations of $H_2S$ or $SO_4^{2-}$ species can result in two types of SEDEX ore fluids. First, a hot (200-300 °C), acidic (pH: <4), and reduced $H_2S$-rich brine which is responsible for generating vent-proximal deposit and contain barite and Au in the ore assemblage, and the second, a cooler (100-250 °C), mildly alkaline (pH: 4-6), and oxidized $SO_4$ rich brine that commonly forms vent-distal deposits and do not contain significant barite or Au.

### 1.2.4 Metal and Sulfur Sources

Lead isotope data suggests that Pb is mainly derived from crustal sources as they fall above the global orogeny growth curve. Intra-deposit homogeneity with respect to the lead isotope data is observed for most of the SEDEX deposits which may indicate that Pb distribution has been homogenized by the circulating hydrothermal fluids or the lead source was already homogenous. Lead model ages show propinquity with host rock ages which suggests that metal was sourced from sediments within the basin (Wilkinson 2014). Sulfur isotopic studies ($\delta^{34}S$) of galena and sphalerite from various SEDEX deposits normally range from -8 to 30‰ that indicate sulfur derivation from seawater, porewater or existing sulfate deposit.

## 1.3 Pb-Zn Mineralized Systems of the ADFB: Current State of Knowledge

The Aravalli-Delhi fold belt (ADFB), one of the richest mineralized belts in India, is well-known for its abundant base metal deposits mainly of Pb, Zn, and Cu, and also for other metals, viz. gold, tin, tungsten, uranium, phosphorites and bauxite (Sarkar and Gupta 2012). A detailed discussion on the regional geology of the ADFB and the local geology of the study area is deferred to Chapter 2. The distribution of the lead and zinc ore mineralization in the ADFB is scattered across the Bhilwara province, Aravalli basin and the Delhi basin. In the Bhilwara province, Zn-Pb mineralization occurs along sub-linear belts at several locations such as Pur-Banera, which hosts the ores in argillaceous, arenaceous and calcareous metasediments such as mica schists, calc-schist and quartz-biotite gneisses, and in Sawar-Bajta, where Zn-Pb-Cu mineralizations occur in dolomitic marble, mica schists and quartzite. However, the major producers of zinc and lead from Bhilwara province are the two most thoroughly studied and well-documented deposits named Rampura-Agucha and Rajpura-Dariba. Zn-Pb (-Ag) base metal mineralization in Rampura-Agucha is hosted in graphite-mica-sillimanite-schist metamorphosed up to upper amphibolite facies (T = 650 ˚C, P = 6kbar; Deb and Sehgal (1997)) and features sphalerite, pyrite, pyrrhotite and galena as major ore minerals, chalcopyrite and arsenopyrite as minor phases, along with a myriad of sulfosalts such as freibergite, tenantite-tetrahedrite, ullmanite, boulangerite etc. Raman spectrometry and fluid inclusion studies indicate mixing and involvement of a low saline (0-8 equivalent wt.% of NaCl) and a highly saline $NaCl_2$+$MgCl_2$-$CaCl_2$ bearing fluid in the ore formation and mobilization (Höller et al. 1996).

The Rajpura-Dariba-Bethumni ore belt hosts large reserves of laminated and stratabound Zn+Pb (-Cu-Ag) mineralization in recrystallized dolostones and graphite-bearing quartz mica schists. The ore assemblage is dominated by pyrite, sphalerite, galena, fahlore and

chalcopyrite with occasional arsenopyrite, pyrrhotite and sulfosalts such as geocronite, pyrargyrite, electrum, argentopyrite etc. The area is metamorphosed up to lower amphibolite facies (Misra 2000; Deb and Pal 2004) with pressures ranging from 5-6 kbar. Primary fluid inclusion studies in quartz revealed the mixing of highly saline metal bearing metamorphogenic carbonic fluid with low saline meteoric fluid as the ore precipitation mechanism. Carbon and sulfur isotopic studies revealed that sulfur may have been sourced from seawater sulfate while carbon was mostly biogenic indicating ample biogenic activity in the ore-bearing basin and the role of carbonaceous shales in formation of such deposits (Deb 1986, 1990). Pb-Pb model age dating of laminated galena have yielded an age of 1.8 Ga, and Pb isotopic ratios suggested that lead was sourced from host sediments that contained components of recycled crustal lead (Deb et al. 1989; Deb and Pal 2004).

In the Aravalli belt, the Zn-Pb mineralization at Zawar stands out due to its remarkable extent, grade, and volume, as well as the distinctive nature of its host rocks. The primary ore-bearing horizon, composed of sphalerite, galena, and pyrite is hosted in carbonaceous dolomitic phyllite. Silver and cadmium are extracted as by-products. The framboidal pyrites and the large variations in sulfur isotopic composition of sulfides, indicate a partial biogenic origin for the sulfur. Studies on carbon and oxygen isotopes from the host dolomite (Sarkar and Banerjee 2004) align with the theory and suggest that these ores were deposited in a marine environment around 1.7 Ga, as measured from Pb-Pb model ages of galena (Deb et al. 1989). Nevertheless, the genetic classification of the Zawar deposit remains a subject of considerable debate since it exhibits characteristics of both SEDEX and MVT types. Additionally, the uncertainty regarding whether the deposition occurred in a deep marine or shallow shelf environment further complicates the genetic classification, leading many researchers to consider it a hybrid deposit similar to the Irish-type ores. In all these deposits, strata-bound and stratiform/stratified ore mineralization is hosted in metasedimentary rocks.

Most of the deposits are considered to be SEDEX type in origin, which were modified during deformation and metamorphism resulting in remobilization of existing ore and/or formation of new ores.

In the NDFB, Zn-Pb mineralization is distributed in Kayad-Madarpura-Ghugra belt and Lohakhan in Ajmer and Manaksas in Khetri sub-basin both of which are severely understudied. In the SDFB, Zn-Pb-Cu type mineralization is found in Deri-Ambaji and Birantiya-Khurd sectors whereas Zn-Cu type deposits occur in Pindwara-Watera sector. Deri-Ambaji deposit is the largest Zn-Pb-Cu deposit in the SDFB however, these ores are thought to be of VMS origin (Deb 2000).

## 1.4 Objectives and Methodologies

SEDEX deposits are not only suppliers of the global Zn-Pb resources, but they also contain a suite of other important minerals such as chalcopyrite, pyrrhotite, pyrite and barite, and/or other precious and critical metals such as Ag, Au, In, Ga, Ge, Cd, Mn, Sb, and Bi which are often mined as by-products from these deposits. This enhances the economic sustainability and resilience of mining operations, enabling optimization of resources, cost reduction, and maximizing profits. Apart from mining, SEDEX deposits also critically contribute to the understanding of Earth's paleoenvironment and tracking the evolving global ocean chemistry (Lyons et al. 2006; Gregory et al. 2017; Large et al. 2017, 2022; Gao et al. 2020; Emmings et al. 2024). However, despite its academic and economic significance, the mechanisms governing the formation of SEDEX deposits are not well constrained thereby posing challenges to effective exploration and extraction. Early theories proposed that these stratiform deposits formed through the exhalation of hot, metalliferous fluids onto the seafloor, with metal precipitation driven by physicochemical changes upon mixing with seawater. However, recent studies suggest that multiple other processes may influence the precipitation

of these deposits. The knowledge gap concerning the SEDEX deposits stems from the limited insights into the sources and chemical compositions of the mineralizing fluids, their migration pathways, interactions with the surrounding rocks and specific temperature and pressure conditions prevalent during the formation of the deposits. To understand the nature of these fluids, primary fluid inclusions in minerals cogenetic with mineralization are mostly relied upon. However, post-ore deformation and metamorphism often lead to the loss or modification of primary fluid inclusions complicating efforts to accurately interpret the original fluid characteristics. As described previously, reliable fluid inclusion data reveal highly saline compositions and low to moderate temperatures. This led to a consensus that seawater primarily contributes to the genesis of SEDEX deposits. However, recent research challenges this notion, proposing involvement of alternative fluid sources such as brine pools, modified seawater, or fluids derived from evaporite (marine/non-marine)-dissolution. Although most SEDEX deposits are rarely economically extractable due to their typical stratiform and stratabound nature, several of the world's largest Pb-Zn deposits such as Sullivan in Canada, Mt. Isa, HYC and Broken Hill in Australia, Jinding and Dongshengmiao in China are classified as remobilized deposits. The mobilization process relocates stratiform ores and transforms them into larger, economically viable deposits suitable for profitable mining. Nevertheless, these mobilization mechanisms remain inadequately understood. Researchers like Gilligan and Marshall (1987), Marshall et al. (1998), Wagner and Cook (1999), Mavrogenes et al. (2001), Frost et al. (2002) have proposed various theories on the mechanisms of mobilization which include solid state flow, chemical dissolution and reprecipitation, or sulfide anatexis and localization of sulfides. However, natural processes are inherently complex, influenced by multiple factors that dictate the nature and efficacy of these mobilization patterns. Therefore, a thorough understanding of the ore-forming and subsequent mobilization processes is vital for advancing the knowledge on origin and evolution of

SEDEX systems. This knowledge will not only help refining exploration models and optimizing extraction processes but also foster the development of sustainable mining practices aimed at minimizing environmental impact.

The present study endeavors to unravel the intricacies of SEDEX systems, focusing on Kayad, one of the prominent high-grade Pb-Zn deposits within the Aravalli Delhi fold belt of India. The overall objective encompasses explaining the fundamental mechanisms governing ore formation, identifying the origin and nature of the fluids responsible for sulfide deposition, and investigating the mobilization processes that have resulted in the genesis of these exceptionally rich ore bodies.

The study area is a zinc-lead deposit in western India's Aravalli Delhi fold belt that forms a part of the Great Indian Proterozoic Fold Belts (GIPFOB). The deposit, called Kayad, is a young deposit from the viewpoint of industrial exploration and even younger from an academic perspective. Zinc and lead occur as medium to high grade sulfide ores which are hosted predominantly in graphite bearing mica schists and partly in quartzite and calc-silicate rocks. Sphalerite and galena form the major ore minerals with minor associated sulfides such as chalcopyrite, pyrrhotite, pyrite and arsenopyrite. Preliminary study shows that there are three different types of Zn-Pb ores: disseminated/laminated, massive and vein type. Pegmatite, aplite and quartz veins some of which contain pyrrhotite and chalcopyrite mineralization are seen to cut across the mica schist containing laminated ores. Although several works exist on the Zn-Pb mineralization in the Aravalli-Delhi Fold Belt, there is no published literature available on the polymetallic mineralization at Kayad. Therefore, it is unclear whether the deposit at Kayad formed and evolved in a similar way or whether it constitutes an integral part of the geological and metallogenic evolution of the entire belt.

Considering the lacunae in our understanding of the origin and physicochemical evolution of SEDEX deposits in general and Kayad polymetallic deposit in particular, the objectives and methodologies of the current research are summarized below.

1. *Identification of host rocks, mode of occurrence and texture of Zn-Pb and Cu-Fe ores*. For this purpose, thorough field work was conducted in Kayad, Ajmer. However, since the surface areas surrounding the Kayad Zn-Pb mine consists of mainly granites and gneisses ("basement rock") with negligible surface outcrops of ore bearing rocks, majority of the sampling was done from the underground mine. Samples collected from different levels and boreholes were studied, and polished thin sections were prepared for some selected samples that represented all the rock types and sulfide assemblages. Petrographic examination was done under transmitted and reflected light microscopes to document mineralogical constituents of the different host rocks, and to identify the main ore minerals and their textural relation with other associated minerals. Scanning Electron Microscope (SEM- EDS) was further used to identify unknown minerals, estimate the approximate modal abundance of sulfides and sulfosalts, and capture variations in chemical compositions in mineral grains using back scattered electron (BSE) images.
2. *Deciphering the mechanism, including the physicochemical conditions (pressure, temperature), of primary mineralization and subsequent remobilization*. This warranted an integrated approach combining mode of occurrences, mineralogy, texture and detailed geochemical investigation of the sulfides and associated silicates. The major and trace element compositions of sulfides and selected silicate minerals were identified using Electron Probe Micro Analyzer (EPMA) and Laser Ablation-Inductively Coupled Plasma Mass Spectrometer (LA-ICPMS) respectively. Element distribution maps of areas showing significant mineral-scale alteration were obtained

using EPMA to fingerprint the elements associated with the altered assemblages and the alteration pathways. Thermometric calculations on the host rock biotite, and arsenopyrite and sphalerite among sulfides, were done using their major and trace element compositions to have an idea about the peak metamorphic temperature attained by the country rock and the temperature of ore remobilization.

3. *Determining the type of Zn-Pb mineralization, and unravelling the nature of fluid responsible for the primary ores and subsequent remobilization of pre-existing ores.* This was achieved by determining the *in situ* multiple sulfur isotope signatures of sulfides, and the major, trace and boron isotope compositions of tourmaline to pin-point the source of fluids. In-situ multiple sulfur isotopic analyses were carried out on Nanoscale Secondary Ion Mass Spectrometer (Nano-SIMS) which were complemented by bulk $\delta^{34}S$ analysis of sphalerite mineral-separates in an Isotope Ratio Mass Spectrometer (IRMS). In-situ $\delta^{11}B$ measurement of different tourmaline types, genetically associated with the sulfide mineralization, was conducted on a Multi-Collector ICPMS (MC-ICPMS) to identify the source of boron.
4. *Identification of critical metal(s) that can be recovered as by-product of Zn-Pb mining* (besides Ag, which is already being recovered) integrating ore mineralogy and mineral chemistry of different ore types.

The details of each procedure and their analytical conditions are laid down in the respective chapters.

## 1.5 Outline of the Thesis

The thesis comprises of six chapters. **Chapter 1** (current chapter) introduces the sedimentary exhalative or SEDEX type Zn-Pb mineralization through a detailed review of the general aspects of the deposit type including classification schemes, tectonic ambience, commonly

observed mineralization and alteration features, and the nature and source of ore fluids and metals as known from published literature. The next part delves into the details of the Zn-Pb mineralization systems in the Aravalli-Delhi metallogenic province in northwestern India which hosts some of the largest and oldest SEDEX ore deposits in the world and within which the study area is located. The chapter ends with a discussion on the origin of the research problem addressed in the thesis in the context of global and regional SEDEX mineralization followed by objectives and methodologies adopted.

**Chapter 2** deals with the geology of the Kayad deposit. The first part includes the regional geology, that is, the litho-stratigraphy, deformation and metamorphic history, and tectonic setup of the Aravalli Delhi fold belts. The next part elucidates the local geology around the Kayad Zn-Pb deposit (the study area) including the litho-contacts, host rock variations, mineralization styles evidenced from surface and sub-surface investigations.

**Chapter 3** elaborates on the Zn-Pb (Fe-Cu) mineralization in Kayad. It comprises the results of petrographic analysis of the host rock and textural and mineralogical studies conducted on ore and gangue minerals utilizing transmitted and reflected microscopy, SEM and EPMA. The three styles of sulfide mineralization recognized from the mode of occurrence of the sulfides are discussed along with the hydrothermal alteration signatures associated with them.

**Chapter 4** presents the results of the geochemical analyses of the sulfide minerals that encompass the major, minor, and trace element compositions of sphalerite, galena, pyrrhotite, chalcopyrite and arsenopyrite along with their multiple sulfur isotope systematics. These analytical results are, in one part, utilized to interpret the distinguishing characteristics of the three different styles of mineralization, and secondly, used to perform thermometric calculations to have an idea about the thermochemical conditions prevailing during ore deposition, and to understand the incorporation and partitioning styles of different trace

elements into the sulfide phases. Lastly, the results of multiple sulfur isotopic studies on the sulfides representative of the different mineralization styles are used to understand the source of sulfur in the deposit.

**Chapter 5** attempts a multiple approach towards answering one of the most fundamental questions pertaining to a hydrothermal ore deposit, that is, the source of fluid. This is achieved by using tourmaline as a mineral proxy, since it is cogenetic with the primary sulfide mineralization and the later remobilized sulfides. The chapter firstly describes the occurrence of tourmaline and proceeds to interpret the major, minor, trace and boron isotopic composition of tourmaline from different sulfide ores.

**Chapter 6** integrates the mineralogical, textural and geochemical interpretations developed in the previous chapters to provide a comprehensive ore-genetic model for the Kayad Zn-Pb deposit (both for primary and remobilized ores) highlighting the mechanism of primary ore mineralization and its remobilization as well as the source of fluid involved in the processes.

**Chapter 7** gives a brief summary on the genesis and evolution of Kayad Zn-Pb deposit highlighting how multifaceted approach can provide important insights into the understanding of SEDEX deposits in general. The chapter ends with the limitations of the current study and future scope of research.

It may be noted that the four major chapters (Chapter 3 to Chapter 6) start with an introduction to the chapter and end with a summary of the chapter.

# CHAPTER 2: Geological Background of Kayad Zn-Pb Deposit

## 2.1 Regional Geology

The Greater Indian landmass is an amalgamation of Archean to Proterozoic crustal domains that underwent accretion along regional-scale shear zones spanning varying ages. These interconnected shear zones form a highly-tectonized belt known as the Greater India Proterozoic Fold Belt, GIPFOB (Fig. 2.1, inset) which consists of Early Proterozoic to Neoproterozoic magmatic and metamorphic rocks (Banerjee et al., 2021; Radhakrishna & Naqvi, 1986). The GIPFOB extends in an east-west orientation in central India curving into an NNE trend in north-west India. It is comprised of the Eastern Ghats Mobile belt (EGMB) in the east, the Central Indian Tectonic Zone (CITZ) or Satpura Mobile Belt (SMB) in the central part, and the Aravalli Delhi Fold Belt (ADFB) in the north-west. In central India, the GIPFOB marks the zone of accretion between the northern Archean Bundelkhand Craton block and the southern ensemble of Archean Singhbhum, Bastar and Dharwar cratons (Radhakrishna and Naqvi 1986; Leelanandam et al. 2006). This intricate geological structure, spanning a vast temporal and spatial range, underscores the dynamic evolution and complexity of the geological history of the Indian subcontinent.

The ADFB constitutes the western part of the GIPFOB (Fig. 2.1) spanning over the states of Rajasthan, Madhya Pradesh and some parts of Uttar Pradesh and Gujarat. The basement, known as the Banded Gneissic Complex or BGC (Heron, 1953), is the oldest geological unit in Rajasthan. It is composed of tonalite-trondjhemite gneiss dated at 2.8-3.3 Ga (Gopalan et al., 1990; Roy & Kröner, 1996; Wiedenbeck et al., 1996) and contains isofacially metamorphosed enclaves of mafic and sedimentary rocks. A significant part of BGC is comprised of late, acidic to intermediate granitoid intrusives which have been dated between 2.9 and 2.5 Ga (Choudhary et al., 1984; Roy & Kröner, 1996; Wiedenbeck et al.,

1996). Among them, the emplacement of the Berach granite between Vindhyan and BGC at 2610 ± 50 Ma (Wiedenbeck et al., 1996) led to the development of granite-greenstone sequence of Rajasthan and marked the late Archean cratonisation in the western shield (Sinha-Roy, 1985).

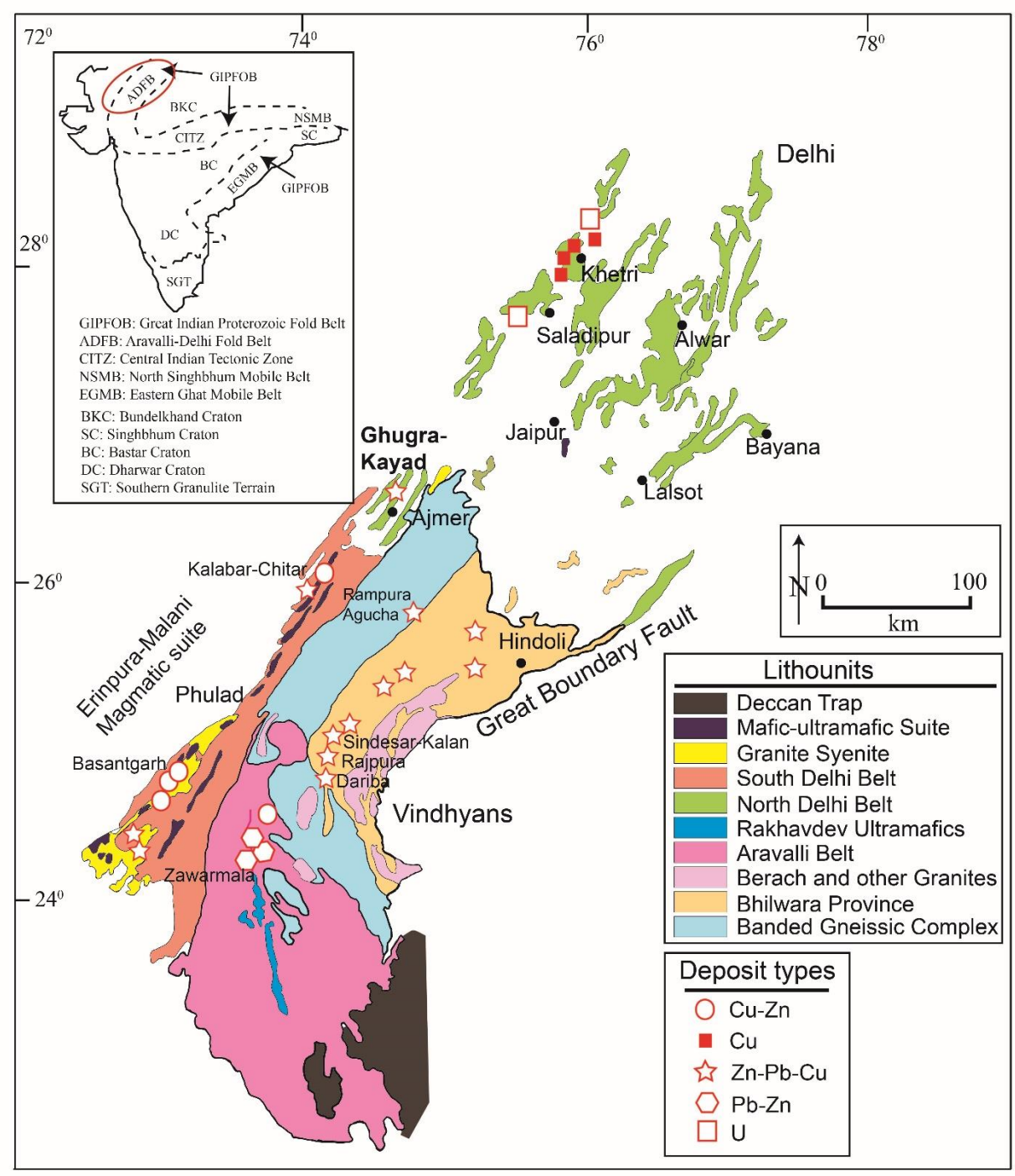


**Figure 2.1:** Geological map of Delhi Aravalli Fold belt with the lithological units and locations of different deposit types (redrawn from Deb et al. 2001). The inset map shows the location of the Delhi Aravalli Fold Belt with reference to the Indian subcontinent and the Great Indian Proterozoic fold belt.

The rocks of the BGC have suffered 3 to 4 phases of deformation. The grade of metamorphism increases from amphibolite facies in the east to granulite facies in the west (Naha & Roy, 1983; Pyne & Bandopadhyay, 1985).

The Aravalli fold belt, overlying the BGC, is a N-S trending, Paleo- to Meso-proterozoic supracrustal belt of rocks. According to the classification scheme of Sinha-Roy et al. (1993), the Aravalli Supergroup is divided into a lower Delwara Group of rocks followed by Debari and Jharol Group(s) of rocks. The Delwara Group comprises mafic volcanic rocks, quartzites, carbonates and banded iron formations, while the Debari Group is represented by polymictic conglomerates, phosphoritic carbonates, phyllites and greywackes. The Jharol Group comprises impure limestone, quartzite, phyllite and biotite schists. The rocks of the Aravalli Supergroup are multiply deformed and metamorphosed with an east to west increase in metamorphic grade from greenschist to amphibolite facies. The granulite-grade supracrustal sequence of the Bhilwara province, consisting of several isolated, sub-parallel and sub-linear supracrustal belts (Rampura-Agucha, Rajpur-Dariba-Bethumni, Pur-Banera and Sawar-Bajta) is known for rich reserves of lead and zinc mineralization. Even though the stratigraphic position of Bhilwara province is debatable, it is currently classified as belonging to both Archean BGC and the Proterozoic Lower Aravalli Group (Srikantappa, 2001). The major rock types representing the Bhilwara group include mica-schists and migmatitic paragneisses. Several elongate bodies of carbonate-sandstones, black shales and ironstones represent the narrow, mineralized belts of Rampura-Agucha, Rajpura-Dariba and Pur Banera.

The Aravalli Supergroup is overlain by the Meso- to Neo-Proterozoic Delhi fold belt (DFB) which spans 700 km from Delhi in the north to Idar (Gujarat) in the south. Geographically, the DFB is divided into the North Delhi fold belt (NDFB) and the South Delhi Fold belt (SDFB), Ajmer being the point of divide (Fig. 2.1). The NDFB is characterized by horst and graben structures in the pre-Delhi basement rocks. The grabens are

filled by sediments of the Raialo Group which consists of basal conglomerate, quartzite and basic volcanics. This is followed by the Alwar Group, which is mostly arenaceous consisting of conglomerate, gritty quartzite, arkose and shale, and the Ajabgarh group, which has a rather argillaceous character represented by shale, phyllite and ferruginous quartzites. Three phases of deformation have been recorded in the NDFB (Naik et al., 2022). The first phase of deformation formed isoclinal folds which were later overprinted by slightly plunging open folds. The third generation shows broad open folds. Based on stratigraphy and metamorphic evolution, the NDFB is divided into three sub-basins namely Khetri, Alwar and Bayana-Lalsot (Fig. 2.1). The metapelites of Khetri basin record three regional metamorphic events where peak temperature-pressure conditions of 550-600°C/5.5 kbar were attained during M2 metamorphism (Sarkar & Dasgupta, 1980). The Alwar sub-basin has undergone two prograde metamorphic phases where M2 records peak conditions of 645°C at 7 kbar (Naik et al., 2022; Pant et al., 2008) whereas the Bayana rocks are less deformed and metamorphosed than Alwar and attained lower greenschist facies conditions (Mehdi et al., 2015; Sarkar & Gupta, 2012). The area under study is located near Ajmer in the southernmost sector of the NDFB. Numerous small-sized granitoid bodies intrude into the metapelites and metavolcanic rocks of NDFB such as Ajmer, Bairat, Ajitgarh, Khetri, Gothra, Jasrapura, Saladipura granites etc. which were emplaced between 1.8 and 1.6 Ga (Ghosh et al., 2022 and references therein). These plutons are associated with large-scale feldspathisation and albitisation.

The South Delhi Fold Belt (SDFB) or the Main Delhi Synclinorium (Heron, 1953) is an intracratonic rift basin which consists of bimodal volcanics, platform carbonates, varied sedimentary rocks and ophiolitic suites. The SDFB rocks show an overall amphibolite facies of metamorphism though there is gradual increase in grade from the east (Staurolite-Kyanite zone near BGC) to the west (Sillimanite-Muscovite) with isograds running parallel to the compositional layering.

## 2.2 Local Geology

### 2.2.1 Geology of Kayad

The Kayad deposit (26° 31’ 50.37” N; 74° 41’ 24.96” E) is located nine kilometers north-northeast of Ajmer city. Most of the lithounits in the area are only sporadically exposed due to thick soil cover. Much of what is known about the geology of the Kayad deposit is from the initial explorations by the Geological Survey of India and pre-mining surveys conducted by Hindustan Zinc Limited, which is currently mining the deposit.

The Kayad-Ghugra belt forms a part of the east-central Proterozoic belt of the Delhi Supergroup. The rocks of the Ajmer-Sambhar area are represented by the upper Ajmer Formation of the Ajabgarh Group. Almost all the quartzite ridges girdling the Anasagar valley to the west of the Ajmer city are underlain by Anasagar migmatites comprising biotite-rich paragneisses, amphibolites, metapsammites, and xenolithic biotite-hornblende orthogneisses (Fareeduddin et al., 2014). Mukhopadhyay et al., (2000) reported an age of 1849±8 Ma for the granite gneisses based on single-zircon evaporation method. The Anasagar migmatite is later intruded by several granitic bodies among which Anasagar granite has been dated at 1600±90 Ma by Choudhary et al. (1984). The lithounits constituting Ajmer formation are represented by Taragarh quartzite, and Kalyanipura sequence that consists of arkose-pelite-greywacke and subordinate carbonates.

### 2.2.2 Deformation and Metamorphism

The rocks around the Kayad deposit record four episodes of deformation: i) The primary folding (F1) is represented by bedding parallel schistosity (S1), minor rootless isoclinal folds, mineral and stripping lineation; ii) The F2 folds, depending upon their position with respect to the major F3 structures, are either reclined NNE/SSW closing folds or E-W closing recumbent folds. The most prominent schistosity in the area is crenulation and zonal cleavage

synchronous with D2 deformation which transposes the S1 schistosity; iii) The F3 folds are NE trending and SW closing folds of regional scale; iv) E-W to ENE-WSW trending warps represent the fourth (F4) phase of folding. Minor longitudinal shears parallel to the trends of rock formation and related to F2 and F3 deformation, locally cause mylonitization and ultra-mylonitization.

The grade of metamorphism increases from east to west starting with kyanite-staurolite zone (middle amphibolite facies) in the east, sillimanite-muscovite zone (upper amphibolite) in the center (Kayad-Ghugra area) and orthopyroxene-bearing zone (granulite facies) in the west. The isograd between eastern and central zone roughly follows the trends of the formations while the isograd between western and central sector is marked by a major ductile shear zone. The upper amphibolite facies metamorphism in the Kayad-Ghugra area is synchronous with the second of four phases of regional deformation (Fareeduddin et al., 2014). Thermo-barometric studies conducted on syn- to post-D2 garnet and staurolite porphyroblasts in the metapelites of the Ajmer-Puskar section yielded peak P-T estimates of 5.7 ±1.5 kbar and 560 ± 50 °C (Chattopadhyay et al., 2012).

### 2.2.3 Kayad Zn-Pb Deposit

#### 2.2.3.1 Stratigraphy

Prior to the initiation of mining, the Kayad prospect occurred as a dome shaped outcrop of quartzite, calc-silicate, pegmatite and amphibolites. Drilling investigations revealed Anasagar gneisses and migmatites occupying the western plain while the eastern side comprised of meta-sediments such as quartzite, quartz-mica schist and calc-silicate. Pegmatite and secondary quartz veins profusely invade these rocks in the form of sills and dykes. Sills of amphibolites are also occasionally noted in the bore holes. The local stratigraphic succession is as follows (Fareeduddin et al., 1995):

| | |
|---|---|
| Intrusives | Quartz/Pegmatite veins |
| | Amphibolite sills |
| Ajmer Formation | Garnet bearing Quartz-Mica schist |
| | ~~~~~~~~ Local shearing~~~~~~~~ |
| | Calc-silicate |
| | Quartzite |
| | ~~~~~~~~~~ Shearing ~~~~~~~~~~ |
| Anasagar Migmatites | Gneisses and Migmatites |

----------Basement (Uncharacterized)----------

#### 2.2.3.2 Deposit Lithology and Structure

The Kayad base metal deposit forms a part of the 20 km long and 4 km wide Ajmer Zn-Pb belt (Fareeduddin et al., 2014) (Fig. 2.2A). The general trend of the formations in Kayad is NNE-SSW to N-E, coinciding with the regional trend of the axis of the Delhi synclinorium. The transverse section of Kayad deposit (Fig. 2.2B) shows an open synformal fold with a shallow NE plunging hinge that strikes N25°E-S25°W. The western limb dips about 60° to 70° due SE but the dip becomes shallower with increasing depth of the ore body such as between 10° and 40° due SE at around 250m from the surface. Primary bedding in the schist is preserved in the form of compositional banding as well as alternating fine- and coarse-grained layers in metasedimentary rocks. The schistosity, marked by stretched quartz and oriented mica grains, is parallel to the axial plane of the $F_2$ folds and constitutes the dominant tectonic fabric in the rocks. The rock types exposed at different mine levels include calc-silicate rocks, pegmatite, quartz-mica-schist and amphibolite (Fig. 2.2B). Massive high-grade ores occur mostly in graphite-bearing quartz mica schist with total reserves of 9.74 million tons at an average grade of 7.23% Zn and 1.17 % Pb as of 2017 (courtesy of HZL). Sphalerite

and galena constitute the major ore minerals together with minor to trace amounts of chalcopyrite, pyrrhotite, arsenopyrite and pyrite. The main ore lens of the deposit varies in width from 5m in the steeper portions to 35m in the flatter hinge areas.

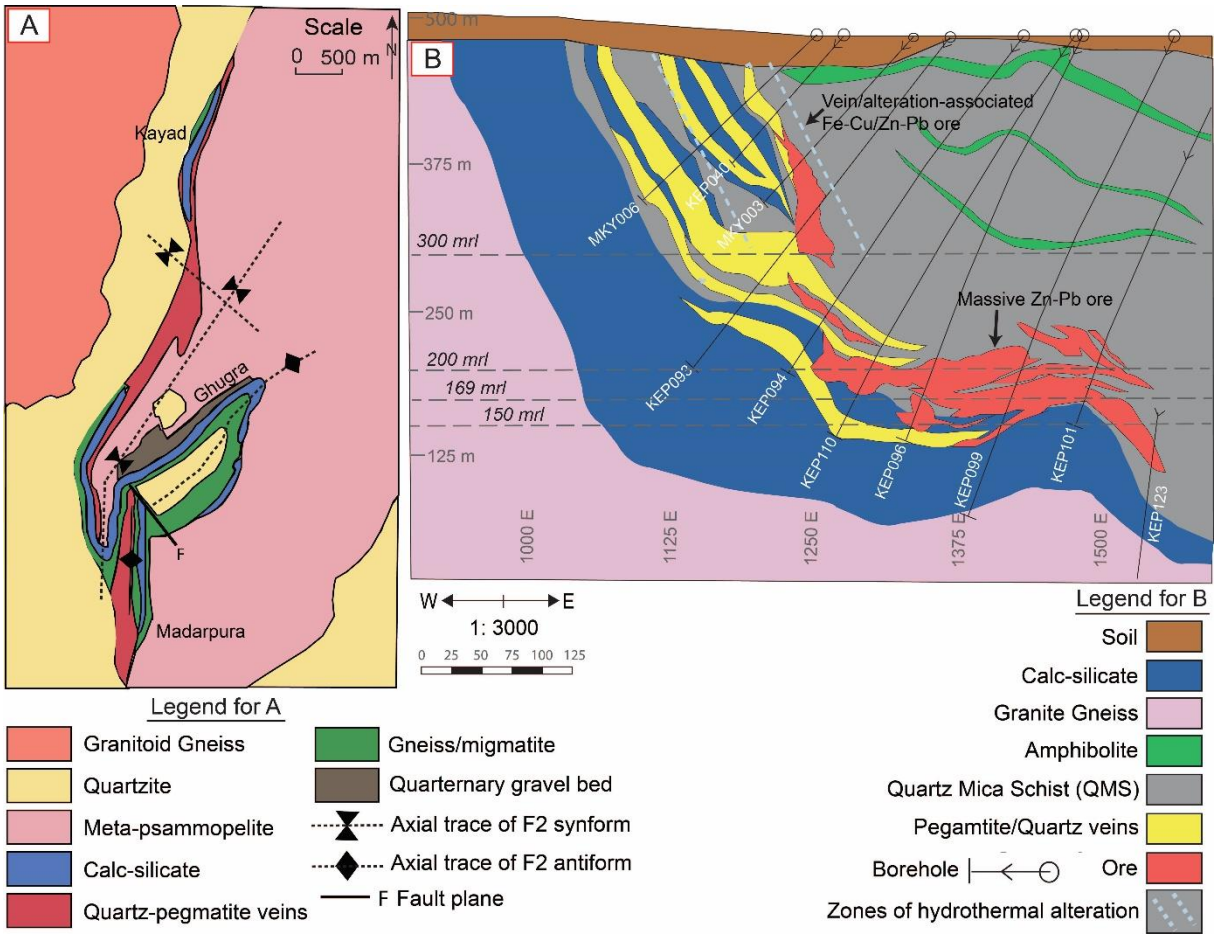


**Figure 2.2:** A) Geological map of Kayad (Chattopadhyaya, 1992); B) Schematic cross-sectional map of Kayad deposit, marked with mining levels (courtesy Hindustan Zinc Limited), mrl is mean reduced level in meters. The host lithounits occur as a synformal fold with the ores at the hinges and eastern limb. Note the localization of massive Zn-Pb ores and vein/alteration-associated Fe-Cu/Zn-Pb ores at the hinge and footwall respectively. Horizontal dashed lines mark the depths at which samples for this study were collected.

The contact between calc-silicate and quartz mica schist in the footwall is characterized by a major shear zone trending N-S to NNE-SSW. This 40 to 100m wide shear zone consists of highly mylonitized and brecciated quartz mica schist, and profuse emplacement of pegmatitic bodies (Fig. 2.2B) that contain abundant chalcopyrite and pyrrhotite with lesser sphalerite and galena mineralization. In the hanging wall side, a 30-40m

thick, prominent zone of alteration of muscovite to sericite and biotite, and hornblende to chlorite is observed. Joints are common in quartzite, quartz mica schist, and calc-silicates with one group having E-W trend and near-vertical dispositions whereas the other set exhibits NNE-SSW trend with 70° to 80° dips due east or west.

## 2.3 Summary

The Greater Indian landmass is a result of accretion of Archean to Proterozoic crustal domains along a highly tectonized belt known as Greater India Proterozoic Fold Belt or GIPFOB that includes the Eastern Ghats Mobile Belt (EGMB), the Central Indian Tectonic Zone (CITZ), also known as the Satpura Mobile Belt (SMB), and the Aravalli Delhi Fold Belt (ADFB). The ADFB, located in the northwest India, lies on the Archean Banded Gneissic Complex (BGC), overlain by Paleo- to Meso-proterozoic Aravalli and Delhi Supergroup of rocks. The Delhi Fold Belt (DFB) is further subdivided into the North Delhi Fold Belt (NDFB) and the South Delhi Fold Belt (SDFB). The area of interest for the current study, known as Kayad, lies at the southernmost sector of the NDFB (Fig. 2.1). The Kayad Zn-Pb deposit is represented by the Ajmer Formation of the Ajabgarh Group belonging to the Delhi Supergroup with the Anasagar migmatite forming the basement. The major rock types around the deposit are quartzite, calc-silicate, pegmatite, and amphibolites, that have experienced four episodes of deformation and up to upper amphibolite facies metamorphism exhibiting peak pressure-temperature conditions of 5.7 kbar and 560°C. The Kayad Zn-Pb deposit occurs in a synformal fold structure, with the high-grade massive ores primarily composed of sphalerite and galena, hosted in graphite-bearing quartz-mica schist, and predominantly concentrated at the hinges of the regional fold. The contact between calc-silicate and quartz-mica schist in the footwall is marked by a major shear zone, which is populated by numerous pegmatite bodies. The pegmatites host significant chalcopyrite and pyrrhotite mineralization and show

signatures of pervasive hydrothermal alteration. Thus, the Kayad deposit hosts complex sulfide mineralization with varying host rocks, mode of occurrence, overprinting deformation and metamorphism with/without associated hydrothermal alteration signatures. Consequently, detailed petrographic analysis is the next required step in deciphering the detailed ore and gangue mineral associations, their textural relations, as well as mineralogy and texture of hydrothermal alteration, which are explored in the next chapter.

# CHAPTER 3: Pb-Zn (Fe-Cu) Mineralization at Kayad: Mode of Occurrences, Textures and Hydrothermal Alterations

## 3.1 Introduction

Among the six rock types, namely graphite-bearing quartz mica schist, quartzite, amphibolite, calcsilicate, granite gneiss and pegmatites, present in the Kayad area and in the underground mine, only quartz mica schist, quartzite and pegmatite hold the majority of the ore mineralization. Subordinate mineralization is noticed in calc-silicate in the form of veins and stringers. Due to thick soil cover, ore samples from the surface could not be collected. To have a comprehensive understanding of the spatial distribution of the rock types and ore bodies, samples were collected from various mining levels such as 125 mrl, 150 mrl, 169 mrl, 200 mrl, and 300 mrl (mrl is mean reduced level in meters and the mine surface level is 487 mrl) (Fig. 3.1). Additional samples were collected from the mine dump and stock pile with their approximate locations in the mines being known. Samples from exploratory boreholes developed through surface drilling and underground drilling were also collected. The schematic transverse section of the Kayad mine along with the location of major ore bodies and the mining levels are given in Figure 2.2B (Chapter 2).

This chapter provides detailed descriptions of the rock types along with the mode of occurrences and textures of the Zn-Pb and Fe-Cu ores present in the Kayad deposit. Some of the ores are associated with prominent hydrothermal alterations, which can provide important clues about the nature of the fluid involved in mineralization and remobilization. This chapter also provides detailed description of the mineralogy and texture of the alteration assemblages and chemistry of selected alteration minerals.

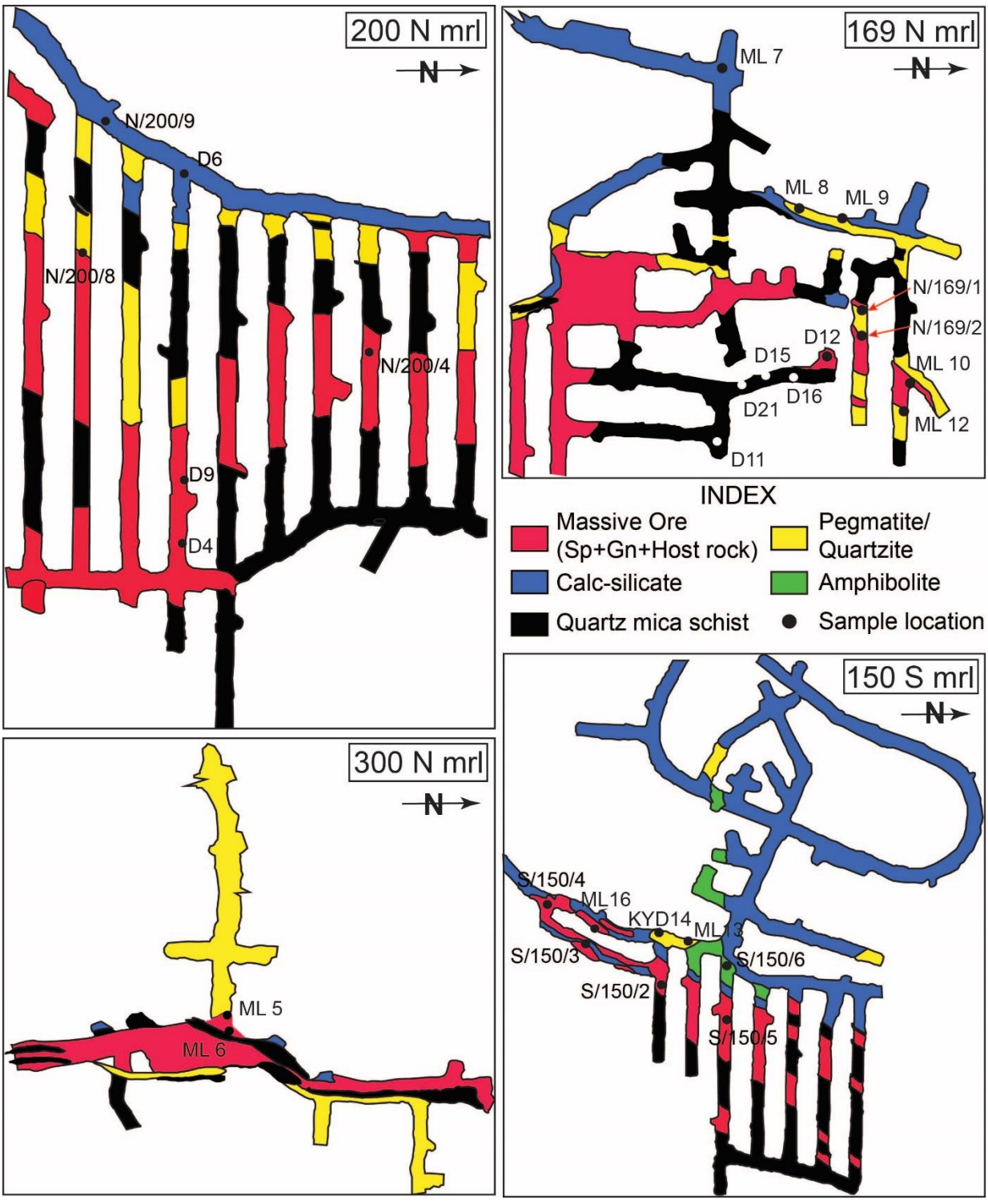


**Figure 3.1:** Plan maps of the levels from which sampling were performed with sample locations (map courtesy Hindustan Zinc Limited). Alphanumeric values on the maps are sample numbers.

## 3.2 Methodology and Analytical Conditions

Petrographic studies were carried out on 50 representative polished thin sections selected from all rock types hosting mineralization using an optical microscope (NIKON100POL), a JEOL JSM-6490 scanning electron microscope (SEM) with an Oxford X-Max$^N$ silicon drift EDS detector, and a ZEISS EVO 18 Analytical SEM. Backscattered electron (BSE) images were used for characterizing textural relationships and intra-grain compositional heterogeneities, if any. The SEM analyses were done at the Department of Geological Sciences, Jadavpur University (ZEISS EVO 18) and at the Department of Geology and Geophysics, Indian Institute of Technology (IIT), Kharagpur (JEOL JSM-6490).

The electron probe micro analyses of silicates were conducted using a Cameca SX-100 instrument with a 20 kV accelerating voltage and a 20 nA beam current, at the Department of Geology and Geophysics, Indian Institute of Technology (IIT), Kharagpur. The operating conditions were 15 kV accelerating voltage and 10 nA beam current with a $LaB_6$ electron source. The X-ray lines and mineral standards used in the analyses are as follows: F-*Kα* (fluorite), Na-*Kα* (albite), Mg-*Kα* (periclase), Al-*Kα* (corundum), Si-*Kα* (peridote), P-*Kα* (apatite), Cl-*Kα* (halite), K-*Kα* (orthoclase), Ca-*Kα* (wollastonite), Ti-*Kα* (rutile), Cr-*Kα* (chromite), Mn-*Kα* (rhodonite), Fe-*Kα* (hematite), and Ba-*Lα* (barite); pure metal was used as a standard for Ni. A second phase of analyses were conducted on a CAMECA SXFive EPMA at Mantle Petrology Lab, DST-SERB National Facility, Department of Geology (Center of Advanced Study), Insititute of Science, Banaras Hindu University. Analyses was done using a CAMECA SXFive instrument operated by SXFive Software at a voltage of 15 kV and current 10 nA with a LaB6 source in the electron gun for generation of electron beam. Natural silicate mineral andardite as internal standard used to verify positions of crystals (SP1-TAP, SP2-LiF, SP3-LPET and SP4-TAP) with respect to

corresponding wavelenght dispersive (WD) spectrometers (SP#) in CAMECA SX-Five instrument. X-ray lines and standards for calibration, X-ray elemental mapping and quantification are the same as used for EPMA in IIT-Kharagpur. In addition, a synthetic glass standard YAG supplied by CAMECA-AMETEK was also used. Routine calibration, acquisition, quantification and data processing were carried out using SxSAB version 6.1 and SX-Results softwares of CAMECA.

## 3.3 Host Rocks

The compositions of the major rock types that host sulfide mineralization are discussed below and the salient features are summarized in Table 3.1.

| **Type of Sulfide Mineralization** | **Host** | **Host Rock/Vein Mineralogy** | **Sulfide Mineralogy** | **Associated Alteration features** |
|---|---|---|---|---|
| Disseminated/ Laminated | Quartz mica schist | Quartz, muscovite, biotite, oligoclase-andesine, graphite, tourmaline | Sphalerite, pyrrhotite ± chalcopyrite ± galena | No alteration |
| | Quartzite | Quartz, tourmaline, graphite ± oligoclase ± muscovite ± biotite | Sphalerite, pyrrhotite, chalcopyrite | No alteration in association with disseminated/laminated ores;<br>chamosite and albite in vicinity of pyrrhotite veins intruding the quartzite. |
| Massive | Quartz mica schist | Quartz, muscovite, biotite, oligoclase-andesine, graphite, tourmaline, apatite | Spahelrite, galena, arsenopyrite, pyrrhotite, chalcopyrite ± sulfosalts | No alteration in and around the massive ores;<br>a) replacement of oligoclase-andesine by K-feldspar and albite and,<br>b) assemblage of monazite + allanite-clinozoisite + apatite in the vicinity of pyrrhotite-chalcopyrite-rich massive Zn-Pb sulfide |

| | | | | |
|---|---|---|---|---|
| Vein/Veinlets | Pegmatite | Vein mineralogy: Oligoclase, quartz, muscovite | Pyrrhotite, chalcopyrite ± sphalerite ± galena | a) Pegmatitic oligoclase-andesine is replaced by K-feldspar + albite<br>b) pegmatitic muscovite is replaced by K-feldspar + albite + biotite + chamosite<br>c) alteration assemblage of Al-pumpellyite + K-feldspar + albite + graphite<br>d) increased proportion of coarse-grained biotite and patchy graphite in the vein wall |
| | Veinlets in Calc-silicate | Calcsilicate mineralogy: augite ± garnet<br>Vein mineralogy: pyrrhotite-sphalerite ± chalcopyrite, sphene, calcite, hornblende | Pyrrhotite, sphalerite ± chalcopyrite | Sphene, chlorite, epidote, calcite, hornblende |
| | Microcline vein-hosted | QMS mineralogy: Muscovite, biotite, quartz, plagioclase > orthoclase, tourmaline, apatite, graphite<br>Vein mineralogy: microcline, quartz ± biotite ± tourmaline | Sphalerite, Galena, Pyrrhotite, ± Chalcopyrite ± Arsenopyrite, | a) Prehnite + pumpellyite + clinochlore ± albite replacing K-feldspar;<br>b) assemblage of monazite + allanite-clinozoisite + apatite in the vicinity of mineralization |

**Table 3.1:** Summary of mineralization style, host rocks/vein mineralogy, ore mineralogy, mineral alteration features and hydrothermal mineral assemblages.

### 3.3.1 Graphite-bearing Quartz Mica Schist

Graphite-bearing quartz mica schist (QMS) occupies the flat terrain lying east of Kayad village but rarely occurs as an outcrop due to soil cover. The rock is dark gray to grayish black in color, exhibits a fine to medium grain texture and displays schistosity.

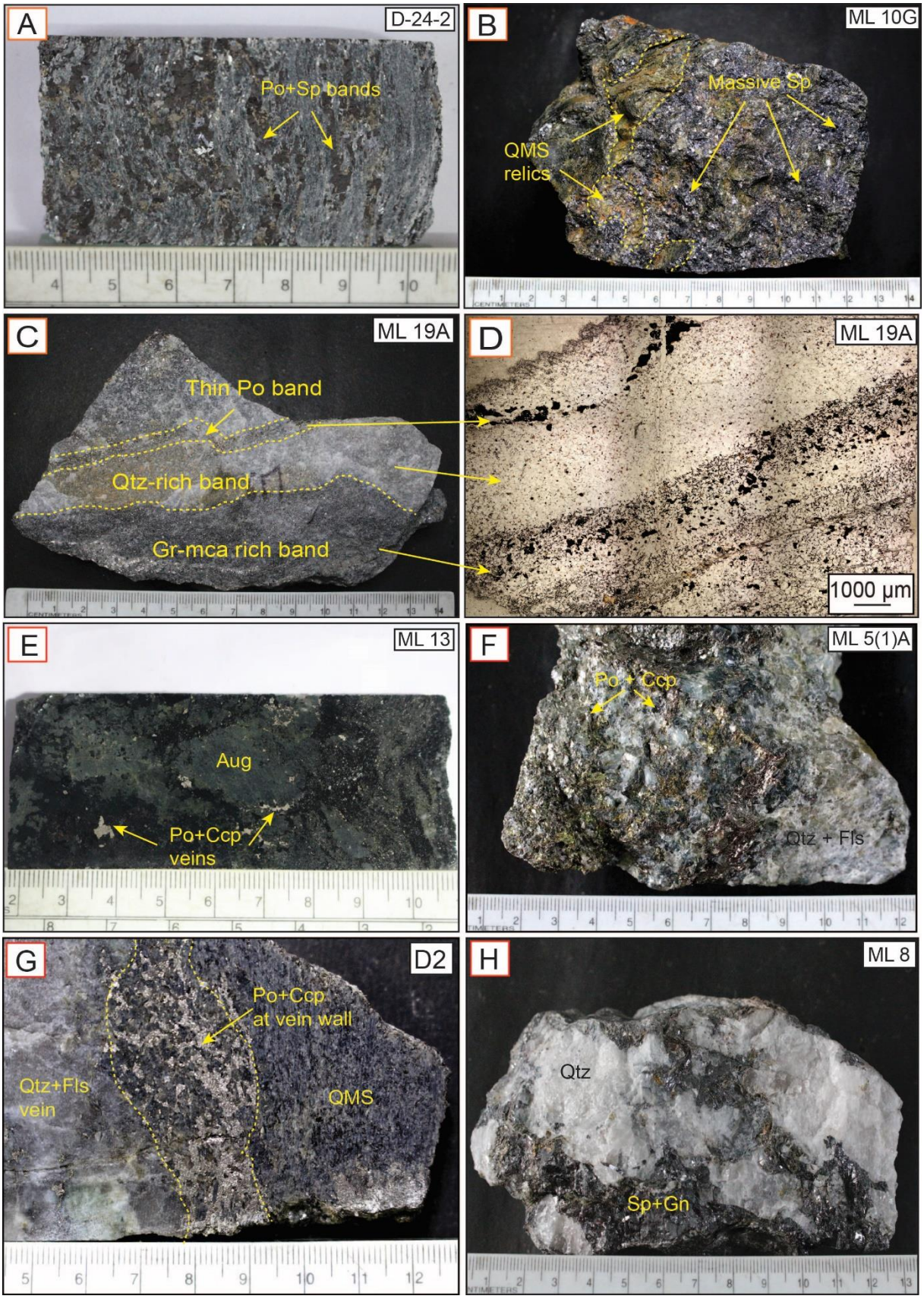
A
D-24-2
Po+Sp bands
B
ML 10G
Massive Sp
QMS
relics
C
ML 19A
Thin Po band
Qtz-rich band
Gr-mca rich band
D
ML 19A
1000 µm
E
ML 13
Aug
Po+Ccp
veins
F
ML 5(1)A
Po + Ccp
Qtz + Fls
G
D2
Po+Ccp
at vein wall
Qtz+Fls
vein
QMS
H
ML 8
Qtz
Sp+Gn

**Figure 3.2: (**on the left, pg. 34**)** Hand specimen photographs (A-C and E-H) and transmitted light photograph (D) of different host rocks along with the mode of occurrences of different ore minerals; A) Laminated quartz mica schist with thin laminae of sulfides (sphalerite and pyrrhotite) paralleling the dominant foliation, B) Massive Zn-Pb ores with relics of host quartz mica schist, C) Banded quartzite with alternating graphite-mica-rich and quartz-rich bands, D) Transmitted light photomicrograph of Fig. C with respective bands shown at the arrow-heads; note the enrichment of sulfide (black) in the graphite-rich band, E) Calcsilicate with Fe-Cu sulfide veinlets, F) Quartzo-feldspathic pegmatite with abundant pyrrhotite and chalcopyrite mineralization, G) Pyrrhotite and chalcopyrite mineralization at the contact of pegmatite vein and quartz mica schist, H) Quartz vein with sphalerite + galena ± pyrrhotite ± chalcopyrite; Galena *Gn*, Pyrrhotite *Po*, Sphalerite *Sp*, Chalcopyrite *Ccp*, Graphite-Mica *Gr-Mca*, Quartz *Qtz*, Augite *Aug*, Feldspar *Fls*. Alphanumeric at the top right of each sub-figure represent sample number.

It is composed predominantly of quartz and feldspar, with the foliation defined by the oriented flakes of muscovite, biotite, and lath-shaped graphite (Fig. 3.2A, B). Accessory minerals include tourmaline, rutile, sphene, and apatite, with infrequent ilmenite and zircon. Quartz and feldspar grains exhibit subhedral shapes; some elongated grains are aligned in the direction of overall schistosity. Oligoclase-andesine and orthoclase significantly exceed albite proportions. Tourmaline is subhedral to anhedral, ranging in size from 50 µm to 300 µm. Rutile and sphene are present as fine, subhedral to anhedral grains measuring up to 30-40 µm. Apatite grains are sub-rounded and fall within a similar size range. The rock has undergone extensive deformation and displays folding on various scales. It is the primary repository of the major Zn-Pb and minor Fe-Cu mineralization in Kayad.

### 3.3.2 Quartzite

The quartzite is dense, fine to medium-grained with color varying from grayish white to whitish brown. It is comprised predominantly of quartz, occasionally intermixed with variable quantities of oligoclase feldspar, muscovite, and biotite; muscovite prevails over biotite (Fig. 3.2C). Scattered throughout the rock, sphene, rutile, tourmaline, and zircon occur as accessory minerals. In some instances, quartzite exhibits a banded pattern, featuring alternating bands rich in graphite, mica and tourmaline (Fig. 3.2D). The mineralogical content within these

bands resembles that of quartz mica schist, with the exception of a heightened quartz concentration. Altered samples of these mica-rich quartzites also contain chlorite and zoisite as secondary phases. This rock features minor sulfide mineralization.

### 3.3.3 Calc-silicate

Outcrop of calc-silicate occurs as an isolated dome-shaped mound east of Kayad village. Below the surface, a thick layer of the rock serves as the basal strata or footwall boundary of the primary ore mineralization in the Kayad mine. It is grayish to yellowish white in color characterized by its ferruginous composition and displays a fine to medium grain texture, primarily composed of diopside, augite, and tremolite (Fig. 3.2E). Chlorite, epidote, sphene, quartz, apatite, and localized patches of calcite occur as minor phases. Though this rock is the main host for lead- zinc mineralization in the nearby Ghugra and Madarpura prospects, in Kayad it is either barren or hosts minor sulfide mineralization in the form of veinlets.

### 3.3.4 Pegmatite

Pegmatites are widely exposed in the area as sills and dykes intruding all the rock types and exhibit a maximum thickness of up to 100 m. Two generations of pegmatite are present in the Kayad underground mine. The older ones occur like sills within the strata and are folded along with the surrounded lithounits, whereas the younger ones mostly concentrate at the sheared contact of calc-silicate and QMS at the footwall, occurring as intrusive apophyses that cut through the pervasive planar fabric of the host rocks and surrounding lithounits. They are extremely coarse grained, composed primarily of quartz, oligoclase, microcline, books of muscovite with occasional tourmaline and garnet, and are heavily mineralized with pyrrhotite and chalcopyrite (Fig. 3.2F-G). Quartz veins, which occur with the younger generation of pegmatites, are composed predominantly of quartz with rare biotite, and are mineralized with sphalerite and galena (Fig. 3.2H).

Apart from pegmatites, amphibolites are present as sills, however they are devoid of any mineralization.

## 3.4 Mode of Occurrence and Textures of Sulfides

### 3.4.1 Disseminated/Laminated Type

Disseminated and laminated forms of sphalerite and pyrrhotite, and to a lesser extent, chalcopyrite and galena occur in quartzite and graphite-bearing quartz mica schist. Since the underground mine was developed primarily to extract the high-grade massive ores, these ores are rarely noticeable in the mine. However, petrographic studies based on borehole and some mine samples show that sphalerite, pyrrhotite, chalcopyrite and galena (in decreasing order of abundance) are aligned parallel to the schistosity defined by mica and graphite (Fig. 3.3A). Notably, sphalerite displays numerous unevenly distributed inclusions of chalcopyrite, a micro-texture commonly known as 'chalcopyrite disease' (Fig. 3.3B). The sulfides harmoniously fold with the surrounding foliation or accumulate at the hinges of microfolds (Fig. 3.3C), similar to their accumulation at the hinge of regional folds (Fig. 2.2B; Chapter 2). Occasional stumpy euhedral to subhedral grains of arsenopyrite are observed at these hinge aggregations. However, at places, clusters and bands comprising dominantly of chalcopyrite and pyrrhotite occur in the schists that disrupt the foliation.

The quartzite exhibits limited mineralization but with a similar sulfide mineralogy as that of QMS. Mineralization is represented primarily by disseminated sphalerite and pyrrhotite with sparse chalcopyrite and galena (10-20 μm in size). In samples with compositional banding, sulfides preferentially aggregate in the bands rich in graphite and tourmaline (Fig. 3.3D). Sphalerite lacks any signs of ‘chalcopyrite disease’. Additional accessory minerals such as rutile and zircon appear as somewhat spherical grains. Pyrite is

sparse in these associations. However, rare relics of pyrite within outsized pyrrhotite are sporadically present in the quartzite and QMS (Fig. 3.3E).

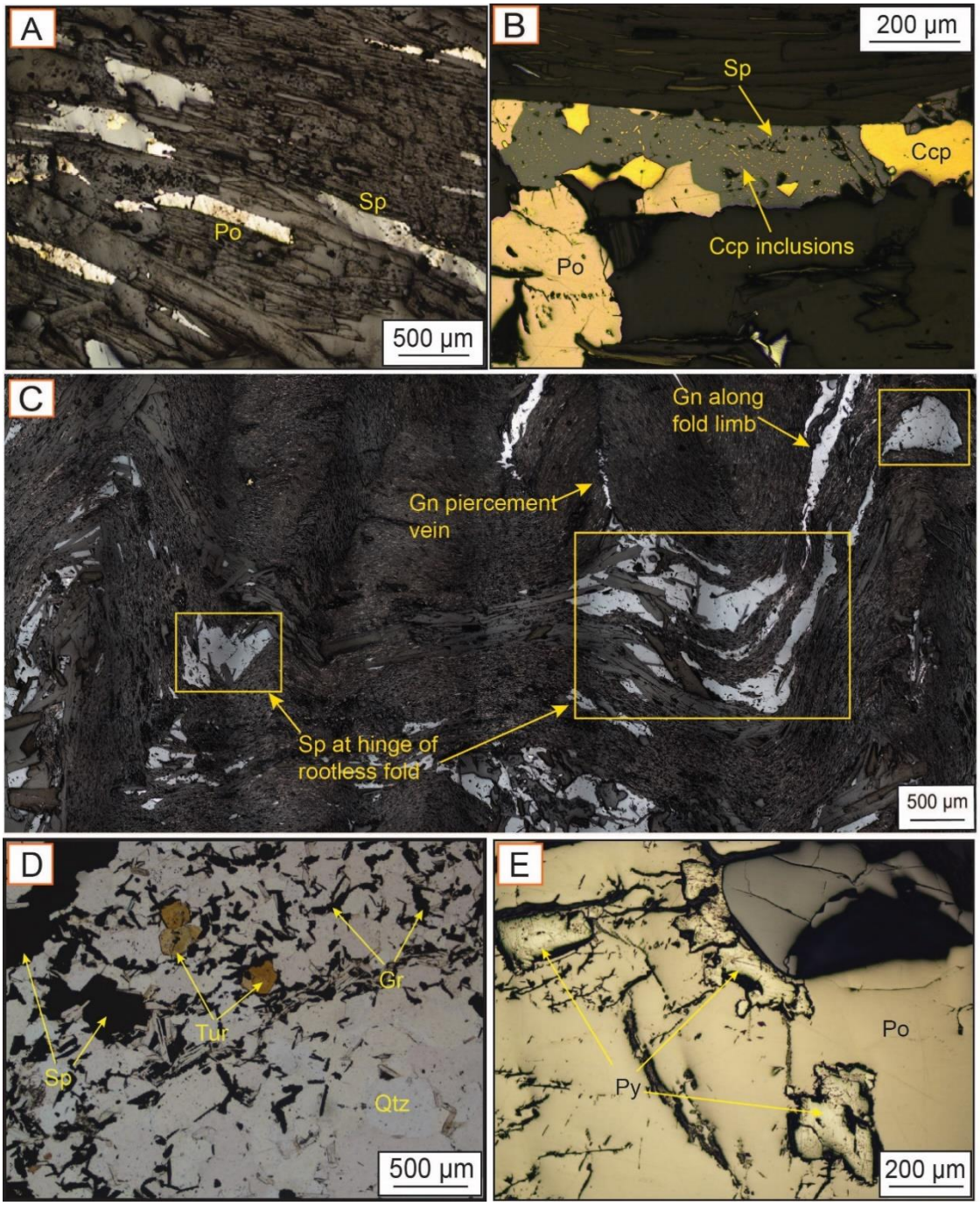


**Figure 3.3:** Transmitted (D) and reflected (rest) plane polarized light photomicrographs showing the mode of occurrence and textures of laminated and disseminated sulfide mineralization in QMS and quartzite. A) Laminated sphalerite and pyrrhotite parallel to the dominant foliation in QMS, B) Chalcopyrite disease in sphalerite of laminated ore, C) Accumulation and attenuation of ore minerals at the fold hinge and limb respectively in QMS, D) Disseminated sphalerite-pyrrhotite and tourmaline grains in the graphite rich band of compositionally banded quartzite, E) Irregular pyrite relics in pyrrhotite. Pyrrhotite *Po*, Sphalerite *Sp*, Chalcopyrite *Ccp*, Galena *Gn*, Graphite *Gr*, Quartz *Qtz*, Tourmaline *Tur*, Pyrite *Py*.

### 3.4.2 Massive Type

Massive ores occur in QMS predominantly featuring large masses of sphalerite and galena, complemented by pyrrhotite, chalcopyrite, and arsenopyrite (Fig. 3.4A). These ores disrupt the pervasive tectonic foliation, and in cases where they have entirely replaced the foliation, other sulfides manifest as inclusions or small pockets, ranging from few tens to hundreds of microns in size, within an extensive matrix of sphalerite. A ubiquitous feature is the presence of ball-shaped or sub-rounded remnants of contorted, folded foliation of the host rock in the sulfide matrix (Fig. 3.4B), commonly known as the 'Durchbewegung' texture (Gilligan and Marshall 1987). Galena displays distinctive cusps and carries textures within sphalerite (Fig. 3.4C). Sizable euhedral grains of arsenopyrite, measuring between 500 to 2000 μm in length exist both within the massive ores and also intersect the foliation in their proximity. Many of these arsenopyrite grains retain remnants of löllingite (Fig. 3.4D).

Another characteristic feature of the massive ore is the frequent presence of an array of sulfosalt grains. Sulfosalts are complex sulfides that encapsulate precious metals and metalloids within their structures and have been identified as recurring components in the lead-zinc massive deposits of the ADFB such as Zawar, Rampura-Agucha, Rajpur-Dariba and Sindesar-Khurd (Sarkar and Gupta 2012). The sulfosalts detected in the Kayad deposit include gudmundite (FeSbS), pyrargyrite ($Ag_3SbS_3$), breithauptite (NiSb), Ag-tetrahedrite [$(Cu, Fe, Ag)_{12}(Sb, As)_4S_{13}$], and some unidentified phases with varying amounts of Cu, Fe, Ag, Sb, and Zn. In most cases, these sulfosalts either manifest as numerous discrete phases or are intimately intergrown with other sulfides. For instance, gudmundite ± pyrargyrite frequently intermingle with pyrrhotite and galena, featuring highly irregular and lobate grain boundaries (Fig. 3.5A-B). In some instances, the volume of gudmundite (estimated from its surface area) nearly equals that of associated sulfides such as sphalerite (Fig. 3.5C).

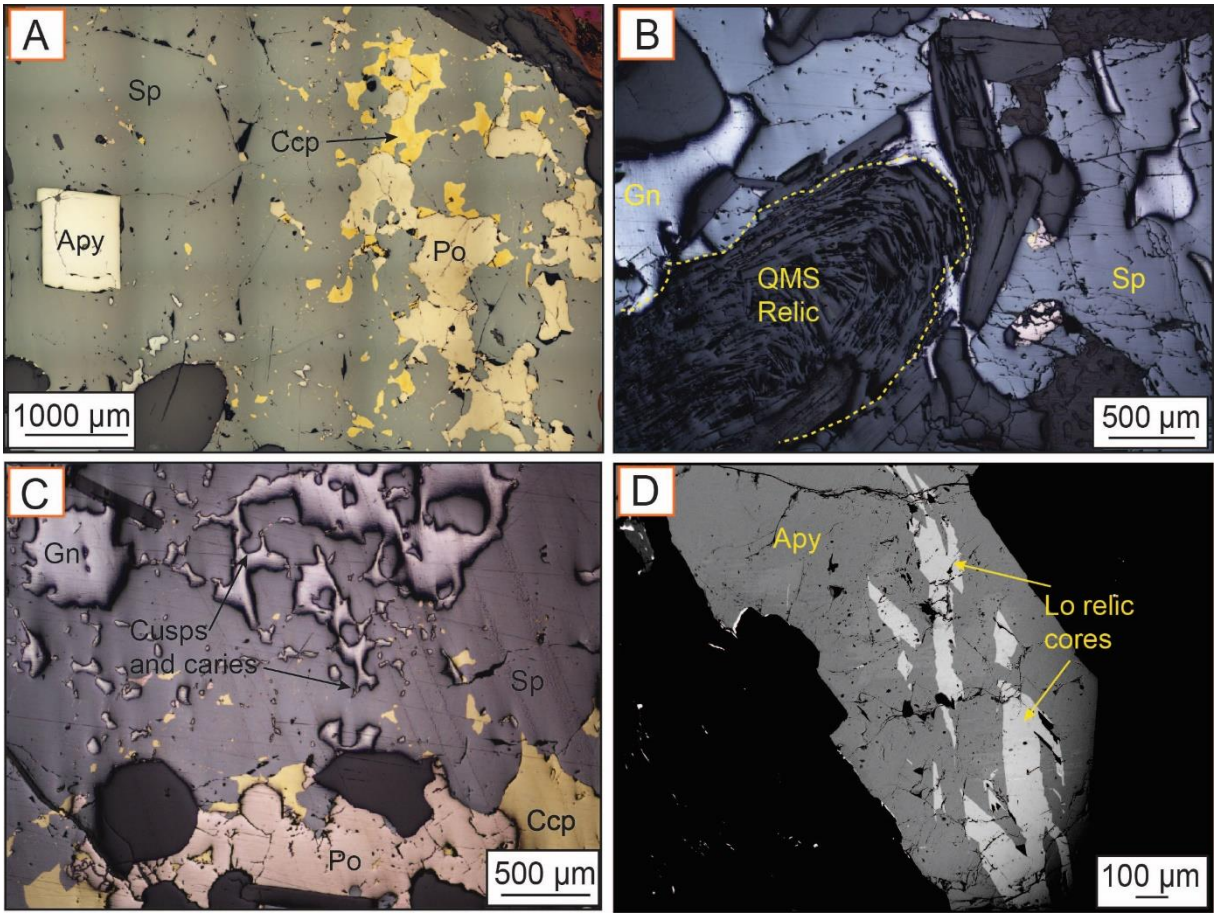


**Figure 3.4:** Reflected plane polarized light photomicrographs (A-C) and BSE image (D) showing the mode of occurrence and textures of massive sulfide mineralization. A) Pyrrhotite, chalcopyrite and arsenopyrite in sphalerite matrix, B) Folded QMS relics in massive sphalerite and galena (Durchbewegung texture), C) Cusps and caries texture exhibited by galena in massive sphalerite, D) Subhedral massive arsenopyrite grain with relics of löllingite. Pyrrhotite *Po*, Sphalerite *Sp*, Chalcopyrite *Ccp*, Galena *Gn*, Arsenopyrite *Apy*, Löllingite *Lo*.

Breithauptite, in most cases, occurs as idiomorphic grains when in contact with galena (Fig. 3.5D) but are irregular or somewhat elongated when juxtaposed against pyrrhotite (Fig. 3.5E-F). Ag-bearing tetrahedrite either shares straight grain boundaries with galena (Fig. 3.5G) or is present as inclusions in the latter (Fig. 3.5H-I). In a few assemblages, scant phases with Sb>80 wt. % and mixed compositions of Ag-Sb can be identified (Fig. 3.5J).

Silicate minerals, including quartz, feldspar, biotite, and tourmaline, show bimodal grain sizes, exhibiting coarser grain size near massive sulfide deposits compared to the rest of the rocks. Biotite and muscovite grains exhibit a haphazard alignment around the coarser

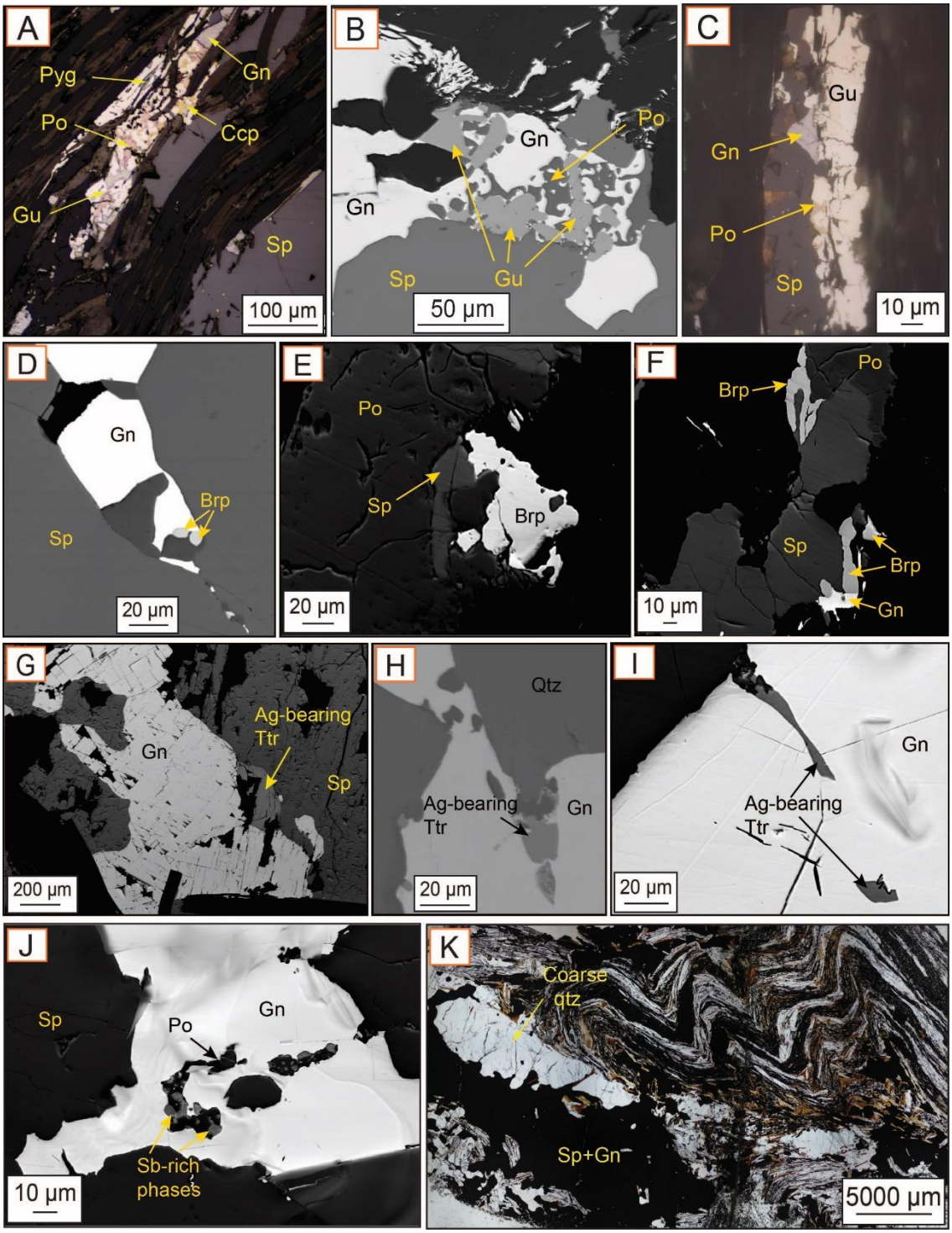


**Figure 3.5:** Photomicrographs (A and C: reflected light, and K: transmitted light) and BSE images (B, D-F, H-J) of sulfosalts and their textures in massive ores. A) Intergrowths of gudmundite, pyrargyrite, galena, pyrrhotite and chalcopyrite, B) Intergrowth texture involving gudmundite, galena and pyrrhotite, C) Gudmundite association with sphalerite, galena and minor pyrrhotite, D) Euhedral breithauptite crystals sharing grain boundaries with galena, E-F) Irregular breithauptite grains with pyrrhotite and minor sphalerite, G) Silver-bearing tetrahedrite grain at the boundaries of galena, H) Intergrowth of Ag-bearing tetrahedrite and galena, I) Inclusions of Ag-tetrahedrite in massive galena, J) Ag-Sb-rich phases as inclusions in galena, K) Sphalerite and galena vein intruding along the limb of the microscopic fold, where sulfides also accumulate at the fold hinge. Pyrrhotite *Po*, Sphalerite *Sp*, Chalcopyrite *Ccp*, Galena *Gn*, Pyrargyrite *Pyg*, Gudmundite *Gu*, Breithauptite *Brp*, Tetrahedrite *Ttr*, Quartz *Qtz*.

sulfides. In most places, the sulfides are encapsulated by a film of recrystallized quartz (Fig. 3.5K). In the foliated parts, quartz, mica (muscovite>biotite), Ca-plagioclase (mostly andesine) and orthoclase constitute the host; however, an increased percentage of recrystallized microcline is observed around the massive sulfides. Rutile is a widespread component of the host rock and is enveloped or replaced by titanite in almost all associations.

### 3.4.3 Vein- type

Pegmatite and quartz veins are frequently encountered in the footwall side of the massive Zn-Pb ores, located at the boundary between calcsilicate rocks and graphite-bearing quartz-mica schist, within the confines of a shear zone/fault zone. Sulfide mineralization linked with these pegmatite veins and minor veinlets predominantly includes pyrrhotite and chalcopyrite, occasionally accompanied by sphalerite and galena (Fe-Cu±Zn±Pb) which are distributed inside the veins or at the vein walls (Fig. 3.6A).

Inside the veins, sulfide minerals cluster together or align along the grain boundaries of the coarse pegmatitic minerals. Some sphalerite grains exhibit a moderate 'chalcopyrite disease', while some chalcopyrite grains display sphalerite stars. Secondary mineral alteration features are conspicuous in the proximity of sulfide-rich masses (Fig. 3.6B) or adjacent to fine veinlets, which are discussed in detailed in the next section. Abundance of pyrrhotite and chalcopyrite in the QMS wall rock gradually decreases away from the vein wall. This infiltration leads to a disruption in the foliation of the intruded host. Biotite and graphite exhibit a progressive increase in abundance towards the vein wall, wherein biotite undergoes a size transition, gradually coarsening towards the vein. The randomly oriented biotite close to the veins contain profuse inclusions of small zircons. The mineralized vein wall also contains an abundance of coarse fluorapatite, measuring between 20-100 µm, and is frequently rimmed by sulfides (Fig. 3.6C). Graphite has two distinct modes of occurrence: the flaky variety

primarily inhabit the host QMS and define the foliation whereas the patchy variety is closely associated with the sulfides in the vein wall. Additionally, spherulitic graphite is observed in close proximity to the sulfide veins (Fig. 3.6D).

In terms of composition, two distinct varieties of calcsilicates are observed, each exhibit unique sulfide mineralogy. Minor Fe-Cu±Zn±Pb mineralization containing pyrrhotite, chalcopyrite, minor sphalerite and galena, along with quartz, calcite, hornblende, sphene, and minor fluorapatite occurs as veinlets traversing the calc-silicates constituted primarily of augite (Fig. 3.6E, F). Notably, there is a bimodal distribution of grain sizes of augite. Larger grains reach dimensions of up to a centimeter in length, while finer grains inhabit their intergranular spaces. In tremolite-rich calcsilicate, Zn-Pb±Fe±Cu mineralization prevails where substantial amounts of galena accompanied by inclusion-free sphalerite tend to congregate along the cleavage planes of tremolite (Fig. 3.6G). In some tremolite grains, diopside relics are observed which indicates replacement of diopside by tremolite. Medium to coarse subhedral grains of sphene are scattered throughout the sample, often accompanied by chlorite and sulfides. Epidote is ubiquitous, frequently lining the cleavage planes of amphibole.

Zn-Pb±Fe±Cu mineralization in veins is subordinate compared to the massive Zn-Pb ores in the fold hinges. However, they reach economic grade in some mining levels (Fig. 2.2 B). For example, it is most pronounced within quartz veins wherein clusters of sphalerite accompanied by minor quantities of galena, pyrrhotite, and chalcopyrite can be observed. Sphalerite grains in the quartz veins are coarse, exceeding a few centimeters in some instances. Furthermore, in mica schists, micro-veins and clusters comprising K-feldspar (microcline>orthoclase) and tourmaline are occasionally observed which predominantly feature sphalerite and galena (Fig. 3.6H). Feldspar (up to 500 µm compared to 10-100 µm in

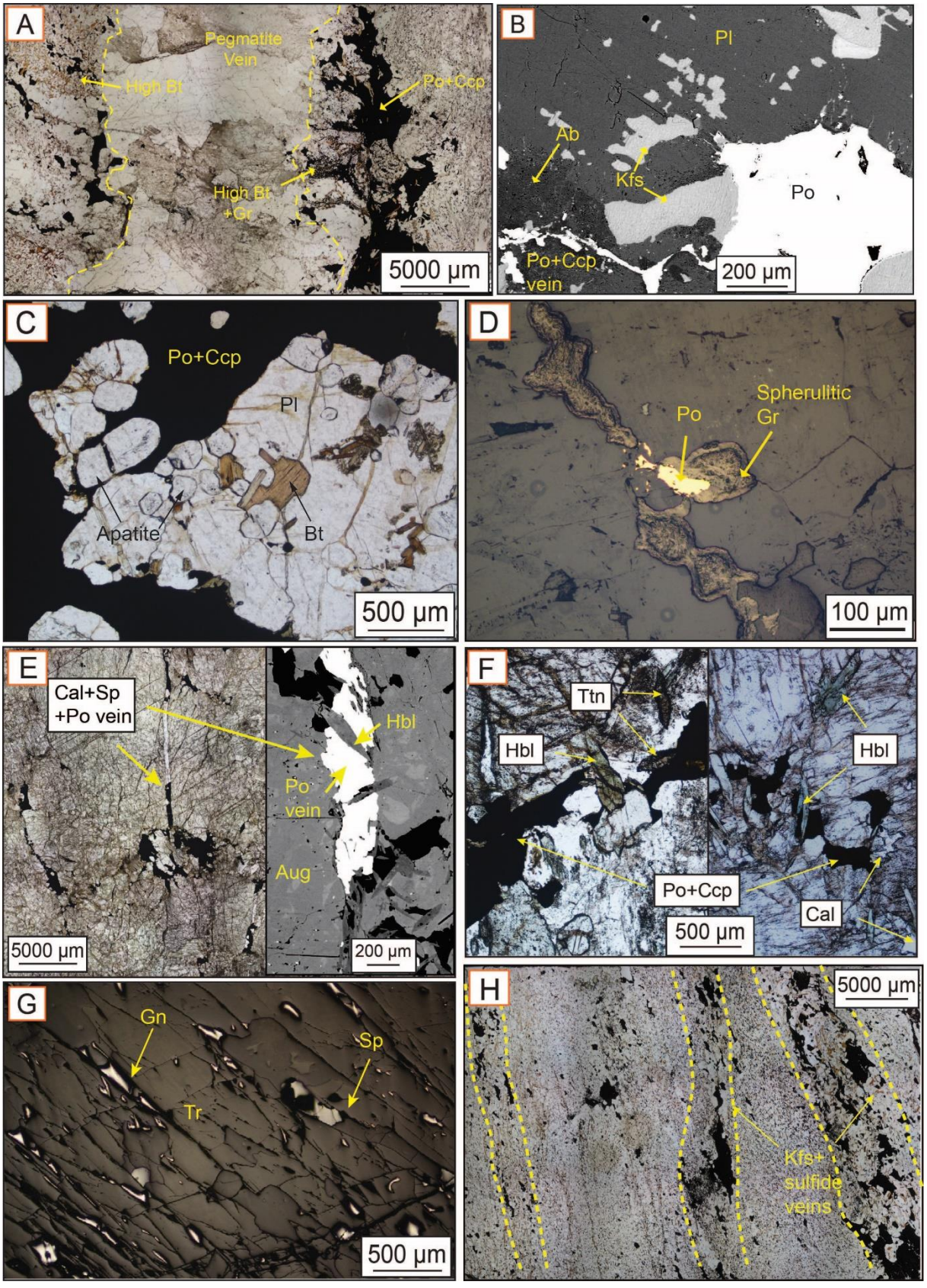
A
Pegmatite Vein
High Bt
Po+Ccp
High Bt +Gr
5000 µm
B
Pl
Ab
Kfs
Po
Po+Ccp vein
200 µm
C
Po+Ccp
Pl
Apatite
Bt
500 µm
D
Po
Spherulitic Gr
100 µm
E
Cal+Sp +Po vein
Hbl
Po vein
Aug
5000 µm
200 µm
F
Ttn
Hbl
Hbl
Po+Ccp
Cal
500 µm
G
Gn
Sp
Tr
500 µm
H
5000 µm
Kfs+ sulfide veins

**Figure 3.6:** (on the left, pg. 44) Transmitted (A, C, E-F, H) and reflected (D, G) light photomicrographs, and BSE image (B) showing the mode of occurrence and textures of vein-type mineralization. A) Sulfide mineralization (pyrrhotite + chalcopyrite) occurring within and along walls of pegmatite veins that intrude the country rock (QMS), B) Secondary alteration products such as K-feldspar and albite ubiquitously associated with sulfide mineralization, C) Increased abundance of fluorapatite associated with Fe-Cu mineralization along pegmatite vein walls, D) Spherulitic variety of graphite associated with chalcopyrite and pyrrhotite veins in pegmatite, E) Sulfide (Pyrrhotite-chalcopyrite-sphalerite) veinlets intrude into augite-rich calcsilicate rock, F) Veinlets comprised of hornblende, titanite and calcite, which are ubiquitously seen in association with Fe-Cu sulfides, intrude into calcsilicate, G) Zn-Pb±Fe±Cu mineralization along cleavage planes of tremolite in tremolite-bearing calcsilicates, H) Fine microcline and orthoclase bearing veins in QMS rocks typified by sphalerite + galena mineralization (areas within yellow dotted lines). Albite *Ab*, K-feldspar *Kfs*, Plagioclase *Pl*, Muscovite *Ms*, Pyrrhotite *Po*, Chalcopyrite *Ccp*, Biotite *Bt*, Chamosite *Chm*, Calcite *Cal*, Hornblende *Hbl*, Titanite *Ttn*, Graphite *Gr*, Tremolite *Tr*, Sphalerite *Sp*, Galena *Gn*.

the host rock) and tourmaline (up to 3 mm compared to 50 µm in the host) in these veins are much coarser than those in the host QMS. Feldspar is often altered to secondary minerals which are intimately associated with lead-zinc sulfides.

## 3.5 Discussion

### 3.5.1 Alteration Signatures

Sulfide mineralization, at places in the Kayad deposit, is accompanied by secondary minerals formed via alteration of the host rock. Extensive petrography and detailed major and minor element analyses of the associated silicate phases (please refer to Appendix Table 1 for complete dataset) have revealed some distinctive patterns of alteration.

In the disseminated and laminated ores of QMS comprising sphalerite, pyrrhotite and chalcopyrite, no alteration is observed, except for in the vicinity of chalcopyrite + pyrrhotite veins where oligoclase grains show signs of replacement by orthoclase, particularly at their cores or along fractures. Albite is only present at altered areas, indicating an association with the transforming orthoclase (Fig 3.7A). Additionally, clusters of allanite, Ce-monazite, and fluorapatite coexist with chalcopyrite and pyrrhotite (Fig. 3.7B). Similarly, no visible alteration is associated with the disseminated sulfides in quartzite. However, pyrrhotite veins

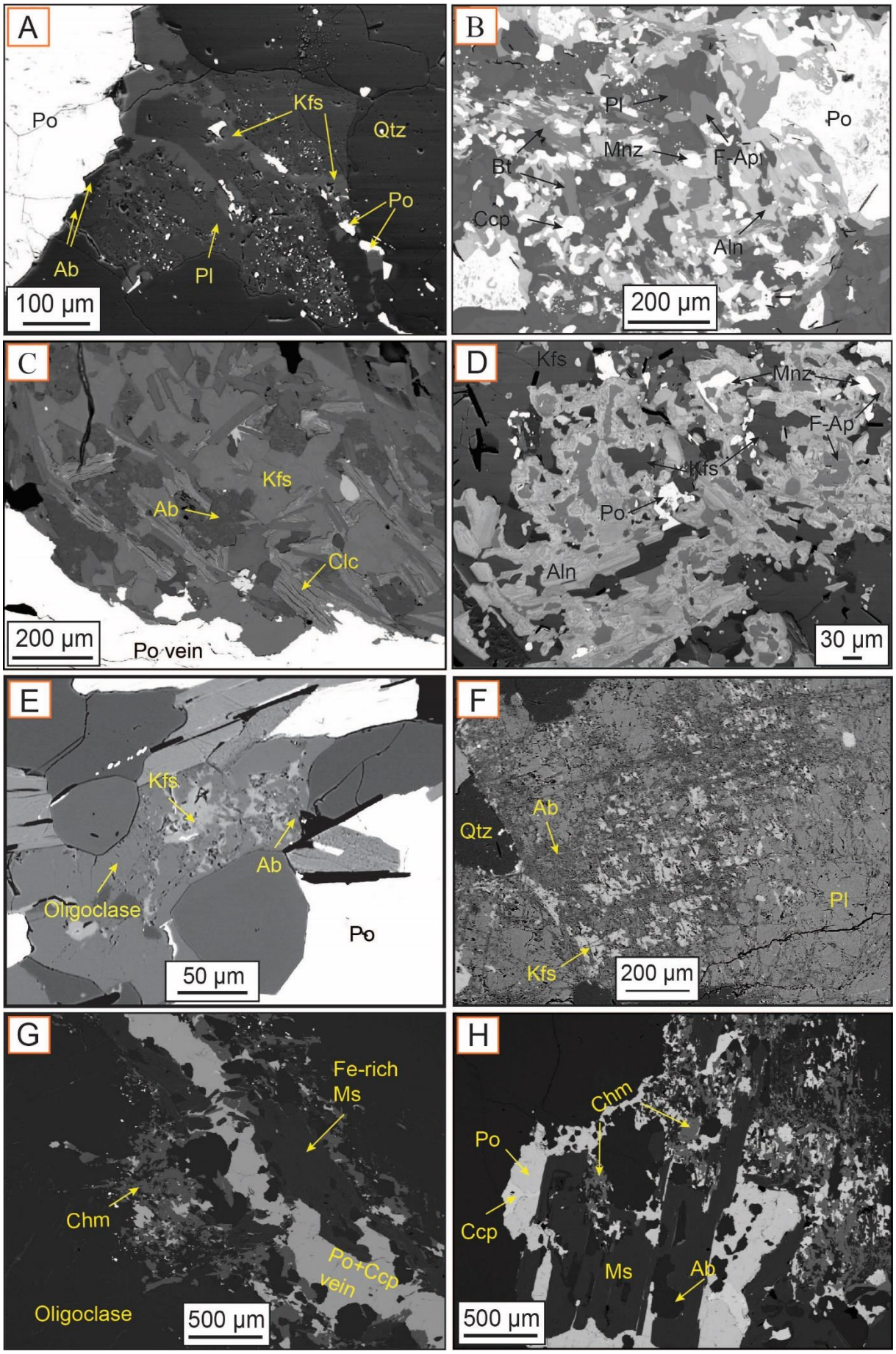
A
Po
Kfs
Qtz
Po
Ab
Pl
100 µm
B
Pl
Po
Mnz
F-Ap
Bt
Ccp
Aln
200 µm
C
Kfs
Ab
Clc
200 µm
Po vein
D
Kfs
Mnz
F-Ap
Kfs
Po
Aln
30 µm
E
Kfs
Ab
Oligoclase
Po
50 µm
F
Ab
Qtz
Pl
Kfs
200 µm
G
Fe-rich
Ms
Chm
Po+Ccp
vein
Oligoclase
500 µm
H
Chm
Po
Ccp
Ms
Ab
500 µm

**Figure 3.7:** (on the left, pg. 46) BSE images depicting alteration features associated with sulfide mineralization. A) K-feldspar and albite replace oligoclase in areas of intense Fe-Cu sulfide mineralization in QMS laminated type. B) Monazite, allanite and fluorapatite co-exist with pyrrhotite-chalcopyrite mineralization in QMS laminated type. C) Presence of clinochlore and replacement of K-feldspar by albite at the contact of the quartzite host and the pyrrhotite vein. D) Assemblage of monazite, allanite, fluorapatite and K-feldspar with pyrrhotite in quartzite host. E) Orthoclase and crypto grains of albite replace oligoclase in Fe-Cu rich areas in the massive type. F) Within pegmatite vein, albite and K-feldspar pervasively replace oligoclase along its cleavage planes. G) Alteration halo around Fe-Cu sulfide vein comprise of chamosite, Fe-rich muscovite, K-feldspar and albite. H) Pegmatitic muscovite is replaced by chamosite, sulfides (pyrrhotite-chalcopyrite), Fe-rich muscovite and albite. Albite *Ab*, K-feldspar *Kfs*, Plagioclase *Pl*, Biotite *Bt*, Clinochlore *Clc*, Chamosite *Chm*, Muscovite *Ms*, Monazite *Mnz*, Fluorapatite *F-Ap*, Allanite *Aln.*

(0.5 to 1 cm in width) that intrude and taper into the rocks have an alteration halo characterized by coarse quartz, iron-rich clinochlore and an increased proportion of biotite and K-feldspar around the veins (Fig. 3.7C). K-feldspar grains are locally replaced by albite, Ce-monazite, Ce-allanite, fluorapatite, pyrrhotite and at places by clinozoisite, similar to the alteration halo in pyrrhotite-chalcopyrite-bearing assemblages that overprint the foliation in the QMS (Fig. 3.7D). Allanite is commonly found near sulfide veins or as inclusions within them.

The massive sulfide ores are practically devoid of alteration features, except within the QMS rocks where pyrrhotite and chalcopyrite take precedence over sphalerite and galena. Oligoclase/andesine undergoes replacement by K-feldspar and albite, which appear as very fine-grained phases (Fig. 3.7E).

Secondary alteration products are conspicuous in the proximity of sulfide-bearing veins and veinlets. The Fe-Cu±Zn±Pb sulfide assemblages within the pegmatites are ubiquitously associated with alteration aureoles defined by replacement of pegmatitic plagioclase by wart-like orthoclase and albite along grain boundaries and cleavage planes (Fig. 3.7F). Wherever present, the secondary mineral pair of orthoclase and albite consistently features abundant micro-pores. This alteration is locally so pervasive that only relics of plagioclase occur as small islands in the altered parts. Most veinlets contain Fe-rich muscovite

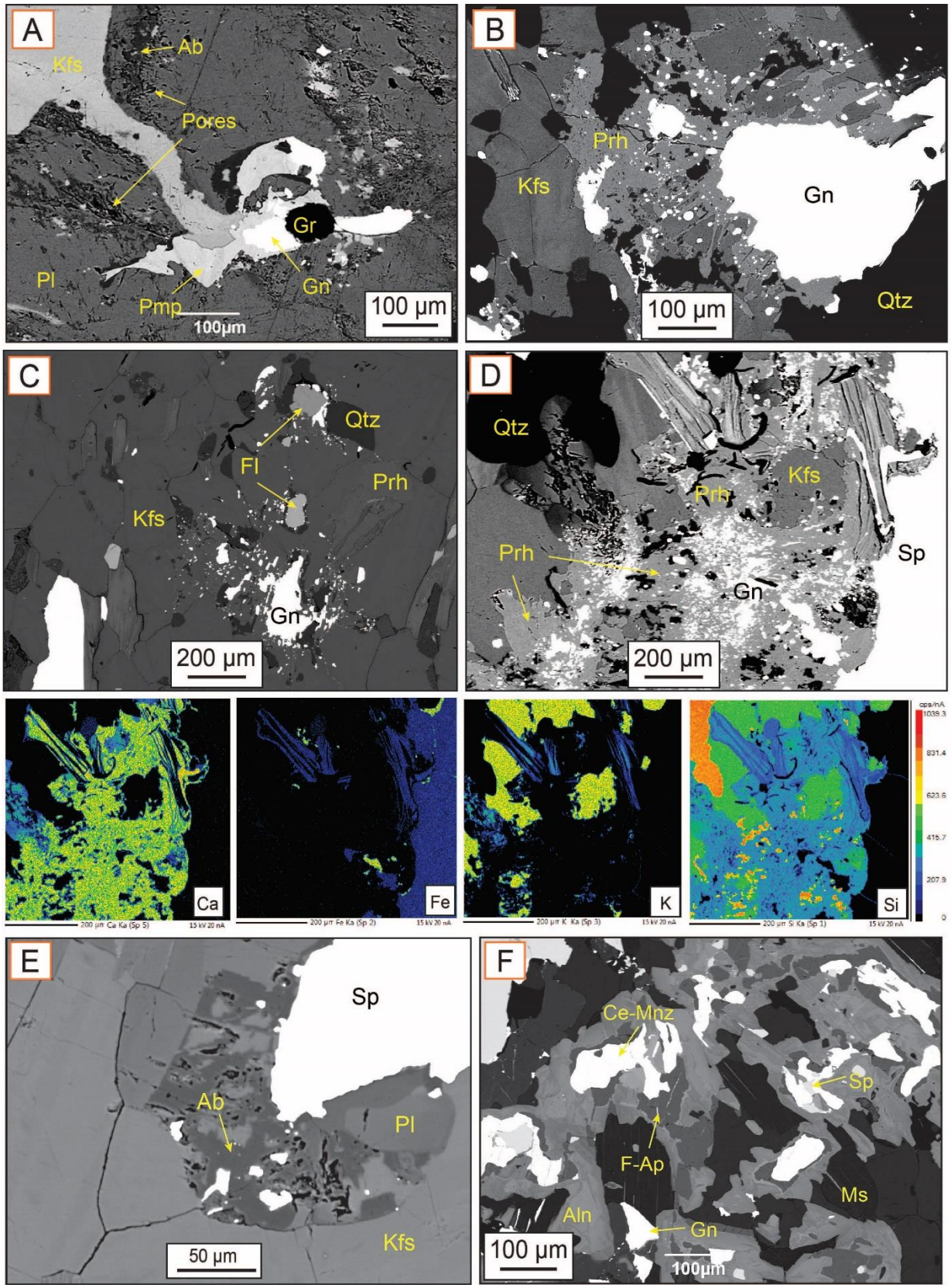
A
Ab
Kfs
Pores
Gr
Pl
Gn
Pmp
100µm
100 µm
B
Prh
Kfs
Gn
Qtz
100 µm
C
Qtz
Fl
Prh
Kfs
Gn
200 µm
D
Qtz
Kfs
Prh
Prh
Sp
Gn
200 µm
Ca
Fe
K
Si
E
Sp
Ab
Pl
Kfs
50 µm
F
Ce-Mnz
Sp
F-Ap
Ms
Aln
Gn
100 µm
100µm

**Figure 3.8:** (on the left, pg. 48) BSE images and X-ray elemental maps of alteration features in vein-hosted sulfide mineralization. A) Pumpellyite, spherulitic graphite, galena and K-feldspar replace oligoclase within pegmatite vein. Innumerable pores (black pit like appearance) have formed at sites of plagioclase replacement by albite, B) Prehnite envelops around galena and replaces K-feldspar of the veins shown in Figure 3.6H, C) Assemblage of galena, fluorite, prehnite and quartz replace K-feldspar vein depicted in Figure 3.6H, D) Galena and sphalerite associated with prehnitic alteration. X-ray elemental maps of Ca, Fe, K and Si for Fig. D is provided below which shows the extent of the alteration aureole, E) Dark albite patches in K-feldspar grains in the proximity of sphalerite-galena mineralization, F) Allanite assemblage with Ce-monazite, fluorapatite, galena and sphalerite in the K-feldspar rich veins. Albite *Ab*, K-feldspar *Kfs*, Plagioclase *Pl*, Sphalerite *Sp*, Galena *Gn*, Prehnite *Prh*, Pumpellyite *Pmp*, Fluorite *Fl*, Quartz *Qtz*, Monazite *Mnz*, Fluorapatite *F-Ap*, Allanite *Aln*.

(FeO >3 wt.%), chamosite, albite, and quartz which replace both pegmatitic plagioclase and muscovite (Fig. 3.7G, H). In other regions, the alteration assemblage is comprised of specks of galena, Al-pumpellyite, graphite, and chalcopyrite, alongside orthoclase and albite (Fig. 3.8A). In a few areas, fluorite appears as small subhedral grains, often in association with chamosite. The presence of both ghost and wart-like myrmekite is a common occurrence throughout the pegmatite vein body.

In the QMS rocks, occasional microcline-orthoclase-rich veins disrupt the foliation (Fig. 3.6H). K-feldspar in these veins is replaced by an assemblage of prehnite (Fig. 3.8B), Al-pumpellyite, clinochlore, albite, and, sometimes fluorite (Fig. 3.8C). Fine grains of galena and sphalerite are consistently interspersed within the prehnitic alteration, pointing to an evident association of the sulfides with the secondary minerals (Fig. 3.8D). X-ray elemental maps of the area confirm the increase of Ca and Fe near the sulfide mineralization that replaces K-feldspar. At the alteration front, K-feldspar shows a turbid appearance with patches of Na-rich domains (Fig. 3.8E). Ce-bearing allanite is also a common phase within this assemblage, frequently occurring alongside Ce-monazite, fluorapatite, clinozoisite, and albite (Fig. 3.8F). Ce-monazite is rimmed by a double corona of fluorapatite and a broad collar of allanite.

### 3.5.2 Thermometry from Biotite

The temperature of metamorphism and ore formation of the ores and the metamorphic temperature of the host rocks of the Kayad deposit have been estimated using several thermometric formulations. Sulfides such as sphalerite and arsenopyrite are utilized to decipher temperature of ore mineral crystallization whereas biotite has been used to understand the peak metamorphic grade achieved by the rocks of Kayad. The calculation of temperature based on sphalerite and arsenopyrite geochemistry is discussed in Chapter 4. Since biotite is intimately associated with the three sulfide mineralization types, it can serve as a proxy for ore deposition temperature. Temperatures were estimated using the Ti-in-biotite thermometer (see Appendix Table 2) of Wu and Chen (2015) (revised after Henry et al., 2005) which is applicable over a temperature and pressure range of 480-840 °C and 0.1-1.9 Gpa, and XTi value of 0.02-0.14. The prerequisite for the application of this thermometer is the presence of Ti-bearing minerals such as ilmenite or rutile which is fulfilled by the abundance of rutile in the rocks of Kayad. The host QMSs contain fine grains of biotite defining the tectonic foliation (metamorphic biotite) whereas coarser biotite is also observed in association with the massive and hydrothermal sulfides.

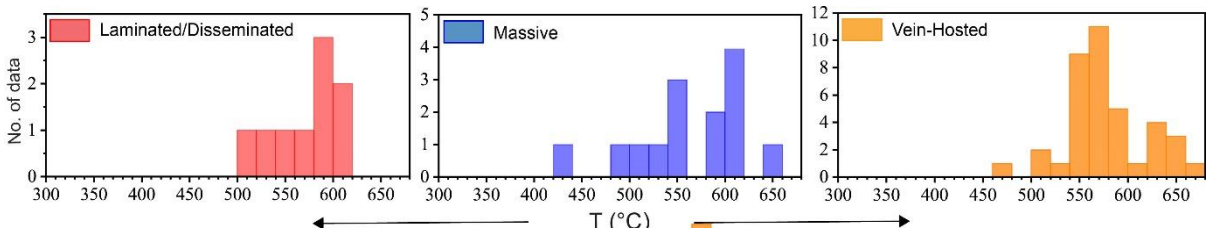


**Figure 3.9:** Histograms showing temperature distribution obtained using Ti-in-biotite thermometry from laminated/disseminated, massive and vein-type sulfides.

For temperature calculations, pressure is assumed at 5.7 kbar as per the P-T estimates of regional metamorphism (refer to Chapter 2, Section 2.2.2). The temperatures obtained using Ti-in-biotite thermometry is summarized in Figure 3.9. The metamorphic biotite as well as those associated with massive sulfides furnish temperatures between 434°C and 664°C

(n=66). However, a large number of the retrieved temperatures lie between 500°C and 600°C with both the metamorphic and ore-associated biotite having overlapping ranges. The highest temperature of ca. 650 °C is consistent with the middle to upper amphibolite facies conditions as had been deduced by previous authors. However, the large spread in the temperatures is suggestive of variable re-equilibration during post-peak retrogression/metamorphic cooling.

## 3.6 Summary

Six different types of rocks namely the graphite-bearing quartz mica schist or QMS, quartzite, calc-silicate, pegmatite, granite gneiss and amphibolite occur in the Kayad zinc-lead deposit. With the exception of granite gneiss and amphibolite, all the rock types carry lead-zinc and iron-copper mineralization in varying proportions. Sulfides occur in three modes namely disseminated/laminated, massive, and vein-hosted types. In terms of mineralization, the QMS is significant being the primary repository for major Zn-Pb and minor Fe-Cu mineralization of the region in the form of both laminated/disseminated and massive types. Quartzite exhibits limited sulfide mineralization in the form of disseminations in graphite-rich bands. The laminated/disseminated ores feature sphalerite, pyrrhotite, and sparse chalcopyrite and galena disposed parallel to the foliation while the massive type is characterized by large masses of sphalerite, galena, pyrrhotite, chalcopyrite and arsenopyrite that disrupt and replace the foliation. The massive ores exhibit distinctive Durchbewegung texture and low dihedral angles (a detailed exercise on dihedral angles is deferred to Chapter 6) between sphalerite and the less competent sulfides such as galena and chalcopyrite. Furthermore, the massive ores are ubiquitously associated with sulfosalts such as gudmundite, pyrargyrite, breithauptite, and Ag-tetrahedrite. Calc-silicate contains sparse mineralization in the form of veinlets of Pb-Zn and Fe-Cu sulfides. Pegmatites that cut through the fabric of the host rock, are heavily mineralized with pyrrhotite and chalcopyrite whereas quartz veins carry mostly sphalerite and

galena. Disseminated and laminated ores in QMS and quartzite, and the massive sulfides in the QMS do not show significant hydrothermal alteration signatures, except for a common secondary assemblage of albite, orthoclase, biotite, chamosite, allanite and fluorapatite associated with higher abundances of pyrrhotite and chalcopyrite. The Fe-Cu±Zn±Pb sulfide assemblages in the pegmatites are ubiquitously associated with alteration of pegmatitic plagioclase by wart-like orthoclase and albite. Pegmatitic plagioclase and muscovite are also replaced by Fe-rich muscovite, chamosite, albite, and quartz. K-feldspar rich veins in QMS show a dissimilar alteration signature, consisting of albite, prehnite, Al-pumpellyite, allanite, apatite and fluorite associated with sphalerite and galena. Further discussion on the implications of the complex alteration assemblage is deferred to Chapter 6. Ti-in-biotite thermometry shows that irrespective of varied mode of occurrences, the different ores were formed at overlapping temperature range (mostly 500 to 600 ˚C). The Kayad deposit has diverse ore mineralogical associations, textural relations and hydrothermal alteration signatures which necessitates detailed geochemical and isotopic analyses of sulfides for a comparison among different ore types and for a better understanding of the ore-forming process which is dealt with in the next chapter (Chapter 4).

# CHAPTER 4: Sulfide Geochemistry: Major and Trace Element and Multiple Sulfur Isotope Compositions

## 4.1 Introduction

The geochemical character of sulfides, that encompasses major and trace element, and sulfur isotopic compositions, holds important clues about the ore-forming processes. Identifying different generations of sulfide mineralization and their intragrain and intergrain variations based on the major and trace element compositions can provide insights into the evolving physicochemical conditions of ore-forming fluids. Sulfur isotopes, on the other hand, are instrumental in distinguishing various sources of sulfur (e.g., magmatic vs. seawater) and have been employed to trace the evolution of ores during deposition in diverse geological settings, ranging from volcanic-hosted massive sulfide deposits to sedimentary exhalative (SEDEX) deposits. Furthermore, multiple sulfur isotopes ($\Delta^{33}S$ and $\Delta^{36}S$) have been utilized in paleoenvironment reconstructions, and tracing ancient sulfur cycles pathways (Farquhar and Wing 2003; Ono et al. 2006, 2009; Ueno et al. 2008; Johnston 2011; Tostevin et al. 2014; Li et al. 2016; LaFlamme et al. 2018a; Barré et al. 2021).

Currently, detailed trace element geochemistry of sulfides from the Aravalli-Delhi fold belt is lacking. Previous studies on the sulfur isotopic compositions of Pb-Zn ores in ADFB have primarily focused on the Rajpura Dariba and Rampura-Agucha deposits in Bhilwara province and Zawar deposit in ADFB, which exhibit a wide range of $\delta^{34}S$ composition. For example, $\delta^{34}S$ values in Rajpura-Dariba sulfide ores vary from +9.1 to -6.7 ‰ with increasingly heavier values towards the stratigraphic top (Deb 1986, 1990). Complemented by carbon isotopic values that indicate biogenic derivation of carbon, the ores are inferred to be of SEDEX type formed by bacteriogenic processes. Similarly, $\delta^{34}S$ values of sphalerite, galena and pyrite in Zawar deposit range from -0.1 to 20.7 ‰ (Deb 1990; Sarkar and Banerjee 2004) supporting SEDEX-type deposit formed by microbial sulfate reduction. Apart from a

recent study by Fareeduddin et al. (2014) on the Bhilwara and Kayad-Ghugra Pb-Zn deposits, there is a notable lack of research addressing the sulfur isotopic variations across different host rocks as well as classes of mineralization. Fareeduddin et al. (2014) reported very low yet compact ranges of $\delta^{34}S$ values (+1.4‰ to +2.0‰) in a limited number of sphalerite samples from tremolite-bearing carbonate hosts, which differ from those obtained from the Pb-Zn deposits in the Bhilwara and Aravalli belts.

In the previous chapter (Chapter 3), the different host rocks, mode of occurrences (such as disseminated/laminated, massive and vein-type), textures and alteration signatures associated with the Zn-Pb and Fe-Cu mineralization in the Kayad deposit are described. It has also been demonstrated that there are multiple generations of sulfide minerals associated with different types of ores. Therefore, accurately constraining the in-situ major and trace element geochemistry and isotopic composition of sulfides from different associations is imperative for developing a comprehensive model of ore genesis. This chapter provides in-depth descriptions of major and trace element geochemistry, and multiple sulfur isotopic compositions of sulfides from each mineralization type to facilitate a genetic comparison of ore forming processes. In-situ measurement of major and trace element composition was done using electron probe micro analyzer (EPMA) and laser ablation inductively coupled plasma mass spectrometer (LA-ICPMS) respectively whereas in-situ and bulk (from mineral separates) sulfur isotope compositions were measured by nano-Secondary Ion Mass Spectrometer (nano-SIMS) and Isotope Ratio Mass Spectrometer (IRMS) respectively.

## 4.2 Methodology and Analytical Conditions

### 4.2.1 Major and Minor Element Analyses by EPMA

The major element compositions of the sulfide phases were determined on a Cameca SX-100 electron probe micro analyzer (EPMA) equipped with four wavelength dispersive

spectrometers at the Department of Geology and Geophysics, IIT, Kharagpur. The analyses were conducted at 20 kV accelerating voltage and 20 nA beam current with ca. 1 μm beam diameter. A total of 99 sphalerite, 75 galena, 48 chalcopyrite, 72 pyrrhotite, and 36 arsenopyrite spots, across all types of mineralization, were analyzed for their major and minor element concentration. The X-ray lines used for the analysis of S, Fe, Cu, Zn, Pb and As are SKα, FeKα, CuKα, ZnKα, PbMα and AsLα respectively. The peak and background acquisition times were set at 10 s and 5 s respectively for all elements except As, for which the peak and background times were 20 s and 10 s respectively. The standards used for calibration of the instrument are as follows: sphalerite for Zn, pyrite for Fe and S, galena for Pb, pure copper metal for Cu, and synthetic GaAs for As.

### 4.2.2 Trace Element Analyses by LA-ICPMS

Concentrations of trace elements in the sulfide phases were measured on a Thermo Fisher Scientific iCap-Q Quadrupole Inductively Coupled Plasma Mass Spectrometer (Q-ICPMS) coupled with a New Wave Research 193nm ArF excimer laser ablation system at the Department of Geology and Geophysics, IIT Kharagpur. The laser was operated at 5 Hz repetition rate and ca. 5 J/cm$^2$ fluence at spot sizes of 45–50 μm. The instrument was optimized for maximum sensitivity using the USGS sulfide standard MASS-1. The raw counts for each isotope were acquired in time-resolved mode with 30s of gas blank measurement and 45s of peak signal measurement. Instrumental mass-bias and drift were corrected by external standardization with ten measurements of unknowns (samples) bracketed by two measurements of the MASS-1 sulfide standard. The data was reduced offline using the GLITTER© data reduction software. The isotopes that were measured include $^{51}$V, $^{55}$Mn, $^{59}$Co, $^{60}$Ni, $^{63}$Cu, $^{71}$Ga, $^{73}$Ge, $^{75}$As, $^{82}$Se, $^{95}$Mo, $^{107}$Ag, $^{111}$Cd, $^{115}$In, $^{118}$Sn, $^{121}$Sb, $^{193}$Ir, $^{195}$Pt, $^{197}$Au, $^{202}$Hg, $^{205}$Tl, and $^{208}$Pb. A total of 62 spots on sphalerite, 43 on

pyrrhotite, 40 on galena and 26 on chalcopyrite were measured. Care was taken to select clean, inclusion-free grains with radii >40 μm to ensure minimal contamination from inclusions or neighboring minerals. The concentrations of V, Ir, Au and Pt are consistently below detection limits in all the sulfides.

### 4.2.3 Multiple Sulfur Isotope Analyses by nano-SIMS and IRMS

In-situ multiple sulfur isotope analyses of sulfides (n=68) were performed on the SHRIMP SI (Sensitive High mass-Resolution Ion Microprobe – Stable Isotope) ion microprobe at the Research School of Earth Sciences, Australian National University. After detailed observation under the microscope, polished thin sections were selected and cast in 25-mm epoxy mounts together with sulfide reference materials. Microphotographs of samples were taken with an automated Leica D6000 microscope and SHRIMP was used to simultaneously analyze sulfate minerals for sulfur isotopes ($^{32}S$, $^{34}S$ and/or $^{33}S$, $^{36}S$) using Faraday cups with iFlex electrometers at resistor and/or charge modes (Ireland et al., 2014). A $Cs^+$ primary beam of ~2 nA was used with e-gun off with the spot size about 25 μm. Source slit was set at 60 μm, and collector slit widths at 300 μm for $^{32}S^-$, 150 μm for $^{33}S^-$, 200 μm for $^{34}S^-$ and 300 μm for $^{36}S^-$ to resolve potential isobaric interferences from hydrates. The detailed analytical procedures and methods are thoroughly described by Ireland et al., (2014) and Philippot et al., (2018). Analyses of the standards were performed typically after every four to five unknowns to correct for instrumental mass-dependent fractionation. All analyses for the unknowns were normalized to either Ruttan pyrite, assuming $\delta^{34}S_{V\text{-}CDT}$ value of +1.2‰ and 0.618‰ for $\delta^{33}S$, 2.281‰ for $\delta^{36}S$, Norilsk chalcopyrite ($\delta^{34}S_{V\text{-}CDT}$ = +8.0‰) or Anderson pyrrhotite ($\delta^{34}S_{V\text{-}CDT}$ = +1.4‰) (Crowe and Vaughan 1996). The average external reproducibility, as estimated from replicate measurements of the sulfur standards, was typically better than ±1.00‰ (2σ) for $\delta^{34}S$ value, and $\Delta^{33}S$ and $\Delta^{36}S$ were generally better than ±0.20‰ and 0.70‰ (2σ),

respectively. The spot-to-spot analytical error (2σ) of YJS65 arsenopyrite ($\delta^{34}S_{V\text{-}CDT}$ = -1.0‰; Xie et al., 2019), Balmat galena ($\delta^{34}S_{V\text{-}CDT}$ = +16.6‰; Kozdon et al., 2010) and Balmat sphalerite ($\delta^{34}S_{V\text{-}CDT}$ = +14.3‰; Crowe and Vaughan, 1996) for $\delta^{34}S$ value were ±0.75‰, ±1.50‰ and ±2.70‰, respectively. $\delta^{34}S$ values were obtained for sphalerite and galena whereas all four isotopes were analyzed for pyrrhotite and chalcopyrite.

For bulk S-isotope analyses, sphalerite (n= 23) was handpicked using a NIKON Stereozoom microscope and analyzed at the IRMS Facility hosted at Department of Earth Sciences, Pondicherry University, Puducherry, India. Samples were cleaned with Mili Q, dried and powdered in agate mortar. About 750 µg fine powder of each sample was oxidized by ultrapure oxygen gas in a pyrocube elemental analyser (EA) at 1150 °C. The EA was connected to an Isotope Ratio Mass Spectrometer (IRMS, Isoprime 100) in continuous flow mode and $SO_2$ gas was injected in the IRMS after analyses of $N_2$ and $CO_2$. Ultrapure $N_2$, $CO_2$ and $SO_2$ were used as reference gases. Repeated analyses of an international standard IAEA-S1 (Silver sulfide, $\delta^{34}S_{VCDT}$ = –0.3 ‰, e.g. Sharp 2007) and an inhouse laboratory standard EP-1 (Magnesium sulfate, $\delta^{34}S_{VCDT}$ = +0.3 ‰) show that analytical precision was better than ±0.2 ‰. The details of the methodology is described in Absar et al. (2024).

## 4.3 Results

### 4.3.1 Major and Trace Element Characteristics

The results of the geochemical analyses of trace elements in the sulfides are discussed below and are graphically presented in Figures 4.1 and 4.2. The complete dataset is provided in the Appendix Tables 3-13. Time-resolved depth profiles for each trace element have also been investigated to examine their nature of incorporation in the sulfide structure or presence in micro-inclusions. Selected depth profiles with concentrations of relevant elements are shown in Figure 4.3.

#### 4.3.1.1 Sphalerite

Sphalerite contains significant iron, around 8.0-12.6 wt.% with minor inter- and intra-sample variations. The trace element concentrations of sphalerite are measured from 62 spots across the three mineralization types and are shown in Fig. 4.1A.

*Manganese* is known to enter sphalerite in the order of several hundreds to thousands of ppm; for example, concentrations higher than 2 wt.% are recorded in epithermal-Au deposits (Cook et al. 2009). Manganese concentrations in sphalerite from Kayad varies between 786 and 3915 ppm with average concentrations of 1574, 1325 and 2292 ppm in disseminated/laminated, massive and vein–hosted types respectively. Smooth time-resolved ablation profiles suggest that Mn is hosted in the crystal structure of sphalerite.

Cadmium concentrations (879 to 1925 ppm) in the disseminated/ laminated, massive and vein–hosted sphalerite cluster with mean values of 1687 ppm, 1234 ppm and 1475 ppm respectively. All the time-resolved depth profiles for Cd are smooth suggesting that Cd occurs as solid solution in sphalerite.

*Cobalt* can concentrate in substantial amounts in sphalerite due to extensive solid solution between CoS and ZnS (Becker and Lutz 1978). Sphalerite from epithermal, MVT and massive sulfide deposits rarely contain more than 200 ppm of Co. However, higher concentrations of Co, reaching up to around 2000 ppm has been consistently observed in sphalerite from skarn deposits (Cook et al. 2009; Ye et al. 2011). In Kayad, up to 141 ppm Co is measured in sphalerite but it is distinctively lower in massive type, averaging around 23.4 ppm. Sphalerite in disseminated and vein-type ores on the other hand have overlapping ranges and average at 88 and 85 ppm respectively.

*Gallium* and *indium* concentrations are often high in sphalerite (up to 0.3 and 6.9 wt.% respectively) due to significant solid solution of $Ga_2S_3$, roquesite ($CuInS_2$) and sakuraiite ($CuZn_2InS_4$) with ZnS. *Tin* concentrations up to 4.3 wt.% has been reported in sphalerite in

earlier studies; however, in most cases, micro-inclusions of Sn-bearing minerals such as stannite are responsible for such inflated values. Tin and In concentrations in sphalerite from Kayad are <2 ppm. Indium concentrations are consistently higher in disseminated/laminated type while Sn (average: ~0.57 ppm) is remarkably uniform in the three mineralization types. Gallium uniformly occurs below 3 ppm in all samples except in massive type where concentrations approach 7 ppm.

*Copper* spans a vast range from as low as 5.7 ppm to 4.3 wt.%. The time-resolved depth profiles for Cu are rarely flat; most spots with > 300 ppm Cu show multiple peaks owing to widespread chalcopyrite disease. In some spot analyses of vein-hosted and massive type sphalerite, Cu mimics depth profiles of silver which indicates nanoscale inclusions of Cu-Ag-bearing mineral.

*Lead* concentrations vary widely within sample and go up to ~300 ppm. Almost all of the time-resolved depth profiles with > 10 ppm of Pb show spikes that are attributable to micro-inclusions of galena. Similarly, for *mercury*, concentrations are fairly clustered for each sample but ablation depth profiles are irregular when Hg exceeds 16 ppm.

*Silver* and *antimony* commonly do not enter sphalerite in significant amounts. Elevated concentrations above 100 ppm are generally due to Ag- and Sb-bearing mineral inclusions (Cook et al. 2009; Ye et al. 2011). In Kayad, Ag occurs up to 27.4 ppm while Sb is even sparse, not exceeding 11 ppm. Silver content markedly varies in each sample. Most of the analyzed spots give ragged depth profiles that almost always correlate with Sb, Pb, Tl, Sn and Cu in the massive type and a few spots of the vein type. Antimony, on the other hand, is remarkably consistent among samples, however, it correlates well with Pb and Ag in most spots that yield ragged depth profiles of Sb. It is likely that similar profiles of Ag, Pb, Tl and Sb are manifestations of nano-inclusions of sulfosalts such as pyrargyrite, boulangerite and

rayite all of which have been reported from the Zn-Pb deposits of the ADFB and also observed (pyrargyrite) in association with massive ores in Kayad (Chapter 3).

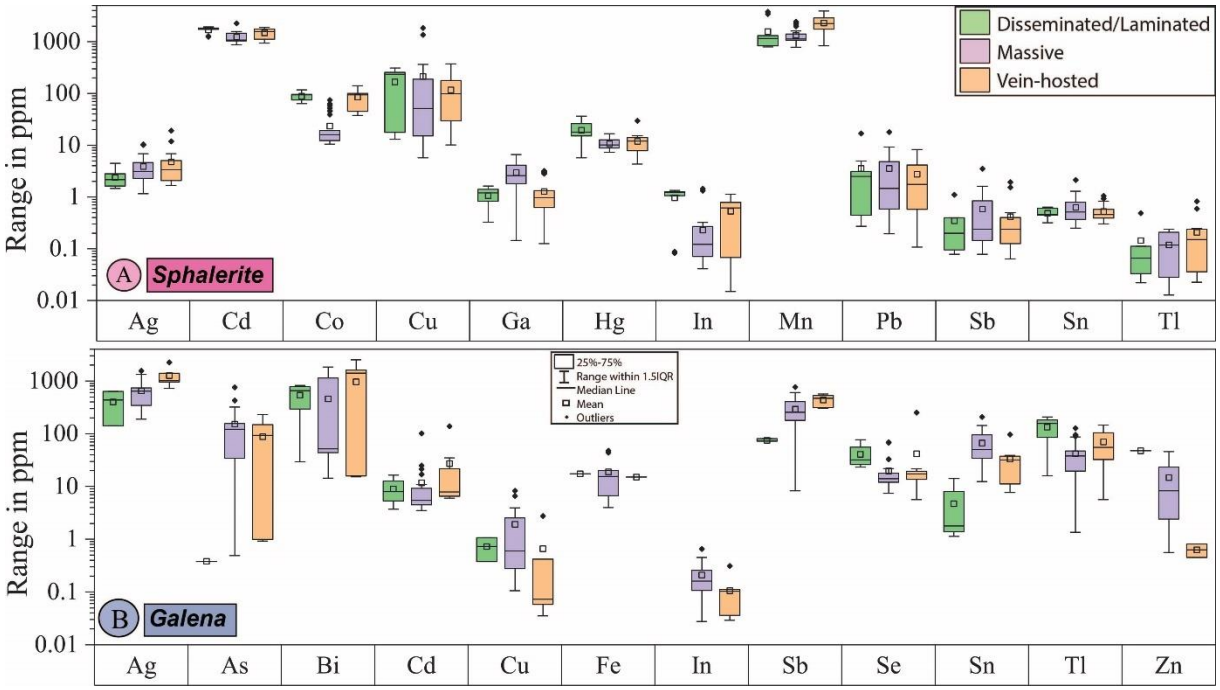


**Figure 4.1:** Box plots of trace elements measured in A) Sphalerite, B) Galena. Only those elements that are above the detection limits for most data points are selected for plotting. Box plots exclude the data with unusually high concentrations pertaining to micro-inclusions. Note that sphalerite contains comparatively higher concentrations of Mn, Cd, Ga and Hg, whereas galena hosts significant Ag, Bi, Sb, and Se.

Bismuth, Mo and Se are below detection limit while Ni and Ge occur in concentrations below 1 ppm and therefore are not included in the graphical presentation. Arsenic is detected only in some spots in QMS massive samples containing large euhedral arsenopyrite.

#### 4.3.1.2 Galena

Concentrations of Pb and S are uniform for all measured grains and follow stoichiometric proportions. Fig. 4.1B summarizes the trace element budget in 41 galena spots across different mineralization types.

*Silver* in the structure of galena from SEDEX and skarn deposits is recorded up to 5000 ppm and 1.5 wt.% respectively (George et al. 2015). About 5000 ppm of *antimony* and

*bismuth* can occur in solid solution; however, Bi is seen to vary greatly among samples from a single deposit. In Kayad, average values of Ag in disseminated/laminated, massive and vein type are 403, 646 and 1268 ppm respectively. Antimony shows similar distribution patterns. LA-ICPMS downhole data for most grains in massive ores that have Ag > 3000 ppm and Sb >600 ppm, show irregular and mimicking Ag and Sb profiles that suggest presence of Ag-antimonides or sulfo-antimonides as micro-inclusions (Palero-Fernández and Martín-Izard 2005). Bismuth ranges from 14.3 to 2507.8 ppm with consistently steady depth profiles.

*Arsenic* is rarely detected in galena, however it is known to occur in structure up to 600 ppm via coupled substitution with Ag (Palero-Fernández and Martín-Izard 2005; Zhou et al. 2020). In Kayad, maximum As concentrations reach 760 ppm but is < 1 ppm or below detection limit in samples that do not contain arsenopyrite in the assemblage. Time-resolved profiles are all smooth suggesting As is incorporated at least up to ~760 ppm in galena.

Due to solid solution between PbS and PbSe, *selenium* can substitute for sulfur leading to several wt.% of Se in galena. On the other hand, *thallium* generally occurs in low amounts via coupled substitution with Sb. 3000 ppm of Se and 300 ppm of Tl in galena from Bleikvassli are the highest concentrations reported thus far among metamorphosed SEDEX deposits (George et al. 2015). In Kayad, Se ranges from 5.6 ppm to 80 ppm with an outlier value of 253 ppm in galena in pegmatite. Thallium occurs up to 208 ppm with the maximum values exhibited by laminated type. Smooth downhole profiles are observed for both elements.

*Indium* and *tin*, recorded in detectable amounts, show compact distribution. Indium occurs only up to 0.6 ppm while Sn occurs up to 209 ppm and both the elements show the highest concentrations in massive type and the lowest in disseminated/laminated type.

In Kayad, extremely high values of *zinc* and *iron*, varying up to three orders of magnitude, are undoubtedly attributed to submicron-scale inclusions of sphalerite evidenced by matching irregular profiles of Zn and Fe for almost all spots that contain these elements in

excess of 50 ppm. Irregular profile of *copper* for concentrations exceeding 10 ppm can result from inclusions of chalcopyrite or Cu-sulfosalts. *Cadmium*, Mn and Hg occur in very low quantities in galena, evenly distributed among all mineralization styles whereas Ga, Ge, Co, Ni and Mo are mostly below detection limit.

#### 4.3.1.3 Pyrrhotite

Figure 4.2A shows the trace element concentrations in pyrrhotite (n=44). Most of the elements are either below detection limit or occur in very low quantities except for *cobalt* and *nickel*, which reach up to 392 ppm and 820 ppm respectively. Cobalt and Ni are comparatively depleted in massive type, a trend also observed in sphalerite. *Arsenic* occurs in appreciable amounts in pyrrhotite up to about 300 ppm, however, it is below detection limit in disseminated/laminated type. Copper, Zn, Cd, Pb and Ag are mostly below 10 ppm; any anomalous amounts result from micro-inclusions of sphalerite or galena or Pb-Cu sulfosalts as confirmed from LA-ICPMS depth profiles.

#### 4.3.1.4 Chalcopyrite

Chalcopyrite is known to be an excellent host for a multitude of trace elements (Fig. 4.2B). *Silver* is a common element in the structure of chalcopyrite and have been reported in concentrations of hundreds to few thousands of ppm (George et al. 2016, 2018; Kampmann et al. 2018; Cave et al. 2020). Shalaby et al. (2004) reported Ag-rich chalcopyrite hosting up to 4.3 wt.% Ag from Um Samiuki VMS deposit of Egypt. In Kayad, Ag in chalcopyrite ranges from 53 ppm to 4089 ppm. All data-points show smooth time-resolved profiles.

*Zinc* is commonly present in chalcopyrite from a few ppm to as much as 5 wt.% both in solid solution and as micron-scale inclusions (George et al., 2018). In the studied chalcopyrite, Zn is strikingly uniform and consolidated across all rock types when below 600 ppm but concentrations above it pertain to sphalerite inclusions.

Chalcopyrite can contain *arsenic* in lattice up to 2000 ppm (Huston et al. 1995; George et al. 2018). In Kayad, up to 428 ppm As is present in chalcopyrite of the vein-hosted type whereas As concentration is negligible or below detection limit in the other two types.

*Tin*, up to 2.3 wt.%, is reported in chalcopyrite from various seafloor hydrothermal systems and volcanogenic massive sulfide deposits (eg. Kase 1987), whereas *indium* is reported to be present at concentrations greater than 2000 ppm due to solid solution between chalcopyrite and roquesite (Cabri et al. 1985; Andersen et al. 2016). In Kayad, Sn occurs below 50 ppm in all mineralization except in massive type where concentrations go up to 500

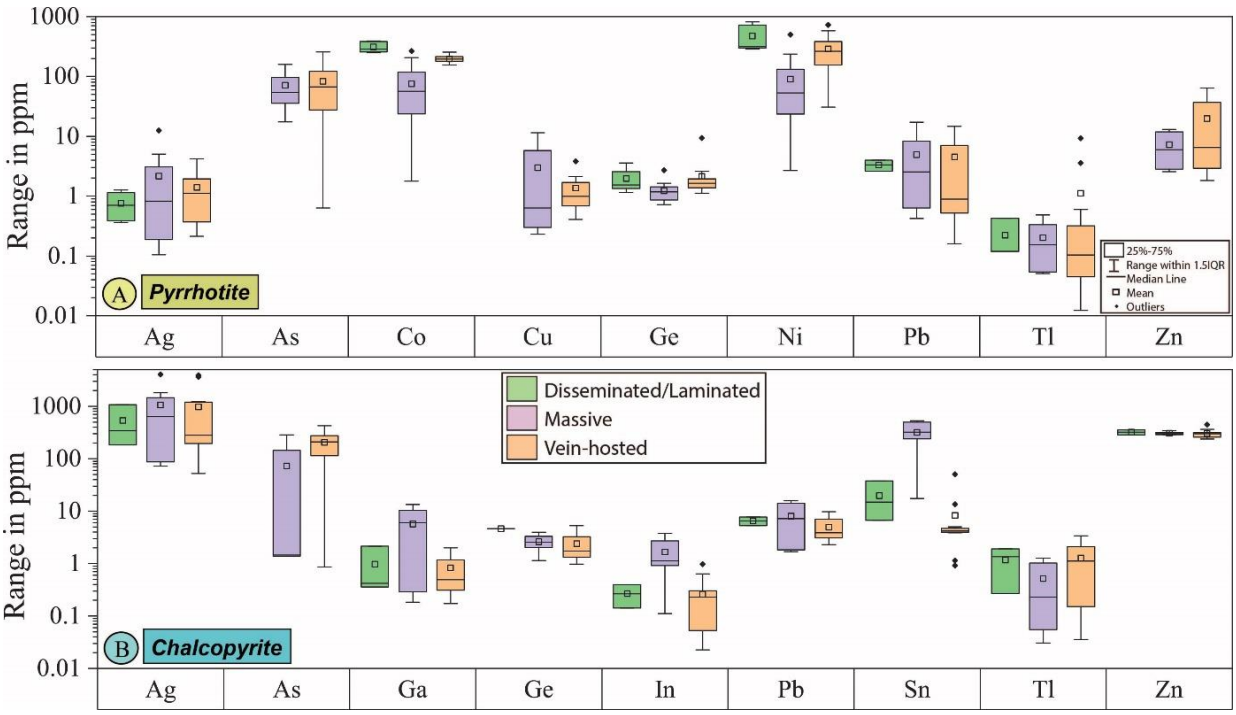


**Figure 4.2:** Box plots of trace elements measured in A) Pyrrhotite, B) Chalcopyrite. Only those elements that are above the detection limits for most data points are selected for plotting. Box plots exclude the data with unusually high concentrations pertaining to micro-inclusions. Pyrrhotite shows higher Co, Ni and As whereas chalcopyrite contains high Ag, Sn, and Ga.

ppm. Few points that exceed 500 ppm also mimic the irregular depth profiles of Zn and Pb and therefore, are considered to be micro-inclusions of sphalerite and Pb-Sn sulfosalts respectively. Indium and gallium concentrations in chalcopyrite are much lower than Sn but the three elements behave in a similar manner, that is, they are highest in massive type than in other groups (Fig. 4.2B).

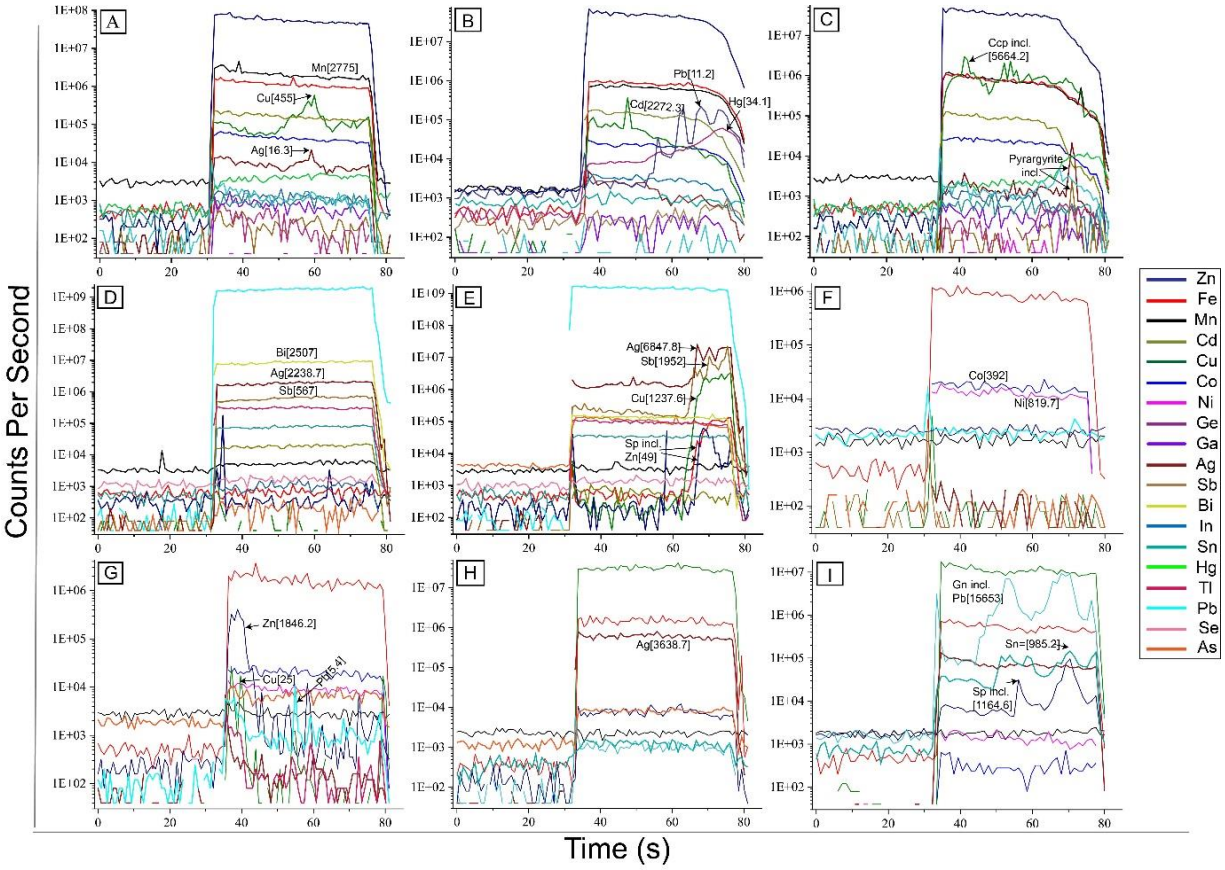


**Figure 4.3:** Selected time-resolved downhole spectra of LA-ICPMS for sphalerite (A-C), galena (D-E), pyrrhotite (F-G) and chalcopyrite (H-I). Similar profiles of Ag and Cu in Fig. A, and Ag and Hg in Fig. B indicates inclusions of Cu-Ag and Pb-Hg bearing minerals/sulfosalts in sphalerite. Peaks in Cu curves in Fig. C indicate chalcopyrite inclusions in the form of chalcopyrite disease. Peaks in Zn, Cu, Ag and Sb in galena (Fig. E) indicate micro-inclusions of sphalerite, chalcopyrite and Ag-Sb-Cu minerals such as pyrargyrite or tetrahedrite. Inclusions of galena, chalcopyrite and sphalerite in pyrrhotite is indicated by sharp peaks in Zn, Cu and Pb curves (Fig. G). Chalcopyrite profile indicates inclusions of sphalerite (from Zn curve) and Pb-Sn sulfosalts (from mirrored profiles of Pb and Sn) in Fig. I.

*Lead* concentrations are often reported within hundreds of ppm (George et al. 2018 and references therein; Cave et al. 2020). In Kayad chalcopyrite, Pb concentrations exceeding 20 ppm palpably have irregular time-resolved profiles attributed to galena inclusions. Cobalt, Cd, Ge, Tl, Bi, Sb and Mn concentrations are less than 10 ppm. Selenium, Mo and Hg concentrations are below their respective detection limits.

#### 4.3.1.5 Arsenopyrite

The major elements, Fe, As and S in arsenopyrite, occur in stoichiometric proportions. Iron ranges from 31.8 to 34.5 wt.%, As varies between 45.5 and 49 wt.% while wt.% of sulfur ranges from 17.1 to 19.7. In similarity with pyrrhotite, Co and Ni consistently occur as minor elements, up to 1.6 wt.% and 1 wt.% respectively. Arsenopyrite, in all samples, is generally barren of trace elements except Sb which consistently occurs up to 238 ppm.

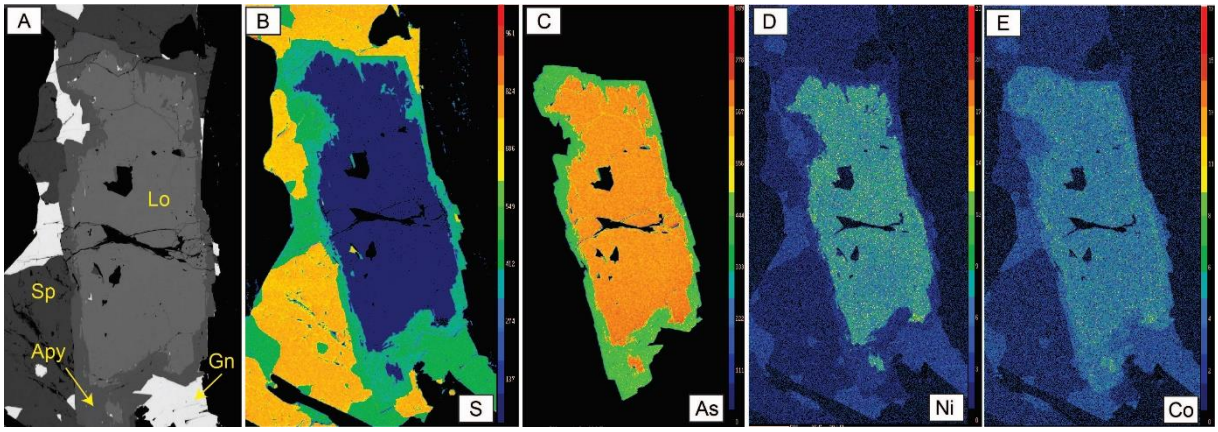


**Figure 4.4:** BSE image (A) and corresponding element distribution maps (B-E) of löllingite (core) grain replaced by arsenopyrite (rim). Boxes at the bottom right correspond to the element which is mapped. Note the corroded contact between of the two minerals indicating dissolution-reprecipitation.

Downhole profiles of laser spectra indicate occasional presence of sphalerite and galena as micro-inclusions. As mentioned in Chapter 3 section 3.4.2, most of the large arsenopyrite grains contain löllingite relics. Iron and arsenic in these relics vary from 24.2 to 27.3 wt.% and 67.7 to 71.3 wt.% respectively. All of them contain minor sulfur in their structure that ranges from 1.7 to 2.8 wt.%. An interesting feature of the löllingite grains is the presence of Co and Ni wherein Ni always outweighs Co in concentration (Fig. 4.4). However, there are inter-sample differences, for example, the mean concentrations of Co and Ni in ML 10H and KYD 16 are 0.72 and 1.56 wt.% respectively whereas in ML 12B, Co and Ni occur at an average value of 1.45 and 2.65 wt.% respectively. A few grains have up to 2.3 ppm of gold.

### 4.3.2 Multiple Sulfur Isotopes of Sulfides

Sphalerite, galena, pyrrhotite and chalcopyrite from samples representing 3 mineralization types were analyzed in-situ using SHRIMP (Table 4.1). $\delta^{34}S$ values of all sulfides, irrespective of host or mineralization type, are consistently positive with the maximum value of 17.2‰ shown by galena of massive type (Fig. 4.5A). $\delta^{34}S_{sphalerite}$ of laminated/disseminated and vein-hosted types have compact ranges whereas massive type shows a larger spread.

| **Sphalerite** | **$\delta^{34}S$** | **Mean** | **±1σ** | **$\Delta^{33}S$** | **Mean** | **±1σ** | **$\Delta^{36}S$** | **Mean** | **±1σ** |
|---|---|---|---|---|---|---|---|---|---|
| Laminated/ Disseminated | +4.3 to +6.4 | +5.4 | 0.80 | | | | | | |
| Massive | +2.7 to +8.9 | +5.8 | 1.93 | | | | | | |
| Vein-hosted | +2.3 to +5.7 | +4.0 | 1.10 | | | | | | |
| **Galena** | | | | | | | | | |
| Laminated/ Disseminated | +11.3 | | | | | | | | |
| Massive | +11 to +17.2 | +13.4 | 2.28 | | | | | | |
| Vein-hosted | +7.8 to +16.9 | +11.7 | 3.77 | | | | | | |
| **Pyrrhotite** | | | | | | | | | |
| Laminated/ Disseminated | +6.5 to +11.3 | +8.6 | 1.71 | -0.07 to +0.14 | 0.0 | 0.06 | -0.49 to +0.28 | -0.01 | 0.21 |
| Massive | +6.1 to +9.2 | +7.8 | 1.08 | -0.15 to -0.03 | -0.05 | 0.05 | -0.07 to +0.22 | +0.11 | 0.11 |
| Vein-hosted | +7 to +8.43 | +7.87 | 0.68 | -0.05 to +0.12 | +0.03 | 0.08 | -0.17 to +0.09 | -0.01 | 0.11 |
| **Chalcopyrite** | | | | | | | | | |
| Laminated/ Disseminated | +6.9 to +7.8 | +7.3 | 0.43 | -0.02 to +0.04 | +0.01 | 0.03 | -0.28 to +0.28 | +0.02 | 0.28 |
| Massive | +7 to +8.4 | +8 | 0.57 | 0.0 to +0.16 | +0.1 | 0.05 | -0.01 to +0.43 | +0.24 | 0.16 |
| Vein-hosted | 6.4-8.9 | +7.8 | 1.19 | -0.03 to +0.44 | +0.2 | 0.23 | -0.45 to +0.02 | -0.28 | 0.22 |

**Table 4.1:** Sulphur isotope systematics of sphalerite, galena, pyrrhotite and chalcopyrite from three types of sulfide mineralization based on Nano-SIMS data.

However, average $\delta^{34}S_{sphalerite}$ of laminated and massive types are similar (5.4‰ ± 0.8 and 5.8‰ ± 1.9 respectively) and slightly higher than vein-hosted type (4.0‰ ± 1.1). Only a

single data could be obtained for galena of laminated/disseminated type due to its rarity and lack of sizeable grains. However, galena of massive type shows the highest $\delta^{34}S$ range of +11 to +17.2‰ (avg. 13.4‰), whereas the vein-hosted type furnishes lower range of +7.8 to +16.9‰ (avg. 11.7‰). $\delta^{34}S$ ranges of pyrrhotite and chalcopyrite, in all mineralization types, are remarkably restricted (+6.1 to +9.2‰) with the exception of $\delta^{34}S_{pyrrhotite}$ in laminated type, which shows a wider range (+9.03 to +11.3‰) in quartzite. For a majority of the data points, $\delta^{34}S_{galena} > \delta^{34}S_{sphalerite}$ and $\delta^{34}S_{pyrrhotite} < \delta^{34}S_{chalcopyrite}$ which indicates a state of isotopic disequilibrium between the coexisting sulfides.

In-situ measurement of S isotope of sphalerite is known to be compromised due to crystal orientation effect which can lead to differences of 1.7 to 3.4‰ among individual grains even from the same sample (Kozdon et al. 2010). The Kayad sphalerite data attracted an external error of avg. 2.75‰ (Appendix Table 14) which is notably higher than that obtained for pyrrhotite, chalcopyrite and arsenopyrite (avgs. 1.1‰, 0.9‰, 0.85‰ respectively). Therefore, a supplementary analysis was done using IRMS to constrain $\delta^{34}S$ data expecting higher accuracy. The results indicate highly positive and narrower range from +5.2‰ to +9.2‰ with similar average values among mineralization types (Table 4.2).

| **Mineralization type** | **No. of samples** | **$\delta^{34}S_{VCDT}$ range** | **Mean** | ±1σ |
|---|---|---|---|---|
| Laminated/Quartzite | 01 | +8.85 | | |
| Massive | 14 | +5.16 to +8.79 | +7.84 | 0.97 |
| Vein-hosted | 08 | +7.04 to +9.18 | +7.94 | 0.75 |

**Table 4.2**: Results of IRMS analyses of sphalerite separates from three different types of sulfide mineralization.

Multiple sulfur isotopes were determined for pyrrhotite and chalcopyrite only (Fig. 4.5B) due to large errors induced by sphalerite and galena. $\Delta^{33}S_{pyrrhotite}$ of laminated and

massive types are mostly negative, ranging from -0.15‰ to +0.01‰ with only one significantly positive value of 0.14‰ (Table 4.1). The vein-hosted type skews slightly towards positive values but does not exceed 0.12‰. $\Delta^{33}S_{chalcopyrite}$, on the other hand, are mostly positive with only two data points showing negative values up to -0.03‰. Most analyzed grains show $\Delta^{33}S$ values between +0.01‰ and +0.16‰ with the exception of 2 points in vein-hosted type that have unusually higher values of +0.33 ‰ and +0.44‰. $\Delta^{36}S$ averaged at +0.03‰ and +0.01‰ ($2\sigma = \pm 0.52$‰) for pyrrhotite and chalcopyrite, respectively.

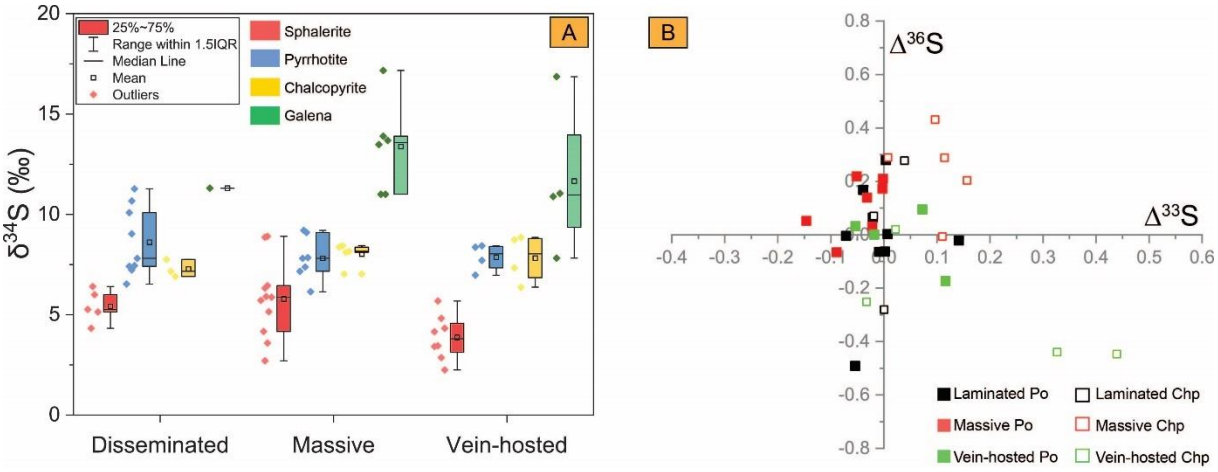


**Figure 4.5:** Graphs showing variations of multiple sulfur isotopes in sulfides in laminated, massive and vein-hosted type; A) Box and whisker plot with statistics on $\delta^{34}S$ values of sphalerite, galena, pyrrhotite and chalcopyrite across the three mineralization types; B) Scatter plot showing the $\Delta^{33}S$ and $\Delta^{36}S$ values of Kayad sulfides.

## 4.4 Implications of Trace Element Geochemistry and S-isotope Compositions of Sulfides

### 4.4.1 Incorporation of Trace Elements in Sulfides

***Sphalerite:*** Extensive work on elemental substitution schemes have put forth numerous mechanisms of trace element incorporation in sphalerite (Cook et al. 2009; Ye et al. 2011; Lockington et al. 2014; Bonnet et al. 2016). The most encountered divalent ions in sphalerite viz $Fe^{2+}$, $Mn^{2+}$, $Co^{2+}$ and $Cd^{2+}$ have similar ionic radii as $Zn^{2+}$ and therefore, isomorphously replace Zn in the sphalerite structure. In Kayad sphalerite, good correlation between Zn and

Fe ($r^2$=0.5) confirms Fe incorporation via the $Zn^{2+} \leftrightarrow Fe^{2+}$ substitution (Fig. 4.6A). A weak positive correlation between Fe and Cd (Fig. 4.6B), especially in the massive samples, can be explained by the coupled substitution $Zn^{2+} \leftrightarrow (Fe^{2+} + Cd^{2+})$. Indium and gallium are shown to enter sphalerite through the coupled substitutions $2Zn^{2+} \leftrightarrow Cu^{+} + In^{3+}$ (Cook et al. 2009) and $2Zn^{2+} \leftrightarrow (Ag, Cu)^{+} + Ga^{3+}$ respectively. The poor correlations between Cu and In (Fig. 4.6C), Cu and Ga (Fig. 4.6D) and Ag and Ga (not shown) in Kayad sphalerite indicate that these substitution schemes did not play important role. However, a lack of pattern could result due to several reasons. Cook et al. (2009) noted that the substitution method involving indium bore best results for samples which are enriched in indium, however, in the Kayad sphalerite, indium barely reaches 2 ppm, indicating a scarcity of enough trivalent cations needed to encourage the process. Secondly, Cu and Ag, in almost all Kayad sphalerite, are present in the form of inclusions of chalcopyrite or Ag-bearing sulfosalts (as discussed in section 4.3.1.1) and there are only few data points that indicate their presence in the structure of sphalerite, which can lead to unsatisfactory correlation trends.

***Galena:*** Solubility of $Ag_2S$ is low in galena, not more than 0.4 mol % at 615°C (Van Hook 1960; George et al. 2015) and restricts direct one-to-one substitution of Pb by $Ag^{+}$. However, presence of Sb and Bi greatly enhances the solubility of Ag in galena (Amcoff 1984; Chutas et al. 2008) due to complete solid solutions between PbS, $AgSbS_2$ (miargyrite) and $AgBiS_2$ (matildite) at 420°C (Van Hook 1960; Amcoff 1984). Consequently, Ag, Bi and Sb show some of the highest concentrations in galena. Several substitution mechanisms have been proposed involving these elements to explain their incorporation. Silver enters the structure of galena via coupled substitutions such as $2Pb^{2+} \leftrightarrow Ag^{+} + (Bi+Sb)^{3+}$ and $(Ag,Cu,Tl)^{+} + (Bi+Sb)^{3+} \leftrightarrow 2Pb^{2+}$ (George et al. 2015). A moderate positive correlation (r=0.5) is observed between Ag and Sb (Fig. 4.6E) with much of the massive type falling close to the Ag:Sb = 1:1 line which indicates significant $2Pb^{2+} \leftrightarrow Ag^{+} + Sb^{3+}$ substitution. The

flat Ag-Bi plots (Fig. 4.6F) for low Bi (<100 ppm) and positive correlation for high Bi along Ag:Bi= 1:1 line suggest $2Pb^{2+} \leftrightarrow Ag^{+} + Bi^{3+}$ did not play significant role when concentration of Bi is low. However, a much better correlation (r=0.83) between Ag and Bi+Sb and near parallel disposition of the best fit line with 1:1 line (Fig. 4.6G) indicates that coupled substitution of $2Pb^{2+} \leftrightarrow Ag^{+} + (Bi+Sb)^{3+}$ collectively is the primary mechanism that governs incorporations of these elements in galena.

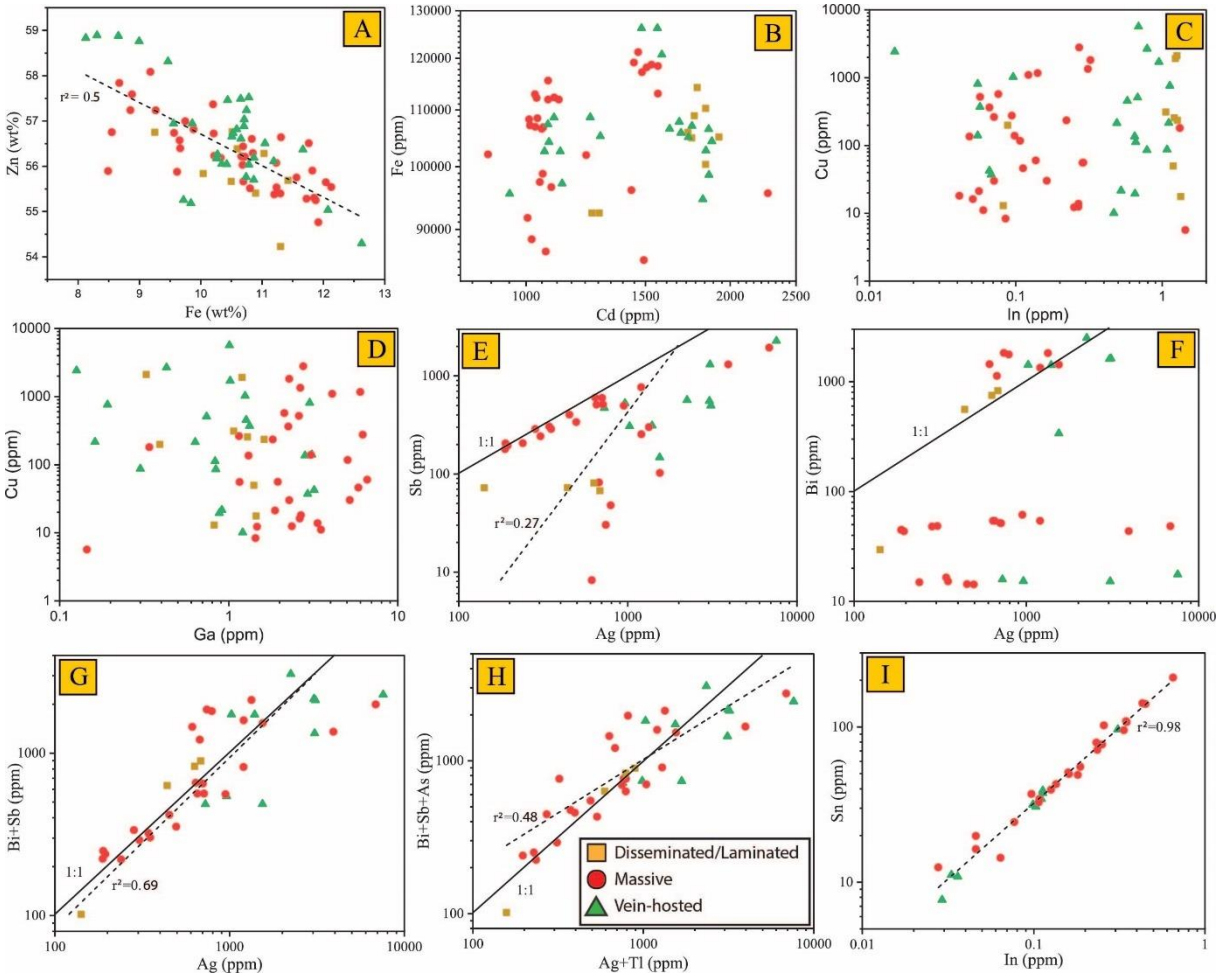


**Figure 4.6:** Bivariate plots of selected major and trace elements in sphalerite (A-D) and galena (E-I). Good negative correlation between Zn and Fe indicates direct substitution of Zn by Fe whereas poor correlation of Cu with In and Ga is due to low In and Ga content of sphalerite and presence of Cu as micro-inclusions of chalcopyrite. Incorporation of Ag, Sb, Bi, and As in galena occurs via $Ag^{+}+(Bi,Sb,As)^{3+} \leftrightarrow 2Pb^{2+}$ substitution while Sn replaces In to enter into the structure of galena.

Coupled substitution between Ag, Sb and Bi warrants that the maximum possible mol. % Ag within the galena lattice should not exceed the mol. % of (Bi+Sb). If, however, the

mol. % of Ag is greater than the mol. % of (Bi+Sb), then the excess Ag might be attributed to the presence of sub-micrometer scale inclusions of Ag-bearing minerals. In Kayad galena, mol. % of Ag is nearly equal to the mol. % of (Bi+Sb) except some spots where mol. % of Ag exceeds the latter by 0.13 to 0.55 mol. %. These points correspond to the ones showing irregular time-resolved signals during LA-ICPMS measurements, and can be explained as the result of micro-inclusions of sulfosalts such as pyrargyrite. Incorporation of As into galena occurs as a trivalent cation via an equivalent coupled substitution with Bi and Sb: $Ag^{+}+(Bi,Sb,As)^{3+}\leftrightarrow 2Pb^{2+}$ which is suggested by a good positive correlation ($r^2$=0.5) between Ag+Tl and Bi+Sb+As (Fig. 4.6H). Tin and In show a good positive correlation ($r^2$=0.98) (Fig. 4.6I) which indicates Sn and In are similarly partitioned into galena.

***Pyrrhotite:*** Pyrrhotite is depleted in most trace elements (< 10 ppm with many grains having concentrations below detection limit) except Co and Ni. Figure 4.7A shows a good positive correlation between Co and Ni which directly substitute for Fe in the pyrrhotite structure via the substitution $2Fe^{2+} \leftrightarrow Co^{2+}+Ni^{2+}$.

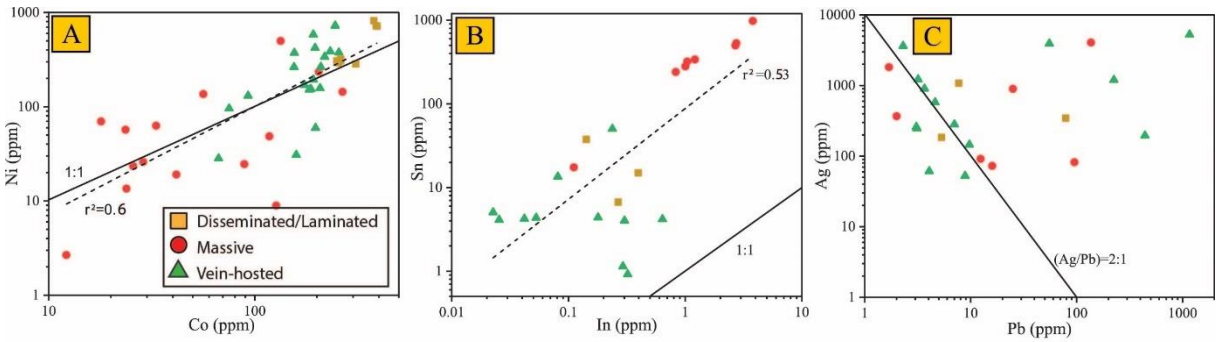


**Figure 4.7:** Bivariate plots of selected trace elements in pyrrhotite (A) and chalcopyrite (B-C). Good correlation between Co and Ni in pyrrhotite suggests a direct substitution of Fe for the incorporation of these elements. Incorporation of some Ag in chalcopyrite occurs by direct substitution of Pb as depicted by the negative correlation between Ag and Pb.

***Chalcopyrite:*** The structure of chalcopyrite, unlike sphalerite or galena, is strongly covalent; valence state of copper can vary between $Cu^{+}$ and $Cu^{2+}$, and iron can be present as $Fe^{2+}$ or $Fe^{3+}$. Since neither of the hypotheses stand disproved, it has been suggested that

chalcopyrite may remain in an intermediate ionic state between $Cu^{+}Fe^{3+}S_2^{2-}$ and $Cu^{2+}Fe^{2+}S_2^{2-}$ (George et al. 2018 and references cited there).

The incorporation of trace elements in chalcopyrite is mainly controlled by the co-crystallizing base metal sulfides (George et al. 2018). Nevertheless, chalcopyrite is known to host high concentrations of Ga, In, Sn and Ag. The ionic radii of $Zn^{2+}$, $Sn^{4+}$ and $In^{3+}$ fall within a window between the radii of $Fe^{3+}$ and $Fe^{2+}$ while $Ag^{+}$ is closest in size to $Cu^{+}$ in tetrahedral coordination. Therefore, $Ag^{+}$ and ($Zn^{2+}$, $In^{3+}$, $Sn^{4+}$) can replace $Cu^{+}$ and $Fe^{2+}/Fe^{3+}$ respectively in the chalcopyrite structure (George et al. 2016). However, poor to weak correlations are observed between Cu and Ag, Zn and Fe, and Sn and Fe ($r^2$=0.3) (not shown) which suggests that these mechanisms were not responsible for the incorporation of Sn, Zn and Ag. A moderately positive correlation between In and Sn (Fig. 4.7B) with roughly 1:1 slope indicates that the elements behave similarly. Silver and Pb on the other hand show a moderate negative correlation (Fig. 4.7C) with a slope of 2:1 (when the analyses inferred to be contaminated by galena micro-inclusions are excluded), suggesting that Ag and Pb compete for similar structural sites hindering each other's incorporation.

### 4.4.2 Thermometry using Sulfides

Sphalerite has commonly been used as a geothermometer and geobarometer. Both minor and trace element concentrations in sphalerite structure, for example, Ga/Ge ratios (Mladenova and Valchev 1998), fractionation of Mn-Cd between sphalerite and galena (Mishra and Mookherjee 1988; Bortnikov et al. 1995), and mol% of FeS in sphalerite (Scott and Barnes 1971; Sarkar et al. 1980; Lynch and Mengel 1995) have been utilized to determine temperature and pressure conditions during ore formation. It was noted that the trace element composition of sphalerite is sensitive to its temperature of formation and re-equilibration. Sphalerite formed at high temperatures can accommodate high proportions of Fe, Mn, In, and

Sn, whereas those that form at low temperatures typically have elevated concentrations of Ga, Ge, As, Sb, Tl and Ag, which may differ by two to three orders of magnitude (Stoiber 1940; Cook et al. 2009; Frenzel et al. 2016; Bauer et al. 2019; Li et al. 2020). Knorsch et al. (2020) also observed an interrelation among the color, chemical composition and temperature of formation of sphalerite. Dark brown and black sphalerites generally contain the highest Fe and Mn and form at higher temperatures (>200°C) than yellow and tan colored sphalerites that are enriched in the low temperature elements. The sphalerites at Kayad are invariably dark black in color with inflated amounts of Fe (8-12 wt%), which is in line with the observations of Knorsch et al. (2020) and have moderate to high Mn and Cd (Fig. 4.1A) while being overall depleted in Ga, Ge, In, Sb, Sn, As and Tl. These patterns indicate that sphalerite deposition took place under moderately high temperatures.

A quantitative approximation of the temperature can be made using the GGIMF thermometer of Frenzel et al. (2016) who conducted principal component analysis on large sets of precise geochemical data of sphalerite, and identified 5 elements, Ga, Ge, In, Mn and Fe, that are sensitive to thermal changes. Temperature estimations of ore deposition in Kayad are made using 62 sphalerite analyses. The highest temperature of 392°C using the GGIMF thermometer is obtained from sphalerite in the pegmatite. The disseminated type and vein-hosted sphalerite furnish similar average temperatures of 351±16 °C and 350±7 °C respectively whereas the massive ores provide slightly lower temperatures (333±17 °C) (Fig. 4.8A). The obtained temperatures, however, coincide with the closure temperatures of sphalerite and since the rocks in and around the Kayad area have undergone at least amphibolite-grade metamorphism, the temperature obtained from sphalerite likely represents post-peak metamorphic cooling rather than peak conditions.

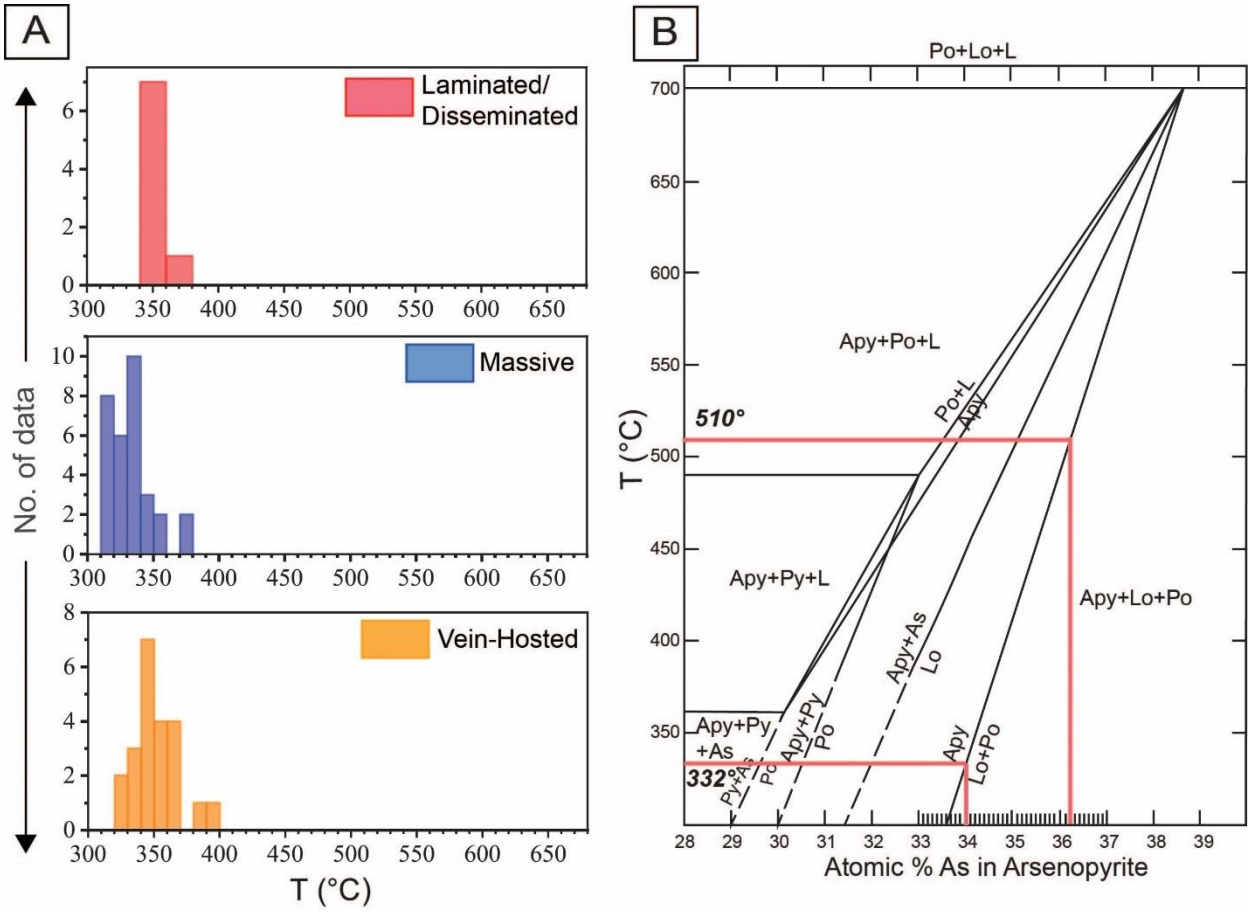


**Figure 4.8:** Thermometry using sphalerite and arsenopyrite. A) Histogram showing temperature ranges of disseminated/laminated, massive and vein-hosted sphalerite obtained from sphalerite GGIMF thermometer. Calculations yield compact and similar ranges for the three mineralization types with average around 350 ˚C which coincides with sphalerite's closure temperature, B) T-X diagram after Kretschmar and Scott (1976) for calculating temperature from atomic% of As in arsenopyrite. Arsenopyrite is a retrograde phase after löllingite however maximum temperature of 510 ˚C obtained advocates for a comparatively higher peak metamorphic temperature. For further discussions on the implication of these temperatures, please refer to Chapter 6.

The As concentration of arsenopyrite changes with the mineralogical association and temperature. The minimum and maximum temperatures were calculated from arsenopyrite-löllingite association in massive ores using atomic% of As in arsenopyrite in the T-X diagram of Kretschmar and Scott (1976). In the massive ore, widespread pseudomorphic replacement of löllingite by arsenopyrite is indicated by the nearly ubiquitous occurrence of löllingite relics in arsenopyrite suggesting the latter to be a product of retrogression. The arsenopyrite contains inclusions of galena and also shares straight grain boundaries with galena and

sphalerite. Using the T-X diagram of Kretschmar and Scott (1976), the minimum and maximum temperatures are constrained at 332 °C and 510 °C from the minimum (34%) and maximum (36.2%) atomic % of As respectively, projected on the löllingite + pyrrhotite - arsenopyrite line (Fig. 4.8B). Since, arsenopyrite-löllingite pairs exhibit a retrograde relationship (Tomkins and Mavrogenes 2001), the temperature derived from arsenopyrite thermometry reflects retrograde metamorphic conditions. The wide range of temperatures is probably due to variable re-equilibration at lower temperatures, potentially influenced by grain size. This also suggests that the peak metamorphic temperature must have exceeded the highest retrograde temperature of 510 °C recorded by arsenopyrite.

### 4.4.3 Source of Sulfur

There are two main isotopic reservoirs of sulfur; *mantle*, where sulfur occurs in reduced state ($H_2S$) with average $\delta^{34}S \approx 0‰$, and *seawater*, where sulfur occurs in oxidized form as sulfate ($SO_4^{2-}$). Any deviation in the $\delta^{34}S$ signature of S-bearing phases is a result of either isotopic fractionation of recycled sulfur during different geological processes, or mixing of sulfur from these end-member reservoirs. In a typical SEDEX system, metal-rich exhalations, generally unrelated with concurrent magmatic activity, interact with seawater to deposit sulfides during basin sedimentation. Therefore, the prevailing consensus, backed by multiple lines of evidence from fluid inclusions and sulfur isotopes in SEDEX Pb-Zn systems, is that the predominant source of sulfur are metalliferous basinal brines derived from highly evaporated seawater and/or connate brines (Leach et al. 2004; Wilkinson 2014). Prior to metal precipitation, the dissolved sulfate in the brine is reduced to $H_2S$ either by biogenic means, known as bacterial sulfate reduction (BSR), or by abiogenic means, called thermochemical sulfate reduction (TSR). The processes of BSR/TSR can occur in a variety of sedimentary

settings, and are responsible for forming sour gas reservoirs due to release of hydrogen sulfide and elemental sulfur as by-products of these reactions (Machel et al. 1995).

In *Bacterial Sulfate Reduction or BSR*, sulfur is released as a result of organic processes which include breakdown of the metabolic residues, such as organic acids and alcohols generated through aerobic degradation, by sulfate reducing anaerobic bacteria. BSR is most effective in low temperature diagenetic environments with temperatures up to about 60-80 °C (Jørgensen et al. 1992) since microbes cease to metabolize at higher temperatures (Machel et al. 1995). $H_2S$ originating from biogenic processes sequester the lighter sulfur isotope and consequently impart a much lighter and often significantly negative $\delta^{34}S$ values to the sulfides. Conversion of $SO_4^{2-}$ to $S^{2-}$ during BSR can cause kinetic fractionation of -15 to -65%. The degree of isotope fractionation is dependent on few factors such as the original $\delta^{34}S$ signature of the source sulfate, formation of intermediate compounds, and whether the system was closed or open with respect to $H_2S$ and $SO_4^{2-}$. This leads to interesting distribution patterns of $\delta^{34}S$ in the sedimentary succession leading to a large spread in $\delta^{34}S$ values of BSR-derived sulfides (Misra 2000). In a system open to both $SO_4^{2-}$ and $H_2S$, $SO_4^{2-}$ is replenished continuously therefore, $\delta^{34}S_{H2S}$ shows a normal distribution of isotopically lighter values. In a system closed to both $SO_4^{2-}$ and $H_2S$, the generated $H_2S$ equilibrates with the $SO_4^{2-}$ and therefore, attains a highly skewed negative $\delta^{34}S$. In a system closed to $SO_4^{2-}$ but open to $H_2S$, produced $H_2S$ escapes the system leaving an increasingly heavier $SO_4^{2-}$. $H_2S$ thus generated from such isotopically heavy $SO_4^{2-}$ gradually attains heavier $\delta^{34}S$ values via Rayleigh fractionation. Consequently, the successive generations of sulfides show an increasing $\delta^{34}S$ trend towards stratigraphic top. Biogenic sulfide has been recognized as the major source of sulfur for many base metal deposits such as Sullivan or Howards Pass.

*Thermochemical Sulfate Reduction or TSR*, on the other hand, occurs in the presence of heat and inorganic reductants such as hydrocarbons or organic matter. It operates at

temperature ranges of 100-140 °C (Worden et al. 1996) and can go even higher in some settings. The kinetic fractionation rate of TSR is low since it progresses through formation of intermediary sulfur species such as polysulfides, thiosulfates and sulfites that are easily reduced by organic compounds (Goldstein and Aizenshtat 1994; Machel 2001; Basuki et al. 2008). This results in lower fractionation relative to the source sulfate, leading to positive $\delta^{34}S$ of sulfides. The rate of TSR depends on temperature, and the presence of catalysts, such as elemental sulfur or bacteriogenic nascent $H_2S$. The catalyzing $H_2S$ needed for the initiation of TSR reaction is normally obtained from initial BSR processes or thermal degradation of organically bound sulfur in the shales via reaction with hydrothermal fluids (Dixon and Davidson 1996). Once initiated, TSR is autocatalyzed by the production of $H_2S$ as an intermediate species. At higher temperatures of 200-350 °C, TSR takes place by interacting with $Fe^{2+}$ bearing minerals by Rayleigh fractionation and above 400 °C, isotopic fractionation between $H_2S$ and $SO_4^{2-}$ occurs in an equilibrium state. Abiological kinetic fractionation produces sulfides about 20‰, 15‰ and 10‰ lighter than the dissolved reactant sulfate at 100 °C, 150 °C, and 200 °C respectively, values further decreasing with increasing temperature since rate of TSR becomes rapid at higher temperatures (Kiyosu and Krouse 1990; Machel et al. 1995).

The consistent positive $\delta^{34}S$ nature of the laminated Pb-Zn sulfides in Kayad and their preferred occurrence in graphite rich bands/rocks seemingly suggest precipitation of the primary sulfides through thermochemical reduction of a heavy sulfate source in the presence of organic matter. Therefore, the possible sources of sulfate would be brines or evaporites (refer to Fig. 4.9), derived from Early Proterozoic seawater with $\delta^{34}S$ measured around 20‰ (Canfield 2004; Crockford et al. 2019), or continental evaporites that have slightly lower $\delta^{34}S$ values due to contribution from groundwater, rainwater, or continent-derived sulfide minerals, etc. (Seal et al. 2000; Gu and Eastoe 2021). Existing fluid inclusion data on SEDEX deposits

around the world constrain a low to moderate temperature of ore formation ranging from 70 ˚C to 280 ˚C. Assuming a $\delta^{34}S$ range of 10 - 20‰ for the original fluid and a temperature of 150 – 200 ˚C, TSR alone could produce isotopic ranges comparable to what is obtained in Kayad. Rayleigh fractionation during BSR in a restricted basin (which was closed to $SO_4^{2-}$ but open to $H_2S$) can also lead to heavy $\delta^{34}S$ values; however, since sulfide samples obtained from different mine levels in Kayad fall within a narrow positive range (Table 4.1) and delineate a symmetric distribution with no observable $\delta^{34}S$ gradation towards stratigraphic top, it precludes BSR in a closed environment.

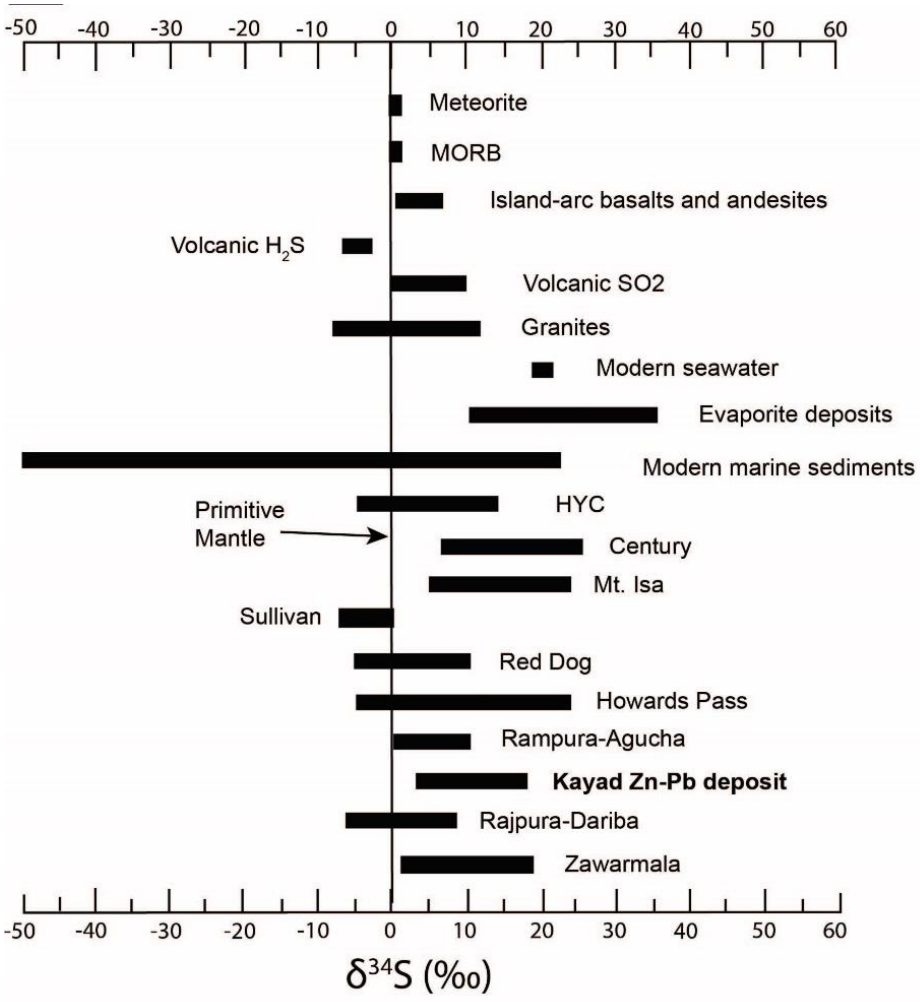


**Figure 4.9:** Distribution of sulfur isotopic compositions in different reservoirs, rock types and SEDEX deposits. Data were obtained from Leach et al., (2005). $\delta^{34}S$ of Kayad sulfides vary from +2.7‰ to +17.2‰.

Linear fractionation trend of sulfur isotopes, also known as mass-dependent fractionation (MDF), are governed principally by their isotope masses. For example, variations in $^{34}S/^{32}S$ ratios would be nearly twice as that for $^{33}S/^{32}S$ ratios and half of $^{36}S/^{32}S$ ratios (Seal 2006). Sulfides in which S-isotopes undergo MDF would follow $\delta^{33}S = 0.515 \times \delta^{34}S$ and $\delta^{36}S = 1.90 \times \delta^{34}S$ relations and the values of $\Delta^{33}S$ ($\delta^{33}S - 0.515 \times \delta^{34}S$) and $\Delta^{36}S$ ($\delta^{34}S - 1.9 \times \delta^{34}S$) would be zero. Consequently, in a $\delta^{34}S$ vs $\delta^{33}S$ bivariate plot, sulfides with MDF would lie on the line defined by a slope of 0.515, called the mass fractionation line (MFL). However, it was observed that in the Archean, these values deviated from the established relation and recorded a non-linear variation independent of mass, known as mass independent fractionation (MIF). Experimental studies concluded that UV-photolysis of $SO_2$ in an anoxic atmosphere was the causative factor for these anomalous fractionations which led to their deviation from MFL and the resultant non-zero values of $\Delta^{33}S$ and $\Delta^{36}S$ in sedimentary sulfides and sulfates (Farquhar et al. 2001; Farquhar and Wing 2003). Therefore, the transition from MIF to MDF signatures in sedimentary sulfides/sulfates serves as a proxy for Earth's transition from an $O_2$-poor atmosphere to an oxygenated one (Farquhar and Wing 2003). Generally, sediments younger than ~2.4 Ga (coincident with Great Oxygenation Event) do not record MIF signatures and have $\Delta^{33}S$ and $\Delta^{36}S$ values of 0±0.2% and 0±0.4% respectively, reflecting MDF signatures, if not contaminated by Archean near-surface sources (Farquhar and Wing, 2003; Young et al., 2013). In Kayad, the majority of $\Delta^{33}S$ and $\Delta^{36}S$ values of both pyrrhotite and chalcopyrite fall between -0.2 to +0.2‰ and -0.3 to +0.3‰ (Fig. 4.10A) respectively and therefore, are largely confined within the traditional MDF envelope (Fig. 4.10B).

LaFlamme et al. (2018) redefined the traditional threshold of MDF-generated $\Delta^{33}S$ values suggesting that unlike equilibrium reactions which proceed with a $\lambda^{33}$ ($\delta^{33}S/\delta^{34}S$) of 0.515, as explained previously, $\lambda^{33}$ in kinetic reactions (associated with BSR or TSR

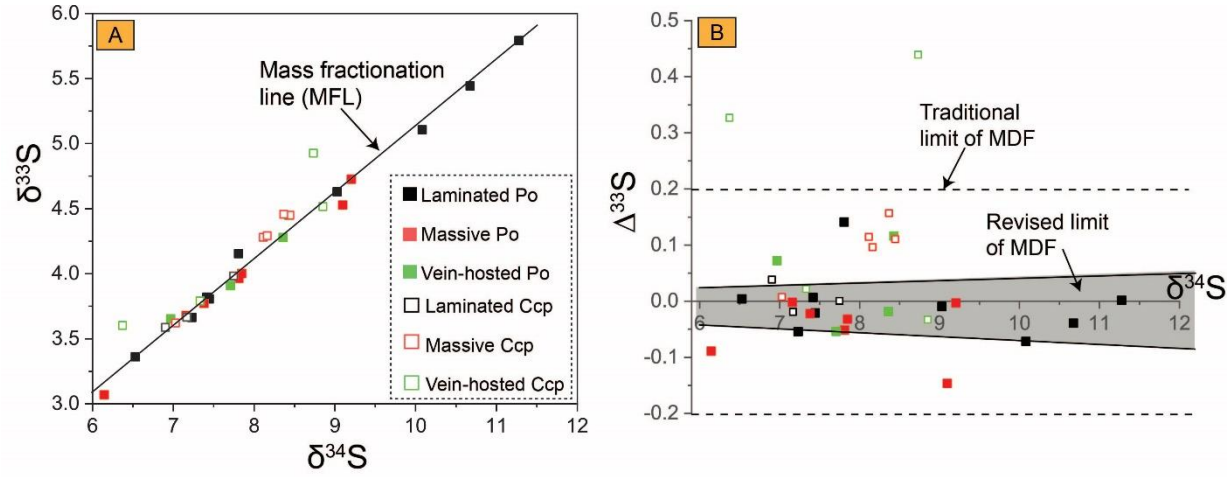


**Figure 4.10**: $^{33}S$ and $^{34}S$ isotopes in pyrrhotite and chalcopyrite of Kayad. A) $\delta^{34}S$ vs $\delta^{33}S$ plot shows most of the data fall along the mass-dependent-fractionation line. B) $\Delta^{33}S$ vs $\delta^{34}S$ scatter diagram shows the $\Delta^{33}S$ values of Kayad sulfides along with the traditional and revised limits of mass-dependent fractionation (please see text).

processes) can range from 0.508 to 0.519, thus attributing variable $\Delta^{33}S$ values to the sulfides. The shaded area in Figure 4.10B represents the new limits of MDF-S, wherein some of the Kayad sulfides plot outside this range. However, such deviations of $\Delta^{33}S$ and $\Delta^{36}S$ have been explained by various processes by earlier authors (Johnston et al. 2005; Ono et al. 2006; Watanabe et al. 2009; Oduro et al. 2011; Young et al. 2013). Oduro et al. (2011) suggested that magnetic-isotope effects (MIEs) during high temperature reduction of sulfates can impart large anomalous $\Delta^{33}S$ values to sulfides but does not significantly affect $\Delta^{36}S$. Since the isotopic data of some Kayad sulfide show somewhat high values for both $\Delta^{33}S$ and $\Delta^{36}S$, it is unlikely for MIE to have affected their magnitudes. Watanabe et al. (2009) showed that abiogenic reduction of sulfate-bearing hydrothermal fluids in the presence of organic compounds can generate $\Delta^{33}S$ values of +0.05 to 0.93 ‰ (avg: +0.28‰) and $\Delta^{36}S$ = -1.1 to +1.1‰ in the produced $H_2S$. The magnitude of this fractionation is temperature-dependent wherein the $\Delta^{33}S_{H_2S}$ increases from +0.05 - +0.57‰ at 150°C -170°C to +0.33 - +0.93‰ at 200° C. Since the $\delta^{34}S$ values of Kayad pyrrhotite and chalcopyrite imply thermochemical reduction of sulfate to sulfide and because the sediments of the Delhi Supergroup were

deposited in Mid-Proterozoic around ca 1.8 Ga, it is inferred that the slight dispersions in $\Delta^{33}S$ and $\Delta^{36}S$ is not due to mass-independent fractionation observed in the Archean sedimentary units but were rather generated during the process of TSR in the presence of organic matter.

## 4.5 Summary

Representative sulfides from the three mineralization types, namely disseminated/laminated, massive, and vein hosted type are analyzed for their major and minor elements, trace elements and sulfur isotopic composition in order to understand the mineralizing processes and the physicochemical environment during ore deposition. Sphalerite contains 8 to 12 wt.% Fe and is highly enriched in Mn and Cd whereas galena shows high concentrations of Ag, Sb, Bi, Se and Tl. Chalcopyrite has higher amounts of Ag, Sn, Ga and In, whereas Co and Ni are mainly concentrated in pyrrhotite and arsenopyrite. Numerous micro-inclusions of Cu-Ag-Tl and Ag-Sb like phases, which pertain to sulfosalt compositions are present in the major sulfides which is in agreement with the presence of visible sulfosalts in the massive ores (Chapter 3).

Mineral thermometry using geochemistry of sphalerite and arsenopyrite is conducted to estimate the temperature during ore formation. The GGIMF thermometer of sphalerite from three different mineralization yields an average temperature around 350˚C that overlaps with the closure temperature range of sphalerite in a regionally deformed and metamorphosed area. Arsenopyrite-löllingite pair is used to derive temperatures of the massive ores using the T-X diagram of Kretschmar and Scott (1976). A maximum temperature of 510 ˚C was obtained with large variations down to 332 ˚C that is inferred to result from progressive cooling and resetting during retrogression. Nevertheless, the maximum temperature is useful in determining that the peak metamorphic temperature was positively greater than 510 ˚C.

The $\delta^{34}S$ values of all sulfides, irrespective of the mineralization style show similar positive ranges that reach up to 17.2‰. Highly positive $\delta^{34}S$ values of sulfides generally pertain to reduction from a heavy S source such as sulfates derived from seawater or evaporitic sources. The sulfate may be reduced to $H_2S$ by bacterial sulfate reduction or thermochemical sulfate reduction. BSR normally results in highly negative and skewed $\delta^{34}S$ patterns and is inferred in case of most SEDEX deposits, however, consistently positive and restricted set of values in Kayad is best explained by TSR, given the Proterozoic seawater composition and the extent of fractionation possible in the known temperature ranges of most SEDEX deposits. A similar conclusion is corroborated by the multiple sulfur isotopic composition of pyrrhotite and chalcopyrite wherein a majority of the data indicate mass-dependent fractionation of sulfur, and the minor deviations of $\Delta^{33}S$ and $\Delta^{36}S$ from the expected distribution around mass fractionation line can be well explained as a result of ore precipitation via TSR in the presence of organic matter. In addition to BSR, TSR has also been implicated as an important process in the formation of vent distal and vent-proximal SEDEX deposits (Cooke et al. 2000; Ireland et al. 2004; Huston et al. 2006; Leach et al. 2010; Gadd et al. 2017). Despite the fact that sulfur isotopic composition suggests a heavy sulfur source, presumably seawater sulfate or evaporite, the data cannot discard a non-marine evaporitic source because seawater, marine evaporite, and non-marine evaporite all have overlapping $\delta^{34}S$ values. Consequently, alternative proxies need to be explored for confirmation of the source of fluid. Major and trace element geochemistry and boron isotope systematics of tourmaline can provide alternative clues about the source of fluid, which are dealt with in the next chapter (Chapter 5).

# CHAPTER 5: Tourmaline: Major and Trace Element Geochemistry and Boron Isotope Systematics

## 5.1 Introduction

Tourmaline, an important borosilicate mineral, is increasingly used as a forensic tool to track a multitude of geological processes. Tourmaline with the general formula, $XY_3Z_6[T_6O_{18}][BO_3]_3V_3W$, includes alkali elements (Na, Ca, K) in the X site, Al in the Z site, a variety of divalent and trivalent cations (e.g., $Al^{3+}$, $Mg^{2+}$, $Fe^{2+}$, $Mn^{2+}$, $Li^{2+}$, $Cr^{3+}$, $Fe^{3+}$, $Cu^{2+}$, $V^{3+}$) in the octahedral Y site, and Si and Al in the tetrahedral or T site. Anions such as OH, F, and Cl occupy the W site. This complex crystal structure allows tourmaline to accommodate a wide range of geochemically diverse elements (Hawthorne and Dirlam 2011). Combined with its robustness, widespread occurrence, and stability across a large pressure (P)–temperature (T)–composition (X) ranges (Dutrow and Henry 2011), tourmaline serves as an ideal petrogenetic indicator.

In igneous systems, tourmaline typically forms late in the crystallization sequence. Due to boron's high incompatibility, it concentrates in late-stage hydrothermal fluids, promoting rapid tourmaline growth. Thus, tourmaline records the evolution of magmatic–hydrothermal systems and provides insights into the composition of both magma and the fluids from which it crystallized. In sedimentary environments, detrital tourmaline, alongside zircon and rutile, is one of the most durable heavy minerals, retaining the signature of its original host rock and making it useful for tracking rock provenance (Henry and Dutrow 1992). Metamorphic rocks are significant hosts for tourmaline, which forms during the release of boron from mica and clays in metapelite during prograde metamorphism (Dutrow et al. 1999). The composition of metamorphic tourmaline may change during its growth, reflecting the evolving P–T–X conditions from low to high metamorphic grades. In hydrothermal ore systems, trace element and stable isotopic compositions of tourmaline are often preserved due to low diffusion rates

(up to 600°C) (Marschall and Jiang 2011; Slack and Trumbull 2011). This allows fingerprinting mineral paragenesis, trace element mobility, and chemical fluctuations (such as redox state and temperature), and tracking fluid provenance, pathways and evolution (Slack and Trumbull 2011). For example, many VMS, SEDEX and even IOCG (Fe-oxide copper gold) deposits are associated with tourmaline-rich rocks or tourmalinites that have been used as a proxy to the ore-forming processes (Plimer and Lees 1988; Griffin et al. 1996; Torres-Ruiz et al. 2003; Čopjaková et al. 2009; Kelly et al. 2020; Trumbull et al. 2020; Pal et al. 2023).

Furthermore, the chemical complexity of the mineral makes it a host to a large number of elements, major and trace alike, that have been used for stable isotopic studies. For instance, boron isotopic signatures of melts and fluids have been widely used for tracking fluid source (Jiang 2001; Dutrow and Henry 2018) and monitoring geological processes in Earth's crust and subduction zones (Ota et al. 2008; Guo et al. 2019). Hydrogen and oxygen isotopes of tourmalines in base metal deposits have been used to identify fluid sources such as modified seawater, metamorphic or granite-derived fluids (Taylor et al. 1992, 1999; Jiang et al. 2002; Beaudoin and Chiaradia 2016; Huang et al. 2016; Adlakha et al. 2017; Zall et al. 2019) and also as a geothermometer (Kotzer et al. 1993). Similarly silicon isotopes have been used to establish ore-forming processes and as a vector to prospective mineralization (Jiang et al. 2000). Li isotopes have been used to track the crystallization of granite-pegmatite systems (Maloney et al. 2008) and isotopic fractionation (Roda-Robles et al. 2019; Xiang et al. 2020) whereas Ar isotopes are successfully used in geochronological studies (Jiang 1998; Bea et al. 2009).

The previous chapter presented detailed information on the geochemical characteristics of sulfides in Kayad, particularly major and trace element composition. Additionally, sulfur isotopic compositions, which are excellent guides to the source of sulfur and by extension, to the source of fluid, were also discussed in different sulfides and the results obtained indicate a heavy isotopic source for sulfur. However, heavy sulfate can be supplied by multiple reservoirs

and therefore, sulfur isotopic compositions singularly does not provide substantial evidence to pinpoint the fluid nature and source.

Petrographical examination of the samples from the Kayad deposit demonstrate the ubiquitous presence of tourmaline in close association with different sulfide mineralization. This co-genetic relationship of sulfides and tourmaline can shed light on the ore-forming processes by serving as a proxy mineral. This chapter deals with the mode of occurrence, major and trace element geochemistry, and boron isotope systematics of tourmaline associated with different types of ores and discusses their possible implications.

## 5.2 Analytical Methods

Tourmaline grains associated with the 1) primary sulfide mineralization in QMS and quartzite, 2) pegmatite vein-associated Fe-Cu sulfide mineralization, and 3) K-feldspar veins-associated Zn-Pb mineralization were selected for further analysis. Major and minor elements were measured from 12 samples while trace element and boron isotopic compositions were measured from 5 representative samples.

### 5.2.1 Major and Minor Elements

Preliminary petrography was done using optical microscopes and SEM. The back scattered electron (BSE) images were obtained using JEOL JSM-6490 SEM with an Oxford X-Max$^N$ silicon drift EDS detector. The major element concentrations were measured on a Cameca SX-100 EPMA. The instrument was operated at 15 kV accelerating voltage and 15nA beam current, with the dwell time set at 10 s on the peak and 5 s on the background. The reference materials and the emission lines used to calibrate the instrument were: jadeite (Na-Kα1, Si-Kα1), diopside (Ca-Kα1, Mg- Kα1), orthoclase (K-Kα1, Al-Kα1), fluorapatite (F-Kα1, P-Kα1), NaCl (Cl-Kα1), $Fe_2O_3$ (Fe-Kα1), rhodonite (Mn-Kα1), $TiO_2$ (Ti-Kα1). The elements F, Na, Al, Si, and

Mg were analyzed on TAP, Ca, Ti, K, and Cl on PET, P on LPET, and Mn and Fe on LIF. The ZAF matrix corrections were performed using the Cameca-supplied PAPSIL® program. Both the SEM and EPM analyses were conducted at the Department of Geology and Geophysics, Indian Institute of Technology (IIT), Kharagpur, India.

### 5.2.2 Trace Elements

The trace element concentrations of tourmaline were measured using a Thermo Fischer Scientific™ iCAP-Q™ quadrupole inductively coupled plasma mass spectrometer (ICPMS) coupled to a NWR 193 nm ArF excimer laser ablation system at the Radiogenic Isotope Facility, Department of Geology and Geophysics, IIT Kharagpur. The laser was operated at 5 Hz repetition rate, 5 J $cm^2$ fluence, and 40–50 μm spot size. The ICP-MS was optimized for maximum sensitivity on $^{7}Li$, $^{58}Co$, $^{115}In$, $^{142}Nd$, $^{208}Pb$, $^{232}Th$, and $^{238}U$ by ablating the NIST 612 reference glass. The oxide production rate, monitored on $^{232}Th^{16}O$, was <1 % for all analytical sessions. The data were acquired in time-resolved mode with measurement of gas/ instrument blank for 35s followed by 45s of ablation with the laser ablating on the sample. External standardization was done by bracketing groups of ten unknowns with two measurements of the NIST 612 reference glass. The data quality was monitored by repeated measurement of the NIST 610 reference glass as unknowns interspersed with the measurements of the samples. The raw data were reduced offline using the GLITTER® software (Griffin et al. 2008). The estimated reproducibility of the trace element concentrations as determined from multiple analyses of the NIST 610 and NIST 612 reference glasses are in the range of 5–10 % for most elements.

### 5.2.3 Boron Isotope

In-situ boron isotope measurements were made using a New Wave Research 193 ArF Excimer Laser Ablation system coupled with a Thermo Fisher Neptune Plus MultiCollector-Inductively

Coupled Plasma-Mass Spectrometer (MC-ICPMS). The ablation was done at a repetition rate of 10 Hz, delivering a fluence of 2–2.5 J/cm² at 40–50 μm spot diameters. Simultaneous measurements of the $^{10}B$ and $^{11}B$ isotopes were done on the L-3 and H-3 Faraday cups respectively. To ensure accuracy, five measurements of the unknown were bracketed by two measurements of the JS-82A-3 reference tourmaline (Palmer and Slack 1989) to correct for instrumental mass-bias and drift. The JS-79N1 (Palmer and Slack 1989) and EB-67-90 (Míková et al. 2014) tourmaline references were measured as unknowns in alternate brackets alongside the samples to estimate the external reproducibility of the method. The results, expressed as $\delta^{11}B$ values, represent per mil (‰) deviations of the $^{11}B/^{10}B$ ratios from the values recommended for the NIST SRM 951 boric acid standard (4.04362 ± 0.00137; Tonarini et al., 2009). The $\delta^{11}B$ values obtained for the JS-79N-1 [-12.3 ± 0.15 ‰ (2σ), n = 7] and the EB-67-90 [11.7 ± 0.19 ‰ (2σ), n = 7] reference tourmalines match within the recommended values (EB 67–90 = 12.3 ± 0.6‰ and JS 79N-1 = -11.63 ± 0.24‰) of Palmer and Slack (1989) and Míková et al. (2014). The boron isotope analyses were also conducted at the Radiogenic Isotope Facility, Department of Geology and Geophysics, IIT Kharagpur.

## 5.3 Mode of Occurrence, Texture and Geochemistry of Tourmaline

### 5.3.1 Mode of Occurrence and Textures

Three varieties of tourmaline associated with two major types of sulfide mineralization (Chapter 3) are encountered in the Kayad deposit. Fine grained (30-250 μm in size), subhedral to euhedral tourmaline (Tur1 hereafter) is closely associated with disseminated/laminated sphalerite and pyrrhotite mineralization in quartz mica schists (Fig. 5.1A) and quartzites (Fig. 5.1B). Most of Tur1 grains display optical zoning (under petrographic microscope) with inclusion-rich brownish cores and inclusion free yellow rims. However, BSE images show up to 3 zones with consistent compositional variations and inclusions of sulfides (Fig. 5.1A-B

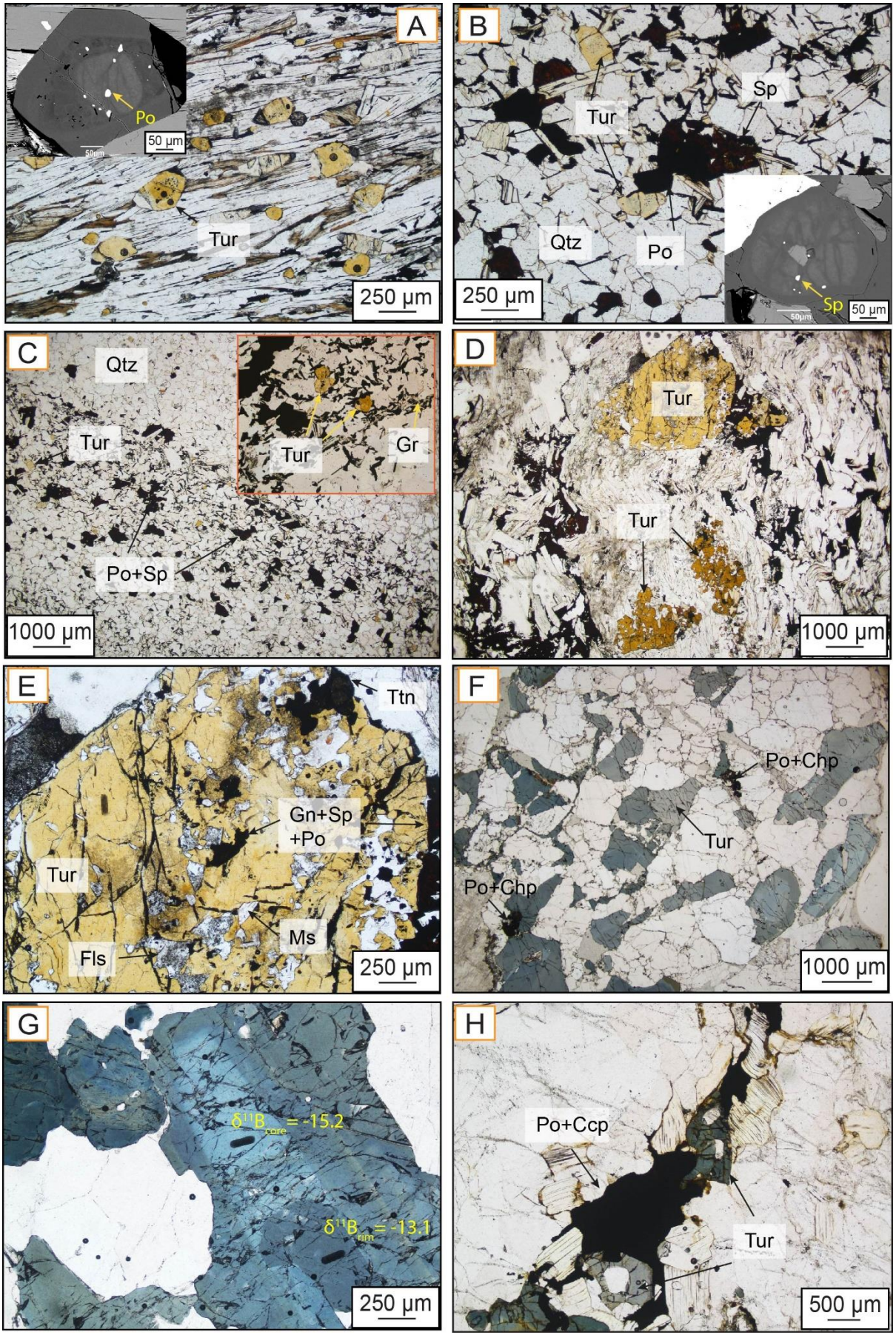
A
Po
50 µm
Tur
250 µm
B
Sp
Tur
Qtz
Po
250 µm
Sp
50 µm
C
Qtz
Tur
Tur
Gr
Po+Sp
1000 µm
D
Tur
Tur
1000 µm
E
Ttn
Gn+Sp
+Po
Tur
Ms
Fls
250 µm
F
Po+Chp
Tur
Po+Chp
1000 µm
G
δ11Bcore = -15.2
δ11Brim = -13.1
250 µm
H
Po+Ccp
Tur
500 µm

**Figure 5.1:** (on the left, pg. 88) Microphotographs of the three varieties of tourmaline: A) Disseminated tourmaline (Tur1) in quartz mica schist (QMS). BSE image of tourmaline (inset) shows 3 compositional zones and inclusions of pyrrhotite, B) Tourmaline in quartzite occurring with sphalerite and pyrrhotite. BSE image of tourmaline (inset) shows atleast 2 compositional zones and inclusions of sphalerite, C) Sulfides and tourmaline occur in higher abundance in graphite-rich bands of quartzite as compared to the quartz rich areas, D) Tourmaline clots (Tur2) in K-feldspar rich veins in QMS associated with sphalerite+galena ±pyrrhotite ±chalcopyrite, E) Inclusions of sphalerite, galena, muscovite, feldspars, quartz and titanite in Tur2 grains. F-H) Pegmatitic tourmaline (Tur3). Note its characteristic bluish color. G) Prominent zoning in Tur3. $\delta^{11}B$ values of the rim are higher than the core, H) Pyrrhotite and chalcopyrite associated with Tur3 within pegmatites. Tourmaline *Tur*, Pyrrhotite *Po*, Sphalerite *Sp*, Chalcopyrite *Ccp*, Graphite *Gr*, Quartz *Qtz*, Galena *Gn*, Feldspar *Fl*, Muscovite *Ms*.

inset). An interesting characteristic of Tur1 in the banded quartzites is their higher abundance in the graphite and sulfide-rich bands as compared to their rare occurrence in the quartz-rich bands (Fig. 5.1C).

Tourmalines are scarce to absent in the vicinity of the massive sulfides, however, abundant yellowish to brown tourmaline occur with the vein-hosted Fe-Cu±Zn±Pb and Zn-Pb±Fe±Cu mineralization. Zn-Pb±Fe±Cu mineralization occur in several K-metasomatised veins made up of mostly microcline and orthoclase that intrude the QMS, and show prominent alteration features in the form of secondary minerals such as albite, pumpellyite, prehnite, clinochlore and fluorite that replace the K-feldspar (Chapter 3, Section 3.5). Ore mineralogy (including sulfosalts) and textures associated with these veins are similar to the massive ores. Tourmaline grains within these veins (Tur2 hereafter) share grain boundaries with the sulfides and are coarser in size than their host counterparts. In some samples with substantial pyrrhotite and chalcopyrite, tourmalines occur as outsized coarse grains or tightly-packed aggregate of the same, measuring 500 to 5000 µm in size (Fig. 5.1D) and show patchy zoning that is observable under transmitted light and in BSE images. In many instances, they are characterized by a high incidence of inclusions predominantly composed of quartz and occasionally accompanied by sphene, sphalerite, and galena (Fig. 5.1E). The third type ($Tur_3$ hereafter) occurs exclusively in pegmatites and quartz veins that contain abundant Fe-Cu±Zn±Pb sulfides and are characterized by alteration assemblages comprising orthoclase, albite, chamosite, biotite, and allanite. Tur3

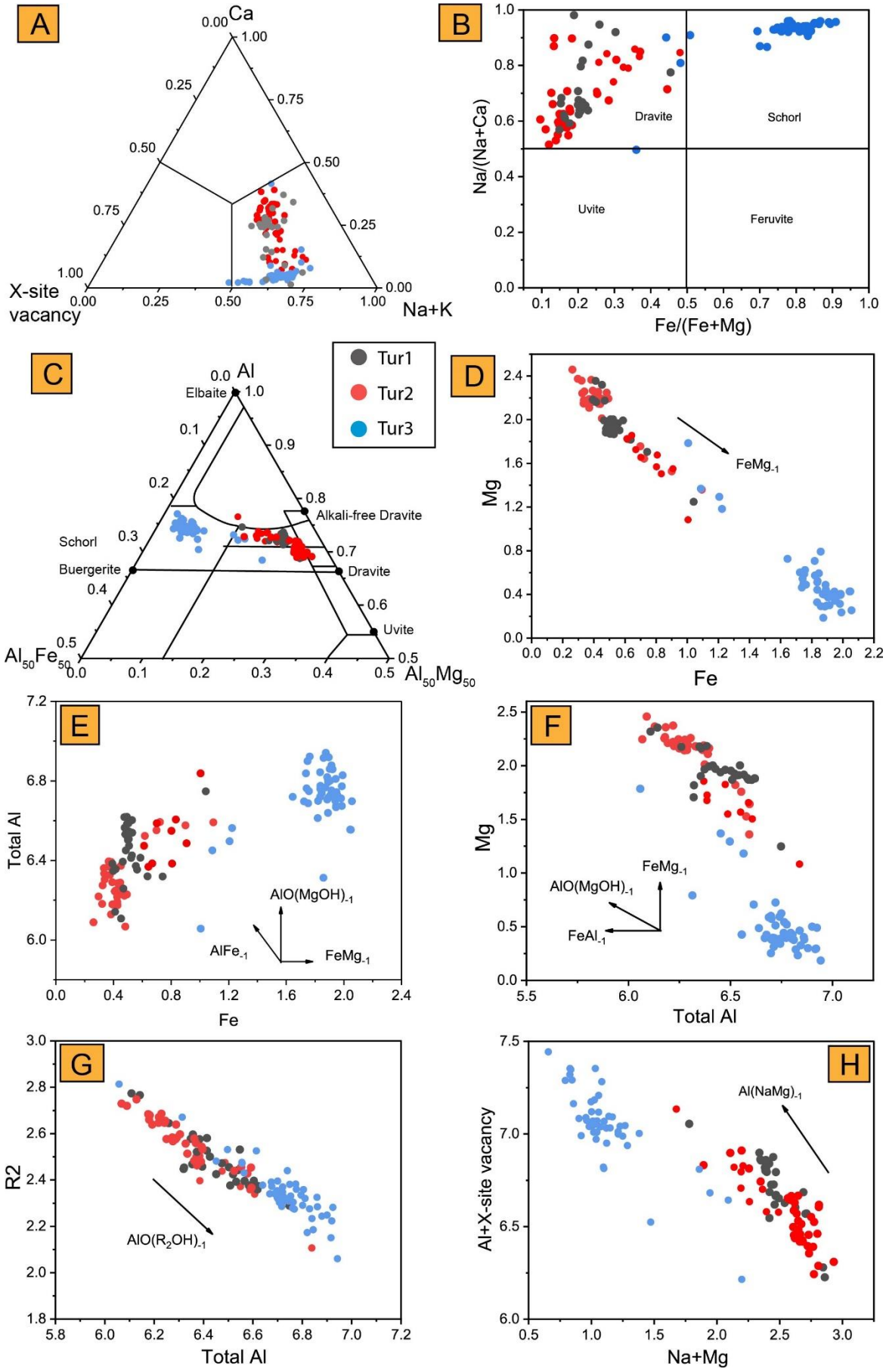
A
Ca
X-site vacancy
Na+K
B
Na/(Na+Ca)
Fe/(Fe+Mg)
Dravite
Schorl
Uvite
Feruvite
C
Al
Elbaite
Schorl
Buergerite
Alkali-free Dravite
Dravite
Uvite
$Al_{50}Fe_{50}$
$Al_{50}Mg_{50}$
Tur1
Tur2
Tur3
D
Mg
Fe
$FeMg_{-1}$
E
Total Al
Fe
$AlO(MgOH)_{-1}$
$AlFe_{-1}$
$FeMg_{-1}$
F
Mg
Total Al
$FeMg_{-1}$
$AlO(MgOH)_{-1}$
$FeAl_{-1}$
G
R2
Total Al
$AlO(R_2OH)_{-1}$
H
Al+X-site vacancy
Na+Mg
$Al(NaMg)_{-1}$

**Figure 5.2:** (on the left, pg. 90) Bivariate and ternary plots of major elements in tourmaline. A) Classification of tourmaline based on X-site occupancy on the Na-Ca-X-site ternary diagram where all tourmalines belong to Alkali group, B) Classification of tourmaline based on Y-site occupancy. Na/(Na+Ca) vs Fe/(Fe+Mg) scatter plot shows Tur1 and Tur2 belong to dravite subgroup and Tur3 is schorl, C) Al-Fe-Mg ternary diagram for tourmaline wherein Tur1 and Tur2 fall in Al-saturated metapsammite and metapelite field whereas Tur3 fall in Li-poor granitoid field, D) Negative correlation of $Mg^{2+}$ and $Fe^{2+}$ show that divalent cations enter tourmaline structure by direct substitution, E) Lack of correlation between Al and Fe indicates negligible $Fe^{3+}$ in tourmaline structure, F-G) Bivariate plots with substitution vectors for major trivalent cation $Al^{3+}$ in the tourmaline structure.

occurs as coarse euhedral grains that range in size between 2mm and 10mm (Fig. 5.1F-H). A distinguishing feature of Tur3 is its blue-green hue as compared to Tur1 and Tur2 which are yellow-brown in color under transmitted light optical microscope. Tur3 grains also exhibit prominent but variable patterns of zoning (Fig. 5.1G).

### 5.3.2 Major Element Composition

The tourmaline formula was calculated by normalizing the sum of the T + Y + Z cations to 15 assuming no vacancies at the tetrahedral and octahedral sites. Based on X-site occupancy, all tourmalines belong to the alkali group (Fig. 5.2A) and based on Y-site occupancy, Tur1 and Tur2 belong to the dravite sub-group while Tur3 belongs to schorl (Fig. 5.2 B; Hawthorne and Henry, 1999). In X-site, Na predominates over Ca [Na/(Na + Ca): 0.5–0.98, avg. 0.78 ± 0.15; X-site vacancies: 0.12–0.5, avg. 0.27 ± 0.07]; the Y site is dominated by Mg over Fe [(Mg/(Mg + Fe): 0.52–0.9, avg. 0.78 ± 0.08] in Tur1 and Tur2, while Tur3 has very high Fe content [(Mg/(Mg + Fe): 0.09–0.3, avg. 0.18 ± 0.05]. Notably, four data points of Tur3 plot in the dravite subgroup- these are cores of brown tourmaline that are subsequently overgrown by blue tourmalines (Fig. 5.2B). All tourmalines are devoid of fluorine (F) or chlorine (Cl), thus classifying them to the hydro-oxy group. In the Al-Fe-Mg diagram, Tur1 and Tur2 plot in the "Al-poor and Al-rich metasediments and metapsammites" field while Tur3 falls in the Li-poor granitoid field (Fig. 5.2C). The EMPA results show very low content and little variation of Mn (≤0.05 apfu), Ti (≤0.14 apfu), and Ca (Tur3: ≤0.1 apfu; Tur1 and Tur2: 0 - 0.4 apfu). Mg apfu plotted against Fe apfu (Fig. 5.2D) reveal strong negative correlation between the two major

bivalent cations across all tourmaline types. The incorporation of the major trivalent cation, Al, into tourmaline occurs through one or a combination of the following substitutions: $AlFe_{-1}$, $\square Al(NaMg)_{-1}$, $\square Al(NaFe)_{-1}$, $\square Al(NaR2)_{-1}$ and $AlO(R2OH)_{-1}$ ($\square$ represents X-site vacancy and R2 is the sum of bivalent cations). None of the tourmaline types show any correlation between Fe and Al suggesting negligible $AlFe_{-1}$ substitution therefore insignificant $Fe^{3+}$ content (Fig. 5.2E). However, all tourmaline compositions show good negative correlation between Al and Mg, and Al and R2 (Mg + Fe + Mn, considering all Fe to be $Fe^{2+}$) (Fig. 5.2F, G) consistent with both $\square Al(NaR)_{-1}$ and $AlO(ROH)_{-1}$ vectors. To examine the relative role of these two substitutions, Al (apfu) is plotted against X-site vacancy (apfu). The slope of the best fit line, on this plot, should be 0 or 1 if Al was incorporated exclusively via $AlO(ROH)_{-1}$ or $\square Al(NaR)_{-1}$ respectively. Good negative correlation ($r^2$ value is 0.62), and a shallow slope (m=0.235) of the data array imply incorporation of substantial Al via $AlO(ROH)_{-1}$ alongwith $\square Al(NaR)_{-1}$ (Medaris et al. 2003).

### 5.3.3 Trace Elements Chemistry

All the tourmaline analyses show smooth down-hole profiles therefore the concentrations of respective trace elements are present in the structure and do not result from mineral inclusions. A graphical representation of the trace element concentrations in tourmaline is shown as box and whisker plots in Figure 5.3 A, B. Overall, the three types of tourmalines are depleted in the large ion lithophile elements such as Rb, Ba, Cs (except for Sr which occurs up to 300 ppm in dravites), and in HFSEs like Zr, Hf, Nb, Ta, U, Th and Y which occur below 1 ppm.

Among the tourmaline types, Tur1 and Tur3 show exclusive enrichment, wherein Tur1 has higher concentrations of Ti and V (>1000 ppm), Cr and Sr (100 to 1000 of ppm), Pb, Sc and Ge (10s to 100 ppm), and Ba, Y and REE (from 0.1 to 10s of ppm) whereas Tur3 has higher

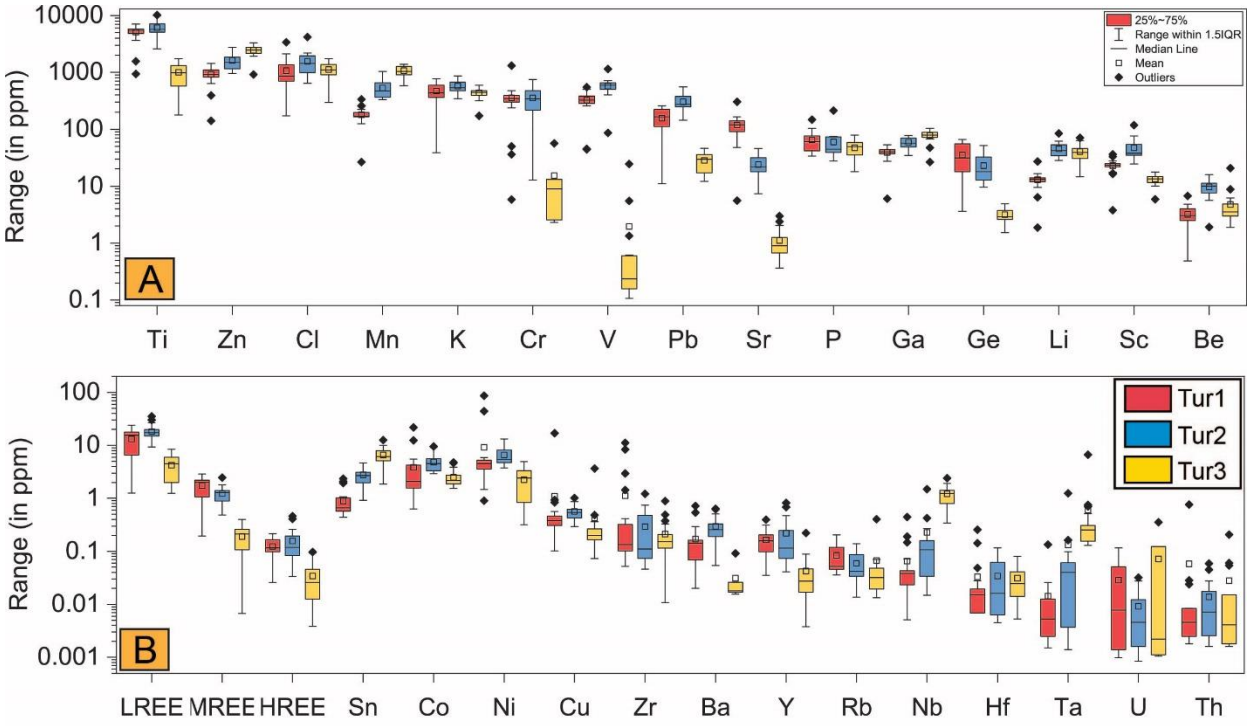


**Figure 5.3**: Box and whisker plots of trace element concentrations of the three types of tourmalines. Note that Tur1 has higher concentrations of Ti, V, Cr, Sr, Ge and REE, whereas Tur3 contains higher Mn, Zn, Li, Ga and also Nb, Sn and Ta. Tur2, on the other hand, either shows similar concentrations as Tur1 or intermediate between Tur1 and Tur3.

concentrations of Mn and Zn (>1000 ppm), Li and Ga (10s to 100 ppm), Nb and Sn (1 to 10 ppm) and Ta (<1 ppm). Tur2, on the other hand, shows similarity to the composition of Tur1 having comparable ranges of trace element concentrations except for Ga (34.6 - 77 ppm), Mn (331.2 – 1042.4 ppm), Sr (7.4 – 45.6 ppm), Zn (958.8 - 2756.7 ppm), Sn (0.9 – 4.7 ppm) and Nb (0.01 – 1.5 ppm) whose concentrations are intermediary between Tur1 and Tur3. For Sc and Pb, Tur2 shows highest average concentrations compared to other two types while for Li it shows compositional similarity with Tur3. Arsenic, Mo, Cd, Cs, W, and Bi are below detection limit for most spot analyses.

Figure 5.4 shows the chondrite-normalized REE patterns of the three tourmaline types. Tur2 has the highest ΣREE+Y (10.2 to 32.5 ppm) closely followed by Tur1 (3.5 – 26.6 ppm) while Tur3 has the lowest REE content (1.3 to 8.8 ppm). In general, all the tourmaline types are

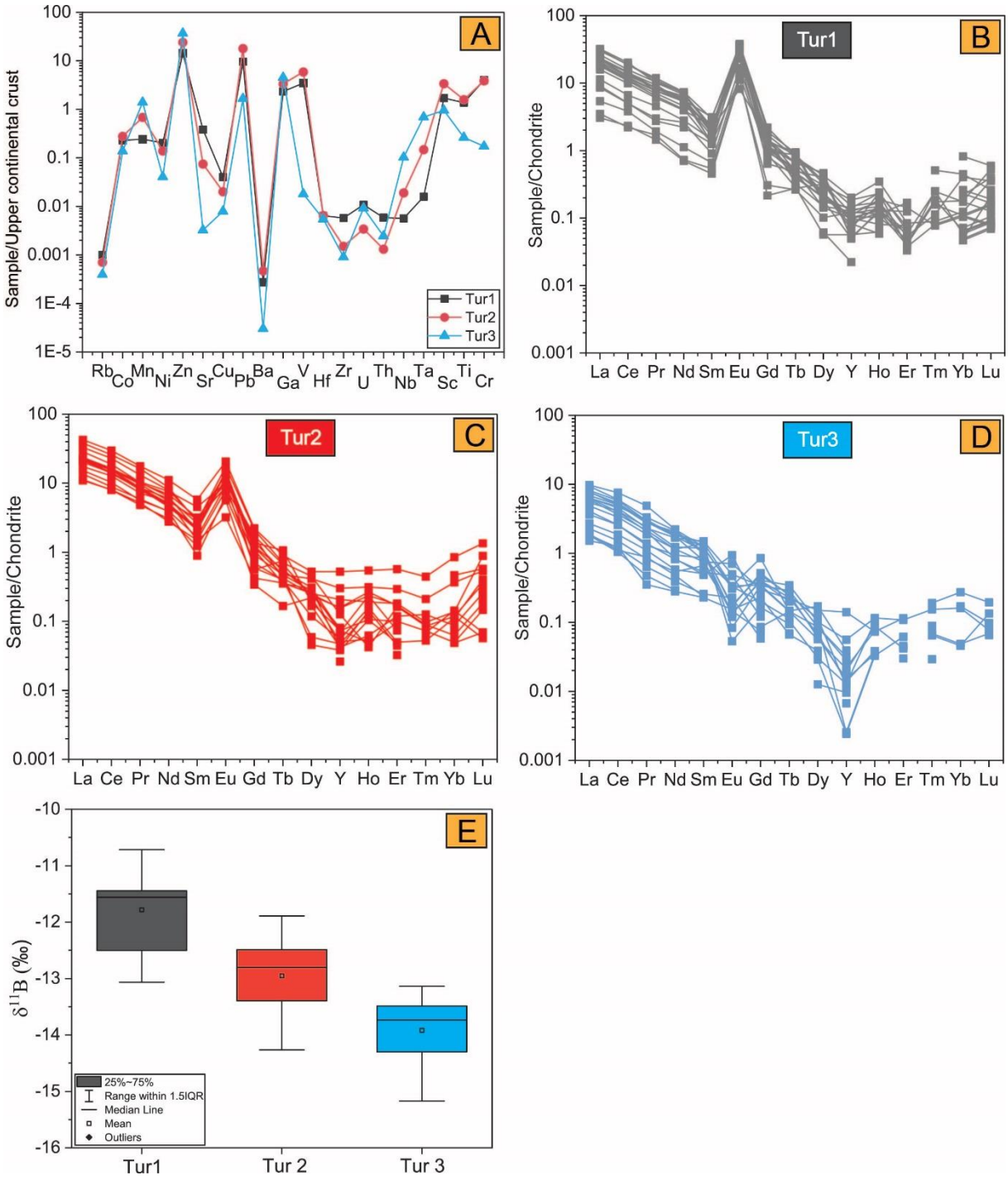


**Figure 5.4**: Plots related to trace elements, REEs and boron isotope composition of tourmaline. A) Continental crust-normalized trace element concentrations of three tourmaline types (average values are used), B-D) Chondrite-normalized REE pattern of Tur 1, Tur 2, and Tur 3 respectively. Note how Tur1 and Tur2 have similar REE patterns which differ from Tur3, E) Boron isotopic concentrations of the three tourmaline types furnish negative vales with $\delta^{11}B$ of Tur1> Tur2> Tur3.

enriched in LREE and show a gradually decreasing chondrite-normalized REE pattern towards HREE (La/Sm = 6.5 to 18.8; avg = 10.9). The REE profile of Tur1 (Fig. 5.4B) is characterized

by a strong positive Eu anomaly (mean Eu/Eu* = 18.8) and is significantly enriched in LREE (La/Sm = 4.8 to 15.3; avg = 9.6). Tur2 shows a similar pattern (Fig. 5.4C), however it has slightly less pronounced Eu anomaly (mean Eu/Eu* = 7.2). Tur3, however, has lower LREE enrichment (La/Sm = 3.4 to 12.9; avg = 6.6) and shows a significantly depleted HREE pattern with most values below detection limit, and is also characterized by a negative Eu anomaly of 0.82 (mean) with some grains showing no Eu anomaly (Fig. 5.4D).

### 5.3.4 `Boron Isotope Composition

A total of 56 spots were analyzed for boron isotope compositions. The complete dataset is provided in Appendix. The $\delta^{11}B$ values are remarkably consistent and highly negative, varying between -15.2‰ and -10.7‰. Even so, a distinct difference in $\delta^{11}B$ can be noted among the tourmaline types (Fig. 5.4E). Tur1 has the highest $\delta^{11}B$ values that range from -13‰ to -10.7‰ (avg -11.8±0.7 ‰) followed by Tur2 that has intermediate ranges of -14.2 ‰ to -11.9 ‰ (avg: -12.9±0.6 ‰). The lightest isotopic compositions are shown by Tur3 with ranges from -15.2 ‰ to -13.1‰ (avg: -13.9±0.6 ‰). The cores and rims of Tur2 show no significant variation in $\delta^{11}B$ but Tur 3, in some instances, exhibits heavier $\delta^{11}B$ at the rim than at the core (Fig. 5.1G).

## 5.4 Discussion

The preferential occurrence of Tur1 in the sulfide associations, coupled with its angular shape, presence of sphalerite and pyrrhotite inclusions, and undisturbed zonation suggest that Tur1 was not mechanically transported from a granitic protolith but was rather authigenic and formed concurrently with the sulfides. This is also supported by the major and trace element composition of Tur1. Based on the Na/(Na+Ca) vs Fe/(Fe+Mg) binary and Al-Fe-Mg ternary diagrams, both Tur1 and Tur2 classify as dravites related to metapsammites/metapelites. Tur1 is characterized by 1) low concentrations of granitophile elements such as Li, Zn, Mn, Ga, 2)

high concentrations of V, Ti, Cr, and REE (Refer to section 5.3.3) which are generally enriched in carbonaceous sediments such as black shales (Abanda and Hannigan 2006; Marks et al. 2013; Duan et al. 2020), and 3) shows prominent positive Eu anomaly (Fig. 5.4B), all of which

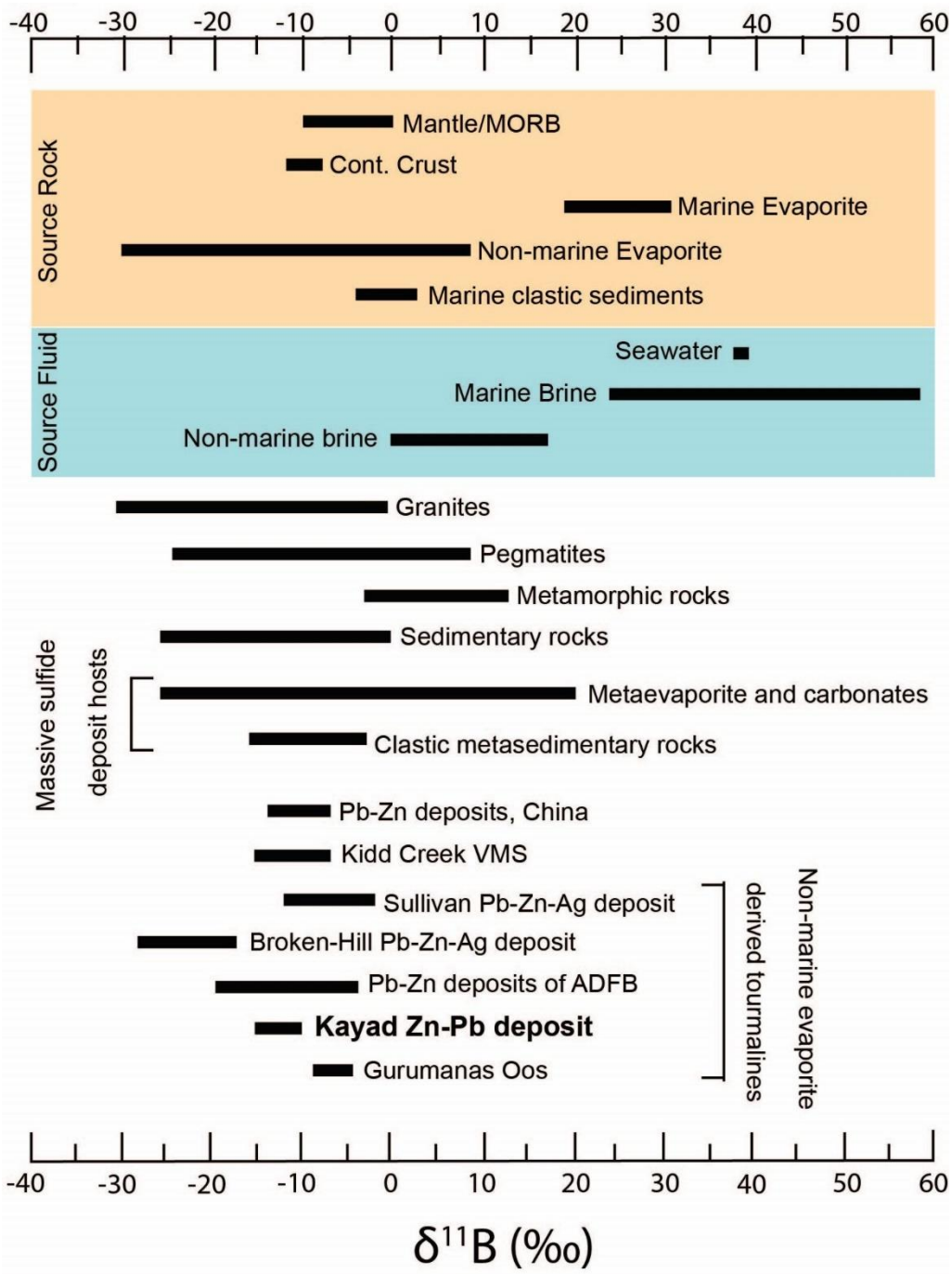


**Figure 5.5**: Distribution of boron isotopic composition across different boron reservoirs and tourmalines; The colored areas show the ranges of $\delta^{11}B$ in boron reservoirs and source rocks/fluids, the uncolored area shows $\delta^{11}B$ measured in tourmalines of host rocks and sulfide deposits, including the results obtained for Kayad tourmalines. Published data were obtained from (Slack et al., 1993; Jiang et al., 1999; Henry et al., 2008; Marschall and Jiang, 2011; Bhuyan et al., 2023)

corroborate non-magmatic origin of Tur1. On the other hand, high Fe/(Fe+Mg) and distribution of Tur3 in the Al-Fe-Mg diagram classifies it as schorl associated with pegmatites or granites. Compared to Tur1 and Tur2, it is evidently enriched in Mn, Zn, Li, Ga and to some extent Nb and Sn which are typically enriched in tourmaline of magmatic and magmatic-hydrothermal affiliation (Yang et al. 2015; Hazarika et al. 2019; Chakraborty and Upadhyay 2020; Zhao et al. 2022). Additionally, low ΣREE content (1.3 to 8.8 ppm; Section 5.3.3), almost flat REE patterns, and pronounced to weak negative Eu anomalies likely due to preferential fractionation of $Eu^{2+}$ into co-crystalizing plagioclase or K-feldspar, are observed in Tur3 (Fig. 5.4D), which are typical characteristics of tourmalines associated with pegmatites (Raith et al. 2004).

Figure 5.5 shows the different reservoirs of boron and their corresponding $\delta^{11}B$ isotope values. Seawater and marine evaporites have high positive $\delta^{11}B$. Consequently, tourmalines crystallized from marine evaporative brines or from fluids derived from evaporite dissolution, show highly positive $\delta^{11}B$ values. Therefore, the consistent negative $\delta^{11}B$ values of tourmaline in QMS of Kayad suggest that boron was not supplied by marine sources but rather could be derived from three possible boron reservoirs, namely, magmatic fluid, clastic metasedimentary rocks and continental evaporites.

## 5.5 Summary

The three major types of sulfide ore mineralization are associated with different tourmaline types that differ by texture, mode of occurrence and chemical composition. The disseminated and laminated sulfides that occur in quartzite and quartz mica schist are co-genetic with Tur1, which occurs as fine euhedral to subhedral grains and show similar distribution as the sulfides. Tourmalines are rare with massive sulfides however they do show a conspicuous enlargement in the vicinity of the sulfide deposition in comparison to their finer counterparts in the foliated quartz mica schist. The Zn-Pb rich sulfide veins that intrude into the QMS feature outsized clots

of tourmaline, Tur2, that range up to 5000 µm and consist of several mineral inclusions such as feldspar, mica, quartz, sphalerite, titanite and galena. The third type of tourmaline, Tur3, occurs within quartzo-feldspathic pegmatites that contain Fe-Cu mineralization. Geochemical analysis of the tourmalines showed that all tourmalines are alkali-rich however, Tur1 and Tur2 that are hosted by QMS are dravites whereas Tur3 in pegmatite is distinctly schorl. Trace element compositions show similar high concentrations of elements such as Ti, V, Cr, Sr, Sc, and Ge in Tur1 and Tur2 which are generally enriched in tourmaline of sedimentary environments whereas Tur3 is depleted in these elements and is more enriched in Mn, Zn, Li, Ga, Nb, and Sn that are normally concentrated in tourmaline of magmatic/magmatic hydrothermal origin. Tur2 shows exceptional similarity with Tur1 in REE patterns and positive Eu anomalies whereas Tur3 shows lower total REE with weak negative Eu anomaly. Boron isotopic compositions that provide reliable evidence about the source of boron, and consequently the possible source of the fluid, show highly negative values with $\delta^{11}B$ decreasing in the following order: Tur1>Tur2>Tur3. Negative $\delta^{11}B$ values of the co-genetic tourmaline discard a marine source and rather advocate involvement of one of the three boron reservoirs, namely clastic metasediment, granite and non-marine evaporite. It may be recalled that the S-isotope composition indicates a heavy S-source related to seawater or evaporite (Chapter 4). Thus, a comprehensive discussion on the possible source(s) of fluid(s) is required by integrating multiple proxies which is dealt with in the next chapter (Chapter 6).

# CHAPTER 6: Discussion: Mechanism of Primary Mineralization and Remobilization at Kayad

## 6.1 Introduction

Deciphering metal and fluid sources in an evolving hydrothermal mineralizing system has always been integral in elucidating the genesis and evolution of mineral deposits. Hydrothermal fluids are responsible for transporting and precipitating economically valuable metals and the source of these fluid (magmatic, metamorphic, seawater, meteoric) can significantly influence the characteristics and spatial distribution of ore bodies which in turn impact the exploration and exploitation strategies. Fluid inclusions and isotopes allow for the reconstruction of the physicochemical conditions of ore formation, including temperature, pressure, and fluid composition. Although results of most fluid inclusion studies are not always unequivocal (discussed elaborately in Chapter 1), published data consistently distinguish SEDEX fluids as moderate to highly saline, typically trapped at low to moderate temperatures (≤ 300 ˚C). Various hypotheses have been proposed to explain the origin of these saline fluids, including intense evaporation of seawater (Leach et al. 2004; Manning and Emsbo 2018), basin hugging brine pools (Sangster 2002), gravitational influx of residual brines (Davidson 1998; Lydon 2004a) observed in deposits such as HYC Zn-Pb-Ag (Ireland et al. 2004) or Howards Pass SEDEX deposit (Gadd et al. 2017), or mixing of two different fluids such as seawater and basinal brine (Sangster 2018; Maghfouri et al. 2021). Involvement of evaporite derived brine has also been advocated however it is considered to be a rare source due to the absence of evaporitic strata in most deposit lithologies (Lydon 2004b).

Similar to the contrasting hypothesis about the source of hydrothermal fluid responsible for the SEDEX mineralization, competing hypothesis exists about the remobilization of SEDEX sulfide that lead to the formation of massive mineable ore loads. The models include

plastic flow, melt-induced remobilization, and fluid-assisted remobilization (Marshall et al. 2000; Tomkins 2007) (Section 6.3).

This chapter integrates the geology, mode of occurrence of ores, ore mineralogy, hydrothermal alterations, and geochemistry of sulfides and gangue minerals described in the previous chapters to decipher the mechanism of primary SEDEX ore formation and post-mineralization remobilization. It also elucidates the nature and source of fluid responsible for sulfide mineralization and remobilization (if any) and provides a working model for the evolution of Kayad deposit in particular and SEDEX deposits in general.

## 6.2 Mechanism of Primary Ore Mineralization and Source of Fluid

### 6.2.1 Primary Ore Mineralization

The identification of a sediment-hosted deposit relies on several key factors, such as lithology, depositional environment, mineralogy of sulfides, and their relationship with the host rock. Sedimentary Exhalative (SEDEX) deposits typically form in low-energy, euxinic environments, amidst clastic sediments and/or carbonate sedimentary rocks. Common minerals found in SEDEX deposits include sphalerite, galena, and pyrite, while pyrrhotite can be notably significant especially in Proterozoic deposits such as Mt. Isa, Sullivan, and Sindesar-Kalan (Deb and Pal 2004; Leach et al. 2005).

In the Kayad deposit, the distribution of sphalerite and pyrrhotite within the quartz-mica schists (QMSs) and quartzite (described as ‘Disseminated/Laminated type’ in Chapter 3), as thin bands and disseminations indicate a sedimentary origin. The elongation of grains and the conformable folding of mineralized laminae with the host rock schistosity suggest subsequent deformation and metamorphism of the ores, which might have obscured the textural and mineralogical alteration features of the original syn-sedimentary hydrothermal mineralization. The presence of graphite-rich mineralized rocks suggests that the protolith of the graphite-

bearing QMS was likely a carbonaceous shale and implies that sulfides initially precipitated under anoxic conditions, with organic matter playing a key role in localizing the mineralization.

Additionally, the high zinc-to-lead ratio and low copper content, which are common characteristics of primary SEDEX mineralization (Shah 2004; Leach et al. 2005), are evident in the Kayad deposit through the abundant sphalerite, and minor occurrences of galena and chalcopyrite in the laminated ores. Consequently, it can be concluded that these low-grade, thinly laminated ores represent the earliest syn-sedimentary/diagenetic strata-bound SEDEX mineralization.

### 6.2.2 Source of Fluid for Primary SEDEX Mineralization

Since SEDEX ores form by hydrothermal processes, insights into the source and nature of the fluid responsible for the mineralization can be obtained from the chemistry of the primary sulfides and minerals co-crystallizing with them. Deciphering the source of fluid(s) in a metamorphosed hydrothermal deposit is always challenging. However, convergence of results from a combination of multiple fluid-proxies can potentially help in tracing the fluid sources. In Kayad, positive $\delta^{34}S$ of the SEDEX sulfides (up to 17.2‰) suggest involvement of fluids derived either from seawater or evaporites. A conventional method to discern the influence of evaporitic brine is the distribution of tourmaline composition along the povondraite-oxydravite join in the Al-Fe-Mg ternary diagram which primarily links to the $FeAl^{-1}$ substitution. However, Tur1, which is cogenetic with the primary SEDEX sulfides, does not conform to the povondraite-oxydravite (P-OD) trend in this ternary diagram and does not show any correlation between Fe and Al indicating insignificant $Fe^{3+}$ content (Fig. 5.2C, E). It may be noted that tourmaline from proven evaporite/meta-evaporite sequences, in several instances, are known to depart from povondraite–oxydravite trend in Al-Fe-Mg plot; for example, Carajas Mineral Province, Brazil, Gurumanas West, Namibia and Liaoning, China, and at places in the

Singhbhum IOCG mineral province, India (Jiang et al., 1997; Henry et al., 2008; Riehl and Cabral, 2018; Pal et al., 2023). Furthermore, P-OD trend has been noted in tourmaline of non-evaporitic settings such as in porphyry deposits (Hohf et al. 2023). Nonetheless, the presence of an oxydravite component in Tur1 is suggested by the $AlO(ROH)_{-1}$ vector (Fig. 5.2G). Additionally, considerable $\square Al(NaMg)_{-1}$ substitution (Fig. 5.2H) has been characteristically noted in tourmalines from evaporitic sediments (Byerly and Palmer 1991). Tourmaline that crystallizes from high salinity fluid often shows deprotonation at the W site due to low activity of $H_2O$ in the fluid. Such tourmaline follows compositional trends consistent with the operation of the $AlO(ROH)_{-1}$ deprotonation vector (Henry and Dutrow 2012; Dutrow and Henry 2018). Therefore, Mg and Na-rich tourmaline, with low X-site vacancies, deprotonation at the W site and an oxydravite component provide strong evidence in favor of evaporite-derived brine. Consistently positive $\delta^{34}S$ value coupled with $\Delta^{33}S$ and $\Delta^{36}S$ signatures provide compelling evidence of TSR of a heavy sulfate source.

However, the $\delta^{11}B$ boron isotope composition of Tur1, ranging from -13 to -10.7‰, starkly contradicts a seawater or marine evaporitic source. Alternative boron reservoirs that can impart strongly negative $\delta^{11}B$ values include granite-related (magmatic or magmatic-hydrothermal), clastic sediments, or non-marine evaporites. However, the major and trace element compositions of tourmaline (Chapter 5) along with strongly positive $\delta^{34}S$ values of cogenetic sulfides argue against a magmatic fluid source. The average boron concentration in unmetamorphosed ocean basin sediments is reported in the range of 45 to around 150 ppm (Trumbull and Slack 2018; Bhuyan et al. 2023). The high abundance of tourmaline associated with the sulfides indicates that the boron sourced solely from its host sediments would be insufficient to form the abundant tourmaline. Therefore, the most plausible explanation for the observed sulfur and boron isotope composition of the co-genetic sulfides and tourmaline is precipitation from a fluid derived from non-marine evaporite source.

Tourmalines that incorporate boron derived from non-marine evaporites show $\delta^{11}B$ ranges of -26 to -17‰ and have been reported from several well-known deposits such as Mt. Isa, McArthur River, Broken Hill in Australia, Sullivan in Canada, Gurumanas Oos in Namibia, Bohemian Massif etc. (Slack et al. 1993; Jiang et al. 1999; Henry et al. 2008; Cabral and Koglin 2012; Krmíček et al. 2021). For example, $\delta^{11}B$ values of -11.1 to -2.9‰ in the Sullivan tourmalinites have been explained by dual boron sources contributed by continental evaporites and clastic sediments, which is analogous to the modern equivalent, Salton Sea (Palmer 1991). Even the sulfur in the Pb-Zn-Ag ores of the Broken Hill deposit is speculated to be derived from sulfate minerals in non-marine evaporites as indicated by the confined $\delta^{34}S$ range of -4 to +7‰. In a recent study, Bhuyan et al. (2023) demonstrate the role of fluid derived from non-marine evaporites in the formation of syn-ore tourmaline in Rajpura-Dariba and Zawarmala Zn-Pb deposits of ADFB. Based on the isotopically light $\delta^{11}B$ values (-18.8 to -4‰) in the tourmalines associated with the SEDEX mineralization in these deposits and presence of evaporite minerals such as gypsum and anhydrite in the metasedimentary hosts, the authors (Bhuyan et al. 2023) emphasize on the involvement of continental evaporites as a source for boron. They posit that the evaporites formed during the rifting phase of the basin, followed by sedimentation and subsequent ore mineralization in the Aravalli and Bhilwara sequences during the sag phase. The metasedimentary packages of the Delhi Supergroup, within which the Kayad deposit is located, are also thought to have been deposited in a similar shallow marine environment (Deb and Sarkar 1990; Verma and Greiling 1995). Moreover, local evaporitic conditions in the Khetri basin of the NDFB have been suggested by previous workers based on the ubiquitous occurrences of metamorphic marialitic scapolite in amphibolite-quartzite rocks of the Ajabgarh group, which pertain to halite-bearing marlitic precursors (Sarkar and Dasgupta 1980). Textural relations and geochemical character of secondary Cl-rich scapolite in biotite schists from the same area have been deduced to be of metasomatic origin formed by evaporite-

derived fluids (Kaur et al. 2016; Baidya et al. 2023). Therefore, formation of non-marine evaporite strata is highly likely in the Kayad area which is a part of the NDFB, even though intense deformation and metamorphism might have obliterated the original characteristics of the evaporites. It is noteworthy that scapolite-bearing marble, similar to those from the other parts of the NDFB, have been reported from the footwall calc-silicate horizon of the Kayad deposit (Fig. 2.2B; Fareeduddin et al., 2014) which can very likely be the metamorphosed equivalent of earlier evaporites. Therefore, the sulfur-isotope compositions of sulfides and major element and boron isotope compositions of tourmaline collectively suggest that the primary disseminated/laminated, metamorphosed SEDEX Zn-Pb mineralization at Kayad was formed by fluid derived from dissolution of non-marine/continental evaporite.

## 6.3 Mechanism of Sulfide Remobilization and Formation of Massive Ores

The mobilization or remobilization of sulfides entails the translocation of pre-existing disseminated or semi-massive mineral deposits during phases of deformation and metamorphism. This process can lead to the modification of the original mineralization or the formation of a distinct and separate daughter mineralization, which, in some instances, may develop into prospective higher-grade ores (Marshall and Gilligan 1993; Marshall et al. 1998). The mechanisms driving sulfide ore remobilization include: i) solid-state dislocation flow, where most sulfide minerals, being more ductile than silicates at lower temperatures, migrate to zones of low stress via plastic flow; ii) melt-assisted remobilization, where partial melts of sulfides form during prograde metamorphism under appropriate physicochemical conditions and are mobilized to low-stress zones; iii) hydrothermal fluid-assisted dissolution and precipitation, in which fluids dissolve the sulfides and transport the elements for subsequent deposition; or iv) a combination of these processes (Marshall et al. 2000; Tomkins 2007).

The effectiveness of sulfide ore remobilization during plastic deformation or sulfide anatexis is influenced by temperature. Therefore, before investigating the potential causes of mobilization at Kayad, it is essential to discuss the metamorphic pressure-temperature (P-T) conditions experienced by the ore and surrounding rocks during regional tectonothermal events. The rocks in and around Kayad were subjected to amphibolite facies metamorphism up to 560±50 ˚C (Chapter 2, Section 2.2.2). As explained in Chapter 4, sphalerite recorded an average temperature of 350 °C, close to its closure temperature of approximately 310±50 °C (Fig. 4.8A; Chapter 4). Similarly, T-X diagram based on Kretschmar and Scott (1976) furnished a maximum temperature of 510 ˚C from arsenopyrite-löllingite retrograde association (Fig. 4.8B; Chapter 4). Finally, the highest temperature of approximately 650 °C is obtained from Ti-in-biotite thermometry (Fig. 3.9; Chapter 3), which aligns with middle to upper amphibolite facies conditions.

### 6.3.1 Remobilization by Plastic Flow

Previous research has well-established the textural features indicative of plastic flow in sulfide ores. Microscale to mesoscale indicators of solid-state transformation include: a) grain-scale brittle and ductile deformation texture such as cataclasis and grain elongation, b) discrete inclusions of a competent mineral within a continuous framework of an incompetent mineral, or alternating bands of both, c) folding of sulfide bands with dislocation features like attenuation at the limbs and thickening at the hinges, and d) Durchbewegung texture. At the macroscale, features such as thickening at fold noses and limb attenuation can indicate the extent of gross remobilization by plastic flow (Barnes 1987; Gilligan and Marshall 1987; Plimer 1987; Marshall and Gilligan 1993).

In Kayad, the morphology of the ores and host rocks closely resembles deposits like Montauban and Broken Hill. The lithologies are intensely folded, leading to limb attenuation

and accumulation of massive sphalerite-galena ±pyrrhotite ±chalcopyrite ores in dilational fold nose regions, which disrupt the pervasive foliation in the quartz-mica schist (QMS) and form the bulk of the mineable lode (Chapter 2: Fig. 2.2 B). The average width of the ore bodies is about 5 meters at the limbs and about 35 meters at the hinges (HZL 2017; https://minedocs.com/22/Kayad-PFS-2017.pdf). This macroscale mechanical mobilization is evident in both hand specimen and microscopic scales (Chapter 3: Fig. 3.3 C). Additionally, prominent Durchbewegung texture, where host rock fragments are embedded within a sphalerite mass (Chapter 3: Fig. 3.4 B), coarsening of gangue minerals associated with massive sulfides (Chapter 3: Fig. 3.5 K), and the presence of piercement veins further support mechanical mobilization of sulfides by plastic flow, particularly sphalerite, in the Kayad deposit. Although hydrothermal fluids could also contribute to ore accumulation in dilational zones, the absence of significant hydrothermal alteration around the Kayad massive ores discounts extensive fluid-induced chemical mobilization.

### 6.3.2 Remobilization Aided by Melt Generation

The concept of sulfide partial melting as a mechanism for remobilization and ore formation, initially proposed by Brett and Kullerud (1967) and Vokes (1969), experienced a resurgence in interest during the early 2000s. This renewed focus was sparked by the first documented evidence of melting at Broken Hill, Australia, leading to comprehensive investigations of all potential melt-mobilized deposits. Common textural attributes identified in these deposits include: a) the presence of multiphase melt inclusions in high-temperature silicate minerals such as quartz, b) accumulations of precious metals such as gold and silver, as well as sulfosalts, in the remobilized ores, c) fracture-filling by sulfides and sulfosalts, and d) very low interfacial angles between sulfides believed to have crystallized from a melt and residual phases, for example, between galena and chalcopyrite with sphalerite (Frost et al. 2002, 2011).

In this context, evidence supporting melt-induced mobilization during metamorphism and deformation at Kayad can be summarized as follows:

1) *Textural evidences*: The massive sulfides in Kayad often exhibit a distinctive texture, where galena and chalcopyrite form cusps and carries against sphalerite (Fig. 3.4 C; Chapter 3). The measured dihedral angles between sphalerite and galena across various samples range from 10.2° to 94.3°, with a mean of 49.6° and a standard deviation of 20.5° (Fig. 6.1A, B). These low dihedral angles indicate that the minerals did not equilibrate in the solid state; instead, galena and chalcopyrite crystallized from a melt that wetted the grain boundaries of sphalerite (Frost et al. 2011). This ubiquitous texture in the massive ores of the Kayad deposit provides compelling evidence for sulfide melting. Unequivocal textural evidence of sulfide anatexis is most convincingly represented by quenched melt textures, as have been demonstrated in numerous experimental studies. Identifying sulfide melts in metamorphic rocks is complicated because sulfide melts formed during metamorphism rarely quench due to slow metamorphic cooling and textural re-equilibration. In section 3.4.2 (Chapter 3), various complex intergrowths among phases such as gudmundite-pyrrhotite-galena and pyrargyrite-gudmundite-galena-pyrrhotite-chalcopyrite have been described. These textures may result from exsolution, breakdown of a metastable phase, or by re-equilibration of a sulfide melt during metamorphic cooling. Exsolution occurs when a phase becomes unstable in its host mineral due to temperature changes, typically appearing as crystallographically oriented laths or lamellae within the host phase. Previous researchers have documented sulfosalt exsolution textures, including laths, lamellae, or acicular grains within larger galena grains (Foord and Shawe, 1989; Simanenko, 2007; Chovan et al., 2021). However, the intergrowth textures illustrated in Figure 3.5A-C, F (Chapter 3) do not exhibit these typical exsolution features. It is also possible that the exsolved phases were expelled from the host mineral during subsequent recrystallization. This process typically leads to simpler textures, such as the accumulation of the exsolved phase

along the grain boundaries of the parent grain (Fig. 3.5D, G-H; Chapter 3), rather than forming a complex intergrowth of multiple phases around the parent grain (e.g., Fig. 3.5A; Chapter 3).

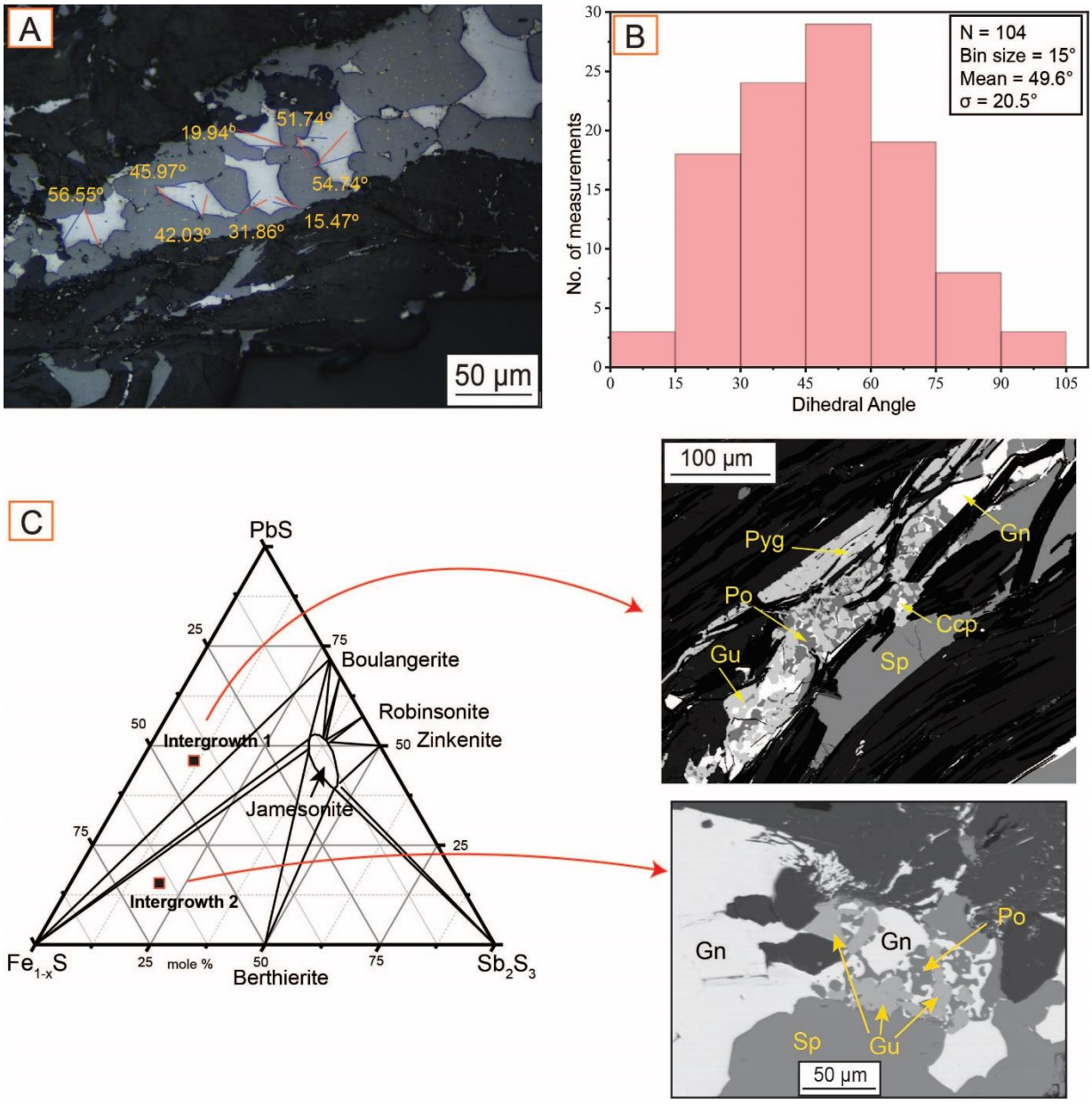


**Figure 6.1:** Textural evidences of remobilization via melting of sulfides. A) Reflected light photomicrograph of galena in sphalerite matrix and the interfacial angles between the two phases measured using image analysis software attached to the microscope, B) Histogram of dihedral angles measured between sphalerite-galena pair. The total no. of data (N) is 104. The mean value is 49.6 ± 20.5˚. C) Projection of the compositions of two intergrowths (indicated on the right) that fall outside the jamesonite field in the $Fe_{1-x}S$-$Sb_2S_3$-PbS ternary diagram by Chang and Knowles (1977). See text for discussion.

Consequently, it is challenging to attribute these intergrowths to simple exsolution. Even some seemingly simple intergrowth textures, such as gudmundite-sphalerite depicted in Fig. 3.5C

(Chapter 3), cannot be adequately explained by exsolution. For instance, sphalerite would need to contain significant dissolved Sb to produce nearly equal volumes of exsolved gudmundite (FeSbS). However, high Sb concentrations in sphalerite are rare (Cook et al. 2009). In Kayad, sphalerite (with or without associated gudmundite) has a maximum Sb concentration of 2 ppm, which is insufficient to form the observed proportions of gudmundite in the intergrowths by exsolution. To examine the alternative mechanism of formation of these intergrowths, that is by destabilization of a metastable phase, the bulk compositions of some selected intergrowths (gudmundite-pyrrhotite-galena and pyrargyrite-gudmundite-galena-pyrrhotite-chalcopyrite; Fig. 3.5A, B; Chapter 3) were calculated based on the volume proportions and elemental compositions of the constituent minerals. The calculated compositions predominantly contain Fe, Sb, and Pb, with minor Cu and Ag, and can best be represented by the PbS-FeS-$Sb_2S_3$ ternary system. The only sulfosalt that could breakdown to provide the necessary elements for these intergrowths would be jamesonite ($Pb_4FeSb_6S_{14}$). The deduced compositions of the intergrowths were therefore plotted in the PbS-FeS-$Sb_2S_3$ ternary diagram proposed by Chang and Knowles (1977), but they fell well outside the jamesonite stability field (Fig. 6.1C). This implies that jamesonite cannot be a precursor phase and hence the intergrowths are not a product of destabilization of a single mineral phase such as sulfosalt. Therefore, we advocate that these complex intergrowths are very likely the re-equilibrated/recrystallized remnants of a pre-existing melt. Nevertheless, we do not discount the possibility that some of the mineralogically simple intergrowths, such as galena and Ag-tetrahedrite (Fig. 3.5D-E, G-J; Chapter 3), and some of the mineral inclusions in the sulfides, inferred as sulfosalts, can potentially be exsolutions.

2) *Mineralogical and chemical evidences:* As discussed above, several aggregates of sulfosalts in association with the massive ores are identified in samples of various mine levels, which suggests their widespread occurrence. Time-resolved ablation signals show spikes in certain

elements such as Ag (>3000 ppm) and Sb (>600) in galena (Fig. 4.3; Chapter 4) in massive ores that indicate the presence of micro-inclusions of Ag-antimonides or sulfo-antimonides (Palero-Fernández and Martín-Izard 2005). Similarly, the co-variation of Ag, Pb, Tl and Sb concentrations in the time-resolved ablation spectra of many sphalerite spot analyses suggest ablation of micro-/nano-inclusions of sulfosalts such as pyrargyrite (which also occurs as a separate phase in the massive ore, refer to section above), boulangerite and rayite. These nano-inclusions may be the result of exsolution of sulfosalt phases from the major sulfides during metamorphic cooling.

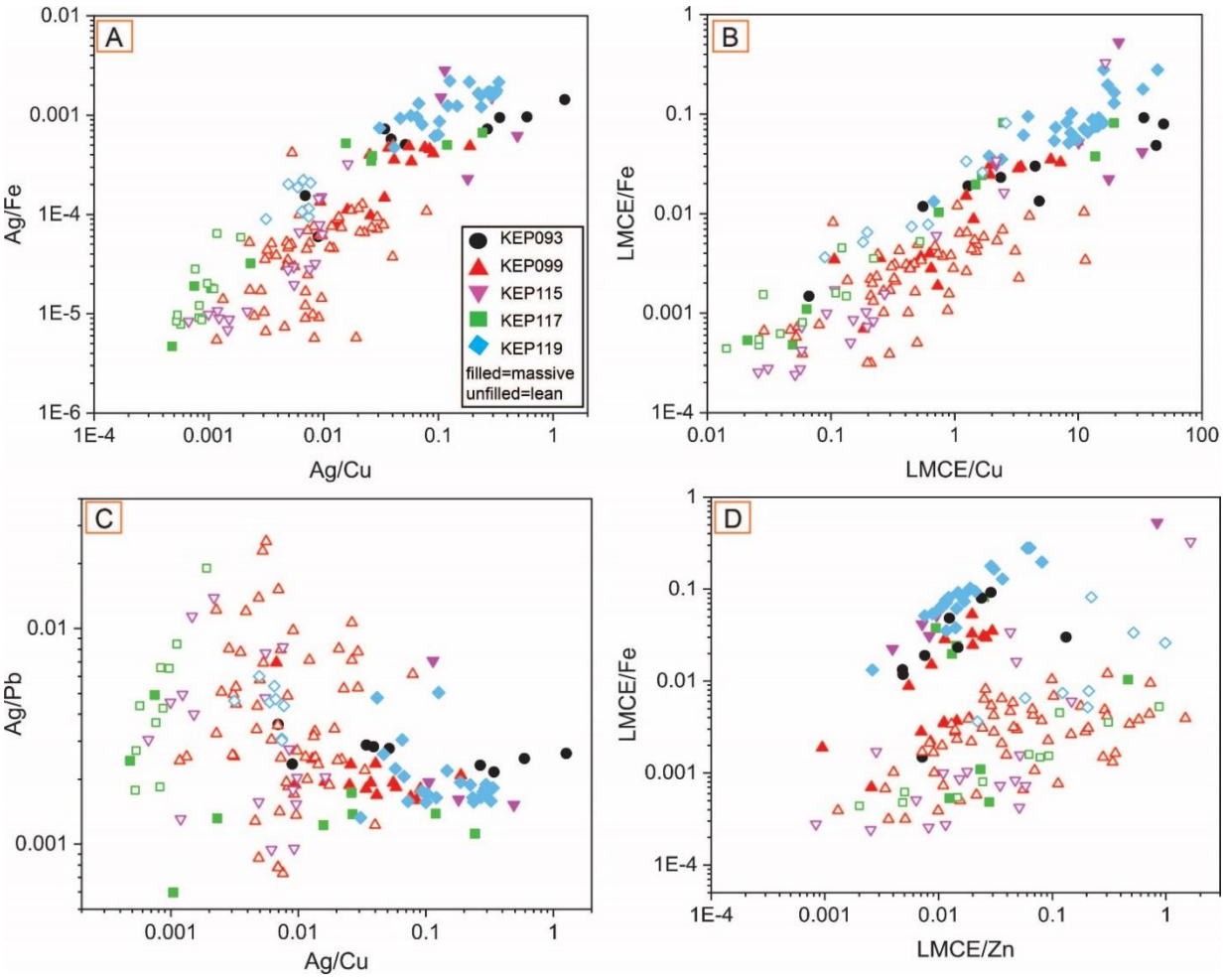


**Figure 6.2:** Bivariate plots of element ratios in massive and laminated ores. Filled symbols are massive ores, unfilled symbols indicate lean ores. LMCE = Ag+As+Bi+Tl+Sb. Different symbols indicate separate boreholes. Note that massive ores have higher Ag/Cu, Ag/Fe, LMCE/Cu and LMCE/Fe ratios than laminated ores. However, Ag/Pb and LMCE/Zn ratios in both the ores overlap. See text for discussion.

The ubiquitous presence of sulfosalts in massive ores provides *prima facie* evidence that the massive ores are enriched in Ag+Bi+As+Tl+Sb. These elements are collectively known as Low Melting Chalcophile Elements (LMCEs) as they can depress the melting temperatures of common sulfide minerals (Frost et al. 2002). To further examine the relative enrichment of LMCEs in the massive ore, bulk concentration ratios of major elements and LMCEs (Ag+Bi+As+Tl+Sb) from massive mobilized ore and laminated SEDEX ore horizons intercepted in different boreholes are plotted (Fig. 6.2). The Ag/Fe vs. Ag/Cu and LMCE/Fe vs. LMCE/Cu plots show a relative enrichment of Ag and the LMCEs over Cu and Fe in the massive ore. This is also justified by the fact that Ag is recovered as a by-product of mining in Kayad. These observations provide evidence for the preferential partitioning of the LMCEs into the melt during sulfide anatexis which contributed to the massive ore. However, Ag/Pb ratios of the two types show overlap. We propose that substantial *en masse* removal of galena from the laminated SEDEX ore (indicated by rarity of galena in the restitic ores) by melting, led to a limited fractionation of Ag from Pb (since galena is the primary host of Ag) between melt and restite resulting in the overlap between the lean and massive ores. Similarly, LMCE/Fe vs. LMCE/Zn shows an interesting distribution where LMCE/Zn values are highly variable in the massive ore and overlap with the lean ores. This pattern may also be attributed to the differential response of mineral species to the processes involved. Notably, galena and chalcopyrite appear to exhibit higher susceptibility to melting, whereas sphalerite appears to be comparatively more influenced by plastic flow, which is unlikely to fractionate Zn and therefore will not lead to any systematic change in elemental ratios involving Zn between restite and the mobilized ores. The textural, mineralogical and geochemical evidence thus collectively suggest that galena and chalcopyrite were most likely mobilized dominantly by sulfide anatexis and sphalerite was mobilized primarily by plastic flow.

Having discussed the evidence of melting, it is important to assess whether the metamorphic conditions were suitable for such melt generations at Kayad. It has been discussed above that some of the sulfide-sulfosalt intergrowths may represent re-equilibrated melt. Presence of LMCEs is critical to the melt-initiation process since the LMCE-bearing sulfosalts start melting at significantly low temperatures. For example, the most common sulfosalts in Kayad namely pyrargyrite and gudmundite can be represented in the Ag-Sb-S and Fe-Sb-S systems respectively, wherein, the first Sb-rich melt in the Ag-Sb-S system forms at 450 °C and all ternary phases melt by 510 °C. Melting of pyrargyrite occurs at 485 °C at 1 atm (Frost et al. 2002). The first melt in the Fe-Sb-S system is known to appear at 545 °C through the reaction of pyrite and stibnite, however, no experiment to synthesize gudmundite has been successful to date (Frost et al. 2002). Clark (1966) demonstrated that As-free gudmundite disintegrates at 280°±10 °C when heated in vacuum. Therefore, we think that the inferred re-equilibrated melt may form by partial melting during amphibolite grade metamorphism. Govindarao et al. (2017) experimentally established that Ag greatly depresses the melting point of the Ni-Sb system and it is possible to generate an Ag-Sb-Bi melt at 680 °C. Presence of elements such as Pb and Cu can further depress the melting point. Removal of Ag through formation of Ag-bearing phases such as $CuPbSbS_3.Ag_2S$, $2FeS.Ag_2S$, $3PbS.Ag_2S$ etc. enriches the residual melt in Ni and Sb which consequently forms breithauptite- and nisbite-like phases. They also demonstrated that in the $ZnS$-$PbS$-$FeS$-$Cu_2S$-$Sb_2S_3$-$As_2S_3$ system, melting is expedited by PbS and As to occur at 500 °C, their occurrence manifested as intergrowths of galena with tetrahedrite in various proportions (Govindarao et al. 2020). The presence of breithauptite and intergrowths of galena with Ag-bearing tetrahedrite in Kayad therefore may suggest the possibility of a sulfosalt melt at temperatures of 600 °C. Partitioning of precious metals and LMCEs, and presence of LMCE-bearing sulfosalts/minerals occasionally with complex intergrowth textures (interpreted as re-equilibrated melt under "Textural evidence") in massive ores metamorphosed to the

middle/upper amphibolite facies, is consistent with sulfide melt mobilization which tends to fractionate melts towards enrichment in LMCEs (Tomkins et al. 2007).

Below we address the possibility of melting and mobilization of the major sulfide minerals. Since the massive ore in Kayad comprises sphalerite + galena ± chalcopyrite ± pyrrhotite, experimental studies involving these minerals are relevant. Experiments at sulfur fugacity that favors the stability of pyrrhotite instead of pyrite show that melting can occur at 830 °C in the PbS-FeS-ZnS system (Mavrogenes et al. 2001) and at 730 °C if $CuFeS_2$ is incorporated (Stevens et al. 2005). The eutectic temperature in the PbS-FeS-ZnS system can be further depressed by about 30 °C if 1 wt. % $Ag_2S$ is added (Mavrogenes et al. 2001). However, the cumulative effect of Cu, Ag and other LMCEs on the depression of melting temperature is not known. Pruseth et al. (2014) demonstrated that melting is possible at 600 °C under high sulfur fugacity conditions to generate a ZnS-rich melt in the ZnS-PbS-FeS-$Cu_2S$ system. From these experimental studies, it appears that sulfide melts ("true melt"; Mavrogenes et al., 2013), from which common minerals such as pyrite, pyrrhotite, chalcopyrite, galena and sphalerite can crystallize, may form during amphibolite facies metamorphism if the S-fugacity is sufficiently high whereas substantially higher temperature is required to generate such melt in low S-fugacity condition. During prograde metamorphism, desulfidation of pyrite to pyrrhotite increases S-fugacity (Tomkins 2007) and may promote melting. The rarity of pyrite in Kayad is apparently at odds with experiments and deposits where significant melting of common sulfides has been demonstrated. In apparent similarity with Kayad, the Sindesar-Khurd deposit in the ADFB is also dominated by pyrrhotite and the peak metamorphic temperature is inferred to be 580-600 °C (Govindarao et al. 2017). Integrating experimental studies and field investigation the authors demonstrated melt-assisted sulfide mobilization at Sindesar-Khurd despite being metamorphosed to relatively lower temperatures, citing pseudomorphs of pyrrhotite after pyrite as evidence of desulfidation during metamorphism. Though pyrrhotite is

the most abundant iron-sulfide in Kayad, irregular pyrite relics are seen within large masses of pyrrhotite (Fig. 3.3E; Chapter 3), which may be construed as evidence of extreme desulfidation of pyrite to release S and increase S-fugacity triggering sulfide melting during metamorphism. Pruseth et al. (2014) showed that even in initial sulfur excess conditions, the melt generated will always be sulfur deficient. Furthermore, the original metal inventory of the SEDEX ore should have been enriched in LMCEs as suggested by abundance of the sulfosalts and minerals in the mobilized massive ore, which might have facilitated melt generation by lowering the melting temperature even further. Once melting is initiated, LMCEs present as traces in sulfide structure feasibly diffused into the melt thus expediting the mechanism of sulfide anatexis (Frost et al. 2002). The higher Ag/Fe, Ag/Cu. LMCE/Fe and LMCE/Cu in the massive ores compared to the lean ores also support this mechanism. It has been noted that localized fluid-induced alteration occur around massive sulfides where pyrrhotite and chalcopyrite dominate which suggests the presence of fluid in the sulfide melt or during melting. Wykes and Mavrogenes (2005) have experimentally shown that at 1.5 GPa, H2O dissolved in melt can depress the eutectic temperature in the PbS-ZnS-FeS system from 900 °C to 865 °C. Therefore, the participation of fluids could have lowered the melting temperature, although we envision that its effect was minimal due to lower pressures (ca. 0.6 GPa) during regional metamorphism. Fluids might have played a more important role in lowering the viscosity of the sulfide melt thereby facilitating its migration.

### 6.3.3 Remobilization Assisted by Fluid

Unlike the massive ores, the vein-hosted Fe-Cu±Zn±Pb mineralization at Kayad comprising pyrrhotite and chalcopyrite is ubiquitously associated with prominent hydrothermal alteration zones (Chapter 3). Replacement of oligoclase by orthoclase + albite (Fig. 3.7A, E, F), orthoclase + chamosite ± Al-pumpellyite (Figs. 3.7G, 3.8A), muscovite by K-feldspar + albite + chamosite + Fe-rich muscovite (Fig. 3.7H), and the preponderance of coarse-grained secondary biotite

along the vein wall (Fig. 3.6A) are evidence of K ± Na ± Fe metasomatism. Plagioclase alteration along grain boundaries and cleavages mark the infiltration paths of K-Na-bearing fluids which co-precipitated orthoclase and albite as suggested by their mosaic-like texture (Nurdiana et al. 2021). Moreover, the crowding of pores in zones of secondary albite is consistent with fluid-driven dissolution-reprecipitation (Putnis 2009). Common replacement texture of K-feldspar by allanite + epidote + monazite in association with Fe-Cu sulfides (Fig. 3.7B, D) suggest calcic alteration by a separate pulse of fluid that postdated earlier potassic alteration.

Zn-Pb±Fe±Cu sulfide mineralization in the discordant K-feldspar veins in QMS suggests that these vein-hosted Zn-Pb mineralization was synchronous with K-metasomatism, similar to the hydrothermal Fe-Cu±Zn±Pb mineralization. The replacement of the vein K-feldspar by prehnite, pumpellyite and albite with traces of clinochlore (Fig. 3.8 B-D) suggests an influx of Ca-Na-rich fluid overprinting an earlier K-metasomatized assemblage. Similar to hydrothermal Fe-Cu sulfide mineralization, replacement of K-feldspar by allanite + epidote + monazite (Fig. 3.8F) suggests an event of Ca-metasomatism following K-metasomatism. Thus, similar hydrothermal alterations are associated with both Fe-Cu sulfide and Zn-Pb mineralization hosted or associated with veins/pegmatites and hydrothermal alterations. Overall, two separate hydrothermal events can be inferred wherein an early K ± Na ± Fe alteration event was overprinted by a later Ca ± Na alteration event, both being associated with sulfide remobilization. Mineralization in calcsilicate is sparse. The association of calcite, albite, quartz, epidote, titanite, hornblende, and chlorite (Fig. 3.6E-F) likely indicates that the pyrrhotite and chalcopyrite veinlets formed during Ca-Na alteration of the host rock.

### 6.3.4 Source of Fluid for Sulfide Remobilization

The remobilized sulfide mineralization is represented by massive ores and vein-hosted/associated ores. The massive sulfides concentrated at the fold hinges, despite having entirely different mode of occurrences from the SEDEX type, possess comparable positive $\delta^{34}S$ values. As described in previous section, the massive ores are envisaged to have formed by partial melting and plastic flow of the pre-existing SEDEX mineralization, subordinately mediated by hydrothermal fluids. Since the sulfur isotopic compositions are not affected during partial melting or crystallization from sulfide melt (Ohmoto and Rye 1979; Marini et al. 2011), the massive sulfides retained the $\delta^{34}S$ signatures of the original laminated SEDEX ores. The Fe-Cu sulfides associated with pegmatite veins, and the minor Zn-Pb sulfide associated with K-feldspar veins, have slightly lower mean $\delta^{34}S$ values compared to those of the massive and laminated sulfides, nonetheless, the ranges overlap (Section 4.3.2; Chapter 4). The $\delta^{34}S$ of the mantle is near about 0‰, and therefore the comparable (to the primary SEDEX sulfides) but slightly lighter $\delta^{34}S$ of pegmatite-hosted sulfides indicates that the sulfur for vein-hosted sulfides was largely remobilized from SEDEX sulfides with minor magmatic contribution.

Despite having similar $\delta^{34}S$ values as that of Tur1, Tur3, which is associated with the Fe-Cu-sulfide-bearing pegmatites, occurs as extremely coarse grained schorls (Fig. 5.1F-G; Chapter 5) with a high Fe content (Fig. 5.2B; Chapter 5), a common characteristic of tourmalines crystallizing from pegmatite or fluids released from moderately fractionated granitic magma (Van Hinsberg et al. 2011). Its igneous affiliation is validated by its major and trace element character (enrichment in granitophile elements, and strongly negative Eu anomaly) as elaborated in Chapter 5, Section 5.4. Although strongly negative $\delta^{11}B$ of Tur3 does not alone confirm a magmatic source, but when boron isotopic composition is interpreted in conjunction with mode of occurrence of the host (thick pegmatitic veins), ubiquitous potassic alteration associated with the veins, and the major and trace element compositions of

tourmaline, Tur3 is best explained by crystallization from a felsic magma or a magmatic-hydrothermal fluid. $\delta^{11}B$ values gradually increase from core to rim of the zoned schorl-type Tur3 (Fig. 5.1G; Chapter 5) implying crystal growth from the same fluid, since the heavier boron fractionates into the fluid phase during tourmaline precipitation resulting in heavier isotope signature of later tourmaline (Meyer et al. 2008). On the other hand, Tur2, associated with K-feldspar-bearing Zn-Pb mineralized vein, is optically and compositionally similar to Tur1 (both Tur1 and Tur2 are dravites) but is distinctively coarser-grained than Tur1 (Fig. 5.1D, E; Chapter 5). Varying concentrations of Mg, Fe and Ti impart a patchy zoned appearance to the Tur2 grains. Such heterogenous composition and outsized grains of Tur2 indicate crystallization from a fluid phase. In terms of trace elements, Tur2 shows identical ranges for most elements and also displays REE patterns (strongly positive but with a slightly depressed positive Eu anomaly compared to Tur1) indistinguishable from Tur1. However, elevated concentrations of selected trace elements such as Mn, Zn, Sn, Ga, Li, Nb, and Ta is noted in Tur2 (Fig. 5.3; Chapter 5), which reflect a trace element compositional trend towards Tur3. This intermediary nature of Tur2 is also replicated by its B-isotopes which straddle between the two end-member types of tourmalines (Tur1 and Tur3) (Fig. 5.4E; Chapter 5). The similar alteration features of vein-associated mineralization containing Tur2 and Tur3, implies their formation from a broadly similar fluid. Since the bulk of the Zn-Pb ores were mobilized during the peak metamorphic phase and the vein-hosted mineralization was concurrent with the mobilization of the ores, the deposit must have been at a depth of 15 to 20 kms (~ 0.6 GPa) below the crust during the formation of these tourmalines. Therefore, it is unlikely for a surface-derived fluid to circulate to such depths during metamorphism. Consequently, crystallization of Tur2 from metamorphic fluid and/or magmatic fluid is likely. One possible explanation for slightly lighter B-isotope signature of Tur2 compared to Tur1 could be boron loss from Tur1 grains during post-formational metamorphism. The heavier boron partitions into the

metamorphic fluid leaving the residual solid phases lighter in $\delta^{11}B$, which is a common process in sediments metamorphosed to amphibolite facies. However, since the formation of Tur2 is reasoned to occur near peak metamorphic conditions of Kayad, and there are no metamorphic events that outlast their precipitation, we envisage that this factor might not have been significantly influential in modifying its boron isotopic composition. Loss of heavier boron due to metamorphic devolatilization of existing Tur1 also does not explain mode of occurrence (in the form of veins), grain size (much coarser than Tur1) and high concentration of granitophile elements in Tur2. Therefore, considering 1) similar major and most trace element composition of Tur1 and Tur2, 2) similar REE pattern and positive Eu anomaly (but with a less positive anomaly in Tur2) of Tur1 and Tur2, 3) similar alteration signatures of Tur2 and Tur3, 4) enrichment in some granitophile elements in Tur2 similar to Tur3, and 5) intermediate boron isotope compositions of Tur2 between Tur1 and Tur3, it is proposed that Tur2 formed by recycling of Tur1 by a magmatic-hydrothermal fluid that was responsible for the formation of Tur3. However, involvement of metamorphic fluid along with magmatic-hydrothermal fluid in the recycling process cannot be ignored.

## 6.4 Implications for Critical Metals

The concept of critical metals encompasses elements that are deemed essential for modern technological advancements and are of strategic importance, yet are characterized by their limited availability. With the current global shift towards sustainable practices in energy-intensive industries like metal extraction and processing, critical metals have become crucial for reducing carbon footprint and promoting environmental sustainability. Metals such as As, Ag, In, Ge, Sb, Li, Co, Ni, REEs, PGEs etc. find diverse applications in high-tech industries like electronics, renewable energy, and transportation. For instance, cobalt and lithium is essential for the production of lithium-ion batteries used in electric vehicles and portable

electronic devices. Meanwhile, rare earth elements are critical components in the manufacture of magnets for wind turbines, electric motors, and smartphones whereas platinum group metals are vital in catalytic converters for emissions control in vehicles. As the society continues to rely more heavily on technology and green energy, this energy transition necessitates vast amounts of minerals, and therefore their demand is expected to rise significantly. As a result, there is a growing need to assess the current scenario of critical metals (Watari et al. 2020). Understanding the geology, nature and origin of critical metals is therefore crucial for researchers to develop strategies that ensure a sustainable supply of these critical elements through discovery of new deposits, upgradation of extraction processes and promoting responsible mining practices.

Sulfides such as sphalerite, galena, pyrite, pyrrhotite, chalcopyrite, arsenopyrite are some of the most important minerals among others that contain substantial reserves of critical metals. For example, sphalerite is known to hold appreciable concentrations of In, Ga, Ge, Mn and Cd which are extracted as byproducts from some deposits. Similarly, global production of Sb and Bi largely comes from galena. It also hosts significant amounts of selenium and precious metals like silver. Pyrite is known for incorporating high levels of Co, Ni, As, Au and Tl while chalcopyrite forms a major ore mineral for Cu. Therefore, the deposits that host huge reserves of Pb-Zn mineralization, such as volcanogenic massive sulfide (VMS) deposits, sedimentary exhalative (SEDEX) deposits, Mississippi Valley-type (MVT) lead-zinc deposits (including Irish-type zinc-lead deposits), Kipushi-type zinc-lead-copper replacement bodies in carbonate rocks etc., are the prime targets for the search of these critical and precious metals. More than one-half of the byproduct indium in the world is produced in southern China from VMS and SEDEX deposits, and much of the remainder is produced from zinc concentrates from MVT deposits. VMS deposits such as Laochang in Yunnan Province, China, and Murchison

greenstone belt in Limpopo Province, South Africa, and SEDEX deposits like Bainiuchang and Dabaoshan in China provide excellent examples of indium-enriched sphalerite deposits.

Section 6.3.2 sheds light on the role of sulfide mobilization and partial melting in concentrating low melting chalcophile elements or LMCEs in metamorphosed Pb-Zn deposits. These LMCEs, that include important critical metals such as Sb, Ag, As, Tl, Bi and Se, are observed to be higher in concentrations in the bulk massive sulfides (Fig. 6.2) formed as a result of partial melting and mobilization, compared to the laminated ores. This fractionation of LMCEs or critical metals into the melt phase during deformation and metamorphism and their accumulation as pockets or veins in the massive ores enhances the economic value of the deposit and provides for new sectors for exploration of these metals. This study consequently demonstrates that identifying the mechanisms contributing to the mobilization of a particular deposit is vital to predict the presence of critical resources and developing strategies for exploration and exploitation.

# CHAPTER 7: Summary and Conclusion

## 7.1 Summary on the Genesis and Evolution of the Kayad Zn-Pb Deposit

Morphology, mode of occurrence, mineralogy, texture and geochemistry of the Zn-Pb sulfide ores and associated tourmaline are investigated to decipher the origin and geochemical evolution of one of the most important yet understudied Zn-Pb deposit in the North Delhi fold Belt named Kayad. The rock types in and around Kayad are represented by graphite-bearing quartz mica schist or QMS, quartzite, calcsilicate and pegmatite, underlain by basement granite gneiss and occasionally intersected by amphibolite sills. Sulfide mineralization, comprising sphalerite, galena, pyrrhotite, chalcopyrite and arsenopyrite, is classified into three distinct styles based on sulfide assemblages, mode of occurrence, micro-textures and associated alteration features. The first type, disseminated/laminated type, predominantly features sphalerite and pyrrhotite appearing as thin bands and disseminations within quartz mica schist and quartzite. The sulfides are conformable with the host rock fabric and concurrently deformed with it. The second style is characterized by massive ores primarily found in quartz mica schist. These ores disrupt the original foliation of the rocks, accumulating en-masse at both macro- and micro-fold hinges. The third style involves mineralization in pegmatites, quartz veins and minor veinlets that disrupts the fabric in surrounding country rock, leading to widespread pyrrhotite, chalcopyrite, and minor sphalerite and galena mineralization within and around the veins. Textures and the modes of occurrence of sulfides in a carbonaceous host establish the laminated type as the primary, syn-sedimentary and syn-diagenetic SEDEX mineralization of the area. This mineralization was subsequently mobilized into the dilational zones of regional fold structures during deformation and metamorphism, forming the massive Zn-Pb ores currently being mined at Kayad.

The massive ores comprise galena, pyrrhotite, chalcopyrite and large euhedral arsenopyrite grains in a sphalerite matrix. The remobilization process occurred through a

combination of mechanical remobilization or plastic flow, partial melting of sulfides, and hydrothermal dissolution, as indicated by distinctive textural, mineralogical, and geochemical footprints. Plastic state flow is demonstrated by diagnostic features such as durchbewegung texture, attenuation of ores at limb and thickening at fold nose, and piercement veins observable in microscopic to regional scales. Partial melting of sulfides is inferred to have occurred during peak metamorphic temperatures of ca 650 °C, as determined by Ti-in-biotite geothermometry (and supported by published peak P-T conditions of metamorphic minerals). Textural evidences include very low dihedral angles among sulfide phases, cusps and carries texture of galena in sphalerite and the presence of LMCE-bearing sulfosalts forming complex intergrowth textures, some of which are interpreted to be recrystallized relics of a former melts. Additionally, high concentrations of low melting chalcophile elements, either in the form of abundant exsolutions and inclusions of Ag-Sb-Cu-Tl phases in the massive sulfides or in the mineral structure, further corroborate the partial melting process. The presence of LMCEs, which include precious and critical metals such as Ag, Sb, Bi, As, Se, Tl etc., facilitated the melting process by lowering the melting temperature of the system. Their selective concentration in the massive ores indicate preferential fractionation into the melt phase during partial melting of sulfide and therefore has implications on the identification of ore mobilization processes and economic assessment of a deposit. The vein-hosted ores, characterized by intense Fe-Cu mineralization with minor Zn-Pb sulfide in the footwall side of the massive ores, are hydrothermal in origin. This conclusion is supported by the pervasive K + Na ± Fe alteration associated with the veins, which are later overprinted by a secondary calcic and sodic alteration. The similar sulfide mineralogy (association of sulfosalts, for example), textures (very low interfacial angle and cusps and carries texture) of the massive ores and some of the vein-hosted/associated Zn-Pb sulfide mineralization (with prominent hydrothermal alteration) suggests minor fluid-induced remobilization. However, the presence of fluid might have depressed the viscosity of the sulfide

melts and facilitated the ductile flow of sulfides thereby accelerating the mobilization process. Consequently, the remobilization of sulfide ores at Kayad is considered to result from a combination of mechanical mobilization (plastic flow), sulfide anatexis and fluid-induced mobilization.

To develop a comprehensive model for the formation of the deposit, it is necessary to address the formation mechanism of the original primary ores, as well as the role of external fluids that aided the mobilization and may have contributed ore metals. Two stable isotope systems, sulfur in sulfides and boron in tourmaline, are employed to trace the source of fluid responsible for the syn-sedimentary/diagenetic SEDEX mineralization and subsequent mobilization. In a metasedimentary environment, tourmaline serves as the primary host of boron thereby providing key insights into the role of fluids influencing an ore-forming system. High positive $\delta^{34}S$ values are observed in all the sulfides, regardless of the mineralization styles. The $\delta^{34}S$ values and multiple sulfur isotopic composition of the sulfides ($\Delta^{33}S$ and $\Delta^{36}S$) indicate mass-dependent fractionation of sulfur via thermochemical sulfate reduction in the presence of organic matter. The values and positive sulfur isotopic ratios typically allude to the involvement of seawater or other brine sources such as marine/non-marine evaporites. However, tourmaline formed contemporaneously with these primary laminated sulfides (Tur1) are dravitic in nature and exhibit considerable negative $\delta^{11}B$ values averaging at -11.8 ± 0.7‰. This precludes the involvement of any marine component and rather confirms a continental evaporitic source. Thus, we hypothesize that the $H_2S$ necessary for sulfide precipitation originated from TSR of non-marine evaporite-derived sulfates in a closed anoxic basin, during the rift phase of the ADFB. Additionally, geochemical analyses of tourmalines associated with the K-rich Zn-Pb bearing veins in QMS (Tur2) and with Fe-Cu bearing pegmatites (Tur3) were conducted to determine the nature of fluids responsible for hydrothermal ore mobilization. Tur3 is schorl in composition and exhibits highly negative $\delta^{11}B$, values as low as -15.2‰, that indicate its

granitic origin. Classification into the Li-poor granitoid field in the Al-Fe-Mg diagram and enrichment in granitophile elements reinforce its granitic lineage. Based on the similar $\delta^{34}S$ values of vein-hosted sulfides and laminated/massive types, it is inferred that the fluid likely recycled sulfur from the host sediments to precipitate the Fe-Cu sulfides. Tur2 occurs as large masses within Zn-Pb veins in quartz mica schist (QMS) and exhibits major and trace element characteristics similar to Tur1. However, unlike Tur1, it shows selective enrichment in granitophile elements present in Tur3 in addition to a lighter boron isotopic composition that falls between Tur1 and Tur3. This intermediate composition suggests a mixing of sedimentary and magmatic boron sources during the leaching of the host metasediments or pre-existing Tur1. Hence, it is concluded that the fluid responsible for this mineralization and sulfide remobilization was granite-derived fluid, which was likely enriched in Fe, Na and K as indicated by the Fe-rich nature of Tur3 and the Na-K±Fe alteration associated with this mineralization.

The Kayad deposit presents a unique contribution to the understanding of SEDEX deposits in general. One key departure is in the source of sulfur for primary mineralization. Globally, most SEDEX deposits are associated with marine or seawater-derived fluids, typically from marine evaporites, which are considered a standard model. However, Kayad's sulfur isotope data points to a continental evaporitic source, signaling the potential for diverse sulfur reservoirs beyond the marine system. Additionally, Kayad reveals a more complex remobilization process than is typically documented in SEDEX deposits. Most global SEDEX deposits undergo single-phase mobilization, often through hydrothermal fluid flow or deformation, but Kayad demonstrates a three-fold mechanism: mechanical remobilization (plastic flow), sulfide anatexis (partial melting), and fluid-induced remobilization. This highlights the role of thermal events in metal enrichment and could help explain high-grade ore zones in other deposits that are inadequately understood with simpler mobilization models.

Finally, it shows that mobilization via sulfide anatexis plays a key role in the accumulation of precious and critical metals which has direct implications for exploration strategies, as it suggests that areas of a deposit experiencing intense mobilization are more likely to host high concentrations of these critical metals. Targeting such zones could enhance the economic viability of SEDEX deposits, particularly in meeting the growing demand for critical metals, which are essential for emerging technologies but are often overlooked in traditional Zn-Pb exploration models.

## 7.2 Limitations and Future Scopes

This study has provided important insights into the origin and evolution of SEDEX deposits but it is essential to highlight its limitations to provide a balanced interpretation of the findings. With respect to the mobilization of the ores, three processes have been proposed based on textural and mineralogical clues. However, the relative importance and impact of each process in forming such extensive deposits remain unquantified. Since each mobilization process is driven by unique factors, measuring their respective contribution can help in precisely identifying ore target zones and estimating the economic potential of a deposit. Secondly, the intermediate $\delta^{11}B$ composition of Tur2 is envisaged to be a result from the blend of two boron sources: external magmatic fluid and clastic sediments/existing tourmaline. However, determining the actual mixing ratios to calculate the resultant $\delta^{11}B$ of Tur2 or $\delta^{34}S$ of pegmatites was beyond the scope of this study.

Potential for further research and refinement lies in the geochronology of the deposit, which has not yet been established. Pb-Pb model age of galena has been obtained from Ghugra ores that furnish age of 1787 Ma (Deb and Thorpe 2004). However, the exact timing of the primary SEDEX mineralization at Kayad is not known. Additionally, it is crucial to ascertain the ages of subsequent melt mobilization and fluid-induced mobilization to confirm whether

they occurred synchronously, as has been hypothesized. Understanding the timeline of the region's metamorphic history will be pivotal in correlating the mobilizations with the peak metamorphic activity. Quantifying the temporal relationship between fluid-induced mobilization and granitic activity in the area will provide strong evidence that fluids derived from granite intrusions facilitated mobilization. Moreover, while this study has addressed potential fluid sources for sulfide precipitation, identifying the sources of metals remains a fundamental question in understanding ore systems. Besides Pb, metal isotopes such as Zn ($\delta^{66}$Zn), Cd ($\delta^{114}$Cd), Fe ($\delta^{56}$Fe) and Cu ($\delta^{65}$Cu) are invaluable in deducing the origins of the base metals. Finally, a comprehensive understanding of ore evolution requires knowledge of the physicochemical conditions of the original SEDEX fluid, including temperature, salinity, and pH which could not be addressed in this study and constitute potential research problems for future work.

**References:**

Abanda PA, Hannigan RE (2006) Effect of diagenesis on trace element partitioning in shales. Chem Geol 230:42–59. https://doi.org/https://doi.org/10.1016/j.chemgeo.2005.11.011

Absar N, Kalam TDA, Raza MQ, et al (2024) Redox conditions of Early Cambrian Ocean as deciphered from multi-proxy geochemical and isotopic studies of Proto-Tethys carbonaceous sediments from Outer Lesser Himalaya, India. J Earth Syst Sci 133:26. https://doi.org/10.1007/s12040-023-02233-8

Adlakha EE, Hattori K, Davis WJ, Boucher B (2017) Characterizing fluids associated with the McArthur River U deposit, Canada, based on tourmaline trace element and stable (B, H) isotope compositions. Chem Geol 466:417–435. https://doi.org/https://doi.org/10.1016/j.chemgeo.2017.06.030

Amcoff Ö (1984) Distribution of silver in massive sulfide ores. Miner Depos 19:63–69. https://doi.org/10.1007/BF00206598

Andersen JCØ, Stickland RJ, Rollinson GK, Shail RK (2016) Indium mineralisation in SW England: Host parageneses and mineralogical relations. Ore Geol Rev 78:213–238. https://doi.org/https://doi.org/10.1016/j.oregeorev.2016.02.019

Ansdell KM, Nesbitt BE, Longstaffe FJ (1989) A fluid inclusion and stable-isotope study of the Tom Ba-Pb-Zn deposit, Yukon Territory, Canada. Econ Geol 84:841–856. https://doi.org/10.2113/gsecongeo.84.4.841

Badham JPN (1981) Shale-hosted Pb-Zn deposits—Products of exhalation of formation waters?: Transactions, Institution of Mining and Metallurgy. Appl Earth Sci 90:70–76

Baidya AS, Saha R, Pal DC, Upadhyay D (2023) Fingerprinting alteration and mineralization in the iron oxide Cu-Au (IOCG) system using biotite chemistry and monazite geochronology: constraints from the Khetri Copper Belt, western India. Miner Depos 58:1445–1476. https://doi.org/10.1007/s00126-023-01190-y

Banerjee A, Sequeira N, Bhattacharya A (2021) Tectonics of the Greater India Proterozoic Fold Belt, with emphasis on the nature of curvature of the belt in west-central India. Earth-Science Rev 221:103758. https://doi.org/https://doi.org/10.1016/j.earscirev.2021.103758

Barnes RG (1987) Multi-stage mobilization and remobilization of mineralization in the broken hill block, Australia. Ore Geol Rev 2:247–267. https://doi.org/10.1016/0169-1368(87)90031-X

Barré G, Thomassot É, Michels R, et al (2021) Multiple sulfur isotopes signature of Thermochemical Sulfate Reduction (TSR): Insights from Alpine Triassic evaporites. Earth Planet Sci Lett 576:117231. https://doi.org/10.1016/j.epsl.2021.117231

Basuki NI, Taylor BE, Spooner ETC (2008) Sulfur isotope evidence for thermochemical reduction of dissolved sulfate in Mississippi Valley-type zinc-lead mineralization, Bongara area, Northern Peru. Econ Geol 103:783–799. https://doi.org/10.2113/gsecongeo.103.4.783

Bauer ME, Burisch M, Ostendorf J, et al (2019) Trace element geochemistry of sphalerite in contrasting hydrothermal fluid systems of the Freiberg district, Germany: insights from LA-ICP-MS analysis, near-infrared light microthermometry of sphalerite-hosted fluid inclusions, and sulfur isotope geochemi. Miner Depos 54:237–262. https://doi.org/10.1007/s00126-018-0850-0

Bea F, Pesquera A, Montero P, et al (2009) Tourmaline 40Ar39Ar chronology of tourmaline-rich rocks from Central Iberia dates the main Variscan deformation phases. Geol Acta 7:399–412. https://doi.org/10.1344/104.000001446

Beaudoin G, Chiaradia M (2016) Fluid mixing in orogenic gold deposits: Evidence from the H-O-Sr isotope composition of the Val-d'Or vein field (Abitibi, Canada). Chem Geol 437:7–18. https://doi.org/https://doi.org/10.1016/j.chemgeo.2016.05.009

Becker W, Lutz HD (1978) Phase studies in the systems CoS1bMnS, CoS1bZnS, and CoS1bCdS. Mater Res Bull 13:907–911. https://doi.org/https://doi.org/10.1016/0025-5408(78)90102-2

Bhuyan N, Hazarika P, Upadhyay D (2023) Continental evaporites as brine sources for formation of SEDEX and MVT deposits: Implications from boron isotope compositions of tourmaline. Geochim Cosmochim Acta 361:82–100. https://doi.org/10.1016/j.gca.2023.10.014

Bonnet J, Mosser-Ruck R, Caumon M-C, et al (2016) Trace Element Distribution (Cu, Ga, Ge, Cd, and Fe) IN Sphalerite From the Tennessee MVT Deposits, USA, By Combined EMPA, LA-ICP-MS, Raman Spectroscopy, and Crystallography. Can Mineral 54:1261–1284. https://doi.org/10.3749/canmin.1500104

Bortnikov NS, Dobrovol'skaya MG, Genkin AD, et al (1995) Sphalerite-galena geothermometers: distribution of cadmium, manganese, and the fractionation of sulfur isotopes. Econ Geol 90:155–180. https://doi.org/10.2113/gsecongeo.90.1.155

Brett R, Kullerud G (1967) The Fe-Pb-S system. Econ Geol 62:354–369. https://doi.org/10.2113/gsecongeo.62.3.354

Byerly GR, Palmer MR (1991) Tourmaline mineralization in the Barberton greenstone belt, South Africa: early Archean metasomatism by evaporite-derived boron. Contrib to Mineral Petrol 107:387–402. https://doi.org/10.1007/BF00325106

Cabral AR, Koglin N (2012) Hydrothermal fluid source constrained by Co/Ni ratios in coexisting arsenopyrite and tourmaline: The auriferous lode of Passagem, Quadrilátero Ferrífero of Minas Gerais, Brazil. Mineral Petrol 104:137–145.

https://doi.org/10.1007/s00710-011-0183-5

Cabri LJ, Campbell JL, Laflamme JHG, et al (1985) Proton-microprobe analysis of trace elements in sulfides from some massive-sulfide deposits. Can Mineral 23:133–148

Canfield DE (2004) The evolution of the Earth surface sulfur reservoir. Am J Sci 304:839–861

Carne RC, Cathro RJ (1982) Sedimentary exhalative (sedex) zinc-lead-silver deposits, northern Canadian Cordillera. CIM Bull 75:840

Cave B, Lilly R, Barovich K (2020) Textural and geochemical analysis of chalcopyrite, galena and sphalerite across the Mount Isa Cu to Pb-Zn transition: Implications for a zoned Cu-Pb-Zn system. Ore Geol Rev 124:103647. https://doi.org/10.1016/j.oregeorev.2020.103647

Chakraborty T, Upadhyay D (2020) The geochemical differentiation of S-type pegmatites: constraints from major–trace element and Li–B isotopic composition of muscovite and tourmaline. Contrib to Mineral Petrol 175:60. https://doi.org/10.1007/s00410-020-01697-x

Chang LLY, Knowles CR (1977) Phase relations in the system PbS-Fe1-xS-Sb2S3 and PbS-Fe1-xS-Bi2S3. Can Mineral 15:374–379

Chapman LH (2004) Geology and mineralization styles of the George Fisher Zn-Pb-Ag deposit, Mount Isa. Econ Geol 99:233–255

Chattopadhyay N, Mukhopadhyay D, Sengupta P (2012) Reactivation of basement: example from the Anasagar Granite Gneiss Complex, Rajasthan, western India. Palaeoproterozoic of India 365:0

Choudhary AK, Gopalan K, Sastry CA (1984) Present status of the geochronology of the Precambrian rocks of Rajasthan. Tectonophysics 105:131–140. https://doi.org/https://doi.org/10.1016/0040-1951(84)90199-9

Chovan M, Mikuš T, Prcúch J, Bača B (2021) Assemblage of Ag-Pb-Bi±Cu sulfosalts from the Bieber vein, Banská Štiavnica deposit, Slovakia. Acta Geol Slovaca 13:191–198

Chutas NI, Kress VC, Ghiorso MS, Sack RO (2008) A solution model for high-temperature PbS-AgSbS2-AgBiS2 galena. Am Mineral 93:1630–1640. https://doi.org/10.2138/am.2008.2695

Clark AH (1966) Heating experiments on gudmundite. Mineral Mag J Mineral Soc 36:1123–1125. https://doi.org/DOI: 10.1180/minmag.1966.036.276.07

Cook NJ, Ciobanu CL, Pring A, et al (2009) Trace and minor elements in sphalerite: A LA-ICPMS study. Geochim Cosmochim Acta 73:4761–4791. https://doi.org/10.1016/j.gca.2009.05.045

Cooke DR, Bull SW, Large RR, McGoldrick PJ (2000) The Importance of Oxidized Brines for the Formation of Australian Proterozoic Stratiform Sediment-Hosted Pb-Zn (Sedex) Deposits. Econ Geol 95:1–18. https://doi.org/10.2113/gsecongeo.95.1.1

Čopjaková R, Buriánek D, Škoda R, Houzar S (2009) Tourmalinites in the metamorphic complex of the Svratka Unit (Bohemian Massif): A study of compositional growth of tourmaline and genetic relations. J Geosci 54:221–243. https://doi.org/10.3190/jgeosci.048

Crockford PW, Kunzmann M, Bekker A, et al (2019) Claypool continued: Extending the isotopic record of sedimentary sulfate. Chem Geol 513:200–225. https://doi.org/https://doi.org/10.1016/j.chemgeo.2019.02.030

Crowe DE, Vaughan RG (1996) Characterization and use of isotopically homogeneous standards for in situ laser microprobe analysis of 34S/32 S ratios. Am Mineral 81:187–193. https://doi.org/10.2138/am-1996-1-223

Davidson GJ (1998) Alkali alteration styles and mechanisms, and their implications for a 'brine factory' source of base metals in the rift-related McArthur group, Australia. Aust J Earth Sci 45:33–49. https://doi.org/10.1080/08120099808728365

Deb, M. and Thorpe RI (2004) Geochronological Constraints in the Precambrian Geology of Rajasthan and Their Metallogenic Implications. In: Sediment-hosted lead-zinc sulphide deposits. Narosa Publishing House, New Delhi, India, pp 246–263

Deb M (2000) VMS Deposits: Geological characteristics, genetic models and a review of their metallogenesis in the Aravalli range, Northwest India. In: Crustal evolution and metallogeny in North Western Indian Shield. Narosa Publishing House, New Delhi, India, pp 329–363

Deb M (1986) Sulfur and carbon isotope compositions in the stratiform Zn-Pb-Cu sulfide deposits of the Rajpura-Dariba belt, Rajasthan, NW India: A model of ore genesis. Miner Depos 21:313–321. https://doi.org/10.1007/BF00204350

Deb M (1990) Isotopic Constitution of Sulfur in the Conformable Base-Metal Sulfide Deposits in the Proterozoic Aravalli-Delhi Orogenic Belt, Nw India. In: Naqvi SMBT-D in PG (ed) Precambrian Continental Crust and its Economic Resources. Elsevier, pp 631–651

Deb M, Pal T (2004) Geology and genesis of the base metal sulfide deposits in the Dariba-Rajpura-Bethumni belt, Rajasthan, India in the light of basin evolution. In: Deb M, Goodfellow WD (eds) Sediment-hosted lead-zinc sulfide deposits. Narosa Publishing House, Delhi, pp 304–327

Deb M, Sarkar SC (1990) Proterozoic tectonic evolution and metallogenesis in the Aravalli-Delhi orogenic complex, northwestern India. Precambrian Res 46:115–137. https://doi.org/https://doi.org/10.1016/0301-9268(90)90069-3

Deb M, Sehgal U (1997) Petrology, geothermobarometry and C-O-H-S fluid compositions in the environs of Rampura-Agucha Zn-(Pb) ore deposit, Bhilwara District, Rajasthan. Proc Indian Acad Sci - Earth Planet Sci 106:343–356. https://doi.org/10.1007/BF02843458

Deb M, Thorpe RI, Cumming GL, Wagner PA (1989) Age, source and stratigraphic implications of Pb isotope data for conformable, sediment-hosted, base metal deposits in the Proterozoic Aravalli-Delhi orogenic belt, northwestern India. Precambrian Res 43:1–22. https://doi.org/https://doi.org/10.1016/0301-9268(89)90002-8

Deb M, Thorpe RI, Krstic D, et al (2001) Zircon U–Pb and galena Pb isotope evidence for an approximate 1.0 Ga terrane constituting the western margin of the Aravalli–Delhi orogenic belt, northwestern India. Precambrian Res 108:195–213. https://doi.org/https://doi.org/10.1016/S0301-9268(01)00134-6

Dixon G, Davidson GJ (1996) Stable isotope evidence for thermochemical sulfate reduction in the Dugald River (Australia) strata-bound shale-hosted zinc-lead deposit. Chem Geol 129:227–246. https://doi.org/10.1016/0009-2541(95)00177-8

Duan Z-P, Jiang S-Y, Su H-M, Zhu X (2020) Tourmaline as a recorder of contrasting boron source and potential tin mineralization in the Mopanshan pluton from Inner Mongolia, northeastern China. Lithos 354–355:105284. https://doi.org/https://doi.org/10.1016/j.lithos.2019.105284

Dutrow BL, Foster CT, Henry DJ (1999) Tourmaline-rich pseudomorphs in sillimanite zone metapelites: Demarcation of an infiltration front. 84:794–805. https://doi.org/doi:10.2138/am-1999-5-615

Dutrow BL, Henry DJ (2011) Tourmaline: A geologic DVD. Elements 7:301–306. https://doi.org/10.2113/gselements.7.5.301

Dutrow BL, Henry DJ (2018) Tourmaline compositions and textures: Reflections of the fluid phase. J Geosci (Czech Republic) 63:99–110. https://doi.org/10.3190/jgeosci.256

Edwards R, Atkinson K (1986) Hydrothermal vein deposits BT - Ore Deposit Geology and its Influence on Mineral Exploration. In: Edwards R, Atkinson K (eds). Springer Netherlands, Dordrecht, pp 143–174

Emmings JF, Poulton SW, Walsh J, et al (2024) Pyrite mega-analysis reveals modes of anoxia through geological time. Sci Adv 8:eabj5687. https://doi.org/10.1126/sciadv.abj5687

Emsbo P (2000) Gold in Sedex Deposits. Gold 2000 13:0

Fareeduddin, Reddy MS, Bose U (1995) Reappraisal of the Delhi Stratigraphy in the Ajmer-Sambhar Sector, North-Central Rajasthan. Geol Soc India; Vol 45, Issue 6, June 1995

Fareeduddin, Venkatesh BR, Hanumantha R, et al (2014) Petrology and stable isotope (S, C, O) studies of selected sedimenthosted basemetal ore deposits in the proterozoic Aravalli-

Delhi Fold Belt, Rajasthan. J Geol Soc India 83:119–141. https://doi.org/10.1007/s12594-014-0024-3

Farquhar J, Savarino J, Airieau S, Thiemens MH (2001) Observation of wavelength-sensitive mass-independent sulfur isotope effects during SO2 photolysis: Implications for the early atmosphere. J Geophys Res Planets 106:32829–32839. https://doi.org/https://doi.org/10.1029/2000JE001437

Farquhar J, Wing BA (2003) Multiple sulfur isotopes and the evolution of the atmosphere. Earth Planet Sci Lett 213:1–13. https://doi.org/10.1016/S0012-821X(03)00296-6

Foord EE, Shawe DR (1989) The Pb-Bi-Ag-Cu-(Hg) chemistry of galena and some associated sulfosalts; a review and some new data from Colorado, California and Pennsylvania. Can Mineral 27:363–382

Frenzel M, Hirsch T, Gutzmer J (2016) Gallium, germanium, indium, and other trace and minor elements in sphalerite as a function of deposit type - A meta-analysis. Ore Geol Rev 76:52–78. https://doi.org/10.1016/j.oregeorev.2015.12.017

Frost BR, Mavrogenes JA, Tomkins AG (2002) Partial melting of sulfide ore deposits during medium- and high-garde metamorphism. Can Mineral 40:1–18. https://doi.org/10.2113/gscanmin.40.1.1

Frost BR, Swapp SM, Mavrogenes J (2011) Textural evidence for extensive melting of the broken hill orebody. Econ Geol 106:869–882. https://doi.org/10.2113/econgeo.106.5.869

Gadd MG, Layton-Matthews D, Peter JM, et al (2017) The world-class Howard's Pass SEDEX Zn-Pb district, Selwyn Basin, Yukon. Part II: the roles of thermochemical and bacterial sulfate reduction in metal fixation. Miner Depos 52:405–419. https://doi.org/10.1007/s00126-016-0672-x

Gao B, Zhang L, Jin X, et al (2020) Rhenium-Osmium isotope systematics of an Early Mesoproterozoic SEDEX polymetallic pyrite deposit in the North China Craton: Implications for geological significance and the marine osmium isotopic record. Ore Geol Rev 117:103331. https://doi.org/https://doi.org/10.1016/j.oregeorev.2020.103331

Gardner HD, Hutcheon I (1985) Geochemistry, mineralogy, and geology of the Jason Pb-Zn deposits, Macmillan Pass, Yukon, Canada. Econ Geol 80:1257–1276. https://doi.org/10.2113/gsecongeo.80.5.1257

George L, Cook NJ, Cristiana C, Wade BP (2015) Trace and minor elements in galena: A reconnaissance LA-ICP-MS study. Am Mineral 100:548–569. https://doi.org/10.2138/am-2015-4862

George LL, Cook NJ, Ciobanu CL (2016) Partitioning of trace elements in co-crystallized sphalerite–galena–chalcopyrite hydrothermal ores. Ore Geol Rev 77:97–116. https://doi.org/https://doi.org/10.1016/j.oregeorev.2016.02.009

George LL, Cook NJ, Crowe BBP, Ciobanu CL (2018) Trace elements in hydrothermal chalcopyrite. Mineral Mag 82:59–88. https://doi.org/10.1180/minmag.2017.081.021

Ghosh S, D'Souza J, Goud BR, Prabhakar N (2022) A review of the Precambrian tectonic evolution of the Aravalli Craton, northwestern India: Structural, metamorphic and geochronological perspectives from the basement complexes and supracrustal sequences. Earth-Science Rev 232:104098. https://doi.org/https://doi.org/10.1016/j.earscirev.2022.104098

Gilligan LB, Marshall B (1987a) Textural evidence for remobilization in metamorphic environments. Ore Geol Rev 2:205–229. https://doi.org/10.1016/0169-1368(87)90029-1

Gilligan LB, Marshall B (1987b) Textural evidence for remobilization in metamorphic environments. Ore Geol Rev 2:205–229. https://doi.org/https://doi.org/10.1016/0169-1368(87)90029-1

Goldstein TP, Aizenshtat Z (1994) Thermochemical sulfate reduction a review. J Therm Anal 42:241–290. https://doi.org/10.1007/BF02547004

Goodfellow W, Lydon J, Turner R (1993) Geology and genesis of stratiform sediment-hosted (SEDEX) zinc-lead-silver sulphide deposits. In: Mineral deposit modeling: Geological Association of Canada: Special Paper 40. pp 201–251

Goodfellow WD (2004) Geology, genesis and exploration of SEDEX deposits, with emphasis on the Selwyn basin, Canada. In: Sediment Hosted LeadZinc Sulfide deposits. Narosa Publishing House, New Delhi, India, pp 24–99

Goodfellow WD, Rhodes D, Abbott JG, Turner RJW (1990) Geological setting, geochemistry and origin of the Tom stratiform Zn-Pb-Ag-barite deposits. In: Mineral deposits of the northern Canadian Cordillera: Ottawa, International Association on the Genesis of Ore Deposits, Eighth Symposium, Field Trip, Vol. 14. pp 177–244

Gopalan K, Macdougall JD, Roy AB, Murali A V (1990) Sm-Nd evidence for 3.3 Ga old rocks in Rajasthan, northwestern India. Precambrian Res 48:287–297. https://doi.org/https://doi.org/10.1016/0301-9268(90)90013-G

Govindarao B, Parihar R, Pruseth KL, Mishra B (2017) The occurrence of breithauptite and nisbite-like sb-ni phases at Sindesar-Khurd, Rajasthan, India: Implications for melt-assisted sulfide remobilization. Can Mineral 55:75–87. https://doi.org/10.3749/canmin.1600025

Govindarao B, Pruseth KL, Mishra B (2020) Sulfide partial melting and galena–tetrahedrite intergrowth texture: An experimental study. Mineral Mag 84:859–868. https://doi.org/10.1180/mgm.2020.79

Gregory DD, Lyons TW, Large RR, et al (2017) Whole rock and discrete pyrite geochemistry as complementary tracers of ancient ocean chemistry: An example from the

Neoproterozoic Doushantuo Formation, China. Geochim Cosmochim Acta 216:201–220. https://doi.org/https://doi.org/10.1016/j.gca.2017.05.042

Griffin W, Powell W, Pearson NJ, O'Reilly S (2008) GLITTER: data reduction software for laser ablation ICP-MS. Short Course Ser 40:308–311

Griffin WL, Slack JF, Ramsden AR, et al (1996) Trace elements in tourmalines from massive sulfide deposits and tourmalinites: Geochemical controls and exploration applications. Econ Geol 91:657–675. https://doi.org/10.2113/gsecongeo.91.4.657

Gu A, Eastoe CJ (2021) The Origins of Sulfate in Cenozoic Non-Marine Evaporites in the Basin and-Range Province, Southwestern North America. Geosciences 11

Guo S, Zhao K, John T, et al (2019) Metasomatic flow of metacarbonate-derived fluids carrying isotopically heavy boron in continental subduction zones: Insights from tourmaline-bearing ultra-high pressure eclogites and veins (Dabie terrane, eastern China). Geochim Cosmochim Acta 253:159–200. https://doi.org/https://doi.org/10.1016/j.gca.2019.03.013

Hawthorne FC, Dirlam DM (2011) Tourmaline the Indicator Mineral: From Atomic Arrangement to Viking Navigation. Elements 7:307–312. https://doi.org/10.2113/gselements.7.5.307

Hawthorne FC, Henrys DJ (1999) Classification of the minerals of the tourmaline group. Eur J Mineral 11:201–216. https://doi.org/10.1127/ejm/11/2/0201

Hazarika P, Bhuyan N, Upadhyay D, et al (2019) The nature and sources of ore-forming fluids in the Bhukia gold deposit, Western India: constraints from chemical and boron isotopic composition of tourmaline. Lithos 350–351:105227. https://doi.org/https://doi.org/10.1016/j.lithos.2019.105227

Henry DJ, Dutrow BL (2012) Tourmaline at diagenetic to low-grade metamorphic conditions: Its petrologic applicability. Lithos 154:16–32. https://doi.org/https://doi.org/10.1016/j.lithos.2012.08.013

Henry DJ, Dutrow BL (1992) Tourmaline in a low grade clastic metasedimentary rock: an example of the petrogenetic potential of tourmaline. Contrib to Mineral Petrol 112:203–218. https://doi.org/10.1007/BF00310455

Henry DJ, Guidotti C V, Thomson JA (2005) The Ti-saturation surface for low-to-medium pressure metapelitic biotites: Implications for geothermometry and Ti-substitution mechanisms. Am Mineral 90:316–328. https://doi.org/10.2138/am.2005.1498

Henry DJ, Sun H, Slack JF, Dutrow BL (2008) Tourmaline in meta-evaporites and highly magnesian rocks: perspectives from Namibian tourmalinites. Eur J Mineral 20:889–904. https://doi.org/10.1127/0935-1221/2008/0020-1879

Hoggard MJ, Czarnota K, Richards FD, et al (2020) Global distribution of sediment-hosted metals controlled by craton edge stability. Nat Geosci 13:504–510. https://doi.org/10.1038/s41561-020-0593-2

Hohf M, Trumbull RB, Cuadra P, Solé M (2023) Tourmaline Breccias from the Río Blanco-Los Bronces Porphyry Copper District, Chile: Constraints on the Fluid Source and the Utility of Tourmaline Composition for Exploration. Econ Geol 118:779–800. https://doi.org/10.5382/econgeo.4991

Höller W, Touret JLR, Stumpfl EF (1996) Retrograde fluid evolution at the Rampura Agucha Pb-Zn-(Ag) deposit, Rajasthan, India. Miner Depos 31:163–171. https://doi.org/10.1007/BF00204024

Huang S, Song Y, Hou Z, Xue C (2016) Chemical and stable isotopic (B, H, and O) compositions of tourmaline in the Maocaoping vein-type Cu deposit, western Yunnan, China: Constraints on fluid source and evolution. Chem Geol 439:173–188. https://doi.org/https://doi.org/10.1016/j.chemgeo.2016.06.031

Huston DL, Mernagh TP, Hagemann SG, et al (2016) Tectono-metallogenic systems — The place of mineral systems within tectonic evolution, with an emphasis on Australian examples. Ore Geol Rev 76:168–210. https://doi.org/https://doi.org/10.1016/j.oregeorev.2015.09.005

Huston DL, Sie SH, Suter GF, et al (1995) Trace elements in sulfide minerals from eastern Australian volcanic- hosted massive sulfide deposits: part I. Proton microprobe analyses of pyrite, chalcopyrite, and sphalerite, and part II. Selenium levels in pyrite: comparison with δ34S values and impli. Econ Geol 90:1167–1196. https://doi.org/10.2113/gsecongeo.90.5.1167

Huston DL, Stevens B, Southgate PN, et al (2006) Australian Zn-Pb-Ag Ore-Forming Systems: A Review and Analysis. Econ Geol 101:1117–1157. https://doi.org/10.2113/gsecongeo.101.6.1117

HZL (2017) Expansion of Kayad lead-zinc ore underground mine from 1.0 million TPA to 1.2 million TPA (ROM)

Ireland T, Bull SW, Large RR (2004) Mass flow sedimentology within the HYC Zn–Pb–Ag deposit, Northern Territory, Australia: evidence for syn-sedimentary ore genesis. Miner Depos 39:143–158. https://doi.org/10.1007/s00126-003-0382-z

Ireland TR, Schram N, Holden P, et al (2014) Charge-mode electrometer measurements of S-isotopic compositions on SHRIMP-SI. Int J Mass Spectrom 359:26–37. https://doi.org/https://doi.org/10.1016/j.ijms.2013.12.020

Ishikawa T, Nakamura E (1993) Boron isotope systematics of marine sediments. Earth Planet Sci Lett 117:567–580. https://doi.org/10.1016/0012-821X(93)90103-G

Jankovic S (1986) The mineral association and genesis of the lead-zinc-barite deposits at Gunga, Khuzdar district, Baluchistan, Pakistan. Pakistan Geol Surv Rec. vLXXI:12

Jiang S-Y, Palmer M, Slack JF, et al (2000) Silicon isotope compositions of tourmalinites and selected silicate minerals from the Sullivan deposit and vicinity, and their signifi cance to mineral exploration and ore genesis. Geol Environ Sullivan Depos Br Columbia Geol Assoc Canada Spec Publ 1:782–790

Jiang S-Y, Palmer MR, Yeats CJ (2002) Chemical and boron isotopic compositions of tourmaline from the Archean Big Bell and Mount Gibson gold deposits, Murchison Province, Yilgarn Craton, Western Australia. Chem Geol 188:229–247. https://doi.org/https://doi.org/10.1016/S0009-2541(02)00107-9

Jiang SY (2001) Boron isotope geochemistry of hydrothermal ore deposits in China: A preliminary study. Phys Chem Earth, Part A Solid Earth Geod 26:851–858. https://doi.org/10.1016/S1464-1895(01)00132-6

Jiang SY (1998) Stable and radiogenic isotope studies of tourmaline: an overview. J. Czech Geol. Soc. 43:75–90

Jiang SY, Palmer MR, Slack JF, Shaw DR (1999) Boron isotope systematics of tourmaline formation in the Sullivan Pb-Zn-Ag deposit, British Columbia, Canada. Chem Geol 158:131–144. https://doi.org/10.1016/S0009-2541(99)00023-6

Johnston DT (2011) Multiple sulfur isotopes and the evolution of Earth's surface sulfur cycle. Earth-Science Rev 106:161–183. https://doi.org/10.1016/j.earscirev.2011.02.003

Johnston DT, Farquhar J, Wing BA, et al (2005) Multiple sulfur isotope fractionations in biological systems: A case study with sulfate reducers and sulfur disproportionators. Am J Sci 305:645–660. https://doi.org/10.2475/ajs.305.6-8.645

Jørgensen BB, Isaksen MF, Jannasch HW (1992) Bacterial Sulfate Reduction Above 100°C in Deep-Sea Hydrothermal Vent Sediments . Science (80- ) 258:1756–1757. https://doi.org/10.1126/science.258.5089.1756

Kampmann TC, Jansson NF, Stephens MB, et al (2018) Syn-tectonic sulphide remobilization and trace element redistribution at the Falun pyritic Zn-Pb-Cu-(Au-Ag) sulphide deposit, Bergslagen, Sweden. Ore Geol Rev 96:48–71. https://doi.org/https://doi.org/10.1016/j.oregeorev.2018.04.010

Kase K (1987) Tin-bearing chalcopyrite from the Izumo Vein, Toyoha Mine, Hokkaido, Japan. Can Mineral 25:9–13

Kaur P, Zeh A, Okrusch M, et al (2016) Separating regional metamorphic and metasomatic assemblages and events in the northern Khetri complex, NW India: Evidence from mineralogy, whole-rock geochemistry and U-Pb monazite chronology. J Asian Earth Sci 129:117–141. https://doi.org/https://doi.org/10.1016/j.jseaes.2016.08.002

Kelley KD, Leach DL, Johnson CA, et al (2004) Textural, compositional, and sulfur isotope variations of sulfide minerals in the Red Dog Zn-Pb-Ag deposits, Brooks Range, Alaska: Implications for Ore Formation. Econ Geol 99:1509–1532. https://doi.org/10.2113/gsecongeo.99.7.1509

Kelly CJ, Davis WJ, Potter EG, Corriveau L (2020) Geochemistry of hydrothermal tourmaline from IOCG occurrences in the Great Bear magmatic zone: Implications for fluid source(s) and fluid composition evolution. Ore Geol Rev 118:103329. https://doi.org/10.1016/j.oregeorev.2020.103329

Kiyosu Y, Krouse HR (1990) The role of organic acid in the abiogenic reduction of sulfate and the sulfur isotope effect. Geochem J 24:21–27. https://doi.org/10.2343/geochemj.24.21

Knauth LP (2005) Temperature and salinity history of the Precambrian ocean: implications for the course of microbial evolution. In: Noffke Concepts, Perspectives NBT-GO (ed). Elsevier, Amsterdam, pp 53–69

Knorsch M, Nadoll P, Klemd R (2020a) Trace elements and textures of hydrothermal sphalerite and pyrite in Upper Permian (Zechstein) carbonates of the North German Basin. J Geochemical Explor 209:106416. https://doi.org/10.1016/j.gexplo.2019.106416

Knorsch M, Nadoll P, Klemd R (2020b) Trace elements and textures of hydrothermal sphalerite and pyrite in Upper Permian (Zechstein) carbonates of the North German Basin. J Geochemical Explor 209:106416. https://doi.org/10.1016/j.gexplo.2019.106416

Kotzer TG, Kyser TK, King RW, Kerrich R (1993) An empirical oxygen- and hydrogen-isotope geothermometer for quartz-tourmaline and tourmaline-water. Geochim Cosmochim Acta 57:3421–3426. https://doi.org/https://doi.org/10.1016/0016-7037(93)90548-B

Kozdon R, Kita NT, Huberty JM, et al (2010) In situ sulfur isotope analysis of sulfide minerals by SIMS: Precision and accuracy, with application to thermometry of ~3.5Ga Pilbara cherts. Chem Geol 275:243–253. https://doi.org/https://doi.org/10.1016/j.chemgeo.2010.05.015

Kretschmar U, Scott SD (1976) Phase relations involving arsenopyrite in the system Fe-As-S and their application. Can Mineral 14:364–386

Krmíček L, Novák M, Trumbull RB, et al (2021) Boron isotopic variations in tourmaline from metacarbonates and associated calc-silicate rocks from the Bohemian Massif: Constraints on boron recycling in the Variscan orogen. Geosci Front 12:219–230. https://doi.org/10.1016/j.gsf.2020.03.009

LaFlamme C, Jamieson JW, Fiorentini ML, et al (2018a) Investigating sulfur pathways through the lithosphere by tracing mass independent fractionation of sulfur to the Lady Bountiful orogenic gold deposit, Yilgarn Craton. Gondwana Res 58:27–38.

https://doi.org/10.1016/j.gr.2018.02.005

LaFlamme C, Sugiono D, Thébaud N, et al (2018b) Multiple sulfur isotopes monitor fluid evolution of an Archean orogenic gold deposit. Geochim Cosmochim Acta 222:436–446. https://doi.org/10.1016/j.gca.2017.11.003

LAND L, MACPHERSON G (1992) Origin of saline formation waters, Cenozoic section, Gulf of Mexico sedimentary basin. Am Assoc Pet Geol Bull 76:1344–1362

Large R, Mukherjee I, Danyushevsky L, et al (2022) Sedimentary pyrite proxy for atmospheric oxygen: evaluation of strengths and limitations. Earth-Science Rev 227:103941. https://doi.org/https://doi.org/10.1016/j.earscirev.2022.103941

Large RR, Bull SW, McGoldrick PJ, et al (2005) Stratiform and Strata-Bound Zn-Pb-Ag Deposits in Proterozoic Sedimentary Basins, Northern Australia. One Hundredth Anniv. Vol. 0

Large RR, Bull SW, Winefield PR (2001a) Carbon and Oxygen Isotope Halo in Carbonates Related to the McArthur River (HYC) Zn-Pb-Ag Deposit, North Australia:Implications for Sedimentation, Ore Genesis, and Mineral Exploration. Econ Geol 96:1567–1593. https://doi.org/10.2113/gsecongeo.96.7.1567

Large RR, McGoldrick PJ (1998) Lithogeochemical halos and geochemical vectors to stratiform sediment hosted Zn–Pb–Ag deposits, 1. Lady Loretta Deposit, Queensland. J Geochemical Explor 63:37–56. https://doi.org/https://doi.org/10.1016/S0375-6742(98)00013-2

Large RR, McPhie J, Gemmell JB, et al (2001b) The Spectrum of Ore Deposit Types, Volcanic Environments, Alteration Halos, and Related Exploration Vectors in Submarine Volcanic Successions: Some Examples from Australia. Econ Geol 96:913–938. https://doi.org/10.2113/gsecongeo.96.5.913

Large RR, Mukherjee I, Gregory DD, et al (2017) Ocean and Atmosphere Geochemical Proxies Derived from Trace Elements in Marine Pyrite: Implications for Ore Genesis in Sedimentary Basins. Econ Geol 112:423–450. https://doi.org/10.2113/econgeo.112.2.423

Leach DL, Bradley DC, Huston D, et al (2010) Sediment-hosted lead-zinc deposits in earth history. Econ Geol 105:593–625. https://doi.org/10.2113/gsecongeo.105.3.593

Leach DL, Marsh E, Emsbo P, et al (2004) Nature of Hydrothermal Fluids at the Shale-Hosted Red Dog Zn-Pb-Ag Deposits, Brooks Range, Alaska. Econ Geol 99:1449–1480. https://doi.org/10.2113/gsecongeo.99.7.1449

Leach DL, Sangster DF, Kelley KD, et al (2005) Sediment-Hosted Lead-Zinc Deposits: A Global Perspective. One Hundredth Anniv. Vol. 0

Leelanandam C, Burke K, Ashwal LD, Webb SJ (2006) Proterozoic mountain building in

Peninsular India: an analysis based primarily on alkaline rock distribution. Geol Mag 143:195–212. https://doi.org/10.1017/S0016756805001664

Lei X-F, Romer RL, Glodny J, Jiang S-Y (2023) Geochemical significance of lithium and boron isotopic heterogeneity evolving during the crystallization of granitic melts. Geology 51:581–585. https://doi.org/10.1130/G50983.1

Leitch CHB, Lydon JW (2000) Fluid inclusion petrography and microthermometry of the Sullivan deposit and surrounding area. Geol Assoc Canada, Miner Depos Div 617–632

Li J, Chen Z, Zhou T, et al (2020) Genesis of the Xiyi Pb–Zn deposit, Yunnan Province, SW China: Evidence from trace element and fluid inclusion data. Ore Geol Rev 119:103348. https://doi.org/10.1016/j.oregeorev.2020.103348

Li L, Wing BA, Bui TH, et al (2016) Sulfur mass-independent fractionation in subsurface fracture waters indicates a long-standing sulfur cycle in Precambrian rocks. Nat Commun 7:. https://doi.org/10.1038/ncomms13252

Lockington JA, Cook NJ, Ciobanu CL (2014) Trace and minor elements in sphalerite from metamorphosed sulphide deposits. Mineral Petrol 108:873–890. https://doi.org/10.1007/s00710-014-0346-2

Lydon J (1983) Chemical parameters controlling the origin and deposition of sediment-hosted stratiform lead-zinc deposits. In: Sediment-hosted stratiform lead-zinc deposits, Short Course Handbook 8. Min Assoc Can Toronto, pp 175–250

Lydon J (2004a) Genetic models for Sullivan and other SEDEX deposits. In: Sediment Hosted LeadZinc Sulfide deposits. Narosa Publishing House, New Delhi, India, pp 149–190

Lydon J (2004b) Geology of the Belt-Purcell basin and the Sullivan deposit. In: Sediment Hosted LeadZinc Sulfide deposits. Narosa Publishing House, New Delhi, India, pp 100–148

Lynch G, Mengel F (1995) Metamorphism of arsenopyrite - pyrite - sphalerite - pyrrhotite lenses, western Cape Breton Island, Nova Scotia. Can Mineral 33:105–114

Lyons TW, Gellatly AM, McGoldrick PJ, Kah LC (2006) Proterozoic sedimentary exhalative (SEDEX) deposits and links to evolving global ocean chemistry. Mem Geol Soc Am 198:169–184. https://doi.org/10.1130/2006.1198(10)

M. HA (1953) The geology of central Rajputana. Mem Geol Soc Ind 79:

Machel HG (2001) Bacterial and thermochemical sulfate reduction in diagenetic settings - old and new insights. Sediment Geol 140:143–175. https://doi.org/10.1016/S0037-0738(00)00176-7

Machel HG, Krouse HR, Sassen R (1995) Products and distinguishing criteria of bacterial and

thermochemical sulfate reduction. Appl Geochemistry 10:373–389. https://doi.org/10.1016/0883-2927(95)00008-8

Maghfouri S, Hosseinzadeh MR, Lentz DR, et al (2021) Nature of ore-forming fluids in the Mehdiabad world-class sub-seafloor replacement SEDEX-type Zn-Pb-Ba-(Cu-Ag) deposit, Iran; constraints from geochemistry, fluid inclusions, and O-C-Sr isotopes. J Asian Earth Sci 207:104654. https://doi.org/https://doi.org/10.1016/j.jseaes.2020.104654

Maloney JS, Nabelek PI, Sirbescu M-LC, Halama R (2008) Lithium and its isotopes in tourmaline as indicators of the crystallization process in the San Diego County pegmatites, California, USA. Eur J Mineral 20:905–916. https://doi.org/10.1127/0935-1221/2008/0020-1823

Manning AH, Emsbo P (2018) Testing the potential role of brine reflux in the formation of sedimentary exhalative (sedex) ore deposits. Ore Geol Rev 102:862–874. https://doi.org/10.1016/j.oregeorev.2018.10.003

Marini L, Moretti R, Accornero M (2011) Sulfur Isotopes in Magmatic-Hydrothermal Systems, Melts, and Magmas. Rev Mineral Geochemistry 73:423–492. https://doi.org/10.2138/rmg.2011.73.14

Marks MAW, Marschall HR, Schühle P, et al (2013) Trace element systematics of tourmaline in pegmatitic and hydrothermal systems from the Variscan Schwarzwald (Germany): The importance of major element composition, sector zoning, and fluid or melt composition. Chem Geol 344:73–90. https://doi.org/10.1016/j.chemgeo.2013.02.025

Marschall HR, Jiang SY (2011) Tourmaline isotopes: No element left behind. Elements 7:313–319. https://doi.org/10.2113/gselements.7.5.313

Marshall B, Gilligan LB (1993) Remobilization, syn-tectonic processes and massive sulphide deposits. Ore Geol Rev 8:39–64. https://doi.org/https://doi.org/10.1016/0169-1368(93)90027-V

Marshall B, Vokes F, Larocque A (2000) Regional metamorphic remobilization: upgrading and formation of ore deposits. Rev Econ Geol 11:19–38

Marshall B, Vokes FM, Larocque ACL (1998) Regional Metamorphic Remobilization: Upgrading and Formation of Ore Deposits. In: Vokes FM, Marshall B, Spry PG (eds) Metamorphic and Metamorphogenic Ore Deposits. Society of Economic Geologists, p 0

Mavrogenes J, Frost R, Sparks HA (2013) Experimental evidence of sulfide melt evolution via immiscibility and fractional crystallization. Can Mineral 51:841–850. https://doi.org/10.3749/canmin.51.6.841

Mavrogenes JA, MacIntoshi IW, Ellis AD (2001) Partial melting of the broken hill galena-sphalerite ore: Experimental studies in the system PbS-FeS-ZnS-(Ag 2S). Econ Geol 96:205–210. https://doi.org/10.2113/gsecongeo.96.1.205

Medaris GL, FOURNELLE JH, HENRY DJ (2003) TOURMALINE-BEARING QUARTZ VEINS IN THE BARABOO QUARTZITE, WISCONSIN: OCCURRENCE AND SIGNIFICANCE OF FOITITE AND "OXY-FOITITE." Can Mineral 41:749–758. https://doi.org/10.2113/gscanmin.41.3.749

Mehdi M, Kumar S, Pant NC (2015) Low grade metamorphism in the Lalsot-Bayana sub-basin of the North Delhi Fold Belt and its tectonic implication. J Geol Soc India 85:397–410. https://doi.org/10.1007/s12594-015-0230-7

Meyer C, Wunder B, Meixner A, et al (2008) Boron-isotope fractionation between tourmaline and fluid: an experimental re-investigation. Contrib to Mineral Petrol 156:259–267. https://doi.org/10.1007/s00410-008-0285-1

Míková J, Košler J, Wiedenbeck M (2014) Matrix effects during laser ablation MC ICP-MS analysis of boron isotopes in tourmaline. J Anal At Spectrom 29:903–914. https://doi.org/10.1039/c3ja50241d

Mishra B, Mookherjee A (1988) Geothermometry based on fractionation of Mn and Cd between coexisting sphalerite and galena from some carbonate-hosted sulfide deposits in India. Miner Depos 23:179–185. https://doi.org/10.1007/BF00204298

Misra KC (2000a) Sediment-Hosted Massive Zinc-Lead Sulfide (SMS) Deposits BT - Understanding Mineral Deposits. In: Misra KC (ed). Springer Netherlands, Dordrecht, pp 497–538

Misra KC (2000b) Interpretation of Mineral Deposits — II BT - Understanding Mineral Deposits. In: Misra KC (ed). Springer Netherlands, Dordrecht, pp 148–237

Mladenova V, Valchev S (1998) Ga/Ge ratio in Sphalerite from the carbonate-hosted Semochilenitsi deposit as a temperature indication of initial fluids. Rev. Bulg. Geol. Soc. 59:49–54

Mukhopadhyay D, Bhattacharya T, Chattopadhyay N, et al (2000) Anasagar gneiss : A folded granitoid pluton in the proterozoic South Delhi Fold belt, central Rajasthan. Proc Indian Acad Sci Earth Planet Sci 109:21–37

Naha K, Roy AB (1983) The problem of the Precambrian basement in Rajasthan, western India. Precambrian Res 19:217–223. https://doi.org/https://doi.org/10.1016/0301-9268(83)90014-1

Naik A, Pant NC, Sharma JJ, et al (2022) Metamorphic evolution of the North Delhi Fold Belt, implications on Delhi orogeny and the Rodinia connection. Geol J 57:3496–3520. https://doi.org/https://doi.org/10.1002/gj.4458

Nurdiana A, Okamoto A, Yoshida K, et al (2021) Multi-stage infiltration of Na- and K-rich fluids from pegmatites at mid-crustal depths as revealed by feldspar replacement textures. Lithos 388–389:106096.

https://doi.org/https://doi.org/10.1016/j.lithos.2021.106096

Oduro H, Harms B, Sintim HO, et al (2011) Evidence of magnetic isotope effects during thermochemical sulfate reduction. Proc Natl Acad Sci 108:17635–17638. https://doi.org/10.1073/pnas.1108112108

Ohmoto, H., and Rye RO (1979) Isotopes of sulphur and carbon. In: Geochemistry of hydrothermal ore deposits, 2nd edn. John Wiley and Sons, Inc., New York, pp 509–567

Ono S, Kaufman AJ, Farquhar J, et al (2009) Lithofacies control on multiple-sulfur isotope records and Neoarchean sulfur cycles. Precambrian Res 169:58–67. https://doi.org/10.1016/j.precamres.2008.10.013

Ono S, Wing B, Johnston D, et al (2006) Mass-dependent fractionation of quadruple stable sulfur isotope system as a new tracer of sulfur biogeochemical cycles. Geochim Cosmochim Acta 70:2238–2252. https://doi.org/10.1016/j.gca.2006.01.022

Ota T, Kobayashi K, Katsura T, Nakamura E (2008) Tourmaline breakdown in a pelitic system: Implications for boron cycling through subduction zones. Contrib to Mineral Petrol 155:19–32. https://doi.org/10.1007/s00410-007-0228-2

Pal DC, Das E, Sasmal A, et al (2023) Role of evaporites in sodium metasomatism and formation of albite-rich rocks in IOCG provinces. Geochim Cosmochim Acta 361:210–227. https://doi.org/https://doi.org/10.1016/j.gca.2023.09.021

Palero-Fernández FJ, Martín-Izard A (2005) Trace element contents in galena and sphalerite from ore deposits of the Alcudia Valley mineral field (Eastern Sierra Morena, Spain). J Geochemical Explor 86:1–25. https://doi.org/10.1016/j.gexplo.2005.03.001

Palmer MR (1991) Boron isotope systematics of hydrothermal fluids and tourmalines: A synthesis. Chem Geol 94:111–121. https://doi.org/10.1016/S0009-2541(10)80023-3

Palmer MR, Slack JF (1989) Boron isotopic composition of tourmaline from massive sulfide deposits and tourmalinites. Contrib to Mineral Petrol 103:434–451. https://doi.org/10.1007/BF01041751

Pant NC, Kundu A, Joshi S (2008) Age of Metamorphism of Delhi Supergroup Rocks - Electron Microprobe Ages from Mahendragarh District, Haryana. Geol Soc India 72:

Philippot P, Ávila JN, Killingsworth BA, et al (2018) Globally asynchronous sulphur isotope signals require re-definition of the Great Oxidation Event. Nat Commun 9:2245. https://doi.org/10.1038/s41467-018-04621-x

Plimer IR (1987) Remobilization in high-grade metamorphic environments. Ore Geol Rev 2:231–245. https://doi.org/https://doi.org/10.1016/0169-1368(87)90030-8

Plimer IR, Lees TC (1988) Tourmaline-rich Rocks Associated with the Submarine Hydrothermal Rosebery Zn-Pb-Cu-Ag-Au Deposit and Granites in Western Tasmania,

Australia. Mineral Petrol 38:81–103. https://doi.org/10.1007/BF01164314

Polito PA, Kyser TK, Golding SD, Southgate PN (2006) Zinc deposits and related mineralization of the Burketown mineral field, including the world-class Century Deposit, Northern Australia: Fluid inclusion and stable isotope evidence for basin fluid sources. Econ Geol 101:1251–1273

Pruseth KL, Jehan N, Sahu P, Mishra B (2014) The possibility of a ZnS-bearing sulfide melt at 600°C: Evidence from the Rajpura-Dariba deposit, India, supported by laboratory melting experiment. Ore Geol Rev 60:50–59. https://doi.org/10.1016/j.oregeorev.2013.12.012

Putnis A (2009) Mineral Replacement Reactions. Rev Mineral Geochemistry 70:87–124. https://doi.org/10.2138/rmg.2009.70.3

Pyne TK, Bandopadhyay A (1985) Structure of Banded Gneissic Complex at and around Bandanwara, Ajmer district, Rajasthan. Indian J Earth Sci 12:9–20

Radhakrishna BP, Naqvi SM (1986) Precambrian continental crust of India and its evolution. J Geol 94:145–166. https://doi.org/10.1086/629020

Raith JG, Riemer Nina née S, Meisel T (2004) Boron metasomatism and behaviour of rare earth elements during formation of tourmaline rocks in the eastern Arunta Inlier, central Australia. Contrib to Mineral Petrol 147:91–109. https://doi.org/10.1007/s00410-003-0548-9

Roda-Robles E, Pesquera-Pérez A, Simmons WB, et al (2019) Evidence for internal fractionation from Li isotopes in tourmaline and mica in the Berry-Havey rare-element pegmatite (Maine, USA). Can Mineral 57:779–782. https://doi.org/10.3749/canmin.AB00020

Roy AB, Kröner A (1996) Single zircon evaporation ages constraining the growth of the Archaean Aravalli craton, northwestern Indian shield. Geol Mag 133:333–342. https://doi.org/DOI: 10.1017/S0016756800009067

Sangster DF (2018) Toward an integrated genetic model for vent-distal SEDEX deposits. Miner Depos 53:509–527. https://doi.org/10.1007/s00126-017-0755-3

Sangster DF (2002) The role of dense brines in the formation of vent-distal sedimentary-exhalative (SEDEX) lead–zinc deposits: field and laboratory evidence. Miner Depos 37:149–157. https://doi.org/10.1007/s00126-001-0216-9

Sangster DF, Hillary EM (1998) Sedex lead-zinc deposits; proposed sub-types and their characteristics. Explor Min Geol 7:341–357

Sarkar SC, Banerjee S (2004) Carbonate-hosted Lead-Zinc deposits of Zawar, Rajasthan, in the context of the world scenario. In: Deb M, Goodfellow WD (eds) Sediment-hosted

Lead-Zinc Sulfide Deposits. Narosa Publishing House, Delhi, pp 328–349

Sarkar SC, Bhattacharyya PK, Mukherjee AD (1980) Evolution of the sulfide ores of Saladipura, Rajasthan, India. Econ Geol 75:1152–1167. https://doi.org/10.2113/gsecongeo.75.8.1152

Sarkar SC, Dasgupta S (1980) Geologic setting, genesis and transformation of sulfide deposits in the northern part of Khetri copper belt, Rajasthan, India — an outline. Miner Depos 15:117–137. https://doi.org/10.1007/BF00206508

Sarkar SC, Gupta A (2012) Crustal Evolution and Metallogeny in India. Cambridge University Press

Scott SD, Barnes HL (1971) Sphalerite geothermometry and geobarometry. Econ Geol 66:653–669. https://doi.org/10.2113/gsecongeo.66.4.653

Seal RR (2006) Sulfur isotope geochemistry of sulfide minerals. Rev Mineral Geochemistry 61:633–677. https://doi.org/10.2138/rmg.2006.61.12

Seal RR, Alpers CN, Rye RO (2000) Stable Isotope Systematics of Sulfate Minerals. Rev Mineral Geochemistry 40:541–602. https://doi.org/10.2138/rmg.2000.40.12

Shah N (2004) Rampura-Agucha, a remobilized SEDEX Deposit, southeastern Rajasthan, India. In: Deb M, Goodfellow WD (eds) Sediment-hosted lead-zinc sulfide deposits. Narosa Publishing House, Delhi, pp 290–303

Shalaby IM, Stumpfl E, Helmy HM, et al (2004) Silver and silver-bearing minerals at the Um Samiuki volcanogenic massive sulphide deposit, Eastern Desert, Egypt. Miner Depos 39:608–621. https://doi.org/10.1007/s00126-004-0427-y

Sharp ZD (2007) Terminology, Standards and Mass Spectrometry. In: Princiles of Stable Isotope Geochemistry. Pearson Education, Inc.

Simanenko LF (2007) Modes of trace element occurrence in galena from the Partizansky base metal-skarn deposit, Primorye. Russ J Pacific Geol 1:144–152. https://doi.org/10.1134/S1819714007020042

Singer DA (1995) World class base and precious metal deposits; a quantitative analysis. Econ Geol 90:88–104. https://doi.org/10.2113/gsecongeo.90.1.88

Sinha-Roy S (1985) Granite-greenstone sequence and geotectonic development of SE Rajasthan. Bull Geol Min Metall Soc India 53:115–123

Sinha-Roy S, Mohanty M, Guha DB (1993) Banas dislocation zone in Nathdwara—Khamnor area, Udaipur District, Rajasthan, and its significance on the basement—cover relations in the Aravalli fold belt. Curr Sci 65:68–72

Slack JF (2004) Multistage Hydrothermal Silicification and Fe-Tl-As-Sb-Ge-REE Enrichment

in the Red Dog Zn-Pb-Ag District , Northern Alaska : Geochemistry , Origin , and Exploration Applications. 99:1451–1508

Slack JF, Palmer MR, Stevens BPJ, Barnes RG (1993) Origin and significance of tourmaline-rich rocks in the Broken Hill district, Australia. Econ Geol 88:505–541. https://doi.org/10.2113/gsecongeo.88.3.505

Slack JF, Trumbull RB (2011) Tourmaline as a recorder of ore-forming processes. Elements 7:321–326. https://doi.org/10.2113/gselements.7.5.321

Srikantappa C (2001) Composition and source of deep-crustal fluids and their role in the evolution of charnockitic granulites of southern India. Geol Surv of India Spl. Pub 5:15–30

Stevens G, Prinz S, Rozendaal A (2005) Partial melting of the assemblage sphalerite + galena + pyrrhotite + chalcopyrite + sulfur implications for high-grade metamorphosed massive sulfide deposits. Econ Geol 100:781–786. https://doi.org/10.2113/gsecongeo.100.4.781

Stoiber RE (1940) Minor elements in sphalerite. Econ Geol 35:501–519. https://doi.org/10.2113/gsecongeo.35.4.501

Taylor BE, Palmer MR, Slack JF (1999) Mineralizing Fluids in the Kidd Creek Massive Sulfide Deposit, Ontario: Evidence from Oxygen, Hydrogen, and Boron Isotopes in Tourmaline*. Giant Kidd Creek Volcanogenic Massive Sulfide Depos. West. Abitibi Subprov. Canada 10:0

Taylor RP, Ikingura JR, Fallick AE, et al (1992) Stable isotope compositions of tourmalines from granites and related hydrothermal rocks of the Karagwe-Ankolean belt, northwest Tanzania. Chem Geol Isot Geosci Sect 94:215–227. https://doi.org/https://doi.org/10.1016/0168-9622(92)90014-2

Tomkins AG (2007) Three mechanisms of ore re-mobilisation during amphibolite facies metamorphism at the Montauban Zn-Pb-Au-Ag deposit. Miner Depos 42:627–637. https://doi.org/10.1007/s00126-007-0131-9

Tomkins AG, Mavrogenes JA (2001) Redistribution of Gold within Arsenopyrite and Löllingite during Pro- and Retrograde Metamorphism: Application to Timing of Mineralization. Econ Geol 96:525–534. https://doi.org/10.2113/gsecongeo.96.3.525

Tomkins AG, Pattison DRM, Frost BR (2007) On the initiation of metamorphic sulfide anatexis. J Petrol 48:511–535. https://doi.org/10.1093/petrology/egl070

Tonarini S, D'Antonio M, Di Vito MA, et al (2009) Geochemical and B–Sr–Nd isotopic evidence for mingling and mixing processes in the magmatic system that fed the Astroni volcano (4.1–3.8 ka) within the Campi Flegrei caldera (southern Italy). Lithos 107:135–151. https://doi.org/https://doi.org/10.1016/j.lithos.2008.09.012

Torres-Ruiz J, Pesquera A, Gil-Crespo PP, Velilla N (2003) Origin and petrogenetic implications of tourmaline-rich rocks in the Sierra Nevada (Betic Cordillera, southeastern Spain). Chem Geol 197:55–86. https://doi.org/10.1016/S0009-2541(02)00357-1

Tostevin R, Turchyn A V., Farquhar J, et al (2014) Multiple sulfur isotope constraints on the modern sulfur cycle. Earth Planet Sci Lett 396:14–21. https://doi.org/10.1016/j.epsl.2014.03.057

Trauth M, Yuen P Lecture Notes in Earth System Sciences

Trumbull RB, Codeço MS, Jiang SY, et al (2020) Boron isotope variations in tourmaline from hydrothermal ore deposits: A review of controlling factors and insights for mineralizing systems. Ore Geol Rev 125:103682. https://doi.org/10.1016/j.oregeorev.2020.103682

Trumbull RB, Slack JF (2018) Boron isotopes in the continental crust: granites, pegmatites, felsic volcanic rocks, and related ore deposits. Adv Isot Geochemistry 249–272. https://doi.org/10.1007/978-3-319-64666-4_10

Turner RJW (1992) Formation of Phanerozoic stratiform sediment-hosted zinc-lead deposits: Evidence for the critical role of ocean anoxia. Chem Geol 99:165–188. https://doi.org/https://doi.org/10.1016/0009-2541(92)90037-6

Ueno Y, Ono S, Rumble D, Maruyama S (2008) Quadruple sulfur isotope analysis of ca. 3.5 Ga Dresser Formation: New evidence for microbial sulfate reduction in the early Archean. Geochim Cosmochim Acta 72:5675–5691. https://doi.org/10.1016/j.gca.2008.08.026

Van Hinsberg VJ, Henry DJ, Marschall HR (2011) Tourmaline: An ideal indicator of its host environment. Can Mineral 49:1–16. https://doi.org/10.3749/canmin.49.1.1

Van Hook HJ (1960) The ternary system Ag2S-Bi2S3 -PbS. Econ Geol 55:759–788. https://doi.org/10.2113/gsecongeo.55.4.759

Verma PK, Greiling RO (1995) Tectonic evolution of the Aravalli orogen ( NW India ): an inverted Proterozoic rift basin ? Int J Earth Sci 84:683–696

Vokes FM (1969) A review of the metamorphism of sulphide deposits. Earth Sci Rev 5:99–143. https://doi.org/10.1016/0012-8252(69)90080-4

Wagner T, Cook NJ (1999) Sphalerite remobilization during multistage hydrothermal mineralization events - Examples from siderite-Pb-Zn-Cu-Sb veins, Rheinisches Schiefergebirge, Germany. Mineral Petrol 63:223–241. https://doi.org/10.1007/bf01164152

Watanabe Y, Farquhar J, Ohmoto H (2009) Anomalous Fractionations of Sulfur Sulfate Reduction. Science (80- ) 324:370–373

Watari T, Nansai K, Nakajima K (2020) Review of critical metal dynamics to 2050 for 48 elements. Resour Conserv Recycl 155:104669. https://doi.org/https://doi.org/10.1016/j.resconrec.2019.104669

Wiedenbeck M, Goswami JN, Roy AB (1996) Stabilization of the Aravalli Craton of northwestern India at 2.5 Ga: An ion microprobe zircon study. Chem Geol 129:325–340. https://doi.org/https://doi.org/10.1016/0009-2541(95)00182-4

Wilkinson JJ (2014) Sediment-Hosted Zinc – Lead Mineralization : Processes and Perspectives

Worden RH, Smalley PC, Oxtoby NH (1996) The effects of thermochemical sulfate reduction upon formation water salinity and oxygen isotopes in carbonate gas reservoirs. Geochim Cosmochim Acta 60:3925–3931. https://doi.org/https://doi.org/10.1016/0016-7037(96)00216-5

Wu C-M, Chen H-X (2015) Revised Ti-in-biotite geothermometer for ilmenite- or rutile-bearing crustal metapelites. Sci Bull 60:116–121. https://doi.org/10.1007/s11434-014-0674-y

Wykes JL, Mavrogenes JA (2005) Hydrous sulfide melting: Experimental evidence for the solubility of H 2O in sulfide melts. Econ Geol 100:157–164. https://doi.org/10.2113/100.1.0157

Xiang L, Romer RL, Glodny J, et al (2020) Li and B isotopic fractionation at the magmatic-hydrothermal transition of highly evolved granites. Lithos 376–377:105753. https://doi.org/https://doi.org/10.1016/j.lithos.2020.105753

Xie G, Mao J, Li W, et al (2019) Granite-related Yangjiashan tungsten deposit, southern China. Miner Depos 54:67–80. https://doi.org/10.1007/s00126-018-0805-5

Yang SY, Jiang SY, Zhao KD, et al (2015) Tourmaline as a recorder of magmatic–hydrothermal evolution: an in situ major and trace element analysis of tourmaline from the Qitianling batholith, South China. Contrib to Mineral Petrol 170:1–21. https://doi.org/10.1007/s00410-015-1195-7

Ye L, Cook NJ, Ciobanu CL, et al (2011) Trace and minor elements in sphalerite from base metal deposits in South China: A LA-ICPMS study. Ore Geol Rev 39:188–217. https://doi.org/10.1016/j.oregeorev.2011.03.001

Young SA, Loukola-Ruskeeniemi K, Pratt LM (2013) Reactions of hydrothermal solutions with organic matter in Paleoproterozoic black shales at Talvivaara, Finland: Evidence from multiple sulfur isotopes. Earth Planet Sci Lett 367:1–14. https://doi.org/10.1016/j.epsl.2013.02.004

Zall F, Tahmasbi Z, Jiang S-Y, et al (2019) Elemental and B-O-H isotopic compositions of tourmaline and associated minerals in biotite-muscovite granite of Mashhad, NE Iran:

Constraints on tourmaline genesis and element partitioning. Lithos 324–325:803–820. https://doi.org/https://doi.org/10.1016/j.lithos.2018.12.012

Zhao Z, Yang X, Zhang T, et al (2022) Geochemical characteristics and boron isotopes of tourmaline from the Baishaziling tin deposit, Nanling Range: Constraints on magmatic-hydrothermal processes. Ore Geol Rev 142:104695. https://doi.org/https://doi.org/10.1016/j.oregeorev.2022.104695

Zhou L, Zeng Q, Liu J, et al (2020) Tracing mineralization history from the compositional textures of sulfide association: A case study of the Zhenzigou stratiform Zn-Pb deposit, NE China. Ore Geol Rev 126:103792. https://doi.org/10.1016/j.oregeorev.2020.103792

# LIST OF PUBLICATIONS

## In Preparation:

**Das, E.**, Pal, D.C.*, Fu, B., Upadhyay, D., Absar, N. Fingerprinting role of multiple fluid sources in formation and remobilization of ores: constraints from multiple sulfur isotopes and boron isotopes of tourmaline.

## Published:

**Das, E.**, Pal, D.C.*, Upadhyay, D., Tripathi, A., Kashyap, V., Meena, K. Sulfide remobilization in the metamorphosed Kayad sedimentary exhalative Zn-Pb deposit, western India: evidence from mode of occurrence, texture, hydrothermal alteration features, and trace element chemistry, *Economic Geology*, 2024, Vol. 119(4), pg. 885-905.

## Related Published Works:

Pal, D.C.*, **Das, E.**, Sasmal, A., Adak, S., Abhinay, K. Role of evaporates in sodium metasomatism and formation of albite-rich rocks in IOCG provinces, *Geochimica Cosmochimica Acta (GCA),* Vol. 361, pg. 210-227.

Baidya, A.S. *, **Das, E.** (2021). "Calculating biotite formula from electron microprobe analysis data using a machine learning method based on principal components regression" by Li et al. (Lithos 356–357 (2020) 105371) - A discussion, *Lithos,* Vol. 412-413.

## Conference Abstracts:

**Das, E.***, Pal, D.C. "Mechanism of Sedex Mineralization and Sulfide Remobilization integrating Textures, Geochemistry, S and B stable Isotopes—Case Study from Kayad Zn-Pb Deposit, Western India" *Japan Geosciences Union (JpGU),* 2024.

**Das, E.***, Pal, D.C., Fu, B. "Hydrothermal alteration and multiple sulfur isotope chemistry of Kayad Zn-Pb deposit, Ajmer, Rajasthan, western India: Implications for ore genesis" *European Geosciences Union (EGU),* 2022.

**Das, E.***, Pal, D.C., De, S. "Trace Element Composition of Sulfides from Kayad Zn-Pb deposit, Ajmer, Western India: Implications for Ore Mineralization" *American Geophysical Union (AGU),* 2020.

# APPENDIX

**Table 1:** Major element chemistry of silicates associated with the three sulfide mineralization types and secondary alteration.

| | Mineral | EPMA Point | Sample | $Na_2O$ | F | MgO | $Al_2O_3$ | $K_2O$ | CaO | $TiO_2$ | $Cr_2O_3$ | MnO | $SiO_2$ | FeO | Cl | $P_2O_5$ | Total |
|---|---|---|---|---|---|---|---|---|---|---|---|---|---|---|---|---|---|
| **Disseminated/ Laminated** | Feldspar | 4 / 1 . | D24-2 | 7.95 | bdl | bdl | 24.49 | 0.13 | 6.36 | bdl | bdl | bdl | 61.53 | bdl | bdl | bdl | 100.60 |
| | | 33 / 1 . | ML19A | 7.21 | bdl | bdl | 25.02 | 0.17 | 7.75 | bdl | bdl | bdl | 58.73 | bdl | bdl | bdl | 98.93 |
| | | 40 / 1 . | ML19A | 0.85 | bdl | bdl | 17.52 | 15.51 | bdl | bdl | bdl | bdl | 63.85 | bdl | bdl | 0.04 | 97.85 |
| | Muscovite | 9 / 1 . | D24-2 | 0.39 | bdl | 1.11 | 33.48 | 10.77 | bdl | 1.51 | bdl | bdl | 46.39 | bdl | bdl | bdl | 94.72 |
| | | 32 / 1 . | ML19A | 0.32 | bdl | 1.31 | 32.73 | 10.78 | bdl | 1.66 | 0.14 | bdl | 46.73 | 1.02 | bdl | bdl | 94.70 |
| | | 35 / 1 . | ML19A | 0.34 | bdl | 1.36 | 30.01 | 8.66 | bdl | 1.24 | bdl | bdl | 42.40 | 9.06 | bdl | bdl | 93.27 |
| | | 39 / 1 . | ML19A | 0.37 | bdl | 1.45 | 32.07 | 10.93 | bdl | 1.62 | bdl | bdl | 46.27 | 1.04 | bdl | bdl | 93.82 |
| | Apatite | 1 / 1 . | D24-2 | 0.06 | 3.87 | bdl | bdl | bdl | 54.66 | bdl | bdl | bdl | 0.04 | bdl | 0.07 | 40.32 | 99.17 |
| **Massive** | Feldspar | 47 / 1 . | ML10H | 5.96 | bdl | bdl | 26.43 | 0.15 | 9.73 | bdl | bdl | 0.11 | 55.73 | bdl | bdl | bdl | 98.25 |
| | | 35 / 1 . | D4 | 8.93 | bdl | bdl | 22.78 | 0.09 | 4.29 | bdl | bdl | bdl | 62.96 | bdl | bdl | 0.06 | 99.28 |
| | | 38 / 1 . | D4 | 0.90 | bdl | bdl | 18.13 | 14.68 | bdl | bdl | bdl | bdl | 64.25 | bdl | bdl | bdl | 98.07 |
| | | 56 / 1 . | D4 | 7.99 | bdl | bdl | 24.00 | 0.17 | 5.92 | bdl | bdl | bdl | 60.75 | bdl | bdl | bdl | 98.95 |
| | | 57 / 1 . | D4 | 8.64 | bdl | bdl | 22.97 | 0.11 | 4.72 | bdl | bdl | bdl | 62.64 | bdl | bdl | bdl | 99.15 |
| | | 58 / 1 . | D4 | 8.54 | bdl | 0.03 | 23.30 | 0.19 | 4.68 | bdl | bdl | bdl | 62.54 | bdl | bdl | 0.05 | 99.38 |
| | | 85 / 1 . | D4 | 9.77 | bdl | bdl | 21.90 | 0.17 | 3.73 | bdl | 0.08 | 0.01 | 64.11 | bdl | bdl | bdl | 99.80 |
| | | 86 / 1 . | D4 | 8.29 | bdl | bdl | 24.53 | 0.08 | 6.26 | bdl | bdl | 0.06 | 60.54 | bdl | bdl | 0.05 | 99.81 |
| | | 87 / 1 . | D4 | 9.58 | bdl | bdl | 23.09 | 0.14 | 4.49 | bdl | bdl | 0.01 | 63.36 | bdl | bdl | 0.01 | 100.68 |
| | | 7 / 1 . | ML 10I | 10.50 | bdl | bdl | 19.95 | 0.07 | 0.35 | bdl | bdl | bdl | 64.64 | 0.31 | 0.02 | 0.02 | 95.861 |
| | | 8 / 1 . | ML 10I | 0.45 | 0.03 | bdl | 17.86 | 15.37 | bdl | bdl | 0.10 | bdl | 64.96 | 0.04 | bdl | 0.06 | 98.9705 |
| | | 9 / 1 . | ML 10I | 1.88 | bdl | bdl | 32.10 | 0.03 | 17.65 | bdl | bdl | bdl | 46.70 | bdl | 0.01 | 0.01 | 98.3641 |
| | | 10 / 1 . | ML 10I | 7.08 | bdl | bdl | 25.88 | 0.19 | 8.82 | bdl | 0.10 | bdl | 56.97 | bdl | bdl | 0.04 | 99.0803 |
| | | 11 / 1 . | ML 10I | 5.06 | 0.03 | bdl | 28.07 | 0.10 | 12.22 | bdl | 0.01 | bdl | 52.30 | bdl | bdl | 0.04 | 97.8218 |
| | | 12 / 1 . | ML 10I | 0.83 | 0.09 | bdl | 17.88 | 14.94 | bdl | 0.01 | bdl | bdl | 64.77 | bdl | 0.02 | 0.02 | 98.7812 |
| | | 19 / 1 . | ML 10I | 12.17 | bdl | bdl | 18.42 | 0.07 | 0.08 | bdl | bdl | bdl | 68.26 | bdl | bdl | 0.02 | 99.0229 |
| | | 20 / 1 . | ML 10I | 4.29 | 0.14 | bdl | 29.76 | 0.10 | 13.21 | bdl | 0.01 | bdl | 52.12 | 0.03 | bdl | bdl | 99.6547 |

| | Mineral | EPMA Point | Sample | $Na_2O$ | F | MgO | $Al_2O_3$ | $K_2O$ | CaO | $TiO_2$ | $Cr_2O_3$ | MnO | $SiO_2$ | FeO | Cl | $P_2O_5$ | Total |
|---|---|---|---|---|---|---|---|---|---|---|---|---|---|---|---|---|---|
| **Massive** | Muscovite | 48 / 1 . | ML10H | 0.26 | bdl | 1.51 | 32.55 | 10.77 | bdl | 1.61 | bdl | bdl | 48.13 | 0.90 | bdl | bdl | 95.86 |
| | | 49 / 1 . | ML10H | 0.27 | bdl | 1.26 | 32.83 | 10.89 | bdl | 1.71 | bdl | bdl | 46.37 | 0.93 | bdl | bdl | 94.34 |
| | | 51 / 1 . | ML10H | 0.37 | bdl | 1.33 | 33.03 | 10.69 | bdl | 1.69 | bdl | bdl | 47.17 | 1.02 | bdl | bdl | 95.38 |
| | | 33 / 1 . | D4 | 0.43 | bdl | 1.17 | 33.05 | 10.33 | bdl | 1.33 | bdl | bdl | 46.31 | 1.59 | bdl | bdl | 94.26 |
| | | 34 / 1 . | D4 | 0.40 | bdl | 1.24 | 32.74 | 10.37 | bdl | 1.68 | bdl | bdl | 46.79 | 1.41 | bdl | bdl | 94.76 |
| | Allanite | 44 / 1 . | ML10H | 0.10 | bdl | 0.38 | 15.51 | bdl | 14.12 | 0.10 | bdl | 0.43 | 31.36 | 6.65 | 0.05 | bdl | 68.69 |
| | | 45 / 1 . | ML10H | 0.35 | bdl | 0.12 | 14.31 | 0.13 | 8.80 | 0.23 | bdl | 0.30 | 32.59 | 7.90 | 0.31 | 0.10 | 65.13 |
| | | 54 / 1 . | ML10I | bdl | bdl | 1.44 | 18.87 | bdl | 13.31 | 0.08 | bdl | bdl | 31.74 | 8.30 | 0.03 | bdl | 73.95 |
| | | 16 / 1 . | ML 10I | 0.13 | 0.76 | 0.17 | 16.05 | 0.09 | 11.77 | 0.21 | 0.14 | 0.46 | 33.39 | 4.65 | 0.06 | 0.13 | 68.2365 |
| | Apatite | 41 / 1 . | ML10H | bdl | 3.58 | bdl | bdl | bdl | 55.93 | bdl | bdl | bdl | bdl | bdl | 0.14 | 42.25 | 102.09 |
| | | 55 / 1 . | ML10I | bdl | 3.77 | bdl | bdl | 0.03 | 55.66 | bdl | bdl | bdl | 0.04 | bdl | 0.06 | 42.58 | 102.15 |
| | | 56 / 1 . | ML10I | bdl | 3.71 | bdl | bdl | bdl | 55.57 | bdl | bdl | bdl | 0.09 | bdl | 0.06 | 42.17 | 101.64 |
| | | 63 / 1 . | ML10I | bdl | 3.94 | bdl | bdl | bdl | 56.13 | bdl | bdl | bdl | 0.05 | bdl | bdl | 42.54 | 102.80 |
| | | 18 / 1 . | ML 10I | 0.04 | 7.40 | bdl | bdl | 0.07 | 54.97 | 0.04 | 0.07 | bdl | bdl | 0.11 | 0.09 | 40.77 | 103.6292 |
| | Monazite | 42 / 1 . | ML10H | bdl | 2.09 | bdl | bdl | bdl | 0.95 | bdl | bdl | bdl | 0.61 | bdl | bdl | 27.67 | 31.33 |
| | Clinozoiste | 17 / 1 . | ML 10I | bdl | 0.09 | bdl | 28.91 | 0.03 | 24.13 | 0.16 | 0.06 | 0.04 | 38.20 | 4.07 | bdl | 0.02 | 95.7762 |
| **Vein Hosted** | Feldspar | 19 / 1 . | ML19C | 0.78 | bdl | bdl | 18.25 | 15.20 | bdl | bdl | bdl | bdl | 64.91 | bdl | bdl | 0.04 | 99.23 |
| | | 20 / 1 . | ML19C | 6.41 | bdl | bdl | 26.47 | 0.13 | 9.13 | bdl | bdl | bdl | 57.04 | bdl | bdl | 0.05 | 99.27 |
| | | 21 / 1 . | ML19C | 1.00 | bdl | bdl | 18.34 | 14.95 | 0.01 | bdl | bdl | bdl | 64.86 | bdl | bdl | bdl | 99.20 |
| | | 22 / 1 . | ML19C | 6.32 | bdl | bdl | 26.26 | 0.12 | 9.21 | bdl | bdl | bdl | 57.30 | bdl | bdl | bdl | 99.23 |
| | | 23 / 1 . | ML 19C | 11.36 | bdl | 0.01 | 19.33 | 0.01 | 1.50 | bdl | 0.09 | 0.01 | 66.49 | bdl | bdl | 0.01 | 98.81 |
| | | 24 / 1 . | ML 19C | 0.01 | 0.03 | 0.03 | 17.43 | 15.69 | 0.02 | 0.01 | 0.04 | bdl | 65.22 | 0.28 | bdl | 0.06 | 98.88 |
| | | 25 / 1 . | ML 19C | 7.95 | bdl | 0.04 | 24.40 | 0.03 | 7.17 | 0.09 | 0.07 | bdl | 58.54 | 0.24 | 0.14 | 0.02 | 98.71 |
| | | 27 / 1 . | ML 19C | 11.65 | bdl | 0.03 | 19.64 | bdl | 1.26 | bdl | 0.15 | bdl | 67.33 | 0.13 | bdl | 0.02 | 100.43 |
| | | 28 / 1 . | ML 19C | 6.93 | bdl | bdl | 25.74 | 0.06 | 8.75 | bdl | 0.07 | bdl | 56.66 | 0.04 | bdl | 0.08 | 98.34 |
| | | 30 / 1 . | ML 19C | 6.50 | 0.29 | bdl | 26.02 | 0.06 | 9.27 | bdl | 0.09 | bdl | 56.08 | 0.11 | bdl | 0.09 | 98.56 |
| | | 32 / 1 . | ML 19C | 6.35 | bdl | 0.01 | 26.42 | 0.09 | 9.91 | bdl | 0.06 | bdl | 55.83 | 0.03 | bdl | 0.04 | 98.79 |
| | | 34 / 1 . | ML 19C | 11.23 | bdl | 0.01 | 19.60 | 0.02 | 1.48 | bdl | 0.07 | bdl | 66.66 | bdl | 0.02 | 0.05 | 99.39 |

| | Mineral | EPMA Point | Sample | $Na_2O$ | F | MgO | $Al_2O_3$ | $K_2O$ | CaO | $TiO_2$ | $Cr_2O_3$ | MnO | $SiO_2$ | FeO | Cl | $P_2O_5$ | Total |
|---|---|---|---|---|---|---|---|---|---|---|---|---|---|---|---|---|---|
| **Vein** | Feldspar | 36 / 1 . | ML 19C | 11.16 | bdl | 0.01 | 20.07 | bdl | 2.03 | bdl | 0.04 | bdl | 65.75 | 0.04 | bdl | 0.04 | 99.33 |
| **Hosted** | | 37 / 1 . | ML 19C | 0.69 | bdl | 0.01 | 17.88 | 14.71 | 0.03 | 0.02 | 0.07 | bdl | 64.25 | bdl | bdl | bdl | 98.05 |
| | | 39 / 1 . | ML 19C | 0.88 | bdl | 0.01 | 17.75 | 14.22 | bdl | bdl | 0.06 | bdl | 64.82 | bdl | bdl | 0.08 | 98.16 |
| | | 40 / 1 . | ML 19C | 1.52 | bdl | 0.02 | 17.51 | 14.90 | 0.13 | bdl | 0.13 | bdl | 64.67 | bdl | bdl | bdl | 98.94 |
| | | 42 / 1 . | ML 19C | 6.42 | bdl | 0.02 | 26.21 | 0.06 | 9.52 | bdl | 0.09 | bdl | 56.24 | bdl | bdl | 0.04 | 98.62 |
| | | 47 / 1 . | ML 19C | 1.44 | 0.12 | 0.02 | 17.41 | 14.13 | bdl | bdl | 0.13 | bdl | 64.29 | bdl | bdl | 0.01 | 97.98 |
| | | 48 / 1 . | ML 19C | 0.66 | 0.21 | 0.02 | 17.53 | 14.27 | 0.02 | bdl | bdl | bdl | 64.01 | 0.01 | bdl | 0.02 | 97.17 |
| | | 49 / 1 . | ML 19C | 6.98 | 0.12 | 0.03 | 25.73 | 0.02 | 8.99 | bdl | 0.13 | bdl | 56.54 | 0.05 | bdl | 0.10 | 98.76 |
| | | 75 / 1 . | ST3 | 0.78 | bdl | bdl | 17.84 | 15.65 | bdl | bdl | bdl | bdl | 64.46 | bdl | bdl | 0.07 | 98.82 |
| | | 76 / 1 . | ST3 | 10.05 | bdl | bdl | 21.33 | 0.07 | 2.58 | bdl | bdl | bdl | 65.29 | bdl | bdl | 0.08 | 99.47 |
| | | 77 / 1 . | ST3 | 10.13 | bdl | bdl | 21.25 | 0.14 | 2.71 | bdl | bdl | bdl | 65.75 | bdl | bdl | 0.08 | 100.10 |
| | | 79 / 1 . | ST3 | 9.81 | bdl | bdl | 20.96 | 0.38 | 2.42 | bdl | bdl | bdl | 66.17 | bdl | bdl | bdl | 99.80 |
| | | 80 / 1 . | ST3 | 9.96 | bdl | bdl | 20.99 | 0.24 | 2.55 | bdl | bdl | bdl | 65.95 | bdl | bdl | 0.05 | 99.86 |
| | | 31 / 1 . | ST 3 | 0.18 | 0.03 | 0.01 | 17.98 | 14.96 | 0.16 | 0.06 | bdl | 0.01 | 65.66 | 0.11 | bdl | 0.02 | 99.27 |
| | | 33 / 1 . | ST 3 | 0.73 | bdl | bdl | 17.89 | 14.51 | 0.06 | 0.02 | bdl | 0.04 | 65.25 | 0.08 | bdl | bdl | 98.65 |
| | | 34 / 1 . | ST 3 | 10.18 | 0.20 | 0.01 | 20.64 | 0.11 | 2.92 | bdl | 0.03 | bdl | 64.15 | 0.03 | bdl | bdl | 98.25 |
| | | 36 / 1 . | ST 3 | 0.54 | bdl | bdl | 17.54 | 15.06 | 0.06 | 0.01 | bdl | bdl | 64.44 | 0.12 | bdl | 0.07 | 97.97 |
| | | 44 / 1 . | ST 3 | 0.38 | 0.37 | 0.02 | 17.44 | 14.69 | 0.02 | 0.02 | 0.15 | bdl | 64.66 | 0.11 | bdl | bdl | 97.91 |
| | | 46 / 1 . | ST 3 | 12.17 | bdl | bdl | 18.20 | 0.03 | 0.08 | bdl | 0.02 | 0.07 | 67.51 | 0.15 | bdl | bdl | 98.22 |
| | | 51 / 1 . | ST 3 | 0.43 | bdl | bdl | 17.58 | 14.62 | bdl | bdl | 0.10 | bdl | 64.42 | 0.11 | bdl | bdl | 97.32 |
| | | 52 / 1 . | ST 3 | 11.19 | 0.03 | bdl | 19.59 | 0.01 | 1.38 | bdl | 0.12 | 0.01 | 65.50 | bdl | bdl | bdl | 97.84 |
| | | 93 / 1 . | ML5-2D | 0.71 | bdl | bdl | 16.50 | 0.48 | 8.16 | bdl | bdl | bdl | 61.40 | bdl | bdl | bdl | 87.55 |
| | | 94 / 1 . | ML5-2D | 0.91 | bdl | bdl | 17.70 | 15.23 | bdl | bdl | bdl | bdl | 64.16 | bdl | bdl | bdl | 98.19 |
| | | 95 / 1 . | ML5-2D | 0.45 | bdl | bdl | 15.16 | 0.18 | 7.96 | bdl | bdl | bdl | 59.79 | bdl | bdl | bdl | 83.60 |
| | | 97 / 1 . | ML5-2D | 0.53 | bdl | bdl | 15.85 | 0.13 | 8.02 | bdl | bdl | bdl | 59.26 | bdl | bdl | 0.05 | 83.90 |
| | | 99 / 1 . | ML5-2D | 0.19 | bdl | bdl | 0.48 | 4.50 | 24.36 | bdl | bdl | bdl | 53.22 | 0.34 | bdl | bdl | 83.13 |
| | | 4 / 1 . | KYD14 | 0.06 | bdl | 0.59 | 35.22 | 10.87 | bdl | bdl | bdl | bdl | 48.13 | 0.55 | bdl | bdl | 95.59 |

| | Mineral | EPMA Point | Sample | $Na_2O$ | F | MgO | $Al_2O_3$ | $K_2O$ | CaO | $TiO_2$ | $Cr_2O_3$ | MnO | $SiO_2$ | FeO | Cl | $P_2O_5$ | Total |
|---|---|---|---|---|---|---|---|---|---|---|---|---|---|---|---|---|---|
| **Vein** | Feldspar | 16 / 1 . | ML 5(1)A | 10.62 | 0.06 | bdl | 20.02 | 0.09 | 1.30 | bdl | 0.09 | bdl | 67.11 | 0.04 | bdl | bdl | 99.34 |
| **Hosted** | | 23 / 1 . | ML 5(1)A | 0.56 | bdl | 0.01 | 17.66 | 14.49 | bdl | 0.02 | 0.04 | bdl | 64.91 | 0.03 | bdl | 0.01 | 97.85 |
| | | 24 / 1 . | ML 5(1)A | 10.75 | 0.11 | bdl | 20.04 | 0.05 | 1.93 | bdl | 0.03 | bdl | 67.22 | 0.04 | bdl | bdl | 100.17 |
| | | 25 / 1 . | ML 5(1)A | 0.39 | 0.21 | 0.03 | 17.94 | 14.28 | 0.09 | 0.02 | bdl | bdl | 65.57 | bdl | bdl | bdl | 98.57 |
| | | 70 / 1 . | ML 5(2)B | 0.79 | bdl | bdl | 17.89 | 15.03 | bdl | bdl | bdl | bdl | 64.33 | bdl | bdl | bdl | 98.12 |
| | | 73 / 1 . | ML 5(2)B | 0.67 | bdl | bdl | 17.76 | 15.02 | bdl | bdl | bdl | bdl | 63.91 | bdl | bdl | bdl | 97.35 |
| | | 74 / 1 . | ML 5(2)B | 11.29 | 0.07 | bdl | 19.82 | bdl | 1.88 | bdl | bdl | bdl | 63.62 | bdl | bdl | bdl | 96.68 |
| | | 75 / 1 . | ML 5(2)B | 12.43 | bdl | bdl | 18.73 | bdl | 0.23 | bdl | bdl | bdl | 67.73 | bdl | bdl | bdl | 99.13 |
| | | 82 / 1 . | ML 5(2)B | 0.79 | bdl | 0.01 | 17.58 | 14.66 | bdl | bdl | 0.01 | bdl | 64.03 | bdl | bdl | 0.07 | 97.44 |
| | | 88 / 1 . | ML 5(2)B | 11.24 | 0.03 | 0.01 | 18.50 | bdl | 0.23 | bdl | bdl | 0.13 | 68.44 | 0.64 | 0.03 | bdl | 99.25 |
| | | 89 / 1 . | ML 5(2)B | 0.12 | 0.06 | 0.02 | 17.37 | 15.32 | bdl | 0.01 | bdl | 0.14 | 63.90 | 1.05 | bdl | bdl | 98.02 |
| | | 95 / 1 . | ML 16A | 0.85 | 0.06 | 0.01 | 17.62 | 14.67 | 0.09 | 0.01 | bdl | 0.05 | 63.39 | bdl | 0.01 | bdl | 96.98 |
| | | 103 / 1 . | ML 16A | 11.31 | bdl | 0.01 | 18.83 | 0.05 | 0.40 | bdl | bdl | bdl | 68.54 | bdl | 0.01 | bdl | 99.15 |
| | | 104 / 1 . | ML 16A | 7.64 | bdl | bdl | 23.82 | 0.17 | 7.07 | bdl | bdl | bdl | 59.97 | bdl | bdl | bdl | 98.67 |
| | | 106 / 1 . | ML 16A | 0.67 | bdl | bdl | 17.72 | 14.66 | 0.03 | bdl | 0.01 | 0.09 | 64.26 | 0.09 | 0.02 | 0.03 | 97.77 |
| | | 114 / 1 . | ML 16A | 0.34 | bdl | bdl | 17.35 | 14.67 | 0.02 | bdl | bdl | bdl | 64.34 | bdl | bdl | 0.03 | 96.76 |
| | | 11 / 1 . | ML 10K | 7.84 | bdl | 0.01 | 24.60 | 0.10 | 7.56 | bdl | 0.07 | bdl | 58.95 | bdl | bdl | bdl | 99.14 |
| | | 12 / 1 . | ML 10K | 2.39 | bdl | 0.01 | 17.86 | 12.84 | 0.22 | bdl | 0.04 | bdl | 66.15 | 0.04 | bdl | 0.04 | 100.01 |
| | Muscovite | 71 / 1 . | ST3 | 0.47 | bdl | 0.86 | 33.95 | 10.82 | bdl | 0.45 | bdl | bdl | 46.50 | 1.06 | bdl | bdl | 94.14 |
| | | 74 / 1 . | ST3 | 0.52 | bdl | 0.86 | 34.10 | 10.63 | bdl | 0.45 | bdl | bdl | 46.81 | 1.72 | bdl | bdl | 95.11 |
| | | 81 / 1 . | ST3 | 0.38 | bdl | 0.68 | 33.96 | 10.41 | bdl | 0.15 | bdl | bdl | 46.61 | 3.07 | bdl | bdl | 95.27 |
| | | 30 / 1 . | ST 3 | 0.05 | 0.85 | 0.66 | 33.69 | 10.10 | bdl | 0.38 | 0.07 | bdl | 46.74 | 1.27 | bdl | bdl | 93.84 |
| | | 32 / 1 . | ST 3 | bdl | 0.44 | 0.81 | 32.37 | 10.59 | bdl | 0.05 | 0.09 | bdl | 46.20 | 2.50 | bdl | bdl | 93.04 |
| | | 35 / 1 . | ST 3 | bdl | 0.34 | 0.60 | 31.33 | 9.34 | 0.04 | 0.07 | bdl | bdl | 44.12 | 6.38 | 0.04 | bdl | 92.26 |
| | | 38 / 1 . | ST 3 | bdl | 0.62 | 0.68 | 29.75 | 9.71 | 0.05 | 0.09 | bdl | 0.04 | 45.04 | 5.96 | bdl | bdl | 91.93 |
| | | 39 / 1 . | ST 3 | bdl | 0.23 | 0.83 | 28.28 | 10.64 | 0.01 | 0.01 | 0.12 | 0.15 | 44.72 | 5.18 | bdl | bdl | 90.25 |
| | | 43 / 1 . | ST 3 | bdl | 0.29 | 0.92 | 29.83 | 10.05 | bdl | 0.05 | 0.16 | 0.19 | 44.55 | 4.78 | bdl | bdl | 90.87 |
| | | 48 / 1 . | ST 3 | bdl | 0.21 | 0.03 | 35.55 | 10.11 | 0.01 | bdl | 0.04 | 0.09 | 46.35 | 1.12 | 0.01 | bdl | 93.53 |

| | Mineral | EPMA Point | Sample | $Na_2O$ | F | MgO | $Al_2O_3$ | $K_2O$ | CaO | $TiO_2$ | $Cr_2O_3$ | MnO | $SiO_2$ | FeO | Cl | $P_2O_5$ | Total |
|---|---|---|---|---|---|---|---|---|---|---|---|---|---|---|---|---|---|
| **Vein** | Muscovite | 54 / 1 . | ST 3 | bdl | 0.28 | 0.62 | 32.63 | 9.27 | 0.01 | 0.02 | 0.07 | 0.04 | 46.07 | 6.93 | bdl | 0.01 | 95.96 |
| **Hosted** | | 60 / 1 . | ST 3 | bdl | 0.18 | 0.03 | 34.93 | 10.14 | 0.04 | 0.04 | 0.16 | 0.03 | 45.49 | 1.08 | bdl | bdl | 92.12 |
| | | 11 / 1 . | KYD14 | 0.64 | bdl | 0.15 | 34.85 | 10.15 | 0.15 | bdl | bdl | bdl | 49.33 | 1.21 | bdl | 0.05 | 96.66 |
| | | 22 / 1 . | KYD14 | 0.37 | bdl | 1.28 | 33.12 | 10.75 | bdl | 1.59 | bdl | bdl | 47.63 | 0.81 | bdl | bdl | 95.61 |
| | | 62 / 1 . | ML13 | 0.15 | bdl | 1.46 | 33.94 | 11.04 | bdl | bdl | bdl | bdl | 49.07 | 0.39 | bdl | bdl | 96.08 |
| | | 85 / 1 . | ML16A | 0.32 | bdl | 1.31 | 33.71 | 10.70 | bdl | 1.50 | bdl | bdl | 47.35 | 0.81 | bdl | bdl | 95.81 |
| | | 11 / 1 . | ML 5(1)A | bdl | 0.38 | 0.90 | 32.89 | 10.42 | 0.04 | 0.06 | bdl | bdl | 46.90 | 2.27 | 0.01 | 0.03 | 93.94 |
| | | 17 / 1 . | ML 5(1)A | bdl | 0.32 | 0.88 | 33.06 | 10.00 | 0.05 | 0.51 | 0.03 | 0.08 | 47.17 | 1.83 | bdl | 0.02 | 94.03 |
| | | 21 / 1 . | ML 5(1)A | bdl | 0.47 | 0.93 | 33.13 | 10.02 | bdl | 0.37 | 0.09 | 0.05 | 46.20 | 1.23 | bdl | bdl | 92.49 |
| | | 67 / 1 . | ML 5(2)B | 0.30 | 0.27 | 0.83 | 32.67 | 10.06 | bdl | 0.40 | bdl | 0.01 | 46.54 | 1.62 | bdl | bdl | 92.70 |
| | | 78 / 1 . | ML 5(2)B | bdl | 0.44 | 0.51 | 33.28 | 10.51 | bdl | bdl | bdl | bdl | 46.85 | 3.07 | bdl | 0.01 | 94.68 |
| | | 79 / 1 . | ML 5(2)B | bdl | 0.37 | 0.62 | 33.59 | 10.30 | bdl | bdl | bdl | bdl | 46.63 | 1.90 | bdl | bdl | 93.41 |
| | | 83 / 1 . | ML 5(2)B | bdl | 0.06 | 0.98 | 33.34 | 10.12 | 0.01 | 0.06 | bdl | bdl | 48.00 | 1.79 | bdl | bdl | 94.36 |
| | | 87 / 1 . | ML 5(2)B | bdl | 0.26 | 0.64 | 32.83 | 10.01 | bdl | 0.75 | bdl | bdl | 45.41 | 1.31 | bdl | bdl | 91.20 |
| | | 31 / 1 . | ML 19C | bdl | bdl | 1.18 | 33.40 | 10.40 | 0.04 | 0.01 | 0.03 | bdl | 45.93 | 1.99 | bdl | 0.03 | 93.04 |
| | | 33 / 1 . | ML 19C | bdl | bdl | 0.10 | 32.64 | 10.25 | bdl | bdl | bdl | 0.14 | 47.49 | 2.84 | bdl | 0.07 | 93.63 |
| | Chlorite/ | 25 / 1 . | ML19C | bdl | bdl | 13.96 | 18.93 | 0.85 | 0.08 | 0.53 | bdl | 0.65 | 28.85 | 25.24 | bdl | 0.03 | 89.23 |
| | Chamosite | 72 / 1 . | ST3 | bdl | bdl | 0.37 | 20.61 | bdl | 0.06 | bdl | bdl | 1.43 | 23.43 | 44.03 | bdl | 0.04 | 90.07 |
| | | 73 / 1 . | ST3 | 0.10 | bdl | 0.20 | 14.72 | 0.09 | 0.27 | bdl | bdl | bdl | 26.61 | 46.16 | bdl | 0.04 | 88.34 |
| | | 78 / 1 . | ST3 | bdl | bdl | 0.10 | 21.31 | bdl | bdl | bdl | bdl | 1.30 | 21.94 | 43.17 | bdl | 0.07 | 87.95 |
| | | 82 / 1 . | ST3 | bdl | bdl | bdl | 20.58 | bdl | 0.04 | bdl | bdl | 1.42 | 21.79 | 43.40 | bdl | bdl | 87.32 |
| | | 83 / 1 . | ST3 | bdl | bdl | bdl | 21.06 | bdl | 0.03 | bdl | bdl | 1.31 | 22.17 | 44.16 | bdl | bdl | 88.85 |
| | | 92 / 1 . | ML5-2D | bdl | bdl | 0.43 | 11.66 | 0.07 | 0.37 | bdl | bdl | bdl | 26.96 | 48.82 | bdl | bdl | 88.36 |
| | | 96 / 1 . | ML5-2D | bdl | bdl | 0.41 | 10.72 | 0.04 | 0.44 | bdl | bdl | bdl | 25.40 | 46.45 | bdl | bdl | 83.54 |
| | | 100 / 1 . | ML5-2D | bdl | bdl | 0.38 | 16.87 | 0.08 | 0.24 | bdl | bdl | bdl | 25.86 | 45.17 | bdl | bdl | 88.63 |
| | | 101 / 1 . | ML5-2D | bdl | bdl | 0.60 | 15.45 | 0.11 | 0.51 | bdl | bdl | bdl | 28.10 | 44.89 | bdl | bdl | 89.80 |
| | | 78 / 1 . | ML13 | bdl | bdl | 23.37 | 18.20 | 0.13 | 0.22 | 0.07 | bdl | 0.53 | 31.66 | 13.00 | bdl | bdl | 87.25 |
| | | 65 / 1 . | ML 5(2)B | bdl | 0.05 | 6.19 | 18.34 | 0.88 | 0.33 | 0.56 | 0.07 | 0.63 | 26.90 | 33.11 | 0.06 | 0.11 | 87.23 |

| | Mineral | EPMA Point | Sample | $Na_2O$ | F | MgO | $Al_2O_3$ | $K_2O$ | CaO | $TiO_2$ | $Cr_2O_3$ | MnO | $SiO_2$ | FeO | Cl | $P_2O_5$ | Total |
|---|---|---|---|---|---|---|---|---|---|---|---|---|---|---|---|---|---|
| **Vein** | Allanite | 13 / 1 . | KYD14 | 0.10 | bdl | 0.47 | 17.12 | bdl | 13.49 | 0.09 | bdl | 0.34 | 32.92 | 6.44 | 0.08 | bdl | 71.12 |
| **Hosted** | | 14 / 1 . | KYD14 | 0.23 | bdl | 0.13 | 17.31 | 0.12 | 11.04 | 0.17 | bdl | 0.28 | 36.63 | 4.76 | 0.03 | bdl | 70.71 |
| | | 15 / 1 . | KYD14 | 0.09 | bdl | 0.40 | 17.47 | bdl | 14.05 | 0.15 | bdl | 0.44 | 32.83 | 6.95 | 0.10 | bdl | 72.50 |
| | | 84 / 1 . | ML16A | bdl | bdl | 0.87 | 19.15 | bdl | 14.12 | 0.15 | bdl | 0.27 | 31.97 | 7.19 | bdl | 0.05 | 73.80 |
| | | 87 / 1 . | ML16A | 0.09 | bdl | 0.29 | 15.99 | bdl | 14.02 | 0.11 | bdl | 0.32 | 33.09 | 7.33 | 0.16 | 0.06 | 71.44 |
| | | 88 / 1 . | ML16A | 0.41 | bdl | 0.20 | 14.14 | 0.22 | 9.45 | 0.15 | bdl | 0.19 | 35.45 | 4.25 | 0.10 | bdl | 64.56 |
| | | 111 / 1 . | ML 16A | bdl | 0.25 | 1.11 | 18.19 | 0.04 | 13.69 | 0.13 | 0.11 | 0.62 | 32.08 | 8.54 | bdl | 0.08 | 74.85 |
| | | 112 / 1 . | ML 16A | bdl | bdl | 0.71 | 20.31 | 0.05 | 15.64 | 0.10 | 0.10 | 0.45 | 33.14 | 7.04 | bdl | bdl | 77.54 |
| | Fluorapatite | 14 / 1 . | ML19C | bdl | 3.82 | bdl | bdl | bdl | 55.16 | bdl | bdl | bdl | 0.04 | 0.20 | 0.03 | 40.83 | 100.08 |
| | | 15 / 1 . | ML19C | bdl | 3.78 | bdl | bdl | bdl | 54.90 | bdl | bdl | bdl | bdl | bdl | bdl | 40.51 | 99.34 |
| | | 84 / 1 . | ML5-2B | 0.11 | 3.82 | bdl | bdl | bdl | 55.58 | bdl | bdl | bdl | bdl | bdl | bdl | 42.35 | 102.14 |
| | | 86 / 1 . | ML5-2B | 0.11 | 3.87 | bdl | bdl | bdl | 55.32 | bdl | bdl | bdl | 0.05 | bdl | bdl | 42.04 | 101.53 |
| | | 88 / 1 . | ML5-2B | 0.10 | 3.78 | bdl | bdl | bdl | 55.17 | bdl | bdl | bdl | bdl | bdl | bdl | 42.23 | 101.53 |
| | | 6 / 1 . | KYD14 | bdl | 3.66 | bdl | bdl | bdl | 54.22 | bdl | bdl | bdl | bdl | bdl | 0.16 | 41.71 | 99.95 |
| | | 12 / 1 . | KYD14 | bdl | 3.87 | bdl | bdl | bdl | 54.59 | bdl | bdl | bdl | 0.06 | bdl | 0.12 | 41.59 | 100.33 |
| | | 77 / 1 . | ML13 | bdl | 3.68 | bdl | bdl | bdl | 54.58 | bdl | bdl | bdl | bdl | bdl | 0.03 | 40.79 | 99.23 |
| | | 94 / 1 . | ML16A | bdl | 3.78 | bdl | bdl | bdl | 55.18 | bdl | bdl | bdl | 0.04 | bdl | 0.10 | 40.55 | 99.70 |
| | | 109 / 1 . | ML 16A | bdl | 6.89 | 0.03 | 0.42 | 0.03 | 53.75 | bdl | bdl | 0.01 | 2.14 | 0.05 | 0.06 | 38.99 | 102.38 |
| | | 110 / 1 . | ML 16A | bdl | 6.44 | 0.02 | bdl | 0.03 | 56.15 | bdl | bdl | bdl | 0.12 | bdl | 0.04 | 40.52 | 103.32 |
| | Prehnite | 97 / 1 . | ML16A | bdl | bdl | 0.42 | 24.07 | bdl | 26.23 | 0.06 | bdl | bdl | 43.25 | 0.48 | bdl | 0.06 | 94.66 |
| | | 98 / 1 . | ML 16A | bdl | bdl | 0.04 | 22.51 | bdl | 27.42 | 0.13 | bdl | bdl | 42.53 | 0.18 | bdl | bdl | 92.82 |
| | | 99 / 1 . | ML 16A | bdl | 0.10 | 0.03 | 23.10 | bdl | 27.41 | bdl | bdl | bdl | 43.57 | 0.40 | bdl | bdl | 94.61 |
| | | 100 / 1 . | ML 16A | bdl | bdl | bdl | 22.47 | bdl | 27.06 | bdl | bdl | bdl | 42.45 | bdl | bdl | 0.07 | 92.05 |
| | | 101 / 1 . | ML 16A | bdl | bdl | 0.01 | 23.83 | bdl | 27.65 | bdl | bdl | bdl | 44.11 | 0.03 | bdl | bdl | 95.64 |
| | | 107 / 1 . | ML 16A | bdl | bdl | 0.03 | 22.30 | 0.03 | 26.64 | bdl | bdl | 0.03 | 43.15 | 0.26 | bdl | 0.03 | 92.46 |
| | | 115 / 1 . | ML 16A | bdl | bdl | bdl | 23.38 | 0.02 | 27.42 | bdl | bdl | bdl | 43.56 | bdl | bdl | 0.03 | 94.42 |
| | | 116 / 1 . | ML 16A | bdl | bdl | 0.02 | 22.74 | bdl | 26.65 | bdl | bdl | 0.04 | 43.43 | 0.08 | bdl | bdl | 92.98 |
| | | 117 / 1 . | ML 16A | bdl | 0.06 | 0.39 | 23.23 | bdl | 27.59 | bdl | bdl | 0.04 | 43.15 | 0.37 | bdl | bdl | 94.83 |

| | Mineral | EPMA Point | Sample | $Na_2O$ | F | MgO | $Al_2O_3$ | $K_2O$ | CaO | $TiO_2$ | $Cr_2O_3$ | MnO | $SiO_2$ | FeO | Cl | $P_2O_5$ | Total |
|---|---|---|---|---|---|---|---|---|---|---|---|---|---|---|---|---|---|
| **Vein** | Prehnite | 21 / 1 . | ML 19C | bdl | bdl | 0.20 | 22.83 | bdl | 26.40 | 0.22 | 0.15 | 0.23 | 42.11 | 0.55 | bdl | 0.07 | 92.81 |
| **Hosted** | Pumpellyite | 102 / 1 . | ML 16A | 0.04 | bdl | 5.14 | 24.25 | 0.05 | 20.82 | 0.03 | 0.06 | 0.24 | 38.17 | 3.05 | 0.03 | bdl | 91.91 |
| | | 26 / 1 . | ML 19C | bdl | bdl | 0.03 | 25.44 | bdl | 22.84 | bdl | 0.03 | 0.10 | 35.85 | 6.97 | 0.01 | 0.07 | 91.51 |
| | | 29 / 1 . | ML 19C | bdl | bdl | 0.03 | 26.80 | bdl | 23.47 | bdl | 0.23 | bdl | 36.02 | 4.29 | bdl | 0.08 | 91.14 |
| | | 35 / 1 . | ML 19C | bdl | bdl | 1.26 | 26.23 | bdl | 23.20 | bdl | 0.26 | 0.04 | 36.39 | 4.65 | bdl | 0.03 | 92.10 |
| | Clinozoisite | 86 / 1 . | ML16A | bdl | bdl | bdl | 29.39 | bdl | 23.87 | 0.09 | bdl | bdl | 38.89 | 3.99 | bdl | bdl | 96.38 |
| | | 89 / 1 . | ML16A | bdl | bdl | bdl | 29.84 | bdl | 23.94 | 0.11 | 0.17 | bdl | 39.53 | 3.32 | bdl | 0.08 | 97.02 |
| | Fluorite | 118 / 1 . | ML 16A | bdl | 52.63 | 0.01 | bdl | 0.02 | 80.41 | bdl | bdl | 0.01 | 0.07 | bdl | bdl | 0.10 | 133.25 |

**Table 2:** Major element chemistry and thermometric data of biotite associated with disseminated/ laminated, massive and vein-hosted sulfides.

| Sulfide Association | EPMA Point | Sample | $SiO_2$ | $TiO_2$ | $Al_2O_3$ | $Cr_2O_3$ | FeO | MnO | MgO | CaO | $Na_2O$ | $K_2O$ | F | Cl | Total | T (˚C) |
|---|---|---|---|---|---|---|---|---|---|---|---|---|---|---|---|---|
| **Laminated/** | 3 / 1 . | D24-2 | 36.76 | 2.82 | 17.14 | 0.11 | 15.11 | 0.24 | 12.44 | bdl | 0.13 | 9.47 | bdl | 0.10 | 94.32 | 603.29 |
| **Disseminated** | 5 / 1 . | D24-2 | 36.61 | 2.49 | 17.06 | bdl | 14.66 | 0.31 | 12.66 | bdl | 0.12 | 9.59 | bdl | 0.09 | 93.57 | 585.18 |
| | 6 / 1 . | D24-2 | 36.43 | 2.59 | 17.74 | bdl | 15.16 | 0.16 | 12.42 | 0.02 | 0.14 | 9.15 | bdl | 0.09 | 93.91 | 592.33 |
| | 10 / 1 . | D24-2 | 37.53 | 2.67 | 17.53 | bdl | 14.75 | 0.24 | 12.73 | bdl | 0.09 | 9.55 | bdl | 0.07 | 95.14 | 597.95 |
| | 12 / 1 . | D24-2 | 37.60 | 2.63 | 18.20 | 0.04 | 14.25 | 0.23 | 12.63 | 0.01 | 0.21 | 9.43 | bdl | 0.10 | 95.32 | 601.64 |
| | 31 / 1 . | ML19A | 37.24 | 1.67 | 16.50 | 0.08 | 13.35 | 0.49 | 14.34 | bdl | 0.17 | 9.86 | 0.01 | 0.05 | 93.74 | 524.57 |
| | 34 / 1 . | ML19A | 37.58 | 1.34 | 16.58 | 0.30 | 12.40 | 0.36 | 14.21 | 0.09 | 0.25 | 9.35 | bdl | 0.06 | 92.52 | 511.38 |
| | 36 / 1 . | ML19A | 37.26 | 2.00 | 16.66 | bdl | 14.09 | 0.41 | 14.25 | 0.01 | 0.22 | 9.55 | bdl | 0.06 | 94.57 | 542.23 |
| | 37 / 1 . | ML19A | 38.46 | 2.22 | 16.30 | 0.08 | 12.59 | 0.43 | 14.73 | bdl | 0.14 | 9.84 | bdl | 0.03 | 94.82 | 564.21 |
| **Massive** | 46 / 1 . | ML10H | 36.72 | 2.70 | 17.63 | 0.01 | 15.32 | 0.20 | 12.91 | bdl | 0.08 | 9.64 | bdl | 0.11 | 95.31 | 590.34 |
| | 50 / 1 . | ML10H | 37.01 | 2.43 | 17.36 | 0.05 | 13.82 | 0.11 | 12.95 | bdl | 0.09 | 9.76 | bdl | 0.13 | 93.72 | 586.30 |
| | 52 / 1 . | ML10H | 36.54 | 2.77 | 17.53 | 0.07 | 13.41 | 0.20 | 13.06 | bdl | 0.15 | 9.88 | 0.01 | 0.29 | 93.91 | 602.95 |
| | 61 / 1 . | ML10I | 36.24 | 0.83 | 18.26 | 0.13 | 14.02 | 0.30 | 15.54 | 0.30 | 0.06 | 7.89 | bdl | 0.05 | 93.61 | 436.51 |
| | 62 / 1 . | ML10I | 37.52 | 1.66 | 17.87 | 0.10 | 12.43 | 0.24 | 15.81 | 0.05 | 0.11 | 8.81 | bdl | 0.07 | 94.66 | 519.20 |
| | 64 / 1 . | ML10I | 37.69 | 1.98 | 17.00 | 0.20 | 11.72 | 0.41 | 14.79 | bdl | 0.09 | 9.89 | bdl | 0.08 | 93.86 | 555.57 |
| | 6 / 1 . | ML 10I | 36.53 | 1.20 | 17.10 | 0.16 | 11.78 | 0.27 | 14.74 | bdl | 0.10 | 9.34 | 0.65 | 0.06 | 92.04 | 497.11 |
| | 13 / 1 . | ML 10I | 36.89 | 2.02 | 16.79 | 0.09 | 12.64 | 0.20 | 14.56 | bdl | 0.09 | 9.02 | 0.97 | 0.08 | 93.52 | 551.38 |
| | 14 / 1 . | ML 10I | 37.43 | 1.95 | 16.93 | 0.27 | 12.05 | 0.18 | 14.26 | bdl | 0.10 | 9.10 | 0.72 | 0.09 | 93.34 | 557.85 |
| | 15 / 1 . | ML 10I | 36.25 | 1.69 | 17.00 | 0.16 | 13.26 | 0.30 | 14.13 | 0.01 | 0.13 | 8.79 | 0.81 | 0.07 | 92.76 | 529.52 |
| | 39 / 1 . | D4 | 35.75 | 2.55 | 16.64 | 0.04 | 20.55 | 0.29 | 8.10 | bdl | 0.09 | 9.30 | 0.02 | 0.11 | 93.44 | 641.31 |
| | 42 / 1 . | D4 | 35.49 | 2.10 | 15.69 | 0.14 | 22.64 | 0.52 | 7.93 | 0.06 | 0.05 | 8.87 | bdl | 0.12 | 93.63 | 611.31 |
| | 45 / 1 . | D4 | 35.88 | 2.05 | 15.97 | 0.04 | 22.06 | 0.38 | 7.86 | bdl | 0.09 | 9.11 | bdl | 0.10 | 93.55 | 613.11 |
| | 83 / 1 . | D4 | 36.75 | 2.42 | 15.92 | 0.04 | 21.11 | 0.50 | 8.86 | 0.04 | 0.11 | 8.85 | 0.77 | 0.15 | 95.62 | 618.69 |
| **Vein-Hosted** | 13 / 1 . | ML19C | 37.40 | 1.95 | 17.63 | bdl | 14.21 | 0.31 | 12.92 | bdl | 0.11 | 9.52 | bdl | 0.06 | 94.11 | 556.75 |
| | 18 / 1 . | ML19C | 37.74 | 1.88 | 17.71 | 0.10 | 14.35 | 0.38 | 13.27 | bdl | 0.11 | 9.63 | bdl | 0.05 | 95.23 | 547.84 |
| | 24 / 1 . | ML19C | 36.93 | 2.13 | 17.57 | 0.15 | 15.72 | 0.36 | 12.35 | bdl | 0.11 | 9.72 | bdl | 0.05 | 95.10 | 564.38 |
| | 22 / 1 . | ML 19C | 34.81 | 2.43 | 16.22 | 0.17 | 16.76 | 0.51 | 12.47 | 0.15 | 0.03 | 7.97 | 0.61 | 0.03 | 92.78 | 568.55 |
| | 43 / 1 . | ML 19C | 36.35 | 2.15 | 15.91 | 0.08 | 15.40 | 0.40 | 11.94 | 0.07 | 0.05 | 8.71 | 0.62 | 0.07 | 92.06 | 571.00 |

| Sulfide Association | EPMA Point | Sample | $SiO_2$ | $TiO_2$ | $Al_2O_3$ | $Cr_2O_3$ | FeO | MnO | MgO | CaO | $Na_2O$ | $K_2O$ | F | Cl | Total | T (˚C) |
|---|---|---|---|---|---|---|---|---|---|---|---|---|---|---|---|---|
| **Vein-Hosted** | 44 / 1 . | ML 19C | 35.27 | 2.15 | 16.16 | 0.07 | 15.31 | 0.48 | 11.78 | 0.06 | 0.02 | 8.56 | 0.59 | 0.04 | 90.78 | 570.48 |
| | 45 / 1 . | ML 19C | 35.76 | 2.19 | 16.94 | 0.15 | 15.19 | 0.36 | 12.98 | 0.03 | 0.03 | 9.16 | 0.94 | 0.07 | 94.57 | 558.61 |
| | 46 / 1 . | ML 19C | 35.87 | 2.34 | 17.12 | 0.17 | 15.90 | 0.40 | 12.96 | 0.03 | 0.08 | 9.21 | 1.02 | 0.07 | 95.61 | 562.61 |
| | 85 / 1 . | ML5-2B | 35.17 | 1.93 | 17.08 | 0.07 | 24.88 | 0.60 | 6.83 | bdl | 0.10 | 9.28 | bdl | 0.26 | 96.26 | 628.20 |
| | 87 / 1 . | ML5-2B | 33.70 | 1.71 | 16.83 | 0.03 | 26.33 | 0.43 | 6.35 | 0.03 | 0.09 | 8.23 | bdl | 0.25 | 93.98 | 620.35 |
| | 62 / 1 . | ML5-2B | 34.64 | 1.20 | 16.87 | bdl | 23.24 | 0.23 | 7.62 | 0.01 | 0.09 | 8.27 | 1.22 | 0.25 | 93.64 | 552.19 |
| | 86 / 1 . | ML5-2B | 34.10 | 2.06 | 16.00 | bdl | 25.63 | 0.53 | 6.32 | 0.03 | bdl | 8.81 | 1.14 | 0.27 | 94.90 | 640.55 |
| | 89 / 1 . | ML5-2D | 35.28 | 2.91 | 16.82 | 0.18 | 22.38 | 0.34 | 7.64 | bdl | 0.01 | 9.37 | bdl | 0.22 | 95.14 | 666.66 |
| | 90 / 1 . | ML5-2D | 35.59 | 2.77 | 16.35 | bdl | 22.74 | 0.32 | 7.74 | 0.01 | 0.10 | 9.37 | bdl | 0.21 | 95.22 | 655.88 |
| | 91 / 1 . | ML5-2D | 34.94 | 2.61 | 16.40 | 0.06 | 22.43 | 0.37 | 7.49 | bdl | 0.03 | 9.34 | bdl | 0.22 | 93.89 | 650.48 |
| | 98 / 1 . | ML5-2D | 35.26 | 2.72 | 16.43 | 0.09 | 22.34 | 0.37 | 8.27 | bdl | 0.06 | 9.41 | bdl | 0.23 | 95.18 | 638.94 |
| | 13 / 1 . | ML 5(1)A | 33.12 | 1.16 | 15.66 | 0.05 | 29.44 | 0.60 | 4.72 | 0.06 | bdl | 7.70 | 0.79 | 0.29 | 93.77 | 623.01 |
| | 18 / 1 . | ML 5(1)A | 34.78 | 1.58 | 16.31 | 0.10 | 26.23 | 0.50 | 6.66 | 0.07 | bdl | 8.34 | 1.12 | 0.41 | 96.25 | 605.40 |
| | 20 / 1 . | ML 5(1)A | 34.65 | 1.57 | 16.39 | 0.04 | 23.65 | 0.44 | 7.62 | 0.11 | bdl | 8.57 | 1.42 | 0.29 | 94.95 | 578.81 |
| | 28 / 1 . | ML 5(1)A | 35.13 | 1.29 | 16.68 | 0.01 | 25.05 | 0.46 | 7.02 | 0.02 | bdl | 8.90 | 1.13 | 0.31 | 96.14 | 572.02 |
| | 29 / 1 . | ML 5(1)A | 34.13 | 1.24 | 15.98 | 0.11 | 25.36 | 0.62 | 6.66 | 0.08 | bdl | 8.52 | 1.12 | 0.48 | 94.49 | 569.95 |
| | 23 / 1 . | BH 164-13 | 36.29 | 2.12 | 18.70 | bdl | 15.65 | 0.18 | 11.58 | 0.04 | 0.30 | 8.66 | 0.31 | 0.12 | 94.05 | 576.84 |
| | 24 / 1 . | BH 164-13 | 36.10 | 2.22 | 18.25 | 0.13 | 16.93 | 0.12 | 11.66 | bdl | 0.27 | 8.51 | 0.23 | 0.13 | 94.68 | 575.17 |
| | 25 / 1 . | BH 164-13 | 36.48 | 2.18 | 18.54 | bdl | 16.85 | 0.25 | 11.30 | bdl | 0.27 | 8.40 | 0.43 | 0.11 | 95.22 | 579.82 |
| | 26 / 1 . | BH 164-13 | 35.55 | 2.10 | 18.08 | bdl | 15.61 | 0.21 | 11.40 | bdl | 0.28 | 8.68 | 0.41 | 0.10 | 92.93 | 575.22 |
| | 38 / 1 . | BH 164-13 | 35.68 | 1.80 | 17.89 | 0.11 | 16.56 | 0.19 | 12.22 | bdl | 0.30 | 8.46 | 0.60 | 0.11 | 94.36 | 540.56 |
| | 6 / 1 . | ML 10K | 36.60 | 2.72 | 17.06 | 0.03 | 14.80 | 0.26 | 12.63 | 0.03 | 0.06 | 8.95 | 0.87 | 0.07 | 94.52 | 596.99 |
| | 7 / 1 . | ML 10K | 36.27 | 2.73 | 17.69 | 0.15 | 15.38 | 0.14 | 12.69 | 0.05 | 0.12 | 9.22 | 0.74 | 0.08 | 95.51 | 592.60 |
| | 9 / 1 . | ML 10K | 35.16 | 2.59 | 17.56 | 0.24 | 15.47 | 0.11 | 12.60 | 0.05 | 0.08 | 9.00 | 0.71 | 0.08 | 94.47 | 583.35 |
| | 14 / 1 . | ML 10K | 35.67 | 2.57 | 17.62 | 0.14 | 15.48 | 0.20 | 12.57 | 0.03 | 0.07 | 8.95 | 0.94 | 0.08 | 94.70 | 583.65 |
| | 17 / 1 . | ML 10K | 35.14 | 2.55 | 17.15 | 0.15 | 15.70 | 0.15 | 12.88 | 0.04 | 0.09 | 8.60 | 0.79 | 0.08 | 93.66 | 576.28 |
| | 18 / 1 . | ML 10K | 36.07 | 2.67 | 16.79 | 0.08 | 16.26 | 0.11 | 12.71 | bdl | 0.08 | 9.19 | 1.14 | 0.10 | 95.76 | 582.01 |
| | 81 / 1 . | ML16A | 37.10 | 1.43 | 16.99 | 0.16 | 12.54 | 0.22 | 15.36 | bdl | 0.09 | 9.68 | 0.01 | 0.06 | 93.64 | 504.13 |

| Sulfide Association | EPMA Point | Sample | $SiO_2$ | $TiO_2$ | $Al_2O_3$ | $Cr_2O_3$ | FeO | MnO | MgO | CaO | $Na_2O$ | $K_2O$ | F | Cl | Total | T (˚C) |
|---|---|---|---|---|---|---|---|---|---|---|---|---|---|---|---|---|
| **Vein-Hosted** | 91 / 1 . | ML16A | 37.86 | 1.94 | 17.51 | 0.13 | 12.95 | 0.29 | 14.36 | bdl | 0.06 | 9.60 | bdl | 0.05 | 94.76 | 549.40 |
| | 93 / 1 . | ML16A | 38.43 | 2.09 | 17.64 | 0.10 | 13.12 | 0.31 | 14.45 | 0.03 | 0.09 | 9.58 | 0.01 | 0.07 | 95.92 | 557.53 |
| | 100 / 1 . | ML16A | 38.14 | 1.08 | 17.96 | 0.03 | 11.46 | 0.26 | 15.64 | 0.02 | 0.08 | 9.40 | bdl | 0.05 | 94.12 | 479.24 |
| | 101 / 1 . | ML16A | 37.80 | 2.02 | 17.95 | 0.05 | 12.66 | 0.35 | 14.56 | bdl | 0.11 | 9.60 | bdl | 0.07 | 95.15 | 553.55 |
| | 91 / 1 . | ML 16A | 36.91 | 1.72 | 16.42 | bdl | 11.79 | 0.10 | 14.43 | 0.08 | bdl | 9.44 | 0.51 | 0.01 | 91.44 | 542.10 |
| | 92 / 1 . | ML 16A | 37.35 | 1.99 | 16.25 | bdl | 12.25 | 0.10 | 14.92 | 0.07 | bdl | 9.35 | 0.13 | 0.03 | 92.44 | 551.34 |
| | 96 / 1 . | ML 16A | 37.77 | 1.56 | 16.91 | 0.01 | 12.64 | 0.16 | 15.55 | bdl | bdl | 9.51 | 0.38 | 0.04 | 94.54 | 512.83 |
| | 1 / 1 . | KYD14 | 37.96 | 2.32 | 17.80 | bdl | 12.42 | 0.25 | 14.59 | bdl | 0.10 | 9.58 | bdl | 0.05 | 95.09 | 574.37 |
| | 7 / 1 . | KYD14 | 36.44 | 1.68 | 17.95 | bdl | 12.99 | 0.14 | 14.51 | 0.02 | 0.13 | 8.99 | bdl | 0.06 | 92.90 | 528.49 |
| | 8 / 1 . | KYD14 | 38.64 | 2.13 | 18.72 | bdl | 12.19 | 0.20 | 15.07 | 0.04 | 0.12 | 9.31 | bdl | 0.07 | 96.49 | 562.82 |

**Table 3:** Major element composition of sphalerite in three types of mineralization.

| | EPMA Point | Sample | S | Fe | Cu | Zn | Pb | Total |
|---|---|---|---|---|---|---|---|---|
| **Laminated/** | 58 / 1 . | D24-2 | 33.243 | 10.595 | bdl | 56.387 | bdl | 100.533 |
| **Disseminated** | 63 / 1 . | D24-2 | 32.837 | 11.424 | bdl | 55.689 | bdl | 100.124 |
| | 65 / 1 . | D24-2 | 33.122 | 10.041 | bdl | 55.841 | bdl | 99.63 |
| | 66 / 1 . | D24-2 | 33.202 | 10.514 | bdl | 56.763 | bdl | 100.838 |
| | 67 / 1 . | D24-2 | 33.035 | 10.896 | bdl | 55.408 | bdl | 99.588 |
| | 68 / 1 . | D24-2 | 33.24 | 11.031 | bdl | 56.285 | bdl | 100.834 |
| | 73 / 1 . | D24-2 | 32.496 | 11.3 | bdl | 54.23 | bdl | 98.233 |
| | 74 / 1 . | D24-2 | 33.401 | 10.496 | bdl | 55.665 | bdl | 99.781 |
| | 2 / 1 . | ML19A | 33.06 | 9.252 | bdl | 56.752 | bdl | 99.22 |
| | 2 / 2 . | ML19A | 33.06 | 9.252 | bdl | 56.752 | bdl | 99.22 |
| **Massive** | 6 / 1 . | KYD34 | 33.487 | 11.847 | bdl | 55.306 | bdl | 100.835 |
| | 10 / 1 . | KYD34 | 34.605 | 11.875 | bdl | 55.252 | bdl | 101.759 |
| | 19 / 1 . | KYD34 | 33.625 | 11.725 | bdl | 55.287 | bdl | 100.647 |
| | 33 / 1 . | KYD21 | 33.433 | 11.309 | 0.096 | 56.644 | bdl | 101.651 |
| | 35 / 1 . | KYD21 | 33.598 | 11.82 | bdl | 55.907 | 4.186 | 101.57 |
| | 37 / 1 . | KYD21 | 33.642 | 11.762 | bdl | 56.511 | bdl | 102.02 |
| | 41 / 1 . | KYD21 | 33.746 | 10.83 | bdl | 56.95 | bdl | 101.552 |
| | 44 / 1 . | KYD21 | 33.671 | 12.041 | bdl | 55.651 | bdl | 101.483 |
| | 47 / 1 . | KYD21 | 34.56 | 8.549 | bdl | 56.757 | bdl | 99.911 |
| | 49 / 1 . | KYD21 | 33.889 | 11.917 | bdl | 54.766 | bdl | 100.729 |
| | 55 / 1 . | KYD21 | 33.952 | 12.127 | bdl | 55.543 | bdl | 101.656 |
| | 76 / 1 . | KYD16 | 34.008 | 10.067 | bdl | 58.051 | bdl | 102.175 |
| | 79 / 1 . | KYD16 | 33.784 | 9.853 | bdl | 57.545 | bdl | 101.272 |
| | 82 / 1 . | KYD16 | 33.88 | 9.821 | bdl | 57.859 | bdl | 101.617 |
| | 84 / 1 . | KYD16 | 33.727 | 9.892 | bdl | 56.635 | bdl | 100.396 |
| | 85 / 1 . | KYD16 | 33.557 | 9.894 | bdl | 56.57 | bdl | 100.233 |
| | 93 / 1 . | KYD16 | 33.113 | 8.376 | bdl | 56.565 | bdl | 98.148 |
| | 94 / 1 . | KYD16 | 33.599 | 9.025 | bdl | 56.96 | bdl | 99.796 |
| | 97 / 1 . | KYD16 | 33.585 | 9.911 | bdl | 57.371 | bdl | 100.93 |
| | 101 / 1 . | KYD16 | 33.74 | 9.73 | bdl | 57.251 | bdl | 100.838 |
| | 104 / 1 . | KYD16 | 33.876 | 9.786 | bdl | 57.237 | bdl | 101.053 |
| | 106 / 1 . | KYD16 | 33.672 | 9.823 | bdl | 57.572 | bdl | 101.211 |
| | 107 / 1 . | KYD16 | 33.791 | 9.925 | bdl | 57.437 | bdl | 101.355 |
| | 1 / 1 . | ML12B | 34.092 | 9.883 | bdl | 56.819 | bdl | 100.934 |
| | 2 / 1 . | ML12B | 33.933 | 9.178 | bdl | 58.086 | bdl | 101.348 |
| | 16 / 1 . | ML12B | 33.589 | 8.852 | bdl | 57.242 | bdl | 99.869 |
| | 21 / 1 . | ML12B | 33.533 | 8.673 | bdl | 57.843 | bdl | 100.205 |
| | 23 / 1 . | ML12B | 33.589 | 8.877 | bdl | 57.592 | bdl | 100.481 |
| | 26 / 1 . | ML12B | 33.014 | 8.489 | bdl | 55.898 | bdl | 97.734 |
| | 76 / 1 . | D4 | 32.488 | 9.565 | bdl | 56.741 | bdl | 99.055 |
| | 87 / 1 . | D4 | 33.223 | 9.654 | bdl | 56.576 | bdl | 99.604 |
| | 88 / 1 . | D4 | 32.965 | 9.616 | bdl | 55.881 | bdl | 98.656 |

| | EPMA Point | Sample | S | Fe | Cu | Zn | Pb | Total |
|---|---|---|---|---|---|---|---|---|
| **Massive** | 17 / 1 . | ML10H | 33.038 | 9.664 | bdl | 56.401 | bdl | 99.203 |
| | 20 / 1 . | ML10H | 32.785 | 10.689 | bdl | 56.44 | bdl | 100.222 |
| | 22 / 1 . | ML10H | 32.703 | 10.696 | bdl | 55.667 | bdl | 99.571 |
| | 23 / 1 . | ML10H | 32.787 | 11.23 | bdl | 56.076 | bdl | 100.324 |
| | 25 / 1 . | ML10H | 32.87 | 11.237 | bdl | 55.538 | bdl | 99.819 |
| | 26 / 1 . | ML10H | 32.856 | 11.562 | bdl | 55.754 | bdl | 100.422 |
| | 34 / 1 . | ML10D | 32.824 | 10.833 | bdl | 56.608 | bdl | 100.447 |
| | 35 / 1 . | ML10D | 33.22 | 10.661 | bdl | 56.22 | bdl | 100.311 |
| | 36 / 1 . | ML10D | 32.964 | 10.803 | bdl | 55.517 | bdl | 99.375 |
| | 40 / 1 . | ML10D | 33.117 | 10.72 | bdl | 56.213 | bdl | 100.178 |
| | 41 / 1 . | ML10D | 33.375 | 10.681 | bdl | 56.033 | bdl | 100.321 |
| | 42 / 1 . | ML10D | 32.889 | 10.212 | bdl | 56.727 | bdl | 100.014 |
| | 48 / 1 . | ML10D | 32.957 | 11.298 | bdl | 55.403 | bdl | 99.876 |
| | 9 / 1 . | ML10I | 33.973 | 10.851 | bdl | 56.294 | bdl | 101.358 |
| | 16 / 1 . | ML10I | 33.428 | 9.267 | bdl | 57.239 | bdl | 100.032 |
| | 20 / 1 . | ML10I | 33.687 | 10.327 | bdl | 56.188 | bdl | 100.501 |
| | 24 / 1 . | ML10I | 33.688 | 10.2 | bdl | 57.372 | bdl | 101.362 |
| | 28 / 1 . | ML10I | 33.734 | 11.198 | bdl | 55.38 | bdl | 100.434 |
| | 28 / 2 . | ML10I | 33.734 | 11.198 | bdl | 55.38 | bdl | 100.434 |
| | 29 / 1 . | ML10I | 33.439 | 10.221 | 0.205 | 56.233 | bdl | 100.266 |
| | 33 / 1 . | ML10I | 33.305 | 9.747 | 0.614 | 56.996 | bdl | 100.779 |
| **Vein Hosted** | 22 / 1 . | KYD14 | 33.441 | 9.864 | 0.279 | 56.947 | bdl | 100.738 |
| | 24 / 1 . | KYD14 | 34.038 | 12.075 | 0.1 | 55.036 | bdl | 101.398 |
| | 30 / 1 . | KYD14 | 33.924 | 12.624 | bdl | 54.299 | bdl | 100.972 |
| | 30 / 1 . | KYD14 | 33.924 | 12.624 | bdl | 54.299 | bdl | 100.972 |
| | 31 / 1 . | KYD14 | 33.989 | 8.997 | bdl | 58.76 | bdl | 102.014 |
| | 35 / 1 . | KYD14 | 33.91 | 10.705 | 0.1 | 56.887 | bdl | 101.779 |
| | 38 / 1 . | KYD14 | 33.69 | 9.467 | bdl | 58.316 | bdl | 101.67 |
| | 41 / 1. | ML13 | 33.9 | 10.51 | bdl | 56.659 | bdl | 101.324 |
| | 45 / 1 . | ML13 | 33.652 | 10.586 | bdl | 56.818 | bdl | 101.222 |
| | 46 / 1 . | ML13 | 34.209 | 10.658 | bdl | 56.612 | bdl | 101.67 |
| | 47 / 1 . | ML13 | 33.602 | 10.438 | bdl | 57.464 | bdl | 101.607 |
| | 49 / 1 . | ML13 | 34.001 | 10.785 | bdl | 57.521 | bdl | 102.414 |
| | 53 / 1 . | ML13 | 33.723 | 10.748 | bdl | 57.239 | bdl | 101.881 |
| | 54 / 1 . | ML13 | 33.713 | 10.651 | bdl | 57.489 | bdl | 102.015 |
| | 56 / 1 . | ML13 | 34.04 | 10.709 | bdl | 57.034 | bdl | 101.94 |
| | 58 / 1 . | D7C | 34.161 | 11.667 | bdl | 56.369 | bdl | 102.395 |
| | 64 / 1 . | D7C | 34.146 | 10.785 | bdl | 56.04 | bdl | 101.165 |
| | 68 / 1 . | D7C | 34.049 | 9.84 | 1.758 | 55.183 | bdl | 100.994 |
| | 71 / 1 . | D7C | 34.148 | 11.191 | bdl | 56.112 | bdl | 101.509 |
| | 3 / 1 . | STOCK3 | 33.892 | 8.309 | 0.45 | 58.893 | bdl | 101.63 |
| | 9 / 1 . | STOCK3 | 33.997 | 10.275 | 0.16 | 56.264 | bdl | 100.938 |
| | 18 / 1 . | STOCK3 | 33.43 | 8.126 | 0.252 | 58.832 | bdl | 100.976 |

| | EPMA Point | Sample | S | Fe | Cu | Zn | Pb | Total |
|---|---|---|---|---|---|---|---|---|
| **Vein Hosted** | 19 / 1 . | KYD-07 | 33.802 | 10.828 | bdl | 56.667 | bdl | 101.341 |
| | 25 / 1 . | KYD-07 | 34.067 | 9.661 | bdl | 57.611 | bdl | 101.603 |
| | 31 / 1 . | ML5_2B | 32.748 | 8.657 | 0.441 | 58.879 | bdl | 101.019 |
| | 27 / 1 . | ML19C | 33.274 | 9.721 | bdl | 55.257 | bdl | 98.423 |
| | 28 / 1 . | ML19C | 32.873 | 9.556 | bdl | 56.943 | bdl | 99.465 |
| | 33 / 1 . | ML19C | 33.662 | 10.739 | bdl | 55.764 | bdl | 100.325 |
| | 35 / 1 . | ML16A | 33.526 | 10.868 | bdl | 56.189 | bdl | 101.111 |
| | 40 / 1 . | ML16A | 33.442 | 10.865 | bdl | 55.699 | bdl | 100.142 |
| | 41 / 1 . | ML16A | 33.601 | 11.047 | bdl | 56.507 | bdl | 101.327 |
| | 43 / 1 . | ML16A | 32.949 | 10.261 | bdl | 56.172 | bdl | 99.837 |
| | 43 / 2 . | ML16A | 32.949 | 10.261 | bdl | 56.172 | bdl | 99.837 |
| | 48 / 1 . | ML16A | 33.555 | 10.425 | bdl | 56.047 | bdl | 100.146 |
| | 50 / 1 . | ML16A | 33.264 | 10.528 | bdl | 56.736 | bdl | 100.662 |
| | 52 / 1 . | ML16A | 33.136 | 10.343 | bdl | 56.052 | bdl | 99.656 |

**Table 4:** Major element composition of galena in three types of mineralization.

| | EPMA Point | Sample | S | Fe | Pb | Total |
|---|---|---|---|---|---|---|
| **Laminated/ Disseminated** | 54 / 1 . | D24-2 | 13.315 | bdl | 85.327 | 98.818 |
| | 55 / 1 . | D24-2 | 13.22 | bdl | 85.518 | 98.84 |
| | 57 / 1 . | D24-2 | 13.318 | bdl | 86.744 | 100.138 |
| | 62 / 1 . | D24-2 | 13.089 | bdl | 84.407 | 97.545 |
| | 71 / 1 . | D24-2 | 13.125 | bdl | 85.772 | 99.032 |
| | 6 / 1 . | ML19A | 13.055 | bdl | 85.216 | 98.697 |
| | 7 / 1 . | ML19A | 12.988 | bdl | 84.296 | 97.365 |
| **Massive** | 4 / 1 . | KYD34 | 13.68 | 0.045 | 87.606 | 101.878 |
| | 5 / 1 . | KYD34 | 14.007 | bdl | 88.903 | 103.064 |
| | 9 / 1 . | KYD34 | 13.935 | bdl | 87.2 | 101.173 |
| | 17 / 1 . | KYD34 | 13.896 | 0.024 | 88.027 | 101.959 |
| | 40 / 1 . | KYD21 | 13.865 | bdl | 88.37 | 102.42 |
| | 42 / 1 . | KYD21 | 13.518 | bdl | 89.184 | 102.766 |
| | 45 / 1 . | KYD21 | 13.752 | bdl | 87.656 | 101.723 |
| | 46 / 1 . | KYD21 | 13.696 | bdl | 88.389 | 102.355 |
| | 50 / 1 . | KYD21 | 13.792 | bdl | 87.345 | 101.23 |
| | 54 / 1 . | KYD21 | 13.75 | 0.019 | 86.074 | 99.91 |
| | 54 / 1 . | KYD21 | 13.75 | 0.019 | 86.074 | 99.91 |
| | 77 / 1 . | KYD16 | 13.576 | bdl | 87.637 | 101.315 |
| | 78 / 1 . | KYD16 | 14.105 | bdl | 88.279 | 102.538 |
| | 80 / 1 . | KYD16 | 13.642 | bdl | 87.213 | 100.941 |
| | 81 / 1 . | KYD16 | 13.634 | bdl | 85.169 | 99.015 |
| | 83 / 1 . | KYD16 | 13.991 | bdl | 87.406 | 101.516 |
| | 88 / 1 . | KYD16 | 13.691 | 0.53 | 87.078 | 101.362 |
| | 95 / 1 . | KYD16 | 13.934 | bdl | 89.124 | 103.514 |

| | EPMA Point | Sample | S | Fe | Pb | Total |
|---|---|---|---|---|---|---|
| **Massive** | 102 / 1 . | KYD16 | 13.606 | bdl | 87.632 | 101.295 |
| | 3 / 1 . | ML12B | 13.654 | bdl | 86.451 | 100.254 |
| | 9 / 1 . | ML12B | 13.542 | 0.807 | 85.415 | 100.54 |
| | 14 / 1 . | ML12B | 13.582 | 0.169 | 86.436 | 100.373 |
| | 15 / 1 . | ML12B | 13.625 | bdl | 86.065 | 99.761 |
| | 22 / 1 . | ML12B | 13.731 | bdl | 87.837 | 101.685 |
| | 25 / 1 . | ML12B | 13.726 | bdl | 87.243 | 101.367 |
| | 27 / 1 . | ML12B | 13.402 | bdl | 86.006 | 99.767 |
| | 33 / 1 . | ML12B | 13.671 | 0.242 | 86.768 | 100.899 |
| | 77 / 1 . | D4 | 13.26 | bdl | 85.276 | 98.658 |
| | 79 / 1 . | D4 | 13.574 | bdl | 87.292 | 100.949 |
| | 80 / 1 . | D4 | 12.892 | bdl | 84.516 | 97.54 |
| | 84 / 1 . | D4 | 13.266 | bdl | 85.399 | 98.843 |
| | 84 / 2 . | D4 | 13.266 | bdl | 85.399 | 98.843 |
| | 89 / 1 . | D4 | 12.855 | bdl | 82.912 | 95.932 |
| | 15 / 1 . | ML10H | 13.158 | bdl | 84.079 | 97.432 |
| | 16 / 1 . | ML10H | 13.071 | bdl | 84.157 | 97.39 |
| | 19 / 1 . | ML10H | 13.037 | bdl | 84.256 | 97.546 |
| | 19 / 2 . | ML10H | 13.037 | bdl | 84.256 | 97.546 |
| | 37 / 1 . | ML10D | 13.09 | bdl | 84.989 | 98.312 |
| | 38 / 1 . | ML10D | 13.238 | bdl | 84.348 | 97.962 |
| | 49 / 1 . | ML10D | 13.236 | bdl | 85.757 | 99.212 |
| | 4 / 1 . | ML10I | 13.686 | bdl | 86.928 | 100.827 |
| | 8 / 1 . | ML10I | 13.863 | bdl | 87.513 | 101.531 |
| | 14 / 1 . | ML10I | 13.654 | bdl | 86.478 | 101.344 |
| | 17 / 1 . | ML10I | 13.583 | bdl | 86.663 | 100.49 |
| | 17 / 2 . | ML10I | 13.583 | bdl | 86.663 | 100.49 |
| | 22 / 1 . | ML10I | 13.61 | bdl | 86.924 | 100.599 |
| | 27 / 1 . | ML10I | 13.691 | bdl | 87.58 | 101.296 |
| | 27 / 2 . | ML10I | 13.691 | bdl | 87.58 | 101.296 |
| **Vein** | 32 / 1 . | KYD14 | 13.528 | 0.316 | 87.206 | 102.565 |
| **Hosted** | 36 / 1 . | KYD14 | 13.67 | bdl | 88.989 | 102.669 |
| | 37 / 1 . | KYD14 | 13.99 | bdl | 88.147 | 102.213 |
| | 43 / 1 . | ML13 | 13.828 | bdl | 87.258 | 101.208 |
| | 48 / 1 . | ML13 | 13.693 | bdl | 87.202 | 101.012 |
| | 50 / 1 . | ML13 | 13.891 | bdl | 86.869 | 100.878 |
| | 51 / 1 . | ML13 | 13.76 | bdl | 86.347 | 100.449 |
| | 51 / 1 . | ML13 | 13.76 | bdl | 86.347 | 100.449 |
| | 57 / 1 . | ML13 | 13.573 | bdl | 86.334 | 100.25 |
| | 23 / 1 . | ML52D | 13.641 | 0.08 | 87.485 | 101.297 |
| | 5 / 1 . | STOCK3 | 14.263 | 2.448 | 87.65 | 104.52 |
| | 7 / 1 . | STOCK3 | 13.695 | bdl | 87.56 | 101.41 |
| | 22 / 1 . | KYD-07 | 13.408 | bdl | 85.798 | 99.358 |
| | 37 / 1 . | ML16A | 13.694 | bdl | 87.256 | 101.223 |

| | EPMA Point | Sample | S | Fe | Pb | Total |
|---|---|---|---|---|---|---|
| **Vein** | 38 / 1 . | ML16A | 13.761 | 0.192 | 87.148 | 101.585 |
| **Hosted** | 42 / 1 . | ML16A | 13.399 | bdl | 86.778 | 100.197 |
| | 46 / 1 . | ML16A | 13.393 | bdl | 86.068 | 99.643 |
| | 49 / 1 . | ML16A | 13.515 | bdl | 86.18 | 99.846 |
| | 51 / 1 . | ML16A | 13.263 | bdl | 85.41 | 99.59 |
| | 53 / 1 . | ML16A | 13.689 | bdl | 87.851 | 101.626 |

**Table 5:** Major element composition of pyrrhotite in three types of mineralization.

| | EPMA Point | Sample | S | Fe | Total |
|---|---|---|---|---|---|
| **Laminated/** | 56 / 1 . | D24-2 | 38.32 | 59.22 | 97.63 |
| **Disseminated** | 61 / 1 . | D24-2 | 38.05 | 59.73 | 98.01 |
| | 64 / 1 . | D24-2 | 38.01 | 58.86 | 98.44 |
| | 70 / 1 . | D24-2 | 38.40 | 59.37 | 97.96 |
| | 72 / 1 . | D24-2 | 37.52 | 59.61 | 97.23 |
| | 1 / 1 . | ML19A | 37.74 | 59.20 | 97.20 |
| | 4 / 1 . | ML19A | 38.18 | 60.28 | 98.68 |
| | 5 / 1 . | ML19A | 37.41 | 58.98 | 96.70 |
| | 5 / 2 . | ML19A | 37.41 | 58.98 | 96.70 |
| **Massive** | 8 / 1 . | KYD34 | 39.12 | 61.06 | 100.31 |
| | 18 / 1 . | KYD34 | 38.87 | 60.89 | 100.31 |
| | 34 / 1 . | KYD21 | 38.49 | 61.65 | 100.21 |
| | 36 / 1 . | KYD21 | 39.27 | 61.20 | 100.56 |
| | 39 / 1 . | KYD21 | 39.22 | 61.80 | 101.10 |
| | 51 / 1 . | KYD21 | 38.76 | 61.40 | 100.23 |
| | 53 / 1 . | KYD21 | 39.12 | 61.20 | 100.38 |
| | 86 / 1 . | KYD16 | 39.74 | 59.44 | 99.43 |
| | 89 / 1 . | KYD16 | 39.90 | 59.55 | 99.84 |
| | 17 / 1 . | ML12B | 39.57 | 59.45 | 99.08 |
| | 24 / 1 . | ML12B | 39.28 | 56.53 | 98.49 |
| | 28 / 1 . | ML12B | 38.17 | 57.87 | 96.08 |
| | 78 / 1 . | D4 | 38.36 | 58.81 | 97.34 |
| | 83 / 1 . | D4 | 38.61 | 58.84 | 97.48 |
| | 86 / 1 . | D4 | 38.20 | 58.89 | 97.27 |
| | 18 / 1 . | ML10H | 37.97 | 58.67 | 96.90 |
| | 21 / 1 . | ML10H | 38.38 | 58.70 | 97.09 |
| | 39 / 1 . | ML10D | 38.15 | 59.96 | 98.83 |
| | 43 / 1 . | ML10D | 38.00 | 59.46 | 97.53 |
| | 10 / 1 . | ML10I | 39.00 | 60.20 | 99.25 |
| | 15 / 1 . | ML10I | 39.99 | 59.56 | 99.70 |
| | 21 / 1 . | ML10I | 39.31 | 58.85 | 98.53 |
| | 26 / 1 . | ML10I | 38.83 | 59.52 | 98.53 |
| | 32 / 1 . | ML10I | 39.05 | 59.26 | 98.47 |
| **Vein** | 20 / 1 . | KYD14 | 38.91 | 60.28 | 99.29 |
| **Hosted** | 26 / 1 . | KYD14 | 39.23 | 60.71 | 99.99 |
| | 28 / 1 . | KYD14 | 39.13 | 61.03 | 100.30 |

| | EPMA Point | Sample | S | Fe | Total |
|---|---|---|---|---|---|
| **Vein** | 34 / 1 . | KYD14 | 40.09 | 59.97 | 100.23 |
| **Hosted** | 40 / 1 . | KYD14 | 39.38 | 60.28 | 99.82 |
| | 42 / 1 . | ML13 | 39.58 | 59.95 | 99.79 |
| | 52 / 1 . | ML13 | 39.33 | 60.26 | 99.91 |
| | 3 / 1 . | ML52D | 38.58 | 61.38 | 100.09 |
| | 9 / 1 . | ML52D | 38.67 | 61.21 | 100.00 |
| | 10 / 1 . | ML52D | 39.41 | 60.58 | 100.06 |
| | 11 / 1 . | ML52D | 39.99 | 60.56 | 100.64 |
| | 14 / 1 . | ML52D | 39.83 | 60.78 | 100.70 |
| | 20 / 1 . | ML52D | 38.93 | 61.53 | 100.64 |
| | 31 / 1 . | ML52D | 39.80 | 60.64 | 100.65 |
| | 56 / 1 . | D7C | 38.81 | 61.17 | 100.23 |
| | 60 / 1 . | D7C | 39.06 | 61.42 | 100.60 |
| | 62 / 1 . | D7C | 39.44 | 60.50 | 100.10 |
| | 65 / 1 . | D7C | 40.06 | 60.13 | 100.34 |
| | 70 / 1 . | D7C | 39.43 | 60.57 | 100.02 |
| | 1 / 1 . | STOCK3 | 39.67 | 60.76 | 100.50 |
| | 8 / 1 . | STOCK3 | 39.80 | 59.94 | 99.91 |
| | 12 / 1 . | STOCK3 | 39.53 | 60.62 | 100.22 |
| | 13 / 1 . | STOCK3 | 39.01 | 61.08 | 100.16 |
| | 13 / 2 . | STOCK3 | 39.01 | 61.08 | 100.16 |
| | 15 / 1 . | STOCK3 | 39.44 | 60.41 | 100.09 |
| | 16 / 1 . | STOCK3 | 39.38 | 61.36 | 100.78 |
| | 23 / 1 . | KYD-07 | 39.08 | 61.16 | 100.38 |
| | 24 / 1 . | KYD-07 | 38.88 | 61.62 | 100.54 |
| | 29 / 1 . | KYD-07 | 38.81 | 61.06 | 100.03 |
| | 33 / 1 . | ML5_2B | 38.43 | 61.51 | 99.99 |
| | 34 / 1 . | ML5_2B | 40.17 | 60.63 | 100.98 |
| | 35 / 1 . | ML5_2B | 38.98 | 61.41 | 100.40 |
| | 36 / 1 . | ML5_2B | 39.01 | 61.19 | 100.22 |
| | 31 / 1 . | ML19C | 37.32 | 59.62 | 97.16 |
| | 31 / 2 . | ML19C | 37.32 | 59.62 | 97.16 |
| | 39 / 1 . | ML16A | 39.64 | 58.74 | 98.70 |
| | 44 / 1 . | ML16A | 38.53 | 59.43 | 98.32 |
| | 45 / 1 . | ML16A | 38.70 | 58.96 | 97.75 |
| | 47 / 1 . | ML16A | 38.23 | 60.28 | 98.71 |

**Table 6:** Major element composition of chalcopyrite in three types of mineralization.

| | EPMA Point | Sample | S | Fe | Cu | Total |
|---|---|---|---|---|---|---|
| **Laminated/** | 59 / 1 . | D24-2 | 33.36 | 29.78 | 34.47 | 97.86 |
| **Disseminated** | 60 / 1 . | D24-2 | 34.18 | 29.58 | 34.19 | 98.44 |
| | 69 / 1 . | D24-2 | 33.71 | 29.98 | 34.23 | 98.43 |
| | 3 / 1 . | ML19A | 33.66 | 29.44 | 34.86 | 98.05 |
| **Massive** | 7 / 1 . | KYD34 | 35.00 | 30.73 | 33.72 | 99.56 |
| | 32 / 1 . | KYD21 | 34.82 | 30.68 | 33.71 | 99.23 |
| | 38 / 1 . | KYD21 | 34.84 | 30.78 | 33.76 | 99.39 |
| | 52 / 1 . | KYD21 | 34.70 | 30.96 | 33.53 | 99.37 |
| | 43 / 1 . | KYD21 | 34.87 | 30.51 | 33.80 | 99.31 |
| | 48 / 1 . | KYD21 | 35.01 | 30.73 | 33.56 | 99.92 |
| | 52 / 1 . | KYD21 | 34.70 | 30.96 | 33.53 | 99.37 |
| | 75 / 1 . | D4 | 32.68 | 29.04 | 34.01 | 96.46 |
| | 81 / 1 . | D4 | 35.22 | 29.14 | 34.68 | 99.14 |
| | 82 / 1 . | D4 | 33.80 | 29.07 | 34.42 | 97.46 |
| | 85 / 1 . | D4 | 34.10 | 28.97 | 33.04 | 96.66 |
| | 19 / 1 . | ML10I | 34.79 | 29.62 | 33.31 | 99.82 |
| | 23 / 1 . | ML10I | 34.98 | 29.20 | 33.59 | 98.89 |
| | 25 / 1 . | ML10I | 34.52 | 29.57 | 34.25 | 98.50 |
| **Vein** | 21 / 1 . | KYD14 | 34.90 | 30.29 | 33.49 | 98.71 |
| **Hosted** | 23 / 1 . | KYD14 | 34.90 | 30.13 | 33.81 | 98.96 |
| | 25 / 1 . | KYD14 | 35.19 | 30.27 | 33.68 | 99.44 |
| | 27 / 1 . | KYD14 | 35.19 | 30.53 | 33.55 | 99.35 |
| | 29 / 1 . | KYD14 | 34.90 | 30.08 | 33.98 | 99.12 |
| | 33 / 1 . | KYD14 | 35.15 | 30.30 | 34.06 | 99.64 |
| | 39 / 1 . | KYD14 | 34.94 | 30.22 | 34.39 | 99.76 |
| | 44 / 1 . | ML13 | 34.73 | 30.46 | 34.01 | 100.10 |
| | 55 / 1 . | ML13 | 34.96 | 30.37 | 34.38 | 100.18 |
| | 15 / 1 . | ML52D | 35.14 | 30.56 | 34.08 | 99.94 |
| | 22 / 1 . | ML52D | 34.79 | 30.53 | 34.20 | 99.58 |
| | 24 / 1 . | ML52D | 35.36 | 30.35 | 34.15 | 99.90 |
| | 57 / 1 . | D7C | 34.91 | 30.99 | 33.96 | 99.95 |
| | 61 / 1 . | D7C | 34.93 | 31.11 | 34.02 | 100.11 |
| | 63 / 1 . | D7C | 34.86 | 30.73 | 34.00 | 99.67 |
| | 66 / 1 . | D7C | 34.82 | 31.20 | 33.54 | 99.56 |
| | 69 / 1 . | D7C | 35.61 | 30.67 | 33.94 | 100.42 |
| | 2 / 1 . | STOCK3 | 35.30 | 30.97 | 33.95 | 100.30 |
| | 4 / 1 . | STOCK3 | 35.69 | 30.62 | 34.05 | 100.56 |
| | 6 / 1 . | STOCK3 | 34.89 | 30.66 | 33.70 | 99.55 |
| | 10 / 1 . | STOCK3 | 35.28 | 30.99 | 33.70 | 100.06 |
| | 14 / 1 . | STOCK3 | 35.19 | 30.54 | 33.66 | 99.43 |
| | 17 / 1 . | STOCK3 | 35.22 | 30.64 | 34.13 | 100.08 |
| | 20 / 1 . | KYD-07 | 34.93 | 30.79 | 34.32 | 100.21 |
| | 26 / 1 . | KYD-07 | 34.78 | 30.95 | 34.38 | 100.18 |
| | 29 / 1 . | ML19C | 34.10 | 29.43 | 34.87 | 98.80 |
| | 32 / 1 . | ML19C | 33.54 | 29.50 | 34.74 | 97.83 |

**Table 7:** Major element composition of arsenopyrite in massive sulfide mineralization.

| EPMA Point | Sample | S | Fe | Co | Ni | As | Total |
|---|---|---|---|---|---|---|---|
| 1 / 1 . | KYD34 | 18.43 | 33.70 | 0.57 | 0.27 | 47.73 | 100.76 |
| 2 / 1 . | KYD34 | 18.57 | 33.79 | 0.60 | 0.30 | 47.69 | 100.96 |
| 3 / 1 . | KYD34 | 18.31 | 33.80 | 0.49 | 0.32 | 47.56 | 100.48 |
| 11 / 1 . | KYD34 | 18.23 | 33.72 | 0.56 | bdl | 47.50 | 100.32 |
| 12 / 1 . | KYD34 | 18.30 | 34.06 | 0.48 | bdl | 47.59 | 100.61 |
| 13 / 1 . | KYD34 | 18.05 | 33.49 | 0.46 | 0.21 | 47.79 | 99.99 |
| 14 / 1 . | KYD34 | 18.01 | 33.83 | 0.51 | 0.28 | 47.75 | 100.40 |
| 15 / 1 . | KYD34 | 18.41 | 33.86 | 0.59 | 0.26 | 47.69 | 100.83 |
| 16 / 1 . | KYD34 | 18.30 | 33.58 | 0.52 | 0.35 | 47.84 | 100.60 |
| 96 / 1 . | KYD16 | 18.47 | 34.21 | 0.41 | bdl | 48.27 | 102.41 |
| 98 / 1 . | KYD16 | 18.47 | 33.94 | 0.42 | bdl | 47.84 | 102.44 |
| 100 / 1 . | KYD16 | 18.06 | 33.62 | 0.63 | 0.22 | 47.26 | 100.08 |
| 103 / 1 . | KYD16 | 19.69 | 34.53 | 0.45 | 0.00 | 46.45 | 101.21 |
| 105 / 1 . | KYD16 | 18.66 | 34.14 | 0.49 | bdl | 47.09 | 100.64 |
| 108 / 1 . | KYD16 | 18.84 | 33.62 | 0.51 | bdl | 46.45 | 99.77 |
| 6 / 1 . | ML12B | 18.54 | 33.55 | 0.69 | 0.24 | 47.33 | 100.56 |
| 10 / 1 . | ML12B | 18.06 | 32.72 | 0.90 | 0.26 | 47.82 | 99.84 |
| 11 / 1 . | ML12B | 18.43 | 33.24 | 0.78 | 0.35 | 47.90 | 100.75 |
| 8 / 1 . | ML10H | 17.11 | 32.96 | 0.57 | 0.27 | 48.46 | 99.37 |
| 11 / 1 . | ML10H | 17.21 | 32.28 | 0.71 | 0.35 | 48.11 | 98.66 |
| 13 / 1 . | ML10H | 17.78 | 33.61 | 0.44 | bdl | 47.67 | 99.69 |
| 14 / 1 . | ML10H | 17.27 | 33.10 | 0.68 | 0.36 | 48.42 | 100.01 |
| 24 / 1 . | ML10H | 18.18 | 33.55 | 0.39 | bdl | 46.12 | 98.32 |
| 44 / 1 . | ML10D | 18.35 | 33.75 | 0.45 | bdl | 45.91 | 98.51 |
| 45 / 1 . | ML10D | 17.28 | 33.09 | 0.62 | bdl | 47.55 | 98.64 |
| 46 / 1 . | ML10D | 17.92 | 33.57 | 0.33 | bdl | 47.88 | 100.55 |
| 1 / 1 . | ML10I | 17.82 | 32.74 | 1.13 | 0.53 | 48.42 | 100.74 |
| 2 / 1 . | ML10I | 19.39 | 33.39 | 0.76 | bdl | 45.48 | 99.15 |
| 3 / 1 . | ML10I | 18.38 | 32.95 | 1.29 | 0.22 | 47.68 | 100.81 |
| 5 / 1 . | ML10I | 17.96 | 32.45 | 1.09 | 0.52 | 48.16 | 100.17 |
| 6 / 1 . | ML10I | 18.99 | 33.33 | 0.90 | bdl | 46.43 | 99.75 |
| 7 / 1 . | ML10I | 18.72 | 33.39 | 0.90 | 0.17 | 47.08 | 100.28 |
| 30 / 1 . | ML10I | 17.61 | 32.15 | 1.35 | bdl | 48.28 | 99.55 |
| 31 / 1 . | ML10I | 18.69 | 33.39 | 0.87 | bdl | 46.22 | 99.27 |

**Table 8:** Major element composition of löllingite in massive sulfide mineralization.

| EPMA Point | Sample | S | Fe | Co | Ni | As | Total |
|---|---|---|---|---|---|---|---|
| 99 / 1 . | KYD16 | 2.81 | 27.33 | 0.70 | 1.17 | 68.63 | 100.63 |
| 4 / 1 . | ML12B | 1.68 | 24.48 | 1.46 | 2.83 | 71.31 | 101.82 |
| 5 / 1 . | ML12B | 1.77 | 24.50 | 1.42 | 2.65 | 70.05 | 100.55 |
| 7 / 1 . | ML12B | 1.99 | 24.53 | 1.54 | 2.46 | 70.29 | 100.85 |
| 8 / 1 . | ML12B | 2.13 | 24.25 | 1.71 | 2.27 | 69.36 | 99.74 |
| 12 / 1 . | ML12B | 1.78 | 24.57 | 1.28 | 2.79 | 69.96 | 100.47 |
| 13 / 1 . | ML12B | 1.80 | 24.42 | 1.30 | 2.88 | 70.01 | 100.43 |
| 9 / 1 . | ML10H | 2.69 | 25.93 | 0.72 | 1.62 | 69.53 | 100.53 |
| 9 / 2 . | ML10H | 2.69 | 25.93 | 0.72 | 1.62 | 69.53 | 100.53 |
| 10 / 1 . | ML10H | 2.53 | 25.49 | 0.74 | 1.86 | 67.77 | 98.43 |

**Table 9:** Major element composition of sulfosalts associated with massive sulfide mineralization.

| Mineral | Gudmundite | | Pyragyrite | | Breithauptite | | |
|---|---|---|---|---|---|---|---|
| EPMA Point | 87 / 1 . | 90 / 1 . | 91 / 1 . | 92 / 1 . | 11 / 1 . | 12 / 1 . | 13 / 1 . |
| Sample | KYD16 | KYD16 | KYD16 | KYD16 | ML10I | ML10I | ML10I |
| S | 15.48 | 15.47 | 17.25 | 17.44 | bdl | bdl | bdl |
| Fe | 27.09 | 27.02 | 0.46 | 0.35 | bdl | bdl | bdl |
| Co | bdl | bdl | bdl | 0.00 | bdl | bdl | bdl |
| Ni | bdl | bdl | bdl | bdl | 32.66 | 32.49 | 32.26 |
| Cu | bdl | 0.18 | 0.00 | 0.00 | bdl | bdl | bdl |
| Zn | 0.10 | 0.48 | bdl | 0.11 | bdl | 0.45 | 0.33 |
| As | 1.66 | 1.79 | 0.38 | 0.39 | 2.51 | 2.59 | 2.50 |
| Se | bdl | bdl | bdl | bdl | bdl | bdl | bdl |
| Ag | bdl | bdl | 58.93 | 58.57 | bdl | bdl | bdl |
| Cd | bdl | bdl | 0.51 | 0.69 | bdl | bdl | bdl |
| Sb | 58.63 | 58.60 | 20.52 | 23.74 | 69.18 | 69.08 | 68.31 |
| Te | bdl | bdl | bdl | bdl | bdl | bdl | bdl |
| Bi | bdl | bdl | bdl | bdl | bdl | bdl | bdl |
| Pb | bdl | bdl | bdl | bdl | bdl | bdl | bdl |
| Total | 103.01 | 103.65 | 98.14 | 101.34 | 104.86 | 104.77 | 103.73 |

**Table 10:** Trace element composition of sphalerite in disseminated/laminated, massive and vein-type mineralization.

| | **Laminated/Disseminated** | | | | | | | | |
|---|---|---|---|---|---|---|---|---|---|
| EPMA Ref | 58 / 1 . | 63 / 1 . | 65 / 1 . | 66 / 1 . | 67 / 1 . | 68 / 1 . | 74 / 1 . | 2 / 1 . | 2 / 2 . |
| Sample No | D24-2 | D24-2 | D24-2 | D24-2 | D24-2 | D24-2 | D24-2 | ML19A | ML19A |
| **V51** | <0.202 | <0.114 | <0.094 | <0.088 | <0.105 | <0.109 | <0.131 | 0.093 | <0.116 |
| **Cr52** | <4.96 | <2.85 | <1.69 | <1.48 | <2.48 | <2.44 | <3.07 | <2.48 | <2.66 |
| **Mn55** | 1184.2 | 1312.48 | 796.32 | 832.63 | 812.42 | 877.01 | 1157.89 | 3424.02 | 3768.39 |
| **Co59** | 116.58 | 94.87 | 91.84 | 93.65 | 63.92 | 65.31 | 96.91 | 97.53 | 74.58 |
| **Ni60** | 0.84 | <0.089 | <0.162 | <0.126 | <0.095 | <0.054 | <0.21 | 0.048 | <0.114 |
| **Cu63** | 2112.83 | 312.08 | 235.55 | 17.68 | 49.85 | 256.55 | 1918.8 | 13.01 | 199.12 |
| **Ga71** | 0.325 | 1.07 | 1.62 | 1.45 | 1.41 | 1.29 | 1.2 | 0.82 | 0.391 |
| **Ge73** | <0.32 | 0.39 | 0.24 | <0.28 | <0.21 | <0.223 | <0.25 | <0.26 | 0.26 |
| **As75** | <0.55 | <0.39 | <3.52 | <3.05 | <0.31 | <0.33 | <0.35 | <0.38 | <0.37 |
| **Se82** | <7.69 | <4.62 | <4.70 | <4.09 | <3.82 | 4.82 | 4.5 | <4.03 | <4.18 |
| **Mo95** | <0.255 | <0.157 | 0.061 | <0.088 | <0.079 | <0.055 | <0.116 | <0.108 | 0.125 |
| **Ag107** | 10.82 | 1.68 | 1.87 | 1.46 | 2.62 | 3 | 4.48 | 1.57 | 2.42 |
| **Cd111** | 1731.97 | 1788.13 | 1839.34 | 1924.55 | 1769.79 | 1839.39 | 1755.01 | 1250.58 | 1281.95 |
| **In115** | 1.26 | 1.06 | 1.27 | 1.34 | 1.19 | 1.21 | 1.23 | 0.082 | 0.088 |
| **Sn118** | <0.71 | 0.64 | 0.32 | 0.44 | <0.38 | 0.45 | <0.44 | 0.47 | 0.61 |
| **Sb121** | 1.1 | <0.164 | 0.095 | 0.078 | 0.229 | 0.397 | 0.174 | <0.152 | <0.176 |
| **Ir193** | <0.00 | <0.00 | <0.00 | <0.00 | <0.00 | <0.00 | <0.00 | <0.0073 | <0.00 |
| **Pt195** | <0.204 | <0.139 | <0.084 | <0.051 | <0.117 | <0.116 | <0.141 | <0.114 | <0.109 |
| **Au197** | 0.29 | <0.124 | <0.075 | <0.062 | <0.108 | <0.102 | <0.143 | <0.107 | <0.099 |
| **Hg202** | 26.22 | 17.97 | 7.28 | 5.7 | 16.56 | 15.23 | 18.06 | 36.63 | 32.9 |
| **Tl205** | 0.485 | <0.028 | 0.033 | <0.0086 | 0.022 | 0.112 | 0.066 | <0.0214 | <0.025 |
| **Pb208** | 2.49 | 0.36 | 0.55 | 0.271 | 0.44 | 3.11 | 16.96 | 2.83 | 4.93 |
| **Bi209** | <0.071 | 0.041 | <0.0144 | <0.0164 | <0.032 | <0.030 | <0.051 | <0.038 | <0.037 |

| | Massive | | | | | | | | | | | | |
|---|---|---|---|---|---|---|---|---|---|---|---|---|---|
| EPMA Ref | 6 / 1 . | 10 / 1 . | 19 / 1 . | 33 / 1 . | 35 / 1 . | 41 / 1 . | 47 / 1 . | 49 / 1 . | 55 / 1 . | 1 / 1 . | 2 / 1 . | 16 / 1 . | 21 / 1 . |
| Sample No | KYD34 | KYD34 | KYD34 | KYD21 | KYD21 | KYD21 | KYD21 | KYD21 | KYD21 | ML12B | ML12B | ML12B | ML12B |
| **V51** | <0.053 | <0.050 | <0.054 | <0.056 | <0.078 | 0.1 | 0.1 | <0.075 | <0.081 | <0.062 | <0.064 | <0.055 | 0.059 |
| **Cr52** | <0.98 | <0.88 | <0.88 | <0.86 | <1.18 | <1.09 | <0.91 | <1.06 | <1.01 | <1.44 | <1.61 | <1.43 | 6.19 |
| **Mn55** | 1089.1 | 1026.3 | 1024.3 | 1261.8 | 1137.8 | 1176.6 | 1135.3 | 1110.7 | 1165.6 | 1393.04 | 1391.58 | 1348.96 | 1414.14 |
| **Co59** | 16.4 | 15.4 | 15.0 | 15.9 | 15.2 | 19.4 | 15.9 | 14.3 | 15.0 | 19.18 | 15.83 | 17.32 | 15.91 |
| **Ni60** | <0.100 | 0.1 | <0.069 | 0.1 | <0.128 | <0.098 | <0.080 | <0.058 | <0.065 | <0.062 | <0.101 | 0.094 | 0.051 |
| **Cu63** | 60.4 | 1172.9 | 30.4 | 1101.9 | 139.8 | 42681.5 | 118.0 | 46.4 | 276.6 | 21.37 | 12.34 | 12.56 | 55.97 |
| **Ga71** | 6.6 | 6.0 | 5.2 | 4.1 | 3.1 | 5.2 | 5.1 | 5.8 | 6.2 | 1.88 | 1.47 | 2.36 | 1.16 |
| **Ge73** | 0.2 | 0.4 | 0.1 | 0.3 | 0.4 | 0.5 | 0.3 | 0.2 | 0.2 | 0.136 | <0.113 | 0.1 | <0.073 |
| **As75** | 3.2 | 2.1 | 1.9 | <0.209 | <0.34 | 0.3 | 0.3 | <0.33 | <0.29 | <0.152 | <0.22 | 1.66 | 1.39 |
| **Se82** | <6.55 | <5.96 | <5.99 | <6.13 | <8.60 | <7.87 | <7.05 | <7.87 | <7.34 | <2.33 | <2.61 | <2.38 | <2.25 |
| **Mo95** | <0.059 | <0.057 | 0.1 | <0.046 | 0.1 | <0.068 | <0.055 | <0.053 | 0.1 | <0.098 | 0.122 | <0.081 | <0.049 |
| **Ag107** | 2.9 | 10.1 | 3.3 | 5.4 | 2.7 | 26.8 | 5.4 | 1.7 | 4.4 | 4.62 | 6.71 | 3.63 | 2.87 |
| **Cd111** | 1564.3 | 1530.7 | 1481.9 | 1564.9 | 1505.6 | 1460.9 | 1491.7 | 1442.1 | 1462.9 | 1058.33 | 1005.49 | 1019.31 | 1069.06 |
| **In115** | 0.1 | 0.1 | 0.2 | 0.1 | 0.1 | 0.2 | 0.1 | 0.1 | 0.1 | 0.056 | 0.25 | 0.268 | 0.286 |
| **Sn118** | 0.6 | 0.5 | 0.5 | 2.1 | 0.4 | 24.0 | 0.9 | 0.6 | 0.7 | 0.86 | 0.83 | 0.42 | 0.56 |
| **Sb121** | 0.2 | 0.6 | 0.1 | 0.5 | 0.2 | 2.6 | 11.0 | 0.1 | 1.1 | <0.076 | 1.1 | 0.344 | 0.553 |
| **Ir193** | 0.0 | <0.00 | <0.00 | <0.00 | <0.0046 | <0.0042 | <0.00 | <0.00 | <0.00 | <0.00 | <0.00 | <0.00 | 0.0011 |
| **Pt195** | 0.0 | <0.0097 | <0.0096 | <0.0177 | 0.0 | <0.0227 | <0.0214 | 0.0 | <0.0201 | <0.066 | <0.064 | <0.065 | <0.052 |
| **Au197** | <0.244 | <0.198 | <0.199 | <0.177 | <0.231 | <0.219 | <0.175 | <0.203 | <0.200 | <0.073 | <0.083 | <0.076 | <0.073 |
| **Hg202** | 10.7 | 9.5 | 9.2 | 10.2 | 13.8 | 8.5 | 16.6 | 14.4 | 12.4 | 10.74 | 25.61 | 14.1 | 14.09 |
| **Tl205** | <0.0065 | 0.0 | 0.0 | 0.0 | <0.0101 | 0.2 | 0.0 | <0.0113 | <0.0102 | 0.0127 | <0.0151 | <0.0110 | <0.0104 |
| **Pb208** | 278.1 | 50.6 | 0.3 | 2.6 | 0.6 | 9.6 | 44.0 | 4.5 | 4.4 | 18.05 | 37.11 | 3.81 | 6.33 |
| **Bi209** | 0.0 | <0.0040 | <0.0040 | <0.0052 | <0.0064 | 0.0 | <0.0066 | <0.0089 | <0.0084 | <0.0214 | 0.072 | <0.0177 | 0.0228 |

| | Massive | | | | | | | | | | | | |
|---|---|---|---|---|---|---|---|---|---|---|---|---|---|
| EPMA Ref | 76 / 1 . | 88 / 1 . | 17 / 1 . | 20 / 1 . | 22 / 1 . | 23 / 1 . | 25 / 1 . | 26 / 1 . | 34 / 1 . | 35 / 1 . | 40 / 1 . | 42 / 1 . | 48 / 1 . |
| Sample No | D4 | D4 | ML10H | ML10H | ML10H | ML10H | ML10H | ML10H | ML10D | ML10D | ML10D | ML10D | ML10D |
| **V51** | <0.111 | 0.07 | <0.076 | <0.076 | <0.104 | <0.100 | <0.099 | <0.096 | <0.108 | <0.103 | <0.073 | <0.079 | <0.072 |
| **Cr52** | 9.03 | 15.95 | <1.53 | <1.53 | <1.62 | <1.60 | <1.73 | <1.49 | 7.49 | <1.91 | <1.56 | <1.52 | <1.65 |
| **Mn55** | 1553.01 | 1618.22 | 1033.01 | 1077.57 | 1093.14 | 1057.29 | 1058.1 | 1124.67 | 788.55 | 785.66 | 1047.69 | 1095.52 | 1136.48 |
| **Co59** | 51.66 | 46.61 | 12.43 | 11.52 | 12.18 | 10.48 | 11.66 | 11.42 | 12.24 | 17.54 | 11.42 | 12.5 | 12.17 |
| **Ni60** | <0.138 | <0.080 | <0.151 | <0.112 | <0.107 | <0.165 | 0.28 | 0.13 | <0.262 | <0.207 | <0.121 | <0.112 | <0.109 |
| **Cu63** | 5.7 | 181.2 | 1832.98 | 1354.36 | 236.05 | 56.13 | 2799.98 | 13.88 | 136.44 | 264.35 | 18.19 | 16.28 | 524.22 |
| **Ga71** | 0.145 | 0.339 | 2.28 | 2.65 | 1.82 | 1.95 | 2.76 | 3.35 | 1.31 | 1.15 | 2.67 | 2.63 | 2.6 |
| **Ge73** | 0.223 | 0.102 | <0.167 | <0.151 | <0.205 | <0.25 | <0.201 | <0.25 | <0.29 | 0.19 | 0.25 | <0.21 | 0.21 |
| **As75** | <0.30 | <0.146 | <1.94 | <1.88 | <2.11 | <2.10 | <2.09 | <2.18 | <1.52 | <1.76 | <1.45 | <1.55 | 3.14 |
| **Se82** | <4.32 | <2.05 | <4.63 | <4.56 | <4.93 | <4.51 | <4.89 | <4.15 | <4.91 | <5.54 | <4.45 | <4.33 | <4.85 |
| **Mo95** | <0.126 | <0.058 | <0.099 | 0.088 | <0.099 | <0.068 | 0.03 | <0.103 | <0.120 | <0.127 | <0.082 | <0.092 | <0.104 |
| **Ag107** | 1.35 | 2.97 | 26.45 | 15.96 | 1.39 | 2.08 | 10.36 | 1.97 | 6.83 | 4.19 | 2.84 | 2.36 | 8.96 |
| **Cd111** | 2272.26 | 1430.03 | 1089.72 | 1059.99 | 1031.95 | 1036.56 | 1100.53 | 1077.55 | 1010.48 | 1055.17 | 1013.7 | 878.97 | 1030.66 |
| **In115** | 1.44 | 1.32 | 0.323 | 0.311 | 0.222 | 0.289 | 0.271 | 0.268 | 0.0483 | 0.071 | 0.0411 | 0.0509 | 0.057 |
| **Sn118** | 0.79 | 0.38 | 1.3 | 0.37 | 0.36 | 0.35 | 0.62 | 0.27 | 1.17 | 0.42 | 0.51 | 0.82 | 0.78 |
| **Sb121** | 0.253 | 0.078 | 3.51 | 1.1 | 0.165 | 0.3 | 1.61 | <0.090 | <0.137 | 1.26 | 0.221 | 0.206 | 0.82 |
| **Ir193** | <0.00 | <0.00 | <0.00 | <0.00 | <0.00 | <0.00 | <0.00 | <0.00 | <0.00 | <0.00 | <0.00 | <0.00 | <0.00 |
| **Pt195** | <0.127 | <0.050 | <0.064 | <0.075 | <0.069 | <0.073 | <0.087 | <0.074 | <0.088 | <0.127 | <0.116 | <0.101 | <0.105 |
| **Au197** | 0.12 | <0.060 | <0.069 | <0.056 | <0.076 | <0.084 | <0.084 | <0.065 | <0.071 | <0.088 | <0.077 | <0.079 | <0.092 |
| **Hg202** | 34.11 | 13.38 | 7.5 | 7.44 | 7.39 | 8.14 | 7.33 | 7.81 | 10.63 | 9.39 | 9.42 | 9.19 | 9.63 |
| **Tl205** | 0.0283 | <0.0111 | 0.235 | 0.151 | <0.0172 | 0.0232 | 0.117 | <0.0119 | <0.044 | 0.207 | <0.0151 | <0.0171 | 0.036 |
| **Pb208** | 11.15 | 25.41 | 19.58 | 9.21 | 0.195 | 0.67 | 1.72 | <0.122 | <0.197 | 0.98 | 8.94 | 0.536 | 1.19 |
| **Bi209** | <0.041 | 0.046 | <0.0201 | 0.0153 | <0.0223 | <0.0236 | <0.0213 | <0.0199 | <0.034 | <0.028 | <0.025 | <0.0242 | <0.025 |

| | Massive | | | | | Vein-Hosted | | | | | | | | |
|---|---|---|---|---|---|---|---|---|---|---|---|---|---|---|
| EPMA Ref | 9 / 1 . | 24 / 1 . | 28 / 1 . | 28 / 2 . | 33 / 1 . | 22 / 1 . | 24 / 1 . | 30 / 1 . | 30 / 1 . | 38 / 1 . | 41 / 1. | 45 / 1 . | 46 / 1 . | 47 / 1 . |
| Sample No | ML10I | ML10I | ML10I | ML10I | ML10I | KYD14 | KYD14 | KYD14 | KYD14 | KYD14 | ML13 | ML13 | ML13 | ML13 |
| **V51** | <0.079 | <0.125 | <0.096 | <0.084 | <0.089 | <0.040 | 0.2 | 0.1 | <0.063 | <0.070 | <0.047 | <0.083 | <0.077 | <0.077 |
| **Cr52** | <1.51 | <1.99 | <1.52 | <1.58 | <1.57 | <0.87 | <0.90 | <0.92 | <1.39 | <1.20 | <0.82 | <1.22 | <1.24 | <1.37 |
| **Mn55** | 2178.03 | 2425.76 | 1973.83 | 2340.75 | 2015.24 | 836.6 | 1182.1 | 1693.6 | 1619.1 | 881.5 | 2774.9 | 2922.7 | 2902.7 | 3275.8 |
| **Co59** | 39.08 | 63.06 | 45.17 | 57.79 | 74.35 | 112.6 | 89.2 | 85.7 | 81.8 | 141.1 | 94.7 | 93.9 | 96.3 | 100.0 |
| **Ni60** | <0.098 | <0.190 | <0.185 | <0.187 | <0.074 | <0.089 | <0.076 | 0.1 | 0.5 | <0.089 | <0.076 | 0.2 | <0.104 | <0.111 |
| **Cu63** | 11.15 | 30.18 | 8.39 | 364.76 | 575.55 | 2675.5 | 509.7 | 112.6 | 5664.2 | 1712.3 | 454.8 | 10.1 | 21.7 | 19.5 |
| **Ga71** | 3.51 | 2.28 | 1.44 | 2.25 | 2.13 | 0.4 | 0.7 | 0.8 | 1.0 | 1.0 | 1.3 | 1.2 | 0.9 | 0.9 |
| **Ge73** | <0.256 | <0.21 | <0.154 | <0.129 | <0.27 | 0.3 | 0.4 | 0.3 | 0.2 | 0.2 | 0.3 | 0.3 | 0.4 | 0.3 |
| **As75** | 3.35 | <3.36 | <2.58 | <2.67 | <2.71 | <1.11 | <1.21 | <1.31 | 3.0 | <1.91 | <0.209 | <0.29 | <0.30 | <0.38 |
| **Se82** | <4.41 | <6.09 | <4.23 | <4.51 | <4.57 | <5.38 | <5.80 | <5.78 | <8.81 | <8.03 | <5.87 | <8.62 | <8.81 | <9.82 |
| **Mo95** | <0.063 | <0.085 | <0.062 | <0.090 | <0.066 | 0.0 | 0.1 | 0.1 | <0.055 | 0.0 | 0.1 | 0.1 | 0.1 | 0.1 |
| **Ag107** | 4.04 | 2.3 | 1.16 | 3.27 | 27.42 | 11.9 | 5.1 | 1.7 | 4.6 | 6.9 | 16.3 | 1.9 | 4.2 | 3.3 |
| **Cd111** | 1039.24 | 1226.27 | 1077.84 | 1117.75 | 1047.75 | 1860.9 | 1586.0 | 1479.8 | 1561.8 | 1822.0 | 1735.2 | 1692.3 | 1628.0 | 1878.8 |
| **In115** | 0.06 | 0.071 | 0.085 | 0.066 | 0.076 | 0.8 | 0.7 | 0.7 | 0.7 | 1.0 | 0.6 | 0.5 | 0.5 | 0.7 |
| **Sn118** | 0.25 | <0.36 | 0.28 | 0.33 | 0.31 | 0.4 | 0.5 | 0.3 | 0.5 | 0.3 | 1.1 | 0.4 | 0.5 | 0.9 |
| **Sb121** | 0.106 | <0.106 | 0.125 | 0.141 | 0.131 | 0.2 | 0.5 | 0.1 | 0.1 | 5.3 | 0.3 | <0.053 | 1.9 | 0.1 |
| **Ir193** | <0.00 | <0.00 | <0.00 | <0.00 | <0.00 | <0.00 | <0.00285 | 0.0 | <0.00 | <0.00 | <0.00 | <0.00 | <0.00 | <0.00 |
| **Pt195** | <0.080 | <0.073 | <0.053 | <0.060 | <0.066 | <0.0190 | <0.0181 | <0.0209 | <0.0147 | <0.0270 | <0.0230 | <0.0194 | <0.024 | <0.039 |
| **Au197** | <0.066 | <0.099 | <0.068 | <0.071 | <0.069 | <0.21 | <0.21 | <0.22 | <0.34 | <0.29 | <0.169 | <0.25 | <0.26 | <0.27 |
| **Hg202** | 12.37 | 13.99 | 13.25 | 10.73 | 10.21 | 4.3 | 9.1 | 7.7 | 7.4 | 7.3 | 6.6 | 13.5 | 15.1 | 12.9 |
| **Tl205** | <0.0175 | <0.0169 | 0.066 | <0.0170 | 0.237 | 4.7 | 1.4 | 0.2 | 0.2 | 5.6 | 0.1 | 0.0 | 0.8 | 0.1 |
| **Pb208** | 0.51 | 0.302 | 5.11 | 0.77 | 2.26 | 4.6 | 1.9 | 0.5 | 1.8 | 11.0 | 0.9 | 0.1 | 82.5 | 1.9 |
| **Bi209** | <0.0192 | <0.0228 | <0.0159 | <0.0205 | <0.0189 | <0.0038 | <0.0033 | <0.0046 | <0.0073 | 0.0 | 0.0 | <0.0057 | 0.0 | <0.0076 |

| | Vein-Hosted | | | | | | | | | | | | |
|---|---|---|---|---|---|---|---|---|---|---|---|---|---|
| EPMA Ref | 49 / 1 . | 54 / 1 . | 56 / 1 . | 9 / 1 . | 27 / 1 . | 28 / 1 . | 33 / 1 . | 35 / 1 . | 40 / 1 . | 43 / 1 . | 43 / 2 . | 48 / 1 . | 50 / 1 . |
| Sample No | ML13 | ML13 | ML13 | STOCK3 | ML19C | ML19C | ML19C | ML16A | ML16A | ML16A | ML16A | ML16A | ML16A |
| **V51** | <0.046 | <0.071 | <0.055 | 0.1 | <0.094 | <0.235 | <0.122 | <0.111 | <0.081 | <0.083 | <0.079 | <0.075 | <0.073 |
| **Cr52** | <0.89 | <1.11 | <0.91 | 1.6 | <2.51 | <5.82 | <2.92 | <1.71 | <1.55 | <1.26 | <1.47 | <1.72 | <1.45 |
| **Mn55** | 2773.1 | 2931.1 | 2810.7 | 2366.6 | 2881.3 | 2259.29 | 3915.19 | 1752.49 | 2212.94 | 2143.99 | 1963.15 | 2161.89 | 2155.9 |
| **Co59** | 100.3 | 111.4 | 100.4 | 93.5 | 100.41 | 106.12 | 115.53 | 41.95 | 37.94 | 44.36 | 45.2 | 41.14 | 44.25 |
| **Ni60** | 0.1 | 0.2 | 0.1 | 0.6 | 0.137 | <0.43 | <0.162 | 0.2 | <0.185 | 0.173 | 0.23 | <0.113 | <0.153 |
| **Cu63** | 136.1 | 85.9 | 215.0 | 2419.4 | 763.25 | 87.16 | 215.81 | 1026.96 | 140.72 | 37.24 | 810.58 | 42.34 | 370.91 |
| **Ga71** | 2.8 | 0.8 | 0.6 | 0.1 | 0.192 | 0.3 | 0.162 | 1.25 | 3.1 | 2.93 | 3.01 | 3.2 | 1.33 |
| **Ge73** | 0.4 | 0.2 | 0.2 | 0.2 | 0.147 | <0.53 | <0.194 | <0.27 | 0.135 | <0.23 | <0.29 | <0.26 | <0.158 |
| **As75** | <0.205 | <0.28 | <0.26 | <2.11 | <1.43 | <3.29 | <1.62 | 4.47 | <2.93 | <2.24 | <2.60 | <3.04 | <2.52 |
| **Se82** | <6.06 | <7.71 | <6.51 | <9.08 | 5.17 | <9.19 | 7.62 | <4.36 | <4.69 | <3.73 | <4.37 | <4.83 | <4.09 |
| **Mo95** | 0.1 | 0.1 | 0.1 | <0.052 | <0.149 | <0.236 | <0.132 | <0.071 | <0.086 | 0.061 | <0.086 | <0.121 | <0.123 |
| **Ag107** | 19.1 | 5.7 | 11.8 | 22.2 | 2.08 | 1.67 | 1.72 | 4.38 | 2.07 | 2.23 | 4.7 | 2.19 | 5.03 |
| **Cd111** | 1682.8 | 1858.9 | 1756.7 | 1841.0 | 1130.62 | 946.2 | 1077.36 | 1243.68 | 1099.97 | 1123.65 | 1064.96 | 1081.14 | 1287.27 |
| **In115** | 0.7 | 0.8 | 0.5 | 0.0 | 1.13 | 1.08 | 1.11 | 0.096 | 0.055 | 0.068 | 0.055 | 0.066 | 0.057 |
| **Sn118** | 0.5 | 0.6 | 0.7 | 0.3 | <0.37 | 0.83 | 0.47 | 0.56 | 0.49 | 0.39 | 0.34 | 0.68 | 0.37 |
| **Sb121** | 0.3 | <0.050 | 1.5 | 0.3 | <0.102 | <0.27 | <0.121 | 0.161 | 0.262 | 0.118 | 0.46 | 0.115 | 0.227 |
| **Ir193** | <0.00 | <0.00 | <0.0033 | <0.00 | <0.00 | <0.00 | <0.00 | <0.00 | <0.00 | 0.0019 | <0.00 | <0.00 | <0.00 |
| **Pt195** | <0.0168 | <0.025 | 0.0 | <0.034 | <0.080 | <0.213 | <0.104 | <0.069 | <0.064 | <0.061 | <0.051 | 0.051 | <0.051 |
| **Au197** | <0.192 | <0.23 | <0.187 | <0.42 | <0.14 | <0.31 | <0.148 | <0.074 | <0.079 | <0.051 | <0.060 | <0.061 | <0.065 |
| **Hg202** | 7.9 | 12.7 | 8.5 | 11.3 | 14.22 | 29.57 | 15.34 | 14.05 | 12.25 | 11.56 | 9.54 | 14.17 | 11.84 |
| **Tl205** | 0.0 | 0.0 | 0.6 | 0.2 | 0.113 | 0.237 | 0.028 | 0.151 | 0.0227 | <0.0093 | 0.247 | <0.0148 | 0.036 |
| **Pb208** | 7.4 | 0.3 | 147.1 | 4.5 | 2.11 | 7.95 | 0.75 | 1.64 | 0.62 | 0.43 | 8.28 | 3.8 | 2.84 |
| **Bi209** | 0.0 | 0.0 | 0.0 | 0.0 | <0.026 | <0.054 | <0.032 | 0.029 | <0.0189 | <0.0177 | <0.0194 | <0.0235 | <0.0168 |

| **Table 11:** Trace element composition galena in disseminated/laminated, massive and vein-type mineralization | | | | | | | | | | | | | |
|---|---|---|---|---|---|---|---|---|---|---|---|---|---|
| | **Laminated/Disseminated** | | | | **Massive** | | | | | | | | |
| EPMA Ref | 57 / 1 . | 62 / 1 . | 71 / 1 . | 7 / 1 . | 4 / 1 . | 5 / 1 . | 9 / 1 . | 40 / 1 . | 45 / 1 . | 54 / 1 . | 54 / 1 . | 14 / 1 . | 22 / 1 . |
| Sample No | D24-2 | D24-2 | D24-2 | ML19A | KYD34 | KYD34 | KYD34 | KYD21 | KYD21 | KYD21 | KYD21 | ML12B | ML12B |
| **V51** | <0.127 | <0.106 | <0.135 | 43.79 | <0.044 | 0.0 | <0.031 | <0.037 | 0.096 | <0.041 | <0.047 | <0.209 | <0.060 |
| **Cr52** | 8.63 | 13.14 | 10.16 | 34.14 | 1.4 | 2.3 | 2.7 | 0.6 | 2.03 | 5.5 | <0.61 | 16.33 | 5.76 |
| **Mn55** | 4.12 | 2.02 | 2.05 | 200.94 | 0.7 | 0.7 | 1.1 | 0.6 | 1.2 | 0.7 | 1.9 | <1.55 | 0.79 |
| **Fe57** | 58.9 | 17.36 | <8.85 | 1928.35 | 958.8 | 6.7 | 148.1 | 4.0 | 51.19 | 4.4 | <4.01 | 12241.48 | 11.38 |
| **Co59** | <0.061 | <0.060 | <0.034 | 0.21 | 0.5 | 0.2 | 1.2 | <0.0092 | 0.0148 | <0.0115 | <0.0097 | 253.35 | <0.029 |
| **Ni60** | <0.179 | <0.086 | <0.121 | 3.17 | 2.2 | 2.2 | 0.1 | 10.4 | 0.422 | <0.034 | 0.0 | 34.43 | 0.086 |
| **Cu63** | 0.73 | 0.375 | <0.152 | 1.07 | 1237.6 | 0.6 | 171.6 | 30.5 | 19.54 | 0.2 | 8.3 | <0.32 | 0.279 |
| **Zn66** | <3.91 | <3.28 | <3.57 | 47.4 | 49.0 | 2.7 | 4.9 | 0.6 | 51.35 | <0.32 | 0.6 | <5.63 | 5.47 |
| **Ga71** | <0.047 | <0.043 | <0.047 | 8.35 | <0.0087 | <0.00 | <0.0056 | 0.0 | 0.007 | 0.0 | 0.0 | <0.095 | <0.038 |
| **Ge73** | <0.40 | <0.273 | <0.202 | 3.84 | 0.0 | <0.063 | 0.0 | <0.073 | <0.151 | <0.087 | <0.104 | <0.37 | <0.122 |
| **As75** | <0.42 | 0.38 | <0.34 | <2.24 | 760.4 | 427.3 | 318.5 | 1.1 | 0.74 | 1.1 | 0.7 | 22483.87 | 154.18 |
| **Se82** | 76.55 | 23.12 | 34.68 | 29.47 | 16.8 | 13.5 | 21.7 | 32.8 | <6.50 | 17.8 | 9.7 | <8.51 | <2.32 |
| **Mo95** | <0.141 | <0.137 | <0.122 | 3.03 | <0.049 | <0.0193 | <0.032 | <0.0245 | <0.088 | <0.027 | <0.026 | <0.141 | <0.058 |
| **Ag107** | 682.84 | 438.47 | 629.95 | 141.28 | 6847.8 | 283.1 | 3923.0 | 188.7 | 187.59 | 194.4 | 304.0 | 739.81 | 790.64 |
| **Cd111** | 3.73 | 9.1 | 6.94 | 16.46 | 5.2 | 5.6 | 9.2 | 5.0 | 4.98 | 3.6 | 3.6 | 4.47 | 3.51 |
| **In115** | <0.0170 | <0.0115 | <0.0123 | <0.070 | 0.2 | 0.2 | 0.1 | 0.2 | 0.187 | 0.2 | 0.2 | 0.336 | 0.346 |
| **Sn118** | 1.65 | 1.14 | 1.94 | 14.2 | 51.1 | 49.2 | 39.5 | 79.6 | 55.55 | 50.0 | 50.0 | 95.46 | 109.14 |
| **Sb121** | 67.59 | 72.71 | 81.03 | 72.27 | 1951.9 | 288.7 | 1314.7 | 205.8 | 179.28 | 195.6 | 243.4 | 30.3 | 48.08 |
| **Ir193** | <0.00 | <0.00 | <0.00 | <0.00 | 0.0 | 0.0 | 0.0 | <0.00 | <0.00 | <0.00 | <0.00 | <0.00 | <0.00 |
| **Pt195** | <0.133 | <0.097 | <0.102 | <0.68 | <0.0166 | <0.0160 | <0.0118 | <0.0093 | <0.0235 | <0.0101 | <0.0139 | <0.221 | <0.060 |
| **Au197** | <0.160 | <0.131 | <0.139 | <0.81 | <0.160 | 0.2 | <0.127 | <0.125 | <0.177 | <0.106 | <0.128 | <0.26 | <0.075 |
| **Hg202** | <0.20 | <0.146 | <0.155 | 0.86 | 132.7 | <0.199 | 3.8 | <0.112 | <0.163 | <0.102 | 0.3 | <0.49 | <0.157 |
| **Tl205** | 208.39 | 154.5 | 156.15 | 16.04 | 38.4 | 37.8 | 41.2 | 38.9 | 47.04 | 1.5 | 7.0 | 21.32 | 20.96 |
| **Bi209** | 827.29 | 560.07 | 749.98 | 29.59 | 48.4 | 48.2 | 43.7 | 44.8 | 44.85 | 43.6 | 48.7 | 1830.8 | 1771 |

| | Massive | | | | | | | | | | | | |
|---|---|---|---|---|---|---|---|---|---|---|---|---|---|
| EPMA Ref | 77 / 1 . | 80 / 1 . | 84 / 1 . | 84 / 2 . | 89 / 1 . | 15 / 1 . | 19 / 1 . | 19 / 2 . | 37 / 1 . | 38 / 1 . | 49 / 1 . | 4 / 1 . | 17 / 1 . |
| Sample No | D4 | D4 | D4 | D4 | D4 | ML10H | ML10H | ML10H | ML10D | ML10D | ML10D | ML10I | ML10I |
| **V51** | 0.251 | <0.063 | 0.25 | <0.25 | 0.72 | <0.091 | <0.075 | <0.073 | <0.070 | <0.077 | <0.080 | <0.063 | <0.086 |
| **Cr52** | 5.69 | 13.73 | 8.99 | 58.34 | 14.34 | 4.77 | 2.02 | 2.38 | 3.15 | 1.63 | 4.41 | 5.68 | 4.1 |
| **Mn55** | 1.8 | 1.08 | <1.21 | 3.01 | 8.74 | 0.52 | 1.12 | 12.55 | 1.3 | 1.09 | 7.73 | 1.05 | 4.49 |
| **Fe57** | 47.8 | <4.74 | <14.03 | <20.98 | 221.17 | <7.03 | <6.56 | 677 | 15.66 | 84.84 | 391.29 | <5.86 | 20 |
| **Co59** | <0.034 | <0.034 | <0.126 | <0.160 | <0.064 | <0.035 | <0.030 | 0.232 | 0.132 | <0.033 | 0.127 | <0.039 | <0.033 |
| **Ni60** | 0.186 | 0.296 | <0.59 | <0.82 | <0.136 | <0.128 | 0.109 | 19.82 | <0.100 | <0.092 | <0.065 | <0.135 | <0.137 |
| **Cu63** | 1.44 | 0.137 | 1.68 | <0.49 | 6.6 | 2.02 | 2.54 | 11.75 | 0.53 | 0.39 | 0.255 | 0.106 | 0.35 |
| **Zn66** | 8.32 | <1.94 | 4.96 | <8.02 | 30.02 | 21.94 | 2.42 | 7580.82 | 23.25 | 13.03 | 3559.58 | <1.26 | 45.83 |
| **Ga71** | <0.026 | <0.035 | <0.149 | <0.183 | <0.057 | <0.031 | <0.0191 | 0.043 | 0.0142 | <0.026 | 0.053 | <0.0160 | <0.029 |
| **Ge73** | 0.099 | <0.086 | <0.46 | <0.52 | <0.25 | <0.149 | <0.075 | <0.074 | <0.27 | <0.218 | <0.157 | <0.241 | <0.162 |
| **As75** | <0.20 | <0.183 | <0.52 | <0.75 | 0.49 | 130.87 | 112.43 | 109.53 | 82.91 | 67.43 | 142.38 | 226.15 | 153.91 |
| **Se82** | 12.07 | 11.85 | 17.36 | 19.15 | 17.22 | 12.83 | 69.35 | 67.54 | 7.57 | 7.45 | 14.62 | 12.01 | 10.5 |
| **Mo95** | 0.9 | <0.053 | <0.25 | <0.38 | 1.2 | <0.102 | <0.051 | <0.088 | <0.104 | 0.019 | 0.251 | <0.096 | <0.125 |
| **Ag107** | 1544.13 | 674.25 | 1202.61 | 1332.85 | 611 | 652.83 | 703.04 | 639.88 | 1199.12 | 712.41 | 946.7 | 238.98 | 342.5 |
| **Cd111** | 17.05 | 25.03 | 100.81 | 17.04 | 5.41 | 3.7 | 4.01 | 21.26 | 6.46 | 3.95 | 10.85 | 4.74 | 5.47 |
| **In115** | 0.431 | 0.65 | 0.45 | 0.257 | 0.349 | 0.0277 | 0.046 | 0.064 | 0.235 | 0.251 | 0.135 | 0.107 | 0.108 |
| **Sn118** | 142.57 | 208.6 | 141.1 | 102.67 | 107.72 | 12.48 | 16.37 | 14.37 | 71.4 | 77.26 | 42.91 | 32.81 | 34.47 |
| **Sb121** | 102.89 | 81.99 | 255.04 | 301.09 | 8.26 | 510.66 | 598.86 | 603.97 | 768.72 | 513.34 | 498.31 | 206.92 | 306.03 |
| **Ir193** | <0.00 | <0.00 | <0.00 | <0.00 | <0.00 | <0.00 | <0.00 | <0.00 | <0.00 | <0.00 | <0.00 | <0.00 | <0.00 |
| **Pt195** | <0.071 | <0.059 | <0.199 | <0.25 | <0.158 | <0.071 | <0.065 | <0.064 | <0.085 | <0.094 | <0.080 | <0.058 | <0.076 |
| **Au197** | <0.092 | <0.068 | <0.21 | <0.30 | 0.77 | <0.063 | <0.057 | <0.063 | <0.073 | <0.070 | <0.082 | <0.050 | <0.075 |
| **Hg202** | 0.67 | <0.084 | 0.36 | <0.40 | 6.95 | <0.196 | <0.174 | <0.183 | 0.2 | <0.171 | 0.43 | <0.166 | <0.20 |
| **Tl205** | 7.85 | 7.5 | 1.35 | 4.35 | 19.61 | 95.08 | 86.97 | 126.31 | 89.08 | 75.42 | 92.75 | 31.81 | 30.65 |
| **Bi209** | 1431.67 | 1130.72 | 1342 | 1825.03 | 1444.48 | 54.33 | 51.86 | 54.3 | 54.34 | 51.6 | 61.64 | 14.98 | 16.57 |

| | Massive | | | Vein-Hosted | | | | | | | | | | |
|---|---|---|---|---|---|---|---|---|---|---|---|---|---|---|
| EPMA Ref | 17 / 2 . | 27 / 1 . | 27 / 2 . | 36 / 1 . | 43 / 1 . | 48 / 1 . | 51 / 1 . | 51 / 1 . | 7 / 1 . | 37 / 1 . | 38 / 1 . | 46 / 1 . | 49 / 1 . | 51 / 1 . |
| Sample No | ML10I | ML10I | ML10I | KYD14 | ML13 | ML13 | ML13 | ML13 | STOCK3 | ML16A | ML16A | ML16A | ML16A | ML16A |
| **V51** | <0.076 | 0.227 | <0.111 | <0.059 | <0.028 | <0.035 | <0.031 | <0.032 | <0.072 | <0.099 | <0.115 | <0.082 | 0.135 | 0.344 |
| **Cr52** | <1.25 | 5.63 | 15 | 3.1 | 2.0 | 2.6 | 2.5 | 0.6 | 11.4 | 9.1 | 5.69 | 3.38 | 8.81 | 4.06 |
| **Mn55** | 2.64 | 3.14 | 1.59 | 0.4 | 1.3 | 1.7 | 1.1 | 0.9 | 0.5 | 1.52 | 58.92 | 2.13 | 3.05 | 8.9 |
| **Fe57** | 12.82 | 43.52 | 15.43 | 435.9 | 6.6 | <3.73 | <3.47 | <3.38 | 15.0 | <9.17 | 1989.92 | <10.41 | 39.23 | 244.47 |
| **Co59** | <0.038 | <0.045 | <0.36 | <0.028 | <0.0085 | <0.0097 | <0.0108 | <0.0100 | <0.029 | 0.116 | 1.88 | <0.036 | <0.042 | <0.058 |
| **Ni60** | <0.111 | <0.122 | <0.29 | <0.118 | 8.5 | 0.1 | 0.4 | 0.9 | 0.5 | <0.115 | <0.201 | 72.12 | 0.39 | 0.3 |
| **Cu63** | <0.103 | 3.39 | 3.95 | 0.2 | 0.0 | 0.1 | 0.1 | <0.031 | 0.4 | <0.129 | 12.7 | 2.74 | 30.05 | 522.97 |
| **Zn66** | 3.47 | 19.69 | 251.59 | 9.3 | 2.0 | 24.9 | 0.5 | 0.8 | <0.85 | <1.79 | 19492.85 | <1.82 | 19.9 | 40.3 |
| **Ga71** | <0.027 | 0.124 | <0.076 | 0.0 | <0.0040 | 0.0 | 0.0 | <0.0058 | <0.0133 | <0.049 | 0.082 | <0.043 | 0.0071 | <0.056 |
| **Ge73** | <0.127 | <0.155 | <0.29 | <0.058 | <0.068 | <0.049 | <0.052 | <0.062 | <0.144 | <0.142 | 0.074 | <0.212 | <0.143 | <0.30 |
| **As75** | 131.15 | 77.66 | 155.5 | 251.7 | 1.1 | 1.0 | 0.9 | 1.0 | 92.9 | 230.58 | 173.68 | 196.98 | 148.41 | 119.1 |
| **Se82** | 12.63 | 15.07 | 13.17 | 46.5 | 19.4 | 18.2 | 21.7 | 17.4 | 252.9 | 14.76 | 15.69 | 13.74 | 11.03 | 5.64 |
| **Mo95** | 0.357 | 0.19 | <0.102 | 0.0 | 0.0 | <0.026 | <0.031 | <0.0230 | <0.053 | 0.04 | 0.146 | 0.057 | 0.39 | 0.43 |
| **Ag107** | 451.44 | 494.7 | 351.02 | 1541.5 | 1391.2 | 2238.7 | 3098.6 | 3036.6 | 1023.9 | 725.57 | 3100.47 | 961.28 | 7558.78 | 3062.47 |
| **Cd111** | 6.56 | 6.88 | 7.58 | 3.2 | 6.2 | 138.0 | 6.7 | 6.5 | 35.1 | 5.96 | 56.21 | 7.91 | 15.96 | 21.48 |
| **In115** | 0.097 | 0.077 | 0.046 | <0.0048 | 0.1 | 0.3 | 0.0 | 0.0 | 0.0 | 0.099 | <0.0155 | 0.111 | 0.113 | 0.113 |
| **Sn118** | 37.13 | 24.43 | 19.9 | 1.0 | 30.6 | 96.7 | 11.2 | 10.9 | 7.7 | 31.63 | 6.05 | 34.37 | 38.94 | 37.52 |
| **Sb121** | 403.97 | 339.08 | 288.07 | 147.5 | 312.5 | 566.8 | 497.3 | 555.9 | 306.2 | 469.36 | 902.88 | 527.5 | 2276.06 | 1311.39 |
| **Ir193** | <0.00 | <0.00 | <0.00 | 0.0 | 0.0 | <0.00 | <0.00 | <0.00 | 0.0 | <0.00 | <0.00 | 0.0019 | <0.00 | <0.00 |
| **Pt195** | <0.069 | <0.058 | <0.055 | <0.0159 | <0.0085 | <0.0097 | <0.0083 | <0.0136 | <0.043 | <0.069 | <0.099 | <0.088 | <0.053 | <0.069 |
| **Au197** | <0.057 | 0.19 | 0.1 | <0.25 | <0.117 | <0.132 | <0.124 | <0.127 | <0.44 | <0.072 | <0.103 | <0.079 | <0.067 | 2.38 |
| **Hg202** | 0.21 | 2.87 | 1.95 | 2.4 | 0.4 | <0.138 | 2.9 | 2.9 | <0.39 | <0.31 | 0.48 | 1.76 | 1.28 | 3.56 |
| **Tl205** | 38.01 | 39.66 | 44.71 | 134.4 | 147.2 | 103.1 | 102.2 | 107.5 | 5.7 | 32.37 | 52.39 | 23.9 | 49.82 | 55.08 |
| **Bi209** | 14.42 | 14.33 | 15.25 | 338.2 | 1414.7 | 2507.8 | 1622.5 | 1607.5 | 1425.0 | 15.89 | 15.82 | 15.32 | 17.61 | 15.22 |

**Table 12:** Trace element composition of pyrrhotite in disseminated/laminated, massive and vein-type mineralization.

| | **Laminated/Disseminated** | | | | | | | | **Massive** | | | | | |
|---|---|---|---|---|---|---|---|---|---|---|---|---|---|---|
| EPMA Ref | 56 / 1 . | 61 / 1 . | 70 / 1 . | 72 / 1 . | 1 / 1 . | 4 / 1 . | 5 / 1 . | 5 / 2 . | 8 / 1 . | 18 / 1 . | 34 / 1 . | 39 / 1 . | 51 / 1 . | 53 / 1 . |
| Sample No. | D24-2 | D24-2 | D24-2 | D24-2 | ML19A | ML19A | ML19A | ML19A | KYD34 | KYD34 | KYD21 | KYD21 | KYD21 | KYD21 |
| **V51** | <0.47 | <0.48 | <0.50 | <0.48 | <0.54 | 0.78 | <0.67 | <0.68 | <0.156 | <0.114 | <0.180 | <0.167 | <0.158 | <0.27 |
| **Cr52** | <11.33 | <11.72 | 27.65 | <12.54 | <13.92 | <16.94 | <14.90 | <14.75 | <2.58 | <2.05 | <2.74 | <2.34 | <2.10 | <2.80 |
| **Mn55** | <3.10 | <2.97 | 3.12 | <3.17 | <3.55 | <4.40 | <3.91 | <4.10 | 1.7 | 2.2 | 1.1 | 2.6 | 6.5 | <0.85 |
| **Co59** | 249.92 | 255.15 | 261.25 | 261.2 | 308.77 | 378.18 | 388.27 | 391.99 | 17.9 | 56.2 | 28.7 | 12.2 | 1.8 | 25.7 |
| **Ni60** | 306.93 | 291.35 | 321.92 | 309.33 | 284.96 | 819.74 | 724.24 | 718.25 | 70.1 | 136.9 | 26.1 | 2.7 | <0.143 | 23.5 |
| **Cu63** | <0.62 | <0.70 | <0.59 | <0.76 | <0.82 | <1.01 | <0.93 | <0.96 | 246.3 | 8.7 | 2.2 | 0.2 | 0.3 | 2.5 |
| **Zn66** | <13.18 | <14.08 | <13.42 | <14.24 | <16.99 | <21.85 | <18.26 | <18.28 | <1.44 | 2.6 | 2.8 | 115.9 | <1.43 | <1.99 |
| **Ga71** | <0.142 | <0.127 | <0.118 | <0.132 | <0.259 | <0.227 | <0.217 | <0.31 | <0.0188 | 0.0 | 0.0 | 0.0 | <0.02 | <0.041 |
| **Ge73** | 1.15 | <1.07 | 1.56 | <1.12 | <1.70 | 3.58 | 1.53 | <1.57 | 1.2 | 1.4 | 1.6 | 1.6 | 1.4 | 2.7 |
| **As75** | <1.50 | <1.28 | <1.13 | <1.52 | <1.99 | <2.49 | <2.09 | <1.88 | 158.2 | 158.6 | <0.79 | <0.67 | <0.60 | <1.04 |
| **Se82** | <17.89 | <18.46 | <17.87 | <19.45 | <21.70 | <27.16 | <22.99 | <24.15 | <17.28 | <13.61 | <20.46 | <16.46 | <15.37 | <21.64 |
| **Mo95** | <0.38 | <0.48 | <0.43 | <0.49 | 0.44 | <0.89 | 0.37 | <0.65 | 0.1 | <0.101 | <0.123 | <0.135 | <0.131 | <0.133 |
| **Ag107** | 1 | 0.362 | 0.41 | <0.27 | <0.30 | 1.27 | <0.26 | <0.31 | 0.4 | 0.2 | 0.2 | 0.9 | 0.8 | 1.1 |
| **Cd111** | <1.89 | <1.80 | <1.64 | <2.05 | <2.37 | <3.72 | <2.49 | <2.33 | 0.2 | 0.2 | <0.35 | <0.34 | <0.260 | <0.24 |
| **In115** | <0.053 | <0.053 | <0.046 | <0.037 | <0.059 | <0.076 | <0.078 | <0.064 | <0.0128 | <0.0107 | <0.085 | <0.0119 | <0.0107 | <0.0126 |
| **Sn118** | <1.67 | <1.71 | <1.67 | <1.75 | <1.88 | <2.45 | <2.15 | <2.29 | <0.40 | <0.33 | <0.50 | <0.41 | <0.38 | <0.50 |
| **Sb121** | <0.65 | <0.67 | <0.61 | <0.66 | <0.87 | <1.00 | <0.93 | <0.90 | 0.1 | <0.085 | <0.130 | <0.134 | <0.120 | <0.193 |
| **Ir193** | <0.00 | <0.0320 | <0.00 | <0.00 | <0.00 | <0.00 | <0.00 | <0.00 | <0.00 | <0.00 | <0.00 | <0.00 | 0.0 | <0.00 |
| **Pt195** | <0.54 | <0.50 | <0.40 | <0.51 | <0.57 | <0.64 | <0.54 | <0.61 | 0.0 | <0.038 | <0.089 | <0.059 | <0.051 | <0.052 |
| **Au197** | <0.49 | <0.49 | <0.48 | <0.50 | <0.55 | <0.70 | <0.58 | <0.62 | <0.62 | <0.46 | <0.55 | <0.47 | <0.40 | <0.57 |
| **Hg202** | <0.67 | <0.64 | <0.65 | <0.73 | <0.69 | <0.95 | <0.67 | <0.67 | <0.57 | <0.42 | <0.54 | <0.65 | <0.42 | <0.65 |
| **Tl205** | 0.427 | <0.111 | <0.095 | <0.109 | 0.119 | <0.168 | <0.132 | 0.119 | <0.0122 | <0.0135 | 0.0 | 0.1 | <0.0192 | 0.2 |
| **Pb208** | 4 | <0.91 | <0.91 | <0.96 | <1.11 | 2.62 | <1.23 | <1.24 | 584.7 | 0.6 | 2.0 | 147.7 | 31.0 | 8.4 |
| **Bi209** | 0.17 | 0.124 | <0.144 | <0.162 | <0.201 | <0.228 | <0.207 | <0.207 | 0.0 | 0.0 | <0.0162 | 0.0 | <0.0156 | <0.0226 |

| | Massive | | | | | | | | | | Vein-Hosted | | | |
|---|---|---|---|---|---|---|---|---|---|---|---|---|---|---|
| EPMA Ref | 17 / 1 . | 78 / 1 . | 83 / 1 . | 86 / 1 . | 18 / 1 . | 21 / 1 . | 43 / 1 . | 10 / 1 . | 26 / 1 . | 32 / 1 . | 20 / 1 . | 26 / 1 . | 28 / 1 . | 40 / 1 . |
| Sample No. | ML12B | D4 | D4 | D4 | ML10H | ML10H | ML10D | ML10I | ML10I | ML10I | KYD14 | KYD14 | KYD14 | KYD14 |
| **V51** | <0.203 | <0.212 | <0.50 | <0.238 | <0.32 | <0.33 | <0.25 | <0.27 | <0.25 | <0.240 | <0.152 | <0.102 | <0.228 | <0.26 |
| **Cr52** | <5.34 | 16.1 | <10.83 | <5.48 | <6.92 | <5.31 | <5.11 | <5.36 | <4.73 | <4.43 | <3.29 | <2.08 | 9.0 | <4.30 |
| **Mn55** | <1.56 | <1.45 | <3.21 | 4.59 | <2.61 | <2.11 | 2.37 | <2.14 | <1.81 | <1.67 | 4.2 | <0.54 | 2.8 | <1.14 |
| **Co59** | 41.63 | 127.04 | 266.43 | 117.63 | 23.56 | 33.19 | 23.83 | 88.85 | 133.44 | 204.55 | 155.0 | 155.6 | 196.3 | 232.3 |
| **Ni60** | 19.11 | 8.95 | 144.34 | 48.72 | 57.11 | 62.97 | 13.58 | 24.63 | 501.23 | 235.21 | 263.5 | 373.8 | 421.1 | 386.7 |
| **Cu63** | <0.34 | 0.63 | 253.96 | <0.41 | 0.57 | <0.41 | <0.33 | <0.42 | 11.47 | 0.37 | 4451.6 | 82.2 | 661.5 | 25.1 |
| **Zn66** | 5.99 | <5.80 | <12.53 | <5.90 | 209.77 | <6.40 | <6.59 | <6.10 | <5.19 | <4.87 | 4614.3 | 1.8 | 4316.9 | 1846.2 |
| **Ga71** | <0.105 | <0.066 | <0.43 | <0.127 | <0.126 | <0.191 | <0.146 | <0.060 | <0.089 | <0.093 | 1.5 | 0.0 | 0.6 | 0.3 |
| **Ge73** | 0.78 | 0.86 | <1.29 | 1.27 | <0.90 | 0.85 | 1.22 | 1.27 | 1.18 | 1.09 | 2.1 | 1.7 | 2.6 | 1.8 |
| **As75** | 46.07 | <0.52 | <1.22 | <0.67 | 37.19 | 85.65 | 34.33 | 100.46 | 61.47 | 91.85 | 147.9 | 80.7 | 211.2 | 256.8 |
| **Se82** | <8.65 | <8.46 | <18.18 | <9.49 | <20.43 | <15.94 | <15.06 | <16.40 | <13.85 | <12.83 | <20.32 | <13.32 | <26.29 | <28.42 |
| **Mo95** | <0.35 | <0.251 | <0.45 | <0.42 | <0.39 | 0.045 | <0.44 | <0.32 | <0.20 | 0.043 | 0.0 | <0.063 | <0.175 | <0.165 |
| **Ag107** | 12.55 | <0.080 | 3.09 | 5.01 | 4.86 | 3.72 | <0.169 | <0.140 | <0.108 | 0.105 | 28.1 | <0.080 | 56.6 | 1.2 |
| **Cd111** | <0.81 | <0.85 | <1.73 | <0.97 | 0.89 | <0.70 | <0.76 | <0.84 | <0.32 | <0.83 | 13.8 | 0.4 | 14.0 | 5.6 |
| **In115** | <0.0158 | <0.026 | <0.108 | <0.0222 | <0.047 | <0.02 | 0.0094 | <0.032 | <0.0192 | <0.0174 | <0.0201 | <0.0121 | <0.0177 | <0.0213 |
| **Sn118** | <0.72 | <0.74 | <1.58 | <0.82 | <1.17 | <0.94 | <0.90 | <0.84 | <0.79 | <0.68 | <0.46 | <0.28 | <0.63 | <0.64 |
| **Sb121** | <0.28 | <0.24 | <0.57 | 0.78 | 2.2 | 0.48 | <0.34 | <0.32 | <0.30 | <0.29 | 2.5 | <0.068 | 0.5 | <0.171 |
| **Ir193** | <0.00 | 0.0034 | 0.024 | <0.00 | <0.00 | <0.00 | <0.00 | <0.00 | <0.00 | <0.0231 | <0.00 | 0.0 | <0.00 | <0.00 |
| **Pt195** | <0.222 | <0.211 | <0.43 | <0.203 | <0.43 | <0.38 | <0.28 | <0.20 | <0.239 | <0.191 | <0.065 | <0.034 | <0.093 | <0.077 |
| **Au197** | <0.29 | <0.25 | <0.54 | <0.27 | <0.28 | <0.29 | <0.26 | <0.25 | <0.198 | <0.170 | <0.77 | <0.48 | <1.00 | <1.03 |
| **Hg202** | <0.61 | <0.43 | <0.75 | <0.42 | <0.96 | <0.70 | <0.64 | <0.74 | <0.76 | <0.67 | <0.70 | <0.43 | <0.97 | <0.83 |
| **Tl205** | <0.040 | 0.054 | <0.081 | 0.051 | 0.323 | 0.483 | <0.054 | <0.052 | 0.054 | <0.040 | 4.4 | 0.0 | 3.6 | 0.6 |
| **Pb208** | 9.97 | <0.38 | 5.93 | 17.13 | 110.32 | 2.04 | 0.65 | 0.58 | 0.42 | <0.32 | 691.3 | 0.2 | 33.2 | 5.4 |
| **Bi209** | 0.191 | <0.058 | 0.68 | 0.8 | <0.083 | <0.066 | <0.081 | <0.075 | <0.060 | <0.064 | 0.0 | 0.2 | 0.1 | <0.0148 |

| | Vein-Hosted | | | | | | | | | | | | | | |
|---|---|---|---|---|---|---|---|---|---|---|---|---|---|---|---|
| EPMA Ref | 42 / 1 . | 52 / 1 . | 9 / 1 . | 14 / 1 . | 20 / 1 . | 1 / 1 . | 12 / 1 . | 13 / 1 . | 13 / 2 . | 16 / 1 . | 31 / 1 . | 31 / 2 . | 39 / 1 . | 45 / 1 . | 47 / 1 . |
| Sample No. | ML13 | ML13 | ML52D | ML52D | ML52D | STOCK3 | STOCK3 | STOCK3 | STOCK3 | STOCK3 | ML19C | ML19C | ML16A | ML16A | ML16A |
| **V51** | 0.1 | <0.130 | <0.220 | 117.0 | <0.107 | <0.104 | 0.2 | 0.1 | <0.088 | <0.117 | <0.47 | <0.29 | <0.24 | <0.26 | <0.238 |
| **Cr52** | 47.0 | <1.97 | <4.20 | 27.0 | <2.32 | <2.88 | <2.85 | <2.36 | <2.24 | <2.85 | <12.13 | <7.17 | <4.35 | <4.57 | <4.23 |
| **Mn55** | 1.9 | 1.9 | 1.7 | 434.9 | 0.8 | <0.71 | 23.8 | 0.7 | 1.0 | <0.72 | <3.22 | <1.98 | <1.58 | <1.71 | 4.8 |
| **Co59** | 192.2 | 245.7 | 192.4 | 209.0 | 174.2 | 207.4 | 158.9 | 187.3 | 183.8 | 197.3 | 255.7 | 218.19 | 66.69 | 92.75 | 75.03 |
| **Ni60** | 582.6 | 725.0 | 194.6 | 264.6 | 170.4 | 157.5 | 30.8 | 154.2 | 151.7 | 59.6 | 375.63 | 338.61 | 28.34 | 130.96 | 95.67 |
| **Cu63** | 0.6 | 0.8 | 0.4 | 953.2 | <0.113 | 1.1 | 94.5 | 3.8 | 2.1 | <0.161 | 0.92 | 1.25 | 5.76 | <0.46 | 0.3 |
| **Zn66** | 9.1 | 23.1 | 7.0 | 64.4 | <1.14 | <1.29 | 3348.2 | <1.00 | <1.04 | 4.0 | <12.25 | <7.39 | 13.09 | <4.98 | 11.88 |
| **Ga71** | 0.0 | <0.0151 | <0.0317 | 7.1 | <0.0249 | <0.00 | 0.6 | <0.037 | 0.0 | <0.0216 | <0.265 | <0.127 | <0.089 | <0.083 | <0.078 |
| **Ge73** | 1.1 | 1.8 | 1.5 | 9.3 | 1.4 | 1.5 | 2.2 | 1.8 | 1.2 | 1.5 | 1.28 | 1.33 | 0.93 | 0.72 | 0.8 |
| **As75** | 0.6 | 0.9 | 128.0 | 30.9 | 72.6 | 116.5 | 34.6 | 61.1 | 49.7 | 94.8 | 24.39 | 17.71 | 39.66 | 29.37 | 17.42 |
| **Se82** | <13.23 | <13.89 | <27.07 | <17.90 | <14.01 | <15.72 | <16.48 | 21.1 | <13.17 | <16.78 | <18.25 | <10.84 | <12.29 | <13.12 | <12.49 |
| **Mo95** | <0.054 | <0.060 | <0.181 | 0.2 | <0.158 | <0.086 | 0.0 | <0.106 | <0.071 | <0.087 | <0.60 | <0.253 | <0.31 | <0.183 | <0.244 |
| **Ag107** | 0.9 | 0.5 | 40.6 | 4.2 | 1.1 | 1.9 | 2.7 | 0.2 | 25.1 | 0.3 | 0.37 | 1.94 | 1.86 | 0.166 | 0.147 |
| **Cd111** | <0.203 | <0.22 | 1.6 | <0.33 | <0.203 | 0.3 | 11.5 | <0.35 | <0.168 | <0.206 | <1.94 | <0.98 | <0.82 | <0.96 | <1.04 |
| **In115** | <0.0071 | <0.0105 | <0.0162 | <0.0130 | <0.0134 | <0.0143 | <0.0080 | 0.0 | <0.0109 | <0.0145 | <0.051 | <0.0201 | <0.0149 | <0.028 | 0.0146 |
| **Sn118** | <0.30 | <0.34 | 0.9 | 0.7 | <0.35 | <0.40 | <0.43 | <0.35 | <0.33 | <0.41 | <1.58 | <0.96 | <0.66 | <0.72 | <0.69 |
| **Sb121** | 0.2 | <0.095 | <0.131 | 0.4 | <0.073 | <0.083 | <0.081 | <0.079 | <0.077 | <0.084 | <0.53 | <0.33 | 0.46 | <0.25 | <0.243 |
| **Ir193** | <0.00 | 0.0 | <0.00 | 0.0 | <0.00 | <0.00 | <0.00 | <0.00 | <0.00 | <0.0102 | <0.00 | <0.00 | <0.00 | <0.00 | <0.00 |
| **Pt195** | 0.0 | <0.046 | <0.107 | <0.063 | <0.00 | 0.0 | <0.068 | <0.048 | <0.053 | 0.0 | 0.38 | <0.26 | <0.138 | <0.195 | <0.144 |
| **Au197** | <0.37 | <0.39 | <1.04 | <0.68 | <0.58 | <0.70 | <0.74 | <0.61 | <0.58 | <0.71 | <0.65 | <0.32 | <0.21 | <0.18 | <0.171 |
| **Hg202** | <0.36 | <0.35 | <0.91 | <0.67 | <0.48 | <0.69 | <0.80 | <0.57 | <0.51 | <0.65 | <1.23 | <0.70 | <0.70 | <0.76 | <0.84 |
| **Tl205** | 0.1 | 0.1 | 0.3 | 9.2 | 0.1 | 0.2 | 0.0 | <0.0118 | 0.0 | 0.0 | <0.100 | 0.265 | 0.346 | <0.036 | <0.045 |
| **Pb208** | 14.7 | 0.5 | 0.9 | 14.7 | 0.5 | 5.4 | 4.9 | 0.5 | 1138.8 | 0.7 | 1.1 | 7.01 | 8.16 | 3.03 | <0.36 |
| **Bi209** | 0.2 | 0.1 | <0.021 | 0.3 | 0.0 | 0.6 | 0.3 | <0.008 | <0.0075 | 0.2 | <0.125 | <0.079 | <0.049 | <0.043 | <0.051 |

**Table 13:** Trace element composition of chalcopyrite in disseminated/laminated, massive and vein-type mineralization

| | **Laminated/Disseminated** | | | **Massive** | | | | | | | |
|---|---|---|---|---|---|---|---|---|---|---|---|
| EPMA Ref | 59 / 1 . | 69 / 1 . | 3 / 1 . | 7 / 1 . | 32 / 1 . | 52 / 1 . | 52 / 1 . | 81 / 1 . | 82 / 1 . | 85 / 1 . | 25 / 1 . |
| Sample No. | D24-2 | D24-2 | ML19A | KYD34 | KYD21 | KYD21 | KYD21 | D4 | D4 | D4 | ML10I |
| **V51** | <0.53 | <0.52 | <0.55 | <0.089 | <0.107 | <0.113 | <0.180 | <0.53 | <0.248 | <0.27 | <0.210 |
| **Cr52** | <12.42 | <11.46 | <12.60 | <1.51 | 2.5 | <1.70 | <1.88 | <12.91 | <4.78 | <5.28 | <3.76 |
| **Mn55** | <3.41 | <3.29 | <3.43 | 3.5 | 4.3 | 4.7 | 0.9 | <3.90 | <1.37 | 5.71 | <1.34 |
| **Co59** | 3.25 | 3.49 | 2.89 | 21.5 | 0.5 | 0.3 | 0.3 | 5.74 | 1.37 | 2.29 | 0.58 |
| **Ni60** | 2.71 | 0.85 | 37.84 | 29.7 | 0.4 | 0.3 | 4.7 | 76.85 | 1.11 | 1.64 | 0.96 |
| **Zn66** | 357.42 | 609.04 | 286.1 | 289.7 | 622.1 | 341.3 | 288.5 | 1164.59 | 318.74 | 606.28 | 300.57 |
| **Ga71** | 2.16 | 0.42 | 0.36 | 13.4 | 7.0 | 10.4 | 6.0 | <0.32 | 0.185 | 0.289 | 2.92 |
| **Ge73** | <1.25 | <1.01 | 4.65 | 3.6 | 2.3 | 1.8 | 2.3 | 3.97 | 2.78 | 3.04 | 1.15 |
| **As75** | <1.72 | <1.57 | <1.66 | 2360.1 | 1.4 | 1.4 | 1.5 | <1.59 | <0.64 | <0.73 | 286.73 |
| **Se82** | <20.51 | <19.44 | <20.85 | <9.79 | <12.35 | <12.31 | <14.12 | <22.32 | <7.89 | <8.97 | <10.49 |
| **Mo95** | <0.78 | <0.55 | <0.54 | <0.046 | <0.091 | <0.070 | <0.125 | <0.87 | <0.210 | 1.53 | <0.298 |
| **Ag107** | 1079.84 | 184.8 | 344.19 | 82.3 | 91.8 | 72.9 | 900.6 | 1078.28 | 1827.22 | 4089.2 | 369.19 |
| **Cd111** | 2.68 | 2.23 | <2.50 | 1.0 | 2.9 | 0.9 | 0.7 | 24.56 | 3.61 | 2.83 | <0.70 |
| **In115** | 0.266 | 0.396 | 0.142 | 1.0 | 0.8 | 1.0 | 1.2 | 3.79 | 2.69 | 2.74 | 0.111 |
| **Sn118** | 6.7 | 15 | 37.69 | 281.3 | 241.0 | 320.8 | 340.7 | 985.16 | 500.89 | 532.47 | 17.47 |
| **Sb121** | 1.7 | 1.45 | 5.07 | 0.6 | 0.5 | 2.1 | 2.4 | 13.67 | <0.26 | 0.96 | 0.3 |
| **Ir193** | 0.009 | <0.036 | <0.00 | <0.00 | <0.00 | <0.0062 | 0.0 | <0.00 | <0.00 | <0.00 | <0.00 |
| **Pt195** | <0.48 | <0.52 | <0.53 | <0.025 | <0.054 | <0.043 | <0.035 | <0.63 | <0.202 | <0.205 | <0.208 |
| **Au197** | <0.58 | <0.55 | <0.53 | <0.38 | <0.34 | <0.35 | <0.42 | <0.61 | <0.24 | <0.27 | <0.140 |
| **Hg202** | <0.59 | <0.61 | 1 | <0.38 | <0.33 | <0.37 | <0.58 | <0.74 | <0.34 | <0.49 | <0.62 |
| **Tl205** | 1.35 | 1.91 | 0.267 | 0.2 | 0.0 | 0.8 | 5.7 | 1.02 | 0.055 | 0.191 | 1.27 |
| **Pb208** | 7.71 | 5.31 | 78.68 | 95.4 | 12.4 | 15.9 | 25.1 | 15653.61 | 1.69 | 136.63 | 2 |
| **Bi209** | <0.169 | <0.152 | <0.191 | 0.0 | <0.0103 | 0.0 | <0.0186 | 22.3 | 0.083 | 0.393 | <0.047 |

| | Vein-Hosted | | | | | | | | | | | | | |
|---|---|---|---|---|---|---|---|---|---|---|---|---|---|---|
| EPMA Ref | 21 / 1 . | 25 / 1 . | 29 / 1 . | 33 / 1 . | 39 / 1 . | 44 / 1 . | 55 / 1 . | 2 / 1 . | 4 / 1 . | 6 / 1 . | 10 / 1 . | 17 / 1 . | 29 / 1 . | 32 / 1 . |
| Sample No. | KYD14 | KYD14 | KYD14 | KYD14 | KYD14 | ML13 | ML13 | STOCK3 | STOCK3 | STOCK3 | STOCK3 | STOCK3 | ML19C | ML19C |
| **V51** | 0.2 | <0.109 | 0.2 | 0.8 | <0.120 | <0.109 | 0.9 | <0.080 | <0.141 | <0.097 | 0.1 | <0.159 | <0.36 | <0.30 |
| **Cr52** | <2.06 | <2.11 | <1.71 | <1.93 | <2.07 | <1.88 | <1.59 | <2.24 | <2.86 | <2.45 | <2.56 | <3.06 | <10.10 | <8.41 |
| **Mn55** | 0.9 | <0.55 | 0.5 | 34.1 | <0.55 | 2.1 | 26.5 | <0.55 | <0.70 | <0.63 | 3.6 | 1.1 | <2.78 | 2.9 |
| **Co59** | 2.0 | 1.8 | 2.2 | 19.4 | 4.6 | 2.1 | 1.8 | 3.4 | 2.2 | 1.6 | 3.8 | 1.9 | 2.38 | 10.69 |
| **Ni60** | 2.5 | 1.1 | 2.4 | 72.0 | 3.5 | 18.9 | 19.6 | 3.5 | 3.0 | 4.6 | 22.7 | 11.3 | 8.09 | 19.04 |
| **Zn66** | 643.2 | 237.7 | 264.2 | 321.8 | 307.2 | 255.1 | 316.9 | 302.0 | 298.8 | 238.0 | 365.4 | 446.9 | 264.61 | 1603.64 |
| **Ga71** | 1.1 | 1.2 | 1.6 | 1.9 | 2.0 | 1.1 | 0.5 | 0.3 | 0.5 | 0.2 | 0.2 | 0.3 | 0.272 | 0.51 |
| **Ge73** | 3.1 | 3.3 | 3.3 | 4.8 | 5.3 | 1.8 | 1.0 | 1.3 | 1.5 | 1.7 | 1.7 | 1.3 | <0.74 | 1.14 |
| **As75** | 275.6 | 261.8 | 332.7 | 344.4 | 428.5 | 1.5 | 0.9 | 193.0 | 218.5 | 204.8 | 173.4 | 224.1 | 112.17 | 114.07 |
| **Se82** | <12.46 | <13.18 | <10.90 | <12.70 | <13.56 | <13.14 | <11.39 | <12.53 | 16.4 | <13.95 | <15.26 | <18.10 | <15.38 | <12.44 |
| **Mo95** | <0.101 | <0.085 | <0.049 | <0.058 | <0.134 | <0.133 | <0.082 | 0.0 | <0.077 | <0.106 | <0.119 | 0.2 | <0.252 | <0.32 |
| **Ag107** | 905.3 | 578.2 | 1227.0 | 1196.6 | 195.1 | 5264.3 | 3941.5 | 259.1 | 245.6 | 3638.7 | 282.1 | 145.5 | 61.07 | 52.62 |
| **Cd111** | 2.8 | 0.8 | 0.9 | 0.9 | 1.3 | 0.6 | <0.25 | 2.1 | 1.9 | 2.9 | 2.1 | 3.0 | <1.25 | 3.94 |
| **In115** | 0.6 | 0.3 | 0.2 | 0.3 | 0.3 | 0.2 | 0.1 | 0.0 | <0.0151 | 0.0 | 0.0 | 0.1 | 0.231 | 0.98 |
| **Sn118** | 4.2 | 4.0 | 4.4 | 0.9 | 1.1 | 50.3 | 4.3 | 4.2 | 3.9 | 5.1 | 4.1 | 13.5 | <1.34 | <0.99 |
| **Sb121** | 0.4 | 0.3 | 0.1 | 7.3 | 0.1 | <0.099 | 3.7 | 0.2 | 0.3 | 0.1 | 0.4 | 2.6 | <0.45 | <0.33 |
| **Ir193** | <0.00 | <0.00 | <0.00 | <0.0069 | <0.00 | 0.0 | <0.0058 | <0.00 | <0.00 | <0.00 | <0.00 | <0.00 | <0.00 | <0.0248 |
| **Pt195** | <0.044 | <0.039 | <0.037 | <0.038 | <0.032 | <0.021 | <0.045 | 0.0 | <0.049 | <0.068 | <0.054 | <0.094 | <0.38 | <0.32 |
| **Au197** | <0.49 | <0.50 | <0.42 | <0.48 | <0.50 | <0.38 | <0.34 | <0.55 | <0.71 | <0.63 | <0.67 | <0.78 | <0.51 | <0.38 |
| **Hg202** | <0.64 | <0.52 | <0.38 | <0.39 | <0.45 | <0.33 | <0.36 | <0.52 | <0.70 | <0.64 | <0.91 | <0.73 | <1.04 | <0.89 |
| **Tl205** | 1.3 | 3.4 | 1.1 | 5.6 | 1.2 | 0.0 | 4.9 | 0.7 | 0.2 | 0.1 | 0.0 | 3.1 | 1.48 | 2.73 |
| **Pb208** | 3.7 | 4.6 | 3.2 | 225.2 | 441.9 | 1164.7 | 55.2 | 3.1 | 3.1 | 2.3 | 7.0 | 9.7 | 4.06 | 8.87 |
| **Bi209** | <0.0096 | 0.3 | <0.0088 | <0.0063 | 0.0 | 1.4 | 0.2 | 0.2 | 0.1 | 0.3 | 0.1 | 0.0 | <0.121 | <0.096 |

**Table 14:** Trace element composition of arsenopyrite in massive sulfide mineralization.

| | **Arsenopyrite** | | | | | | | | | | | | | |
|---|---|---|---|---|---|---|---|---|---|---|---|---|---|---|
| EPMA Ref | 1 / 1 . | 2 / 1 . | 3 / 1 . | 11 / 1 . | 13 / 1 . | 14 / 1 . | 15 / 1 . | 16 / 1 . | 10 / 1 . | 11 / 1 . | 8 / 1 . | 14 / 1 . | 24 / 1 . | 44 / 1 . |
| Sample No. | KYD34 | KYD34 | KYD34 | KYD34 | KYD34 | KYD34 | KYD34 | KYD34 | ML12B | ML12B | ML10H | ML10H | ML10H | ML10D |
| **V51** | 0.2 | <0.115 | <0.104 | <0.096 | <0.106 | <0.102 | <0.156 | <0.109 | <0.26 | <0.26 | 0.39 | <0.33 | 0.42 | <0.47 |
| **Cr52** | <1.85 | <1.81 | <1.78 | <1.58 | <1.54 | <1.80 | <2.34 | <1.74 | <5.91 | <5.68 | <7.08 | <5.65 | <6.17 | <8.75 |
| **Mn55** | <0.51 | <0.49 | <0.49 | <0.44 | <0.43 | 1.2 | <0.65 | <0.47 | <1.68 | <1.62 | 5.27 | <2.25 | 5.16 | <3.02 |
| **Co59** | 4957.6 | 5533.4 | 4934.4 | 4526.3 | 3831.8 | 5148.4 | 4764.4 | 4748.9 | 7289.52 | 6674.73 | 4111.46 | 5407.31 | 3151.99 | 2805.83 |
| **Ni60** | 1892.8 | 1917.6 | 2105.7 | 1119.6 | 1330.9 | 1767.2 | 2018.5 | 1875.2 | 1600.9 | 1688.28 | 1347.83 | 1289.02 | 472.78 | 332.94 |
| **Cu63** | 0.3 | 0.5 | 3.5 | <0.095 | <0.070 | 0.4 | <0.138 | 9.1 | <0.29 | 0.71 | 1.14 | <0.47 | 2.08 | <0.87 |
| **Zn66** | 148.6 | 5.0 | 12.9 | 2.9 | 2.9 | 12.6 | <1.36 | <1.25 | <6.52 | <6.13 | 52.93 | <7.43 | 26.35 | <12.06 |
| **Ga71** | 0.0 | 0.0 | <0.0132 | <0.0124 | <0.0114 | <0.0195 | <0.0179 | <0.0127 | <0.137 | <0.105 | <0.221 | <0.176 | 0.168 | <0.194 |
| **Ge73** | 0.8 | 0.9 | 0.8 | 0.8 | 0.9 | 0.9 | 1.6 | 0.7 | <0.54 | 0.79 | <1.06 | 1.03 | 1.22 | <1.24 |
| **Se82** | <12.91 | <12.64 | <11.87 | <11.08 | <10.55 | <12.36 | <15.83 | <11.65 | <9.75 | <9.43 | <20.65 | <16.43 | <17.88 | <25.37 |
| **Mo95** | <0.083 | 0.1 | <0.118 | 0.1 | 0.1 | 0.1 | 0.3 | 0.2 | <0.32 | <0.33 | <0.42 | <0.24 | 0.21 | <0.52 |
| **Ag107** | 41.6 | 15.6 | 2.4 | 0.6 | <0.086 | 5.1 | <0.122 | <0.074 | <0.100 | <0.067 | 2.43 | <0.129 | <0.117 | <0.184 |
| **Cd111** | 0.5 | 0.2 | 0.1 | 0.1 | <0.158 | <0.211 | <0.29 | <0.160 | <0.92 | <0.84 | <1.26 | <0.66 | <0.98 | <1.35 |
| **In115** | 0.2 | 0.2 | 0.2 | 0.2 | 0.2 | 0.2 | 0.2 | 0.2 | 0.22 | 0.259 | 0.191 | 0.179 | 0.134 | 0.147 |
| **Sn118** | <0.28 | <0.28 | <0.27 | <0.25 | <0.242 | <0.29 | <0.38 | <0.27 | <0.84 | <0.79 | <1.22 | <0.99 | <1.04 | <1.47 |
| **Sb121** | 238.1 | 169.4 | 155.3 | 155.3 | 175.5 | 169.4 | 221.1 | 168.9 | 49.39 | 34.63 | 113.66 | 121.05 | 106.6 | 103.28 |
| **Ir193** | <0.00 | <0.00 | 0.0015 | <0.00 | <0.00 | <0.0067 | <0.00 | 0.0071 | <0.00 | <0.00 | <0.00 | <0.00 | <0.00 | <0.00 |
| **Pt195** | 0.2 | 0.1 | 0.1 | <0.027 | <0.043 | <0.042 | <0.067 | 0.2 | <0.31 | <0.194 | <0.40 | <0.27 | <0.27 | <0.68 |
| **Au197** | <0.44 | <0.44 | <0.42 | <0.36 | <0.34 | <0.40 | <0.54 | <0.39 | <0.31 | <0.28 | <0.37 | <0.31 | <0.28 | <0.50 |
| **Hg202** | 0.5 | <0.36 | 0.6 | 0.5 | <0.30 | <0.34 | <0.44 | <0.46 | <0.56 | <0.55 | <0.98 | 0.85 | <0.92 | <1.23 |
| **Tl205** | 0.3 | 0.1 | 0.037 | 0.017 | 0.3 | 0.2 | <0.0181 | 0.1 | <0.055 | <0.056 | 0.152 | 0.104 | 0.099 | 0.16 |
| **Pb208** | 2.4 | 716.3 | 423.7 | 4.2 | 359.9 | 175.8 | 379.5 | 0.3 | <0.48 | <0.44 | 69.99 | <0.48 | 65.59 | 8.22 |
| **Bi209** | 5.9 | <0.0099 | 0.0 | 0.1 | 0.5 | 3.1 | 14.4 | <0.0122 | <0.069 | <0.061 | <0.095 | <0.073 | <0.088 | <0.136 |

| | Arsenopyrite | | | | | | | | | | |
|---|---|---|---|---|---|---|---|---|---|---|---|
| EPMA Ref | 45 / 1 . | 46 / 1 . | 1 / 1 . | 2 / 1 . | 3 / 1 . | 5 / 1 . | 6 / 1 . | 7 / 1 . | 30 / 1 . | 34 / 1 . | 36 / 1 . |
| Sample No. | ML10D | ML10D | ML10I | ML10I | ML10I | ML10I | ML10I | ML10I | ML10I | ML16A | ML16A |
| **V51** | <0.39 | <0.42 | <0.28 | <0.28 | <0.32 | <0.26 | <0.223 | <0.201 | 0.28 | <0.29 | <0.29 |
| **Cr52** | <6.85 | <7.14 | <5.50 | <5.47 | <5.73 | <5.31 | <4.65 | <3.88 | <4.73 | <4.65 | <5.44 |
| **Mn55** | <2.44 | 8.67 | <2.10 | <2.12 | <2.14 | <1.99 | <1.78 | <1.45 | <1.80 | <1.68 | <2.07 |
| **Co59** | 3911.14 | 4053.41 | 10185.86 | 8088.73 | 10294.73 | 9768.42 | 6477.58 | 6158.23 | 10423.46 | 10938.72 | 16494.11 |
| **Ni60** | 748.21 | 1023.6 | 2984.32 | 785.19 | 1516.54 | 2949.16 | 541.43 | 697.54 | 1651.67 | 5073.66 | 1980.48 |
| **Cu63** | <0.60 | 2.32 | <0.33 | <0.40 | <0.54 | <0.35 | 1.1 | <0.30 | <0.33 | 0.39 | 6.37 |
| **Zn66** | <9.41 | <9.56 | <6.66 | <6.08 | <6.44 | <5.55 | <5.20 | <4.52 | <5.34 | <5.11 | <5.74 |
| **Ga71** | <0.112 | <0.208 | <0.124 | <0.151 | <0.170 | <0.081 | 0.063 | <0.071 | <0.103 | <0.124 | <0.105 |
| **Ge73** | <0.72 | <0.82 | 0.46 | <0.48 | 0.76 | 0.81 | <0.61 | 0.59 | 0.87 | <0.67 | 0.51 |
| **Se82** | <20.55 | <22.05 | <16.13 | <17.11 | <16.97 | <16.16 | <14.44 | <10.57 | <13.61 | <12.97 | <14.54 |
| **Mo95** | <0.35 | <0.48 | 0.31 | <0.235 | <0.245 | <0.00 | <0.190 | <0.155 | <0.34 | <0.18 | <0.233 |
| **Ag107** | <0.165 | 0.85 | 0.048 | <0.065 | <0.096 | 0.058 | 1.23 | <0.074 | <0.094 | <0.111 | 0.341 |
| **Cd111** | <1.51 | <1.17 | <1.10 | 0.86 | <0.70 | <1.01 | <1.08 | <0.25 | <0.73 | <0.61 | <1.03 |
| **In115** | 0.24 | 0.156 | 0.145 | 0.197 | 0.174 | 0.105 | 0.159 | 0.176 | 0.142 | 0.152 | 0.167 |
| **Sn118** | <1.15 | <1.22 | <0.99 | <0.87 | <0.94 | <0.88 | <0.79 | <0.63 | <0.76 | <0.77 | <0.97 |
| **Sb121** | 121.28 | 124.97 | 211.17 | 135.91 | 181.2 | 194.43 | 129.28 | 125.16 | 162.52 | 100.67 | 191.69 |
| **Ir193** | <0.00 | <0.00 | <0.00 | <0.00 | <0.00 | <0.00 | <0.00 | <0.00 | <0.00 | <0.00 | <0.00 |
| **Pt195** | <0.46 | <0.56 | <0.31 | <0.26 | <0.29 | <0.28 | 0.27 | <0.183 | <0.239 | <0.239 | 0.21 |
| **Au197** | <0.37 | <0.32 | <0.238 | <0.252 | <0.26 | <0.245 | <0.208 | <0.173 | <0.200 | <0.22 | <0.24 |
| **Hg202** | <0.92 | <0.95 | <0.82 | <0.85 | <0.84 | <0.91 | 0.83 | 0.71 | 0.78 | <0.78 | <1.00 |
| **Tl205** | <0.061 | 0.194 | 0.027 | <0.027 | <0.063 | <0.035 | <0.044 | <0.025 | <0.047 | <0.049 | <0.045 |
| **Pb208** | 1.62 | 362.02 | <0.47 | <0.48 | <0.47 | <0.66 | <0.45 | 0.39 | <0.35 | <0.32 | 0.82 |
| **Bi209** | <0.112 | <0.105 | <0.056 | <0.074 | <0.073 | 0.084 | <0.057 | <0.046 | <0.063 | <0.059 | <0.072 |

**Table 15:** Trace element composition of löllingite in massive sulfide mineralization.

| | **Löllingite** | | | | |
|---|---|---|---|---|---|
| EPMA Ref | 7 / 1 . | 8 / 1 . | 12 / 1 . | 9 / 1 . | 9 / 2 . |
| Sample No. | ML12B | ML12B | ML12B | ML10H | ML10H |
| **V51** | <1.45 | 1.09 | <1.13 | <1.59 | <1.05 |
| **Cr52** | <36.86 | <27.87 | <22.90 | <24.36 | <18.28 |
| **Mn55** | <10.27 | <7.78 | <6.96 | <9.70 | <6.94 |
| **Co59** | 14634.49 | 14075.76 | 12273.82 | 7609.58 | 7608.5 |
| **Ni60** | 17552.26 | 14312.79 | 19005.25 | 12688.21 | 10878.62 |
| **Cu63** | <2.35 | <1.71 | <1.29 | <1.90 | 3.86 |
| **Zn66** | <44.91 | <31.10 | <26.02 | <32.46 | <22.77 |
| **Ga71** | <0.66 | 0.47 | <0.54 | <0.60 | <0.34 |
| **Ge73** | <1.93 | <2.86 | <1.92 | <3.33 | <2.84 |
| **Se82** | <59.69 | <49.23 | <38.33 | <76.89 | <53.49 |
| **Mo95** | <1.54 | <1.58 | <1.41 | <1.77 | <1.04 |
| **Ag107** | 2.89 | <0.45 | 1.76 | <0.56 | <0.35 |
| **Cd111** | <6.97 | <5.51 | <3.99 | <4.65 | <2.90 |
| **In115** | 1.2 | 1.09 | 1.04 | 0.91 | 0.63 |
| **Sn118** | <5.19 | <4.06 | <3.38 | <4.61 | <3.08 |
| **Sb121** | 67.25 | 59.33 | 69.09 | 211.43 | 173.2 |
| **Ir193** | <0.00 | <0.00 | <0.00 | <0.138 | <0.00 |
| **Pt195** | <1.75 | <1.10 | <0.75 | <1.55 | <0.94 |
| **Au197** | <1.92 | 1.5 | 2.29 | 1.26 | 1.73 |
| **Hg202** | <4.05 | <2.79 | 2.66 | <3.28 | <2.46 |
| **Tl205** | <0.35 | <0.26 | <0.228 | <0.188 | <0.201 |
| **Pb208** | 695.56 | 10.64 | 124.79 | 2.71 | <1.52 |
| **Bi209** | 4.47 | 0.6 | 2.36 | <0.36 | <0.254 |

**Table 16:** In-situ $\delta^{34}S$ isotope compositions of sphalerite and galena, and multiple sulfur isotopes ($\delta^{34}S$, $\Delta^{33}S$, $\Delta^{36}S$) of pyrrhotite and chalcopyrite measured using Nano-SIMS. (contd. in next page).

| | | Sphalerite | | Galena | | Arsenopyrite | | Pyrrhotite | | | | | |
|---|---|---|---|---|---|---|---|---|---|---|---|---|---|
| | **Sample** | $\delta^{34}S_{sp}$ | ±2σ | $\delta^{34}S_{gn}$ | ±2σ | $\delta^{34}S_{apy}$ | ±2σ | $\delta^{34}S_{po}$ | ±2σ | $\delta^{33}S_{po}$ | ±2σ | $\delta^{36}S_{po}$ | ±2σ |
| **Laminated** | D-24-2 | 5.14 | 2.75 | 11.31 | 2.52 | | | 7.23 | 1.16 | 3.66 | 0.57 | 13.29 | 1.95 |
| | D-24-2 | 5.27 | 2.78 | | | | | 7.42 | 1.12 | 3.82 | 0.57 | 14.14 | 1.95 |
| | D-24-2 | | | | | | | 7.45 | 1.14 | 3.81 | 0.57 | 14.26 | 1.95 |
| | D-24-2 | | | | | | | 6.53 | 1.12 | 3.36 | 0.57 | 12.72 | 1.95 |
| | D-24-2 | | | | | | | 7.81 | 1.11 | 4.15 | 0.57 | 14.86 | 1.95 |
| | 19A | 6.00 | 2.76 | | | | | 10.67 | 1.11 | 5.44 | 0.57 | 20.55 | 1.95 |
| | 19A | 6.40 | 2.74 | | | | | 9.03 | 1.11 | 4.63 | 0.57 | 17.16 | 1.95 |
| | 19A | 4.32 | 2.77 | | | | | 10.08 | 1.11 | 5.11 | 0.57 | 19.23 | 1.95 |
| | 19A | | | | | | | 11.28 | 1.12 | 5.79 | 0.57 | 21.47 | 1.95 |
| **Massive** | KYD-34 | 5.90 | 2.75 | 17.18 | 1.69 | 9.39 | 0.84 | 7.81 | 1.15 | 3.96 | 0.57 | 15.11 | 1.95 |
| | KYD-34 | 3.59 | 2.76 | 13.90 | 2.64 | 9.02 | 0.80 | 6.14 | 1.15 | 3.07 | 0.57 | 11.64 | 1.95 |
| | KYD-34 | 6.45 | 2.79 | | | | | | | | | | |
| | KYD-34 | 6.33 | 2.75 | | | | | | | | | | |
| | KYD-21 | 2.70 | 2.74 | 11.00 | 2.21 | 7.14 | 0.85 | 7.38 | 1.13 | 3.77 | 0.57 | 14.10 | 1.95 |
| | KYD-21 | 4.17 | 2.72 | 11.01 | 1.84 | 8.41 | 0.93 | 9.10 | 1.11 | 4.53 | 0.57 | 17.41 | 1.95 |
| | KYD-21 | 8.91 | 2.72 | | | | | | | | | | |
| | KYD-21 | 5.15 | 2.75 | | | | | | | | | | |
| | D4 | 8.86 | 2.72 | 13.69 | 1.51 | | | 9.20 | 1.14 | 4.73 | 0.57 | 17.73 | 1.95 |
| | D4 | 5.72 | 2.75 | 13.48 | 2.31 | | | 7.85 | 1.16 | 4.00 | 0.57 | 15.10 | 1.95 |
| | D4 | 5.87 | 2.76 | | | | | 7.16 | 1.11 | 3.68 | 0.57 | 13.86 | 1.96 |
| **Vein** | 19C | 4.83 | 2.78 | 16.86 | 2.45 | | | 7.71 | 1.13 | 3.91 | 0.57 | 14.73 | 1.95 |
| **Hosted** | 19C | 5.68 | 2.78 | | | | | 6.97 | 1.11 | 3.65 | 0.57 | 13.37 | 1.95 |
| | 19C | | | | | | | 8.43 | 1.12 | 4.45 | 0.58 | 15.90 | 1.95 |
| | 19C | | | | | | | 8.36 | 1.12 | 4.28 | 0.58 | 15.94 | 1.95 |
| | ML13 | 3.45 | 2.75 | 7.82 | 1.55 | | | | | | | | |
| | ML13 | 4.32 | 2.76 | 11.05 | 1.52 | | | | | | | | |
| | ML13 | 2.26 | 2.72 | 10.89 | 1.85 | | | | | | | | |
| | ML13 | 3.41 | 2.76 | | | | | | | | | | |
| | ML13 | 4.15 | 2.82 | | | | | | | | | | |

| | Pyrrhotite | | | | Chalcopyrite | | | | | | | | | |
|---|---|---|---|---|---|---|---|---|---|---|---|---|---|---|
| **Sample** | $\Delta^{33}S_{po}$ | ±2σ | $\Delta^{36}S_{po}$ | ±2σ | $\delta^{34}S_{ccp}$ | ±2σ | $\delta^{33}S_{po}$ | ±2σ | $\delta^{36}S_{po}$ | ±2σ | $\Delta^{33}S_{ccp}$ | ±2σ | $\Delta^{36}S_{ccp}$ | ±2σ |
| D-24-2 | -0.05 | 0.15 | -0.49 | 0.52 | 7.17 | 0.79 | 3.67 | 0.42 | 13.73 | 1.59 | -0.02 | 0.16 | 0.07 | 0.34 |
| D-24-2 | 0.01 | 0.14 | 0.00 | 0.51 | 7.75 | 0.82 | 3.98 | 0.41 | 14.49 | 1.55 | 0.00 | 0.16 | -0.28 | 0.35 |
| D-24-2 | -0.02 | 0.15 | 0.06 | 0.52 | 6.90 | 0.91 | 3.59 | 0.42 | 13.43 | 1.60 | 0.04 | 0.18 | 0.28 | 0.36 |
| D-24-2 | 0.00 | 0.13 | 0.28 | 0.50 | | | | | | | | | | |
| D-24-2 | 0.14 | 0.13 | -0.02 | 0.50 | | | | | | | | | | |
| 19A | -0.04 | 0.14 | 0.17 | 0.50 | | | | | | | | | | |
| 19A | -0.01 | 0.14 | -0.06 | 0.49 | | | | | | | | | | |
| 19A | -0.07 | 0.14 | 0.00 | 0.52 | | | | | | | | | | |
| 19A | 0.00 | 0.13 | -0.06 | 0.51 | | | | | | | | | | |
| KYD-34 | -0.05 | 0.13 | 0.22 | 0.49 | 8.11 | 0.98 | 4.28 | 0.51 | 15.76 | 1.18 | 0.11 | 0.10 | 0.29 | 0.74 |
| KYD-34 | -0.09 | 0.14 | -0.07 | 0.50 | 8.44 | 0.80 | 4.45 | 0.41 | 16.10 | 1.52 | 0.11 | 0.17 | -0.01 | 0.33 |
| KYD-34 | | | | | | | | | | | | | | |
| KYD-34 | | | | | | | | | | | | | | |
| KYD-21 | -0.02 | 0.14 | 0.03 | 0.50 | | | | | | | | | | |
| KYD-21 | -0.15 | 0.15 | 0.05 | 0.52 | | | | | | | | | | |
| KYD-21 | | | | | | | | | | | | | | |
| KYD-21 | | | | | | | | | | | | | | |
| D4 | 0.00 | 0.13 | 0.17 | 0.51 | 7.03 | 0.84 | 3.62 | 0.41 | 13.68 | 1.53 | 0.01 | 0.16 | 0.29 | 0.37 |
| D4 | -0.03 | 0.14 | 0.14 | 0.52 | 8.16 | 0.85 | 4.29 | 0.42 | 16.00 | 1.55 | 0.10 | 0.16 | 0.43 | 0.35 |
| D4 | 0.00 | 0.13 | 0.21 | 0.51 | 8.37 | 0.81 | 4.46 | 0.42 | 16.16 | 1.56 | 0.16 | 0.16 | 0.20 | 0.36 |
| 19C | -0.05 | 0.13 | 0.03 | 0.49 | 8.85 | 0.96 | 4.52 | 0.50 | 16.63 | 1.14 | -0.03 | 0.08 | -0.25 | 0.73 |
| 19C | 0.07 | 0.15 | 0.09 | 0.52 | 8.73 | 0.97 | 4.93 | 0.54 | 16.21 | 1.19 | 0.44 | 0.20 | -0.45 | 0.78 |
| 19C | 0.12 | 0.20 | -0.17 | 0.50 | 6.37 | 1.20 | 3.60 | 0.53 | 11.70 | 1.18 | 0.33 | 0.16 | -0.44 | 0.76 |
| 19C | -0.02 | 0.17 | 0.00 | 0.51 | | | | | | | | | | |
| ML13 | | | | | 7.33 | 0.98 | 3.79 | 0.51 | 13.99 | 1.15 | 0.02 | 0.08 | 0.02 | 0.73 |
| ML13 | | | | | | | | | | | | | | |
| ML13 | | | | | | | | | | | | | | |
| ML13 | | | | | | | | | | | | | | |
| ML13 | | | | | | | | | | | | | | |

**Table 17:** $\delta^{34}S$ isotope compositions of sphalerite separates measured using IRMS.

| | Sample No. | $\delta^{34}S_{VCDT}$ |
|---|---|---|
| **Laminated/ Disseminated** | ML 16A | 8.85 |
| | D14 | 7.09 |
| | D15 | 8.65 |
| | D16 | 8.79 |
| | D21 | 8.49 |
| **Massive** | ML 12B | 8.29 |
| | ML 10G | 7.57 |
| | ML 10E | 8.6 |
| | ML 16(1) | 8.21 |
| | ML 6(A) | 7.63 |
| | KYD 1 | 8.5 |

| | Sample No. | $\delta^{34}S_{VCDT}$ |
|---|---|---|
| **Massive** | KYD 20 | 7.86 |
| | KYD 21 | 6.82 |
| | KYD 26 | 5.16 |
| | KYD 34 | 8.04 |
| **Vein Hosted** | D7 | 8.03 |
| | D7c | 8.13 |
| | D7c | 8.76 |
| | ML 13 | 7.62 |
| | ML 8F | 7.09 |
| | ST-2 | 7.65 |
| | St-11 | 9.18 |
| | ST-13 | 7.04 |

**Table 18:** Major element chemistry of the three tourmaline types (Tur1, Tur2, Tur3).

| | Sample No. | EPMA Point | $Na_2O$ | MgO | $Al_2O_3$ | $K_2O$ | CaO | $TiO_2$ | $Cr_2O_3$ | MnO | $SiO_2$ | FeO | F | Cl | Total |
|---|---|---|---|---|---|---|---|---|---|---|---|---|---|---|---|
| | D24-2 | 2 / 1 . | 1.58 | 8.14 | 33.51 | 0.04 | 1.42 | 0.87 | 0.00 | bdl | 36.69 | 3.89 | bdl | bdl | 86.22 |
| | D24-2 | 7 / 1 . | 2.02 | 7.88 | 33.27 | bdl | 0.52 | 0.64 | 0.13 | bdl | 37.54 | 4.17 | bdl | bdl | 86.23 |
| | D24-2 | 8 / 1 . | 1.56 | 8.13 | 33.29 | bdl | 1.50 | 0.73 | bdl | bdl | 37.05 | 4.09 | bdl | bdl | 86.46 |
| | D24-2 | 11 / 1 . | 1.51 | 8.27 | 33.63 | 0.03 | 1.55 | 0.79 | bdl | bdl | 36.53 | 4.34 | bdl | bdl | 86.79 |
| | BH-149-3 | 61 | 1.40 | 8.16 | 34.31 | 0.03 | 1.43 | 0.77 | bdl | bdl | 37.01 | 3.73 | bdl | bdl | 87.24 |
| | BH-149-3 | 62 | 1.76 | 7.83 | 34.41 | bdl | 0.71 | 0.59 | bdl | bdl | 37.68 | 3.77 | bdl | bdl | 86.87 |
| | BH-149-3 | 63 | 1.55 | 8.23 | 33.28 | bdl | 1.54 | 0.73 | bdl | bdl | 36.53 | 3.82 | bdl | bdl | 85.76 |
| | BH-149-3 | 64 | 1.64 | 8.06 | 33.88 | bdl | 1.22 | 0.76 | bdl | bdl | 37.34 | 3.60 | bdl | bdl | 86.62 |
| **Tur1** | BH-149-3 | 65 | 1.47 | 8.23 | 33.99 | 0.03 | 1.60 | 0.74 | bdl | 0.15 | 35.69 | 3.71 | bdl | bdl | 85.76 |
| | BH-149-3 | 66 | 1.51 | 7.91 | 34.16 | 0.06 | 1.40 | 0.78 | 0.12 | bdl | 36.77 | 3.55 | bdl | bdl | 86.59 |
| | BH-149-3 | 67 | 1.53 | 7.77 | 34.57 | 0.05 | 1.40 | 0.83 | bdl | bdl | 36.72 | 3.73 | bdl | bdl | 86.88 |
| | BH-149-3 | 68 | 1.61 | 7.81 | 34.70 | 0.05 | 1.40 | 0.79 | bdl | bdl | 36.63 | 3.52 | bdl | bdl | 86.73 |
| | BH-149-3 | 69 | 1.80 | 7.83 | 34.60 | bdl | 0.83 | 0.65 | bdl | bdl | 36.93 | 3.65 | bdl | bdl | 86.39 |
| | BH-149-3 | 70 | 1.45 | 7.79 | 34.65 | 0.05 | 1.47 | 0.83 | 0.46 | bdl | 36.07 | 3.64 | bdl | bdl | 86.58 |
| | BH-149-3 | 71 | 1.50 | 8.01 | 34.24 | 0.03 | 1.43 | 0.84 | bdl | bdl | 36.86 | 3.69 | bdl | bdl | 86.66 |
| | BH-149-3 | 72 | 1.51 | 7.92 | 34.25 | 0.04 | 1.42 | 0.78 | bdl | bdl | 36.55 | 3.52 | bdl | bdl | 86.08 |
| | BH-149-3 | 73 | 1.50 | 7.93 | 34.27 | 0.04 | 1.40 | 0.79 | bdl | bdl | 36.58 | 3.92 | bdl | bdl | 86.50 |
| | BH-149-3 | 74 | 1.92 | 7.57 | 33.26 | bdl | 0.19 | 1.12 | bdl | bdl | 37.78 | 4.72 | bdl | bdl | 86.67 |
| | BH-149-3 | 75 | 1.48 | 8.07 | 33.63 | 0.05 | 1.54 | 0.77 | bdl | bdl | 36.49 | 3.73 | bdl | bdl | 85.87 |
| | BH-149-3 | 76 | 1.52 | 7.72 | 34.51 | 0.06 | 1.44 | 0.90 | bdl | bdl | 36.28 | 3.90 | bdl | bdl | 86.43 |
| | ML19A | 26 / 1 . | 1.65 | 5.06 | 34.59 | 0.04 | 0.87 | 0.69 | bdl | bdl | 35.51 | 7.52 | bdl | bdl | 86.04 |
| | ML19A | 27 / 1 . | 1.47 | 8.96 | 33.28 | 0.05 | 1.62 | 0.84 | bdl | 0.14 | 36.69 | 3.06 | bdl | bdl | 86.14 |
| | ML19A | 28 / 1 . | 2.23 | 8.31 | 33.68 | bdl | 0.08 | 0.28 | bdl | bdl | 37.96 | 3.45 | bdl | bdl | 86.00 |
| | ML19A | 29 / 1 . | 1.45 | 8.91 | 32.39 | 0.09 | 1.81 | 0.88 | bdl | bdl | 36.53 | 3.42 | bdl | bdl | 85.73 |

| | Sample No. | EPMA Point | $Na_2O$ | MgO | $Al_2O_3$ | $K_2O$ | CaO | $TiO_2$ | $Cr_2O_3$ | MnO | $SiO_2$ | FeO | F | Cl | Total |
|---|---|---|---|---|---|---|---|---|---|---|---|---|---|---|---|
| | ML19A | 30 / 1 . | 1.65 | 8.92 | 32.83 | 0.04 | 1.39 | 0.78 | bdl | bdl | 36.45 | 2.90 | bdl | bdl | 85.12 |
| | ML19A | 38 / 1 . | 1.64 | 8.80 | 32.51 | 0.07 | 1.50 | 0.80 | bdl | bdl | 35.66 | 2.82 | bdl | bdl | 83.86 |
| **Tur1** | ST-8 | 40 / 1 . | 1.50 | 9.38 | 30.91 | bdl | 2.06 | 0.89 | 0.01 | bdl | 35.46 | 2.92 | bdl | bdl | 83.43 |
| | ST-8 | 41 / 1 . | 1.67 | 9.36 | 31.14 | bdl | 1.92 | 0.78 | bdl | 0.01 | 36.20 | 3.25 | bdl | bdl | 84.74 |
| | ST-8 | 54 / 1 . | 2.19 | 6.83 | 32.00 | bdl | 0.34 | 1.14 | bdl | bdl | 36.34 | 5.29 | bdl | bdl | 84.51 |
| | D4 | 37 / 1 . | 1.72 | 6.75 | 33.92 | 0.08 | 1.09 | 0.72 | bdl | bdl | 36.20 | 5.09 | bdl | bdl | 85.67 |
| | D4 | 40 / 1 . | 1.67 | 7.40 | 33.18 | 0.07 | 1.25 | 0.86 | bdl | bdl | 36.12 | 4.42 | bdl | bdl | 85.03 |
| | D4 | 43 / 1 . | 1.81 | 6.79 | 32.69 | 0.08 | 0.85 | 0.91 | bdl | 0.14 | 36.20 | 5.83 | bdl | bdl | 85.41 |
| | D4 | 44 / 1 . | 1.78 | 6.40 | 33.77 | 0.05 | 0.85 | 0.83 | bdl | bdl | 36.33 | 5.83 | bdl | bdl | 85.92 |
| | D4 | 50 / 1 . | 1.74 | 4.15 | 33.07 | 0.03 | 0.57 | 0.20 | bdl | 0.12 | 34.37 | 6.85 | bdl | bdl | 81.12 |
| | D4 | 51 / 1 . | 2.01 | 5.75 | 31.87 | 0.05 | 0.60 | 0.32 | bdl | bdl | 34.19 | 5.67 | bdl | bdl | 80.49 |
| | D4 | 52 / 1 . | 1.97 | 6.65 | 31.08 | 0.06 | 0.67 | 0.81 | bdl | bdl | 35.07 | 4.59 | bdl | bdl | 80.96 |
| | D4 | 53 / 1 . | 1.88 | 7.16 | 31.02 | 0.04 | 0.79 | 0.69 | bdl | bdl | 34.69 | 4.42 | bdl | bdl | 80.73 |
| | D4 | 54 / 1 . | 1.91 | 6.03 | 31.88 | 0.04 | 0.70 | 0.47 | bdl | 0.12 | 34.62 | 6.29 | bdl | bdl | 82.06 |
| **Tur2** | ML16A | 82 / 1 . | 1.34 | 8.99 | 32.42 | 0.06 | 2.00 | 0.90 | bdl | bdl | 36.74 | 3.36 | bdl | bdl | 85.87 |
| | ML16A | 90 / 1 . | 1.45 | 8.88 | 32.45 | 0.08 | 1.92 | 0.92 | 0.16 | bdl | 36.98 | 3.04 | bdl | bdl | 85.89 |
| | ML16A | 92 / 1 . | 1.45 | 9.14 | 32.33 | 0.04 | 1.86 | 0.68 | bdl | bdl | 37.10 | 3.11 | bdl | bdl | 85.76 |
| | ML16A | 95 / 1 . | 1.59 | 7.28 | 34.31 | bdl | 1.39 | 0.51 | 0.13 | bdl | 36.49 | 5.16 | bdl | bdl | 86.92 |
| | ML16A | 96 / 1 . | 1.51 | 9.22 | 32.61 | 0.06 | 1.68 | 0.73 | bdl | bdl | 37.74 | 3.17 | bdl | bdl | 86.72 |
| | ML16A | 98 / 1 . | 1.50 | 9.23 | 31.95 | 0.05 | 1.89 | 0.62 | bdl | bdl | 36.98 | 3.12 | bdl | bdl | 85.49 |
| | ML16A | 99 / 1 . | 2.03 | 8.40 | 33.63 | bdl | 0.42 | 0.35 | bdl | bdl | 38.07 | 3.36 | bdl | bdl | 86.31 |
| | ML 10K | 13/1 | 1.61 | 8.08 | 32.37 | bdl | 1.41 | 0.76 | 0.12 | bdl | 35.24 | 4.00 | bdl | bdl | 83.97 |
| | ML 10K | 19/1 | 1.76 | 7.69 | 32.63 | bdl | 1.46 | 0.85 | 0.25 | 0.08 | 35.49 | 4.65 | bdl | bdl | 85.33 |
| | ML 10K | 20/1 | 1.60 | 7.74 | 33.05 | bdl | 1.32 | 0.71 | 0.16 | 0.08 | 35.00 | 4.40 | bdl | bdl | 84.30 |
| | KYD14 | 2 / 1 . | 1.66 | 9.49 | 33.47 | bdl | 1.54 | 0.67 | bdl | bdl | 37.67 | 2.53 | bdl | bdl | 87.21 |
| | KYD14 | 3 / 1 . | 1.37 | 9.00 | 33.68 | 0.06 | 1.80 | 0.88 | bdl | bdl | 37.01 | 2.86 | bdl | bdl | 86.67 |

| | Sample No. | EPMA Point | $Na_2O$ | MgO | $Al_2O_3$ | $K_2O$ | CaO | $TiO_2$ | $Cr_2O_3$ | MnO | $SiO_2$ | FeO | F | Cl | Total |
|---|---|---|---|---|---|---|---|---|---|---|---|---|---|---|---|
| | KYD14 | 5 / 1 . | 1.54 | 9.31 | 32.73 | 0.03 | 1.72 | 0.68 | bdl | bdl | 37.18 | 3.02 | bdl | bdl | 86.37 |
| | KYD14 | 9 / 1 . | 1.36 | 8.97 | 33.51 | 0.06 | 1.67 | 0.85 | bdl | bdl | 36.87 | 2.72 | bdl | bdl | 86.08 |
| | KYD14 | 10 / 1 . | 1.41 | 9.82 | 32.15 | 0.03 | 2.26 | 0.71 | bdl | bdl | 37.34 | 2.83 | bdl | bdl | 86.59 |
| | KYD14 | 17 / 1 . | 1.36 | 9.85 | 32.61 | 0.06 | 1.85 | 0.63 | bdl | bdl | 37.30 | 2.19 | bdl | bdl | 85.96 |
| | KYD14 | 18 / 1 . | 1.45 | 9.42 | 32.44 | 0.05 | 1.84 | 0.85 | bdl | bdl | 37.49 | 2.91 | bdl | bdl | 86.58 |
| | KYD14 | 19 / 1 . | 1.35 | 9.10 | 33.48 | 0.07 | 1.99 | 0.77 | bdl | bdl | 37.05 | 2.74 | bdl | bdl | 86.64 |
| | KYD14 | 20 / 1 . | 1.75 | 6.80 | 34.45 | 0.05 | 0.69 | 0.35 | bdl | bdl | 36.94 | 5.32 | bdl | bdl | 86.39 |
| | KYD14 | 21 / 1 . | 1.53 | 10.36 | 32.43 | bdl | 1.80 | 0.75 | 0.13 | bdl | 38.20 | 1.96 | bdl | bdl | 87.17 |
| | KYD14 | 23 / 1 . | 1.83 | 6.31 | 34.34 | bdl | 0.59 | 0.50 | bdl | bdl | 36.52 | 6.62 | bdl | bdl | 86.80 |
| | KYD14 | 24 / 1 . | 2.15 | 9.07 | 33.95 | 0.03 | 0.44 | 0.20 | bdl | bdl | 38.57 | 2.51 | bdl | bdl | 86.95 |
| | KYD14 | 25 / 1 . | 1.46 | 8.81 | 33.74 | 0.04 | 1.58 | 0.86 | 0.11 | bdl | 37.44 | 2.75 | bdl | bdl | 86.83 |
| **Tur2** | KYD14 | 26 / 1 . | 1.30 | 9.74 | 32.29 | bdl | 2.20 | 0.71 | 0.19 | bdl | 37.11 | 2.37 | bdl | bdl | 86.03 |
| | KYD14 | 27 / 1 . | 1.65 | 7.46 | 33.77 | 0.13 | 1.29 | 1.01 | bdl | bdl | 36.08 | 4.51 | bdl | bdl | 85.94 |
| | KYD14 | 28 / 1 . | 1.40 | 8.97 | 32.55 | 0.03 | 1.55 | 0.77 | bdl | bdl | 36.79 | 2.85 | bdl | bdl | 84.91 |
| | KYD14 | 29 / 1 . | 1.43 | 8.94 | 33.15 | 0.06 | 1.55 | 0.80 | bdl | bdl | 36.60 | 3.02 | bdl | bdl | 85.72 |
| | KYD14 | 30 / 1 . | 1.48 | 9.01 | 33.02 | 0.05 | 1.84 | 0.92 | bdl | bdl | 36.93 | 2.76 | bdl | bdl | 86.05 |
| | ML10I | 58 / 1 . | 1.69 | 8.93 | 33.04 | 0.06 | 1.26 | 0.66 | 0.22 | bdl | 37.46 | 3.27 | bdl | bdl | 86.68 |
| | ML10I | 59 / 1 . | 2.02 | 9.05 | 33.26 | bdl | 0.55 | 0.38 | bdl | bdl | 37.79 | 2.48 | bdl | bdl | 85.61 |
| | ML10I | 60 / 1 . | 1.46 | 8.86 | 32.80 | 0.08 | 1.79 | 0.90 | 0.25 | bdl | 36.88 | 3.16 | bdl | bdl | 86.20 |
| | ML10I | 65 / 1 . | 1.61 | 9.24 | 32.67 | bdl | 1.24 | 0.57 | 0.14 | bdl | 37.25 | 2.39 | bdl | bdl | 85.16 |
| | ML10I | 66 / 1 . | 1.64 | 9.15 | 31.23 | 0.05 | 1.64 | 0.91 | 0.26 | bdl | 36.75 | 3.50 | bdl | bdl | 85.17 |
| | ML10I | 67 / 1 . | 1.66 | 5.53 | 33.88 | 0.07 | 1.20 | 0.50 | bdl | bdl | 35.69 | 7.92 | bdl | bdl | 86.46 |
| | ML10I | 68 / 1 . | 1.54 | 9.14 | 32.93 | 0.05 | 1.60 | 0.75 | bdl | bdl | 37.60 | 3.55 | bdl | bdl | 87.25 |
| | ML10I | 69 / 1 . | 1.48 | 9.05 | 32.49 | 0.06 | 1.89 | 0.96 | bdl | bdl | 36.69 | 3.62 | bdl | bdl | 86.29 |
| | ML10I | 70 / 1 . | 1.44 | 8.98 | 32.57 | 0.06 | 1.91 | 1.03 | bdl | bdl | 36.30 | 3.26 | bdl | bdl | 85.63 |

| | Sample No. | EPMA Point | $Na_2O$ | MgO | $Al_2O_3$ | $K_2O$ | CaO | $TiO_2$ | $Cr_2O_3$ | MnO | $SiO_2$ | FeO | F | Cl | Total |
|---|---|---|---|---|---|---|---|---|---|---|---|---|---|---|---|
| | N-169 | 11 | 1.84 | 1.51 | 33.64 | 0.04 | 0.28 | 0.11 | bdl | bdl | 35.31 | 13.72 | bdl | bdl | 86.85 |
| | N-169 | 12 | 1.57 | 1.30 | 34.15 | 0.04 | 0.15 | 0.11 | bdl | 0.16 | 35.04 | 12.90 | bdl | bdl | 85.88 |
| | N-169 | 13 | 1.88 | 1.56 | 33.72 | 0.05 | 0.30 | 0.21 | bdl | 0.17 | 34.66 | 13.47 | bdl | bdl | 86.48 |
| | N-169 | 14 | 1.98 | 1.58 | 33.70 | 0.05 | 0.24 | 0.16 | bdl | bdl | 35.58 | 13.86 | bdl | bdl | 87.62 |
| | N-169 | 15 | 1.95 | 1.56 | 34.05 | 0.04 | 0.23 | 0.23 | bdl | bdl | 35.22 | 13.65 | bdl | bdl | 87.50 |
| | N-169 | 16 | 2.02 | 1.69 | 32.69 | 0.05 | 0.30 | 0.16 | bdl | bdl | 34.99 | 14.36 | bdl | bdl | 86.49 |
| | N-169 | 17 | 2.04 | 1.70 | 32.77 | 0.07 | 0.32 | 0.19 | bdl | bdl | 35.03 | 14.43 | bdl | bdl | 86.91 |
| | N-169 | 18 | 2.08 | 3.16 | 31.76 | 0.04 | 0.56 | 0.71 | bdl | 0.14 | 35.14 | 13.17 | bdl | bdl | 86.89 |
| | N-169 | 19 | 2.04 | 1.60 | 33.90 | 0.05 | 0.27 | 0.18 | bdl | bdl | 35.04 | 13.21 | bdl | bdl | 86.45 |
| | N-169 | 20 | 1.86 | 1.58 | 33.89 | 0.05 | 0.24 | 0.22 | bdl | bdl | 35.50 | 13.45 | bdl | bdl | 87.36 |
| | N-169 | 21 | 1.54 | 1.16 | 34.48 | 0.03 | 0.12 | 0.08 | bdl | bdl | 35.74 | 13.43 | bdl | bdl | 86.80 |
| | N-169 | 22 | 1.79 | 1.46 | 33.47 | 0.05 | 0.26 | 0.27 | bdl | bdl | 34.69 | 13.72 | bdl | bdl | 86.04 |
| **Tur3** | N-169 | 23 | 1.95 | 1.50 | 33.24 | 0.06 | 0.32 | 0.21 | bdl | bdl | 33.88 | 13.11 | bdl | bdl | 84.50 |
| | N-169 | 24 | 1.95 | 1.48 | 33.79 | bdl | 0.24 | 0.23 | bdl | 0.23 | 35.12 | 13.48 | bdl | bdl | 86.72 |
| | N-169 | 25 | 1.61 | 1.14 | 34.17 | bdl | 0.14 | 0.06 | bdl | bdl | 34.51 | 12.94 | bdl | bdl | 85.03 |
| | N-169 | 26 | 1.64 | 1.18 | 34.68 | 0.04 | 0.14 | 0.07 | bdl | 0.22 | 34.55 | 13.38 | bdl | bdl | 86.19 |
| | N-169 | 27 | 1.87 | 1.52 | 34.42 | 0.04 | 0.35 | 0.24 | bdl | bdl | 34.44 | 13.45 | bdl | bdl | 86.47 |
| | N-169 | 28 | 1.85 | 1.46 | 33.22 | 0.06 | 0.29 | 0.25 | bdl | bdl | 33.56 | 13.36 | bdl | bdl | 84.44 |
| | N-169 | 29 | 1.81 | 1.31 | 32.68 | 0.05 | 0.16 | 0.13 | bdl | 0.15 | 33.86 | 13.31 | bdl | bdl | 83.46 |
| | N-169 | 30 | 1.59 | 1.18 | 34.10 | 0.04 | 0.13 | 0.05 | bdl | 0.20 | 34.31 | 13.37 | bdl | bdl | 85.29 |
| | KYD-4 | 31 | 1.96 | 2.47 | 33.79 | 0.05 | 0.27 | 0.27 | bdl | bdl | 34.44 | 12.40 | bdl | bdl | 86.01 |
| | KYD-4 | 32 | 1.74 | 1.96 | 34.01 | 0.05 | 0.13 | 0.09 | bdl | bdl | 33.93 | 12.14 | bdl | bdl | 84.19 |
| | KYD-4 | 33 | 1.65 | 1.95 | 34.68 | 0.03 | 0.12 | 0.09 | bdl | 0.20 | 34.15 | 12.45 | bdl | bdl | 85.74 |
| | KYD-4 | 34 | 1.85 | 1.75 | 33.69 | 0.06 | 0.28 | 0.22 | bdl | bdl | 34.15 | 13.21 | bdl | bdl | 85.36 |
| | KYD-4 | 35 | 2.02 | 1.67 | 33.56 | 0.05 | 0.28 | 0.22 | bdl | 0.28 | 33.77 | 13.14 | bdl | bdl | 85.10 |
| | KYD-4 | 36 | 1.77 | 2.81 | 33.23 | 0.04 | 0.49 | 0.18 | bdl | bdl | 34.57 | 12.88 | bdl | bdl | 86.35 |
| | KYD-4 | 37 | 1.97 | 2.30 | 33.89 | 0.03 | 0.30 | 0.25 | bdl | bdl | 35.02 | 12.98 | bdl | bdl | 86.86 |
| | KYD-4 | 38 | 1.98 | 2.86 | 33.41 | 0.04 | 0.30 | 0.40 | bdl | bdl | 34.33 | 11.52 | bdl | bdl | 85.56 |

| | Sample No. | EPMA Point | $Na_2O$ | MgO | $Al_2O_3$ | $K_2O$ | CaO | $TiO_2$ | $Cr_2O_3$ | MnO | $SiO_2$ | FeO | F | Cl | Total |
|---|---|---|---|---|---|---|---|---|---|---|---|---|---|---|---|
| | KYD-4 | 39 | 1.86 | 1.61 | 33.37 | 0.07 | 0.21 | 0.17 | bdl | bdl | 34.85 | 13.99 | bdl | bdl | 86.50 |
| | KYD-4 | 40 | 1.97 | 2.39 | 33.56 | 0.06 | 0.27 | 0.23 | bdl | bdl | 35.13 | 12.17 | bdl | bdl | 85.92 |
| | KYD-4 | 41 | 1.90 | 2.32 | 33.20 | 0.06 | 0.27 | 0.26 | bdl | bdl | 33.60 | 12.82 | bdl | bdl | 84.78 |
| | KYD-4 | 42 | 1.94 | 1.95 | 33.51 | 0.05 | 0.25 | 0.23 | bdl | bdl | 35.43 | 13.44 | bdl | bdl | 87.20 |
| | KYD-4 | 43 | 1.90 | 2.33 | 33.47 | 0.04 | 0.23 | 0.28 | bdl | bdl | 35.02 | 12.36 | bdl | bdl | 85.92 |
| | KYD-4 | 44 | 1.89 | 1.70 | 33.68 | 0.05 | 0.22 | 0.25 | bdl | bdl | 35.20 | 13.84 | bdl | bdl | 87.18 |
| | KYD-4 | 45 | 1.90 | 2.16 | 33.90 | 0.04 | 0.22 | 0.23 | bdl | 0.13 | 34.88 | 12.30 | bdl | bdl | 85.96 |
| | KYD-4(2) | 46 | 2.25 | 5.57 | 33.14 | 0.05 | 0.45 | 0.49 | bdl | 0.18 | 36.37 | 7.87 | bdl | bdl | 86.39 |
| | KYD-4(2) | 47 | 2.03 | 5.26 | 33.37 | 0.06 | 0.86 | 0.96 | bdl | 0.22 | 35.44 | 8.73 | bdl | bdl | 87.13 |
| **Tur3** | KYD-4(2) | 48 | 2.10 | 4.78 | 33.49 | 0.05 | 0.38 | 0.42 | bdl | 0.17 | 35.80 | 8.80 | bdl | bdl | 86.58 |
| | KYD-4(2) | 49 | 1.27 | 7.20 | 30.88 | 0.07 | 2.33 | 1.13 | bdl | 0.16 | 35.98 | 7.23 | bdl | bdl | 86.45 |
| | KYD-4(2) | 50 | 2.08 | 1.78 | 34.27 | 0.05 | 0.24 | 0.25 | bdl | bdl | 35.43 | 13.11 | bdl | bdl | 87.58 |
| | KYD-4(2) | 51 | 1.88 | 1.60 | 34.31 | 0.05 | 0.25 | 0.27 | bdl | bdl | 34.09 | 13.54 | bdl | bdl | 86.05 |
| | KYD-4(2) | 52 | 1.44 | 0.75 | 35.12 | 0.04 | 0.12 | bdl | bdl | bdl | 35.76 | 13.36 | bdl | bdl | 87.06 |
| | KYD-4(2) | 53 | 2.02 | 1.01 | 33.59 | 0.06 | 0.17 | 0.15 | bdl | 0.30 | 35.06 | 14.53 | bdl | bdl | 87.53 |
| | KYD-4(2) | 54 | 1.90 | 0.94 | 34.36 | 0.05 | 0.18 | 0.13 | bdl | 0.35 | 34.86 | 14.12 | bdl | bdl | 86.91 |
| | KYD-4(2) | 55 | 1.87 | 2.06 | 33.79 | 0.05 | 0.29 | 0.30 | bdl | bdl | 34.25 | 12.92 | bdl | bdl | 85.84 |
| | KYD-4(2) | 56 | 2.06 | 1.60 | 34.39 | 0.07 | 0.28 | 0.29 | bdl | bdl | 34.76 | 14.21 | bdl | bdl | 88.07 |
| | KYD-4(2) | 57 | 1.86 | 1.59 | 33.90 | 0.06 | 0.21 | 0.22 | bdl | 0.16 | 35.52 | 13.42 | bdl | bdl | 87.28 |
| | KYD-4(2) | 58 | 1.78 | 1.25 | 33.60 | 0.05 | 0.17 | 0.11 | bdl | 0.27 | 35.06 | 13.98 | bdl | bdl | 86.63 |
| | KYD-4(2) | 59 | 1.82 | 1.85 | 34.42 | 0.03 | 0.17 | 0.08 | bdl | 0.23 | 35.11 | 12.32 | bdl | bdl | 86.49 |
| | KYD-4(2) | 60 | 1.96 | 2.06 | 34.02 | 0.05 | 0.23 | 0.25 | bdl | bdl | 35.21 | 13.09 | bdl | bdl | 87.06 |

**Table 19:** Trace and REE chemistry of tourmaline from representative samples.

| | Tur1 | | | | | | | | | | | | | | |
|---|---|---|---|---|---|---|---|---|---|---|---|---|---|---|---|
| **EPMA Ref** | 19 / 1 . | 18 / 1 . | 51 / 1 . | 53 / 1 . | 55 / 1 . | 57 / 1 . | 56 / 1 . | 59 / 1 . | 58 / 1 . | 48 / 1 . | 29 / 1 . | 30 / 1 . | 26 / 1 . | 61 / 1 . | 70 |
| **Sample No.** | KYD14 | KYD14 | KYD14 | KYD14 | KYD14 | KYD14 | KYD14 | KYD14 | KYD14 | KYD14 | KYD14 | KYD14 | KYD14 | KYD14 | BH-149-3 |
| **Li7** | 13.11 | 13.17 | 15.63 | 9.53 | 16.29 | 9.49 | 27.07 | 14.82 | 6.41 | 12.66 | 11.17 | 12.52 | 16.54 | 14.36 | 13.15 |
| **Be9** | 3.88 | 3.11 | 2.68 | 3.70 | 4.10 | 4.06 | 4.82 | 3.89 | 1.91 | 2.77 | 2.97 | 4.20 | 6.74 | 4.80 | 2.79 |
| **P31** | 51.66 | <26.11 | 33.73 | 63.16 | 147.07 | <24.40 | <43.18 | 34.81 | <22.59 | 50.19 | 42.08 | 38.95 | 61.36 | 40.94 | 76.33 |
| **Cl35** | 693.90 | 765.82 | 586.50 | 870.00 | 3361.39 | 722.20 | 1347.64 | 682.80 | 709.61 | 735.65 | 645.33 | 801.09 | 2121.57 | 1406.93 | 884.92 |
| **K39** | 571.97 | 594.56 | 582.50 | 536.77 | 606.91 | 420.72 | 690.63 | 597.84 | 328.32 | 588.29 | 281.75 | 611.98 | 769.59 | 633.19 | 409.46 |
| **Sc45** | 24.97 | 24.74 | 21.37 | 33.25 | 24.76 | 17.67 | 36.34 | 22.78 | 16.82 | 22.45 | 16.38 | 23.13 | 27.07 | 22.76 | 22.35 |
| **Ti48** | 2917.0 | 3146.0 | 2784.5 | 2754.8 | 3170.5 | 2172.9 | 4043.6 | 3029.8 | 946.6 | 2934.9 | 2104.6 | 3319.8 | 3920.5 | 3165.6 | 3148.3 |
| **Ti49** | 4952.9 | 5450.8 | 4991.9 | 4517.7 | 5511.4 | 3794.5 | 7072.4 | 5282.7 | 1557.6 | 5119.0 | 3665.9 | 5792.7 | 6989.0 | 5528.5 | 5614.6 |
| **V51** | 359.25 | 382.48 | 340.59 | 257.16 | 387.28 | 283.86 | 546.53 | 372.76 | 45.14 | 372.17 | 280.38 | 396.31 | 503.10 | 425.04 | 287.56 |
| **Cr52** | 342.74 | 287.30 | 362.84 | 36.17 | 338.36 | 239.31 | 1310.13 | 351.28 | 5.81 | 348.25 | 258.55 | 339.32 | 439.73 | 340.63 | 316.56 |
| **Mn55** | 166.18 | 170.81 | 171.58 | 256.62 | 189.89 | 124.49 | 257.55 | 187.21 | 335.40 | 165.32 | 140.29 | 169.64 | 215.67 | 189.09 | 167.17 |
| **Co59** | 1.75 | 1.70 | 1.46 | 21.81 | 1.84 | 1.04 | 12.46 | 1.91 | 2.25 | 1.33 | 1.30 | 1.36 | 1.84 | 1.68 | 3.68 |
| **Ni60** | 3.61 | 4.23 | 3.95 | 44.18 | 4.59 | 2.96 | 86.46 | 4.45 | 1.48 | 3.50 | 3.16 | 3.12 | 4.91 | 4.23 | 5.66 |
| **Cu63** | 0.34 | 0.38 | 0.38 | 0.34 | 0.51 | 0.26 | 16.93 | 0.56 | 0.41 | 0.28 | 0.20 | 0.40 | 0.52 | 0.27 | 0.35 |
| **Zn66** | 821.62 | 843.07 | 753.26 | 781.04 | 909.76 | 637.65 | 1296.17 | 946.03 | 910.05 | 831.39 | 395.33 | 910.47 | 1021.97 | 925.84 | 1154.40 |
| **Ga71** | 38.00 | 40.03 | 34.29 | 51.34 | 41.18 | 27.89 | 52.30 | 38.22 | 41.07 | 37.13 | 27.50 | 39.63 | 53.32 | 45.55 | 40.18 |
| **Ge73** | 54.36 | 59.60 | 58.61 | 8.96 | 66.48 | 40.36 | 36.79 | 56.56 | 5.24 | 54.72 | 46.58 | 54.11 | 65.95 | 66.35 | 20.06 |
| **As75** | <1.06 | <0.98 | <0.92 | <1.02 | <0.79 | <0.91 | 1.55 | <0.87 | <0.83 | <0.87 | 1.14 | <1.01 | 0.93 | <1.07 | <0.98 |
| **Rb85** | <0.029 | <0.036 | 0.20 | <0.018 | 0.05 | <0.031 | 0.08 | <0.026 | 0.16 | 0.04 | <0.035 | <0.035 | <0.034 | 0.05 | <0.018 |
| **Sr88** | 138.81 | 128.13 | 146.71 | 78.01 | 144.50 | 93.26 | 302.79 | 152.30 | 5.57 | 119.84 | 164.37 | 121.78 | 151.07 | 136.49 | 89.86 |
| **Y89** | 0.21 | 0.17 | 0.29 | 0.20 | 0.32 | 0.08 | 0.13 | 0.16 | 0.39 | 0.12 | 0.04 | 0.22 | 0.24 | 0.16 | 0.08 |
| **Zr90** | 0.10 | 0.11 | 0.14 | 0.30 | 0.34 | 0.09 | 0.41 | 0.15 | 0.09 | 0.13 | 0.05 | 0.18 | 0.15 | 0.10 | 0.13 |
| **Nb93** | 0.03 | 0.04 | 0.04 | 0.19 | 0.02 | 0.03 | 0.15 | 0.04 | 0.45 | 0.05 | 0.02 | 0.04 | 0.07 | 0.04 | 0.03 |
| **Mo95** | <0.106 | 0.18 | <0.134 | <0.068 | <0.076 | <0.057 | <0.143 | 0.04 | <0.142 | <0.143 | <0.082 | <0.131 | <0.058 | <0.201 | <0.093 |

| | Tur1 | | | | | | | | | | | | | | |
|---|---|---|---|---|---|---|---|---|---|---|---|---|---|---|---|
| **EPMA Ref** | 19 / 1 . | 18 / 1 . | 51 / 1 . | 53 / 1 . | 55 / 1 . | 57 / 1 . | 56 / 1 . | 59 / 1 . | 58 / 1 . | 48 / 1 . | 29 / 1 . | 30 / 1 . | 26 / 1 . | 61 / 1 . | 70 |
| **Sample No.** | KYD14 | KYD14 | KYD14 | KYD14 | KYD14 | KYD14 | KYD14 | KYD14 | KYD14 | KYD14 | KYD14 | KYD14 | KYD14 | KYD14 | BH-149-3 |
| **Cd111** | <0.33 | <0.34 | <0.27 | <0.193 | 0.13 | <0.228 | 0.69 | <0.239 | <0.24 | <0.22 | <0.26 | <0.26 | <0.268 | 0.46 | <0.26 |
| **Sn118** | 0.62 | 0.67 | 0.57 | 2.35 | 0.52 | 0.44 | 2.08 | <0.37 | 1.02 | 0.86 | 0.61 | 0.57 | 0.72 | 0.65 | 0.54 |
| **Cs133** | <0.00 | 0.00 | 0.01 | <0.0091 | 0.01 | <0.0076 | 0.02 | <0.0092 | 0.02 | <0.00 | 0.00 | 0.00 | 0.01 | <0.00 | <0.00 |
| **Ba137** | 0.02 | 0.23 | 0.29 | 0.54 | <0.30 | 0.15 | 0.72 | 0.15 | 0.10 | 0.23 | <0.063 | 0.15 | 0.12 | 0.16 | 0.02 |
| **La139** | 5.25 | 4.45 | 2.03 | 7.63 | 3.77 | 4.63 | 2.15 | 2.69 | 1.07 | 4.94 | 0.83 | 5.57 | 7.45 | 7.13 | 5.17 |
| **Ce140** | 7.91 | 6.80 | 3.09 | 12.33 | 6.07 | 7.14 | 3.11 | 4.09 | 2.05 | 7.53 | 1.35 | 8.94 | 11.45 | 11.54 | 9.04 |
| **Pr141** | 0.79 | 0.65 | 0.28 | 0.94 | 0.56 | 0.71 | 0.26 | 0.42 | 0.18 | 0.71 | 0.16 | 0.77 | 1.10 | 1.03 | 0.77 |
| **Nd146** | 2.73 | 2.08 | 1.20 | 3.07 | 1.81 | 2.59 | 1.01 | 1.28 | 0.61 | 2.52 | 0.33 | 2.74 | 3.37 | 3.23 | 2.57 |
| **Sm147** | 0.27 | 0.36 | 0.13 | 0.31 | 0.34 | 0.31 | 0.19 | 0.22 | 0.15 | 0.20 | 0.08 | 0.27 | 0.44 | 0.33 | 0.46 |
| **Eu153** | 1.53 | 1.47 | 0.95 | 0.46 | 1.37 | 1.37 | 0.66 | 1.30 | 0.06 | 1.50 | 0.63 | 1.59 | 2.10 | 2.06 | 1.70 |
| **Gd157** | 0.26 | 0.24 | 0.19 | 0.33 | 0.34 | 0.23 | 0.04 | 0.13 | 0.10 | 0.30 | <0.041 | 0.19 | 0.28 | 0.38 | 0.31 |
| **Tb159** | 0.02 | 0.01 | 0.02 | 0.01 | 0.03 | 0.02 | 0.01 | 0.02 | 0.02 | 0.02 | <0.00 | 0.03 | 0.03 | 0.03 | 0.02 |
| **Dy163** | 0.05 | 0.05 | 0.08 | 0.04 | 0.11 | 0.12 | 0.08 | 0.04 | 0.07 | 0.06 | 0.02 | 0.04 | 0.09 | <0.263 | 0.10 |
| **Ho165** | 0.01 | 0.01 | 0.01 | 0.01 | 0.02 | 0.01 | 0.01 | 0.00 | 0.02 | 0.01 | <0.00 | 0.01 | 0.01 | 0.01 | 0.01 |
| **Er166** | <0.00 | 0.02 | 0.01 | 0.01 | 0.01 | 0.01 | 0.01 | 0.01 | 0.01 | <0.00 | 0.01 | 0.01 | 0.01 | 0.01 | 0.01 |
| **Tm169** | <0.00 | 0.00 | <0.0067 | 0.00 | 0.00 | <0.0057 | 0.01 | <0.00 | <0.00 | 0.00 | <0.00 | 0.00 | 0.00 | <0.00 | 0.01 |
| **Yb172** | 0.02 | 0.02 | 0.04 | 0.03 | 0.02 | 0.01 | 0.03 | 0.04 | 0.05 | 0.02 | 0.01 | 0.02 | 0.07 | 0.01 | 0.01 |
| **Lu175** | 0.00 | 0.00 | 0.01 | 0.01 | 0.01 | 0.00 | 0.00 | 0.00 | 0.01 | 0.00 | 0.00 | 0.00 | 0.01 | 0.00 | 0.00 |
| **Hf178** | <0.00 | 0.01 | 0.02 | <0.022 | 0.01 | 0.01 | 0.02 | 0.01 | 0.02 | 0.01 | <0.00 | 0.01 | 0.02 | 0.02 | 0.01 |
| **Ta181** | 0.01 | 0.00 | 0.00 | 0.01 | 0.01 | 0.00 | 0.03 | <0.0083 | 0.14 | 0.00 | 0.00 | <0.00 | 0.01 | 0.01 | 0.00 |
| **W182** | <0.0197 | 0.01 | <0.00 | <0.00 | 0.01 | <0.00 | <0.033 | <0.00 | 0.01 | <0.00 | <0.00 | <0.00 | <0.00 | <0.00 | <0.00 |
| **Pb208** | 162.78 | 165.67 | 141.90 | 11.11 | 167.26 | 120.97 | 48.73 | 161.39 | 95.68 | 160.40 | 37.83 | 175.31 | 210.88 | 191.76 | 250.84 |
| **Bi209** | <0.034 | <0.031 | <0.033 | <0.029 | <0.039 | <0.027 | <0.045 | <0.032 | <0.026 | <0.038 | <0.027 | <0.035 | <0.028 | <0.038 | <0.031 |
| **Th232** | 0.00 | <0.00 | 0.00 | 0.77 | 0.00 | 0.00 | 0.02 | <0.00 | 0.00 | <0.00 | 0.01 | 0.00 | 0.01 | 0.00 | <0.00 |
| **U238** | <0.00 | <0.00 | 0.01 | 0.08 | 0.00 | <0.00 | 0.02 | 0.00 | 0.00 | <0.00 | 0.00 | <0.00 | <0.00 | <0.00 | <0.00 |

| | Tur1 | | | | | | | | | Tur2 | | | | | |
|---|---|---|---|---|---|---|---|---|---|---|---|---|---|---|---|
| **EPMA Ref** | 71 | 74 | 73 | 66 | 67 | 68 | 64 | 63 | 61 | 50 / 1 . | 53 / 1 . | 54 / 1 . | 44 / 1 . | 43 / 1 . | 37 / 1 . |
| **Sample No.** | BH-149-3 | BH-149-3 | BH-149-3 | BH-149-3 | BH-149-3 | BH-149-3 | BH-149-3 | BH-149-3 | BH-149-3 | D4 | D4 | D4 | D4 | D4 | D4 |
| **Li7** | 13.64 | 1.87 | 13.77 | 13.43 | 13.20 | 13.22 | 10.25 | 13.08 | 12.76 | 39.37 | 47.57 | 32.02 | 61.12 | 61.93 | 29.63 |
| **Be9** | 1.49 | 0.49 | 3.30 | 2.47 | 3.57 | 1.86 | 2.92 | 1.95 | 2.51 | 10.16 | 15.96 | 7.62 | 11.13 | 14.04 | 5.63 |
| **P31** | 75.30 | <6.96 | 47.83 | 73.37 | 94.71 | 88.49 | 49.14 | 103.88 | 60.20 | 213.24 | 74.41 | 39.55 | 49.96 | <32.05 | 27.66 |
| **Cl35** | 837.71 | 172.12 | 1234.41 | 1664.54 | 1773.35 | 1362.33 | 617.35 | 937.48 | 915.98 | 4162.24 | 1474.37 | 705.01 | 1359.99 | 1258.30 | 971.82 |
| **K39** | 416.32 | 38.86 | 255.36 | 304.01 | 424.14 | 443.04 | 328.59 | 430.01 | 396.50 | 363.74 | 502.59 | 345.48 | 467.92 | 503.07 | 521.34 |
| **Sc45** | 23.62 | 3.76 | 27.84 | 27.57 | 23.31 | 23.14 | 19.71 | 25.46 | 22.57 | 27.29 | 49.74 | 29.52 | 76.77 | 118.43 | 24.69 |
| **Ti48** | 3312.76 | 545.28 | 3688.47 | 3350.42 | 3224.98 | 3133.90 | 2680.72 | 3299.06 | 3051.02 | 1455.33 | 3483.13 | 2207.75 | 3144.97 | 3142.43 | 2733.15 |
| **Ti49** | 5769.15 | 938.51 | 6471.79 | 5898.16 | 5583.36 | 5697.88 | 4721.64 | 5679.87 | 5266.26 | 2575.46 | 6006.02 | 3927.57 | 5465.30 | 5717.76 | 4909.61 |
| **V51** | 293.89 | 44.37 | 312.22 | 390.71 | 308.08 | 328.06 | 257.33 | 321.49 | 288.05 | 86.37 | 401.97 | 500.07 | 718.22 | 1140.55 | 404.75 |
| **Cr52** | 386.71 | 49.90 | 337.82 | 378.04 | 411.75 | 455.90 | 369.20 | 476.28 | 401.78 | 12.90 | 41.03 | 154.35 | 387.92 | 681.86 | 216.43 |
| **Mn55** | 172.07 | 26.54 | 206.07 | 223.58 | 163.88 | 174.96 | 139.42 | 170.74 | 153.96 | 670.14 | 654.22 | 338.75 | 440.05 | 454.54 | 338.79 |
| **Co59** | 4.33 | 0.63 | 5.47 | 5.25 | 3.79 | 4.43 | 2.97 | 4.13 | 3.70 | 4.64 | 4.95 | 3.66 | 2.93 | 3.33 | 2.93 |
| **Ni60** | 4.87 | 0.90 | 5.60 | 5.92 | 4.46 | 5.55 | 4.62 | 4.58 | 4.86 | 5.18 | 8.18 | 4.62 | 3.98 | 3.87 | 4.71 |
| **Cu63** | 0.40 | 0.10 | 0.84 | 0.93 | 0.33 | 0.41 | 0.19 | 0.42 | 0.37 | 0.41 | 0.47 | 0.29 | 0.39 | 0.62 | 0.48 |
| **Zn66** | 1094.10 | 141.26 | 978.57 | 1425.74 | 1125.38 | 1192.49 | 846.37 | 1188.07 | 1057.45 | 1873.70 | 1849.33 | 958.76 | 1314.31 | 1477.85 | 1127.51 |
| **Ga71** | 44.48 | 6.01 | 43.15 | 48.99 | 38.24 | 42.68 | 33.22 | 41.72 | 37.41 | 51.64 | 56.46 | 34.61 | 58.47 | 69.72 | 48.77 |
| **Ge73** | 18.18 | 3.60 | 22.41 | 25.78 | 14.65 | 18.71 | 14.52 | 19.51 | 17.57 | 9.85 | 10.30 | 11.13 | 29.60 | 33.63 | 12.93 |
| **As75** | <1.44 | <0.27 | <1.34 | <1.52 | <1.28 | <1.08 | <1.25 | <1.18 | 1.29 | <0.73 | <1.18 | <0.65 | <0.76 | <1.13 | 1.14 |
| **Rb85** | <0.056 | <0.0044 | 0.05 | 0.05 | <0.027 | <0.040 | <0.035 | <0.0214 | <0.0160 | <0.044 | <0.020 | <0.027 | 0.04 | <0.041 | <0.027 |
| **Sr88** | 105.76 | 47.73 | 118.56 | 132.68 | 89.85 | 99.13 | 88.07 | 112.61 | 98.62 | 7.37 | 11.00 | 14.21 | 22.07 | 18.63 | 29.63 |
| **Y89** | 0.08 | 0.05 | 0.19 | 0.09 | 0.13 | 0.16 | 0.15 | 0.18 | 0.11 | 0.32 | 0.68 | 0.09 | 0.11 | 0.25 | 0.12 |
| **Zr90** | 0.07 | 1.44 | 11.11 | 8.37 | 0.13 | 2.94 | 0.10 | 0.12 | 0.19 | 0.56 | 0.48 | 0.08 | 0.11 | 0.75 | 0.11 |
| **Nb93** | <0.031 | 0.01 | <0.0237 | <0.028 | 0.02 | 0.04 | 0.02 | 0.02 | 0.04 | 0.42 | 1.50 | 0.09 | 0.01 | 0.03 | 0.11 |
| **Mo95** | <0.170 | 0.01 | <0.161 | <0.189 | 0.17 | <0.149 | <0.132 | 0.08 | <0.084 | 0.10 | <0.152 | <0.089 | <0.092 | <0.077 | <0.102 |

| | Tur1 | | | | | | | | | Tur2 | | | | | |
|---|---|---|---|---|---|---|---|---|---|---|---|---|---|---|---|
| **EPMA Ref** | 71 | 74 | 73 | 66 | 67 | 68 | 64 | 63 | 61 | 50 / 1 . | 53 / 1 . | 54 / 1 . | 44 / 1 . | 43 / 1 . | 37 / 1 . |
| **Sample No.** | BH-149-3 | BH-149-3 | BH-149-3 | BH-149-3 | BH-149-3 | BH-149-3 | BH-149-3 | BH-149-3 | BH-149-3 | D4 | D4 | D4 | D4 | D4 | D4 |
| **Cd111** | <0.58 | <0.033 | <0.26 | 0.93 | <0.54 | <0.35 | <0.26 | 0.44 | 0.17 | <0.24 | <0.26 | <0.193 | <0.219 | 0.30 | <0.162 |
| **Sn118** | 1.07 | <0.073 | 0.53 | 0.60 | 1.94 | 0.91 | 0.46 | 0.80 | 1.03 | 1.91 | 2.43 | 0.92 | 2.94 | 3.09 | 2.33 |
| **Cs133** | <0.00 | <0.00 | <0.0123 | <0.00 | <0.00 | <0.0089 | 0.01 | 0.00 | <0.00 | <0.00 | <0.0100 | 0.00 | <0.00 | <0.00 | <0.0078 |
| **Ba137** | 0.08 | 0.03 | 0.13 | 0.07 | <0.111 | 0.14 | 0.15 | 0.05 | 0.04 | <0.066 | 0.26 | 0.07 | 0.16 | 0.48 | 0.19 |
| **La139** | 5.44 | 0.41 | 0.73 | 1.28 | 4.74 | 5.18 | 4.24 | 6.25 | 5.61 | 2.60 | 4.15 | 3.23 | 4.78 | 5.13 | 7.82 |
| **Ce140** | 8.74 | 0.61 | 1.43 | 2.35 | 8.12 | 8.83 | 6.63 | 9.68 | 8.70 | 4.92 | 8.06 | 5.44 | 8.69 | 9.94 | 14.08 |
| **Pr141** | 0.87 | 0.06 | 0.13 | 0.18 | 0.79 | 0.71 | 0.60 | 0.96 | 0.79 | 0.48 | 0.70 | 0.55 | 0.80 | 0.97 | 1.22 |
| **Nd146** | 2.42 | 0.18 | 0.32 | 0.51 | 2.57 | 2.43 | 1.86 | 3.33 | 2.92 | 1.27 | 2.17 | 1.78 | 2.76 | 3.48 | 3.62 |
| **Sm147** | 0.24 | 0.02 | 0.07 | 0.10 | 0.30 | 0.30 | 0.19 | 0.30 | 0.19 | 0.22 | 0.46 | 0.13 | 0.39 | 0.67 | 0.43 |
| **Eu153** | 2.04 | 0.16 | 0.63 | 0.74 | 1.70 | 1.72 | 1.61 | 2.14 | 1.59 | 0.18 | 0.26 | 0.37 | 0.63 | 0.57 | 0.79 |
| **Gd157** | 0.27 | 0.01 | 0.06 | 0.18 | 0.21 | 0.20 | 0.16 | 0.44 | 0.24 | 0.08 | 0.30 | 0.14 | 0.23 | 0.34 | 0.27 |
| **Tb159** | 0.03 | 0.00 | 0.01 | 0.01 | 0.02 | 0.02 | 0.02 | 0.03 | 0.02 | 0.01 | 0.02 | 0.01 | 0.02 | 0.02 | 0.04 |
| **Dy163** | 0.05 | 0.02 | 0.03 | 0.01 | <0.045 | 0.06 | 0.05 | 0.08 | 0.06 | 0.06 | 0.09 | 0.03 | 0.07 | 0.06 | 0.05 |
| **Ho165** | <0.00 | 0.00 | 0.01 | 0.00 | 0.00 | 0.01 | 0.01 | 0.01 | 0.01 | 0.01 | 0.03 | 0.01 | 0.01 | 0.01 | 0.01 |
| **Er166** | 0.01 | 0.01 | 0.03 | <0.00 | <0.00 | 0.02 | 0.01 | <0.00 | 0.01 | 0.03 | 0.05 | 0.01 | 0.01 | 0.03 | 0.02 |
| **Tm169** | <0.00 | 0.00 | <0.0093 | 0.01 | <0.00 | <0.00 | 0.00 | <0.00 | <0.00 | 0.00 | 0.02 | 0.00 | <0.00 | 0.00 | 0.00 |
| **Yb172** | <0.00 | 0.02 | 0.13 | 0.07 | <0.00 | 0.01 | 0.01 | 0.04 | 0.01 | 0.02 | 0.14 | 0.02 | 0.02 | 0.01 | 0.01 |
| **Lu175** | <0.00 | 0.00 | 0.01 | 0.01 | 0.00 | 0.00 | 0.00 | 0.00 | 0.01 | 0.02 | 0.05 | <0.00 | 0.01 | 0.00 | 0.00 |
| **Hf178** | <0.00 | 0.05 | 0.14 | 0.26 | 0.01 | 0.03 | <0.00 | 0.02 | 0.02 | 0.12 | 0.11 | 0.01 | 0.01 | 0.08 | 0.02 |
| **Ta181** | 0.00 | <0.00 | 0.00 | <0.00 | 0.00 | 0.01 | <0.0064 | <0.0067 | 0.01 | 0.16 | 1.24 | 0.03 | <0.00 | 0.00 | <0.00 |
| **W182** | <0.00 | <0.00 | 0.01 | 0.02 | <0.00 | <0.00 | <0.00 | <0.00 | <0.00 | 0.01 | 0.05 | 0.01 | <0.00 | 0.01 | 0.01 |
| **Pb208** | 251.19 | 20.10 | 102.04 | 123.34 | 232.68 | 248.33 | 188.33 | 257.86 | 233.70 | 144.23 | 238.00 | 184.03 | 249.68 | 279.88 | 259.44 |
| **Bi209** | <0.059 | <0.0080 | <0.045 | <0.050 | <0.048 | <0.041 | <0.036 | <0.037 | <0.027 | <0.040 | 0.04 | 0.04 | <0.024 | <0.036 | <0.0225 |
| **Th232** | <0.00 | 0.01 | 0.03 | 0.01 | <0.00 | 0.00 | <0.00 | <0.00 | <0.00 | 0.01 | 0.03 | 0.00 | 0.02 | 0.01 | 0.00 |
| **U238** | <0.00 | 0.02 | 0.12 | 0.08 | <0.00 | 0.01 | 0.00 | <0.00 | <0.00 | 0.03 | 0.01 | 0.00 | 0.00 | 0.01 | <0.00 |

| | Tur2 | | | | | | | | | | | | Tur3 | | |
|---|---|---|---|---|---|---|---|---|---|---|---|---|---|---|---|
| **EPMA Ref** | 40 / 1 . | 37 / 1 . | 37 / 1 . | 40 / 1 . | 40 / 1 . | 37 / 1 . | 43 / 1 . | 37 / 1 . | 37 / 1 . | 44 / 1 . | 52 / 1 . | 37 / 1 . | 24 | 23 | 24 |
| **Sample No.** | D4 | D4 | D4 | D4 | D4 | D4 | D4 | D4 | D4 | D4 | D4 | D4 | N-169 | N-169 | N-169 |
| **Li7** | 84.63 | 39.03 | 49.13 | 45.09 | 47.34 | 35.08 | 30.04 | 34.32 | 53.29 | 54.45 | 28.27 | 38.77 | 29.72 | 70.84 | 40.18 |
| **Be9** | 9.99 | 10.06 | 13.48 | 11.26 | 10.38 | 12.94 | 8.74 | 1.91 | 5.67 | 9.48 | 6.13 | 10.79 | 3.53 | 3.74 | 3.01 |
| **P31** | <35.09 | 73.33 | <34.44 | 73.66 | 43.87 | 44.83 | 58.88 | 43.78 | 35.04 | 46.65 | 39.10 | 34.81 | <19.66 | <30.15 | 53.63 |
| **Cl35** | 1946.18 | 815.56 | 1275.40 | 993.27 | 2182.08 | 2044.25 | 641.16 | 1690.16 | 1510.55 | 1796.02 | 1375.63 | 1990.93 | 919.02 | 1360.40 | 1130.34 |
| **K39** | 808.79 | 543.67 | 608.84 | 864.10 | 813.31 | 720.26 | 476.86 | 668.59 | 542.69 | 528.87 | 410.32 | 644.05 | 434.28 | 595.76 | 434.95 |
| **Sc45** | 53.85 | 24.66 | 38.45 | 37.01 | 35.23 | 37.72 | 38.80 | 52.32 | 66.01 | 72.20 | 35.75 | 37.19 | 11.32 | 16.93 | 10.58 |
| **Ti48** | 3235.53 | 3032.08 | 4071.80 | 5797.45 | 5661.55 | 4248.05 | 2941.04 | 4022.51 | 2914.74 | 3751.07 | 2414.72 | 3974.87 | 706.91 | 947.97 | 587.64 |
| **Ti49** | 5664.54 | 5075.47 | 7236.47 | 10138.20 | 9977.95 | 7420.19 | 5082.90 | 7032.80 | 5271.41 | 6489.32 | 4299.64 | 7095.19 | 1207.54 | 1656.24 | 1030.45 |
| **V51** | 688.68 | 415.35 | 689.57 | 608.39 | 503.09 | 557.25 | 614.75 | 654.77 | 574.05 | 630.76 | 499.80 | 631.52 | 0.17 | 0.27 | 0.11 |
| **Cr52** | 217.43 | 246.84 | 754.33 | 496.87 | 476.39 | 445.68 | 576.15 | 414.81 | 466.29 | 280.33 | 295.92 | 263.29 | <1.41 | <2.09 | 9.99 |
| **Mn55** | 626.72 | 331.21 | 595.78 | 1042.42 | 935.63 | 669.18 | 401.91 | 365.86 | 353.20 | 524.82 | 376.36 | 489.66 | 930.23 | 1392.00 | 887.82 |
| **Co59** | 5.65 | 3.09 | 6.17 | 9.52 | 9.07 | 6.32 | 3.13 | 4.57 | 3.31 | 4.51 | 4.09 | 4.92 | 1.72 | 2.52 | 1.56 |
| **Ni60** | 6.34 | 5.04 | 8.71 | 12.21 | 13.26 | 9.05 | 5.26 | 6.35 | 3.75 | 5.04 | 5.59 | 6.95 | <0.192 | <0.31 | <0.196 |
| **Cu63** | 0.57 | 0.43 | 0.81 | 1.02 | 0.60 | 0.87 | 0.39 | 0.70 | 0.51 | 0.58 | 0.45 | 0.60 | 0.24 | 0.48 | 0.11 |
| **Zn66** | 2115.83 | 1161.22 | 1767.36 | 2756.72 | 2691.23 | 1845.70 | 1123.60 | 1708.15 | 1323.88 | 1508.62 | 1067.34 | 1472.77 | 2155.46 | 3148.43 | 1921.56 |
| **Ga71** | 68.16 | 45.05 | 75.21 | 71.98 | 70.94 | 77.05 | 43.57 | 67.90 | 53.34 | 56.24 | 43.72 | 69.74 | 73.84 | 102.00 | 73.10 |
| **Ge73** | 51.53 | 17.93 | 16.49 | 26.44 | 18.01 | 15.80 | 13.80 | 38.02 | 42.24 | 32.36 | 9.67 | 21.64 | 2.65 | 3.60 | 2.93 |
| **As75** | 1.97 | <1.12 | 1.07 | <1.81 | 2.52 | <1.03 | <0.85 | 2.12 | <0.94 | <1.10 | 0.53 | <0.78 | <0.73 | <1.36 | <0.62 |
| **Rb85** | 0.09 | <0.031 | <0.032 | <0.040 | <0.063 | 0.14 | <0.025 | <0.033 | 0.03 | 0.05 | 0.01 | <0.019 | 0.04 | <0.020 | 0.03 |
| **Sr88** | 45.60 | 31.13 | 20.97 | 31.77 | 32.18 | 17.98 | 21.66 | 32.54 | 32.04 | 21.27 | 13.32 | 27.06 | 0.88 | 1.19 | 1.09 |
| **Y89** | 0.82 | 0.13 | 0.12 | 0.07 | 0.04 | 0.47 | 0.07 | 0.06 | 0.20 | 0.24 | 0.08 | 0.06 | 0.02 | 0.03 | 0.09 |
| **Zr90** | 0.40 | 0.07 | 0.07 | 0.10 | 0.17 | 1.22 | 0.07 | 0.07 | 0.55 | 0.30 | 0.10 | 0.05 | 0.12 | 0.16 | 0.49 |
| **Nb93** | 0.03 | <0.0143 | 0.11 | 0.16 | 0.27 | 0.13 | <0.0135 | <0.00 | <0.0167 | 0.03 | 0.08 | <0.00 | 1.00 | 1.42 | 1.43 |
| **Mo95** | <0.191 | <0.081 | <0.084 | <0.148 | <0.150 | 0.05 | <0.077 | <0.087 | <0.067 | <0.147 | <0.069 | <0.101 | <0.066 | <0.130 | <0.067 |

| | Tur2 | | | | | | | | | | | | Tur3 | | |
|---|---|---|---|---|---|---|---|---|---|---|---|---|---|---|---|
| **EPMA Ref** | 40 / 1 . | 37 / 1 . | 37 / 1 . | 40 / 1 . | 40 / 1 . | 37 / 1 . | 43 / 1 . | 37 / 1 . | 37 / 1 . | 44 / 1 . | 52 / 1 . | 37 / 1 . | 24 | 23 | 24 |
| **Sample No.** | D4 | D4 | D4 | D4 | D4 | D4 | D4 | D4 | D4 | D4 | D4 | D4 | N-169 | N-169 | N-169 |
| **Cd111** | <0.26 | <0.192 | <0.28 | <0.29 | <0.29 | 0.71 | 0.18 | <0.33 | 0.04 | 0.30 | 0.18 | <0.27 | 0.34 | 0.20 | <0.158 |
| **Sn118** | 2.83 | 2.54 | 3.81 | 4.27 | 4.27 | 4.68 | 1.91 | 1.84 | 2.40 | 3.00 | 1.96 | 3.04 | 5.54 | 8.70 | 6.12 |
| **Cs133** | <0.00 | <0.00 | <0.00 | 0.00 | <0.00 | 0.01 | 0.00 | <0.00 | <0.00 | 0.00 | <0.0064 | <0.00 | <0.00 | <0.0098 | 0.03 |
| **Ba137** | 0.62 | 0.33 | 0.22 | 0.64 | 0.51 | 0.20 | 0.25 | 0.19 | 0.27 | 0.33 | 0.05 | 0.28 | <0.00 | <0.00 | <0.00 |
| **La139** | 10.10 | 6.77 | 5.03 | 5.53 | 5.17 | 4.13 | 3.64 | 5.28 | 9.01 | 5.61 | 2.68 | 5.05 | 1.63 | 1.82 | 1.83 |
| **Ce140** | 18.26 | 11.58 | 9.58 | 9.51 | 8.44 | 7.84 | 6.32 | 9.42 | 15.83 | 10.06 | 4.90 | 8.87 | 3.10 | 3.29 | 3.12 |
| **Pr141** | 1.64 | 0.95 | 0.90 | 0.77 | 0.76 | 0.67 | 0.52 | 0.80 | 1.51 | 0.93 | 0.45 | 0.74 | 0.26 | 0.27 | 0.26 |
| **Nd146** | 5.09 | 2.92 | 2.51 | 2.07 | 2.27 | 2.45 | 1.81 | 2.33 | 3.96 | 3.15 | 1.39 | 2.19 | 0.81 | 0.87 | 0.94 |
| **Sm147** | 0.86 | 0.30 | 0.44 | 0.32 | 0.34 | 0.22 | 0.25 | 0.32 | 0.41 | 0.47 | 0.18 | 0.31 | 0.16 | 0.18 | 0.15 |
| **Eu153** | 1.16 | 0.86 | 0.50 | 0.82 | 0.85 | 0.45 | 0.53 | 0.82 | 0.98 | 0.57 | 0.32 | 0.69 | 0.01 | 0.02 | 0.01 |
| **Gd157** | 0.44 | 0.24 | 0.28 | 0.18 | 0.11 | 0.18 | 0.12 | 0.24 | 0.42 | 0.33 | 0.07 | 0.22 | 0.10 | 0.08 | 0.08 |
| **Tb159** | 0.03 | 0.02 | 0.02 | <0.0113 | 0.03 | 0.02 | 0.01 | 0.02 | 0.03 | 0.02 | 0.01 | 0.01 | 0.01 | 0.01 | 0.01 |
| **Dy163** | 0.13 | 0.06 | 0.08 | 0.04 | <0.046 | 0.10 | 0.01 | 0.01 | 0.11 | 0.06 | 0.05 | 0.07 | 0.03 | <0.00 | 0.03 |
| **Ho165** | 0.03 | <0.00 | 0.00 | 0.00 | <0.00 | 0.02 | 0.01 | 0.01 | 0.00 | 0.01 | 0.00 | 0.01 | <0.00 | 0.00 | 0.01 |
| **Er166** | 0.09 | 0.01 | 0.02 | 0.02 | <0.00 | 0.05 | <0.00 | 0.01 | 0.03 | 0.03 | <0.0145 | 0.01 | <0.00 | 0.01 | 0.02 |
| **Tm169** | 0.01 | <0.00 | <0.00 | 0.00 | <0.00 | 0.01 | 0.00 | <0.00 | 0.00 | <0.00 | <0.0067 | <0.00 | 0.00 | <0.00 | 0.00 |
| **Yb172** | 0.14 | 0.01 | <0.038 | 0.01 | <0.00 | 0.06 | 0.02 | 0.01 | 0.02 | 0.08 | 0.02 | <0.00 | 0.01 | <0.00 | 0.03 |
| **Lu175** | 0.03 | 0.00 | 0.01 | 0.01 | 0.01 | 0.01 | 0.00 | <0.00 | 0.01 | 0.01 | 0.00 | 0.01 | <0.00 | 0.00 | 0.00 |
| **Hf178** | <0.025 | 0.01 | 0.02 | <0.00 | <0.00 | 0.05 | 0.01 | 0.02 | 0.06 | 0.01 | 0.00 | 0.01 | 0.02 | 0.04 | 0.08 |
| **Ta181** | 0.00 | <0.00 | 0.04 | 0.10 | 0.06 | 0.05 | 0.00 | <0.00 | 0.00 | 0.01 | 0.04 | <0.00 | 0.16 | 0.28 | 0.25 |
| **W182** | 0.06 | <0.00 | 0.02 | <0.00 | <0.00 | <0.00 | <0.00 | <0.00 | 0.01 | 0.05 | 0.02 | <0.0238 | <0.0154 | 0.01 | 0.01 |
| **Pb208** | 395.40 | 276.54 | 395.24 | 558.50 | 449.07 | 368.39 | 259.07 | 303.48 | 276.53 | 273.38 | 221.22 | 375.73 | 33.46 | 38.33 | 37.54 |
| **Bi209** | <0.039 | 0.02 | <0.034 | <0.040 | <0.037 | <0.037 | <0.024 | <0.033 | <0.026 | <0.030 | 0.06 | <0.032 | <0.025 | <0.033 | 0.03 |
| **Th232** | 0.05 | 0.00 | 0.01 | <0.00 | <0.00 | 0.00 | 0.00 | 0.00 | 0.01 | 0.06 | 0.01 | 0.01 | <0.00 | 0.01 | 0.21 |
| **U238** | 0.01 | <0.00 | 0.00 | <0.00 | <0.00 | 0.03 | <0.00 | <0.00 | 0.00 | 0.00 | 0.00 | <0.00 | <0.00 | <0.0048 | 0.12 |

| | Tur3 | | | | | | | | | | | | | | |
|---|---|---|---|---|---|---|---|---|---|---|---|---|---|---|---|
| **EPMA Ref** | 30 | 29 | 28 | 17 | 19 | 21 | 14 | 15 | 26 | 27 | 50 | 51 | 59 | 58 | 57 |
| **Sample No.** | N-169 | N-169 | N-169 | N-169 | N-169 | N-169 | N-169 | N-169 | N-169 | N-169 | KYD-4(2) | KYD-4(2) | KYD-4(2) | KYD-4(2) | KYD-4(2) |
| **Li7** | 31.83 | 63.45 | 47.65 | 36.28 | 37.72 | 27.49 | 38.60 | 62.53 | 42.73 | 43.19 | 26.73 | 21.34 | 44.00 | 33.30 | 43.45 |
| **Be9** | 2.99 | 3.30 | 2.11 | 8.78 | 3.50 | 2.45 | 2.77 | 3.57 | 3.07 | 4.86 | 3.23 | 6.22 | 4.91 | 6.14 | 4.04 |
| **P31** | <29.80 | <32.55 | 63.07 | 35.45 | <21.90 | 40.17 | 29.47 | 57.63 | <31.17 | 79.19 | 28.07 | 58.61 | 42.15 | 52.37 | 46.55 |
| **Cl35** | 1393.58 | 1059.86 | 1704.66 | 1733.16 | 1259.56 | 874.66 | 1170.85 | 1392.47 | 1536.95 | 1126.73 | 552.51 | 849.51 | 898.66 | 1091.59 | 943.15 |
| **K39** | 382.51 | 460.17 | 574.23 | 542.31 | 473.78 | 318.44 | 478.73 | 468.71 | 394.31 | 558.95 | 378.84 | 452.08 | 420.82 | 442.76 | 450.74 |
| **Sc45** | 13.51 | 14.46 | 14.78 | 14.98 | 11.79 | 11.42 | 12.02 | 13.36 | 14.22 | 15.92 | 10.12 | 15.30 | 17.80 | 12.77 | 14.50 |
| **Ti48** | 275.50 | 554.33 | 1023.64 | 729.12 | 690.48 | 244.62 | 547.29 | 679.37 | 289.58 | 964.49 | 528.93 | 987.45 | 367.84 | 446.72 | 759.09 |
| **Ti49** | 473.85 | 939.42 | 1721.73 | 1282.59 | 1202.30 | 417.81 | 911.37 | 1203.87 | 515.21 | 1643.33 | 903.19 | 1675.97 | 627.79 | 781.22 | 1347.75 |
| **V51** | 0.14 | <0.147 | 0.25 | 0.13 | 0.17 | <0.086 | 0.17 | 0.16 | 0.22 | 0.32 | 5.54 | 24.56 | 0.45 | 0.60 | 1.34 |
| **Cr52** | <2.08 | <2.24 | <2.26 | <1.79 | <1.51 | <1.55 | 2.31 | <1.89 | <2.25 | <2.34 | 13.15 | 56.72 | <1.95 | <1.41 | 7.82 |
| **Mn55** | 1046.28 | 1189.90 | 1287.40 | 1271.89 | 1015.74 | 892.75 | 969.76 | 1078.17 | 1152.70 | 1268.48 | 782.44 | 869.03 | 1015.27 | 1320.13 | 997.13 |
| **Co59** | 1.99 | 1.94 | 2.16 | 2.34 | 1.80 | 1.55 | 1.94 | 2.30 | 1.98 | 2.16 | 4.66 | 4.74 | 3.65 | 2.76 | 3.90 |
| **Ni60** | <0.24 | <0.34 | 0.36 | <0.168 | <0.25 | <0.32 | <0.196 | 0.32 | <0.36 | <0.41 | 4.94 | 4.08 | 2.57 | 0.84 | 3.34 |
| **Cu63** | 0.27 | <0.102 | 0.19 | 0.36 | 0.17 | <0.126 | 0.11 | 0.20 | <0.140 | 0.36 | 3.67 | 0.19 | 0.26 | 0.21 | 0.20 |
| **Zn66** | 2380.08 | 2766.88 | 3144.24 | 2910.26 | 2351.13 | 2027.48 | 2176.83 | 2401.53 | 2529.99 | 3308.06 | 1941.16 | 2723.83 | 2520.28 | 2320.05 | 2756.47 |
| **Ga71** | 82.30 | 97.17 | 96.44 | 88.08 | 80.31 | 72.12 | 84.12 | 81.56 | 89.03 | 103.17 | 47.31 | 72.38 | 74.71 | 67.71 | 72.05 |
| **Ge73** | 2.92 | 2.64 | 4.70 | 3.39 | 2.64 | 2.32 | 4.00 | 3.41 | 2.48 | 4.93 | 4.13 | 2.61 | 2.19 | 3.88 | 2.93 |
| **As75** | <0.97 | <1.11 | <0.89 | <0.78 | <0.63 | <0.82 | <0.86 | <1.10 | <0.92 | <1.20 | <0.52 | <0.82 | <1.02 | 1.06 | <0.78 |
| **Rb85** | <0.028 | 0.02 | <0.037 | 0.02 | 0.03 | 0.01 | 0.03 | <0.0177 | <0.043 | 0.03 | 0.40 | <0.031 | <0.027 | 0.07 | 0.05 |
| **Sr88** | 0.41 | 0.66 | 0.97 | 0.91 | 1.14 | 0.36 | 0.89 | 0.86 | 0.49 | 1.33 | 2.39 | 2.05 | 0.83 | 0.68 | 1.40 |
| **Y89** | <0.00 | <0.0187 | 0.04 | 0.04 | 0.03 | 0.00 | 0.02 | 0.02 | 0.01 | 0.05 | 0.22 | 0.00 | <0.0166 | <0.0117 | 0.06 |
| **Zr90** | 0.11 | 0.12 | 0.33 | 0.17 | 0.12 | 0.15 | 0.21 | 0.11 | 0.14 | 0.21 | 0.90 | 0.08 | 0.19 | 0.16 | 0.07 |
| **Nb93** | 0.59 | 1.11 | 1.21 | 1.43 | 1.21 | 0.57 | 1.83 | 1.26 | 0.71 | 1.70 | 0.89 | 1.41 | 0.57 | 1.92 | 1.32 |
| **Mo95** | <0.105 | <0.116 | <0.115 | <0.064 | 0.08 | <0.056 | 0.05 | <0.094 | <0.080 | <0.120 | <0.057 | <0.081 | <0.142 | <0.050 | <0.089 |

| | Tur3 | | | | | | | | | | | | | | |
|---|---|---|---|---|---|---|---|---|---|---|---|---|---|---|---|
| **EPMA Ref** | 30 | 29 | 28 | 17 | 19 | 21 | 14 | 15 | 26 | 27 | 50 | 51 | 59 | 58 | 57 |
| **Sample No.** | N-169 | N-169 | N-169 | N-169 | N-169 | N-169 | N-169 | N-169 | N-169 | N-169 | KYD-4(2) | KYD-4(2) | KYD-4(2) | KYD-4(2) | KYD-4(2) |
| **Cd111** | <0.25 | <0.22 | <0.27 | <0.214 | <0.181 | <0.213 | <0.25 | 0.43 | <0.26 | <0.28 | 0.23 | <0.194 | 0.29 | <0.197 | 0.30 |
| **Sn118** | 5.01 | 7.28 | 7.52 | 5.88 | 6.20 | 4.10 | 8.22 | 5.52 | 4.94 | 8.78 | 3.84 | 7.12 | 5.19 | 10.00 | 7.32 |
| **Cs133** | <0.00 | <0.00 | <0.00 | <0.0084 | <0.00 | 0.00 | 0.00 | 0.00 | <0.00 | <0.00 | 0.10 | 0.00 | <0.00 | <0.00 | 0.03 |
| **Ba137** | <0.00 | <0.00 | <0.00 | <0.00 | 0.02 | <0.00 | <0.00 | <0.00 | <0.00 | 0.03 | 0.09 | <0.00 | <0.00 | 0.02 | <0.056 |
| **La139** | 0.36 | 0.64 | 1.51 | 1.29 | 1.93 | 0.44 | 2.22 | 1.50 | 0.45 | 2.32 | 1.16 | 0.97 | 0.54 | 1.42 | 0.87 |
| **Ce140** | 0.77 | 1.15 | 2.80 | 2.51 | 3.57 | 0.74 | 3.69 | 2.93 | 0.68 | 4.63 | 2.06 | 1.59 | 0.94 | 2.26 | 1.59 |
| **Pr141** | 0.03 | 0.10 | 0.22 | 0.22 | 0.28 | 0.06 | 0.31 | 0.29 | 0.08 | 0.45 | 0.18 | 0.13 | 0.08 | 0.20 | 0.12 |
| **Nd146** | 0.13 | 0.27 | 0.77 | 0.56 | 0.87 | 0.18 | 0.98 | 0.81 | 0.22 | 1.02 | 0.53 | 0.38 | 0.25 | 0.53 | 0.43 |
| **Sm147** | 0.03 | 0.08 | 0.22 | 0.18 | 0.21 | 0.04 | 0.16 | 0.12 | 0.04 | 0.19 | 0.11 | 0.08 | 0.10 | 0.21 | 0.13 |
| **Eu153** | 0.01 | <0.00 | 0.03 | 0.02 | 0.02 | 0.01 | 0.01 | 0.01 | <0.00 | 0.00 | 0.04 | 0.03 | 0.01 | 0.00 | 0.02 |
| **Gd157** | 0.05 | 0.02 | 0.07 | 0.04 | 0.17 | 0.01 | 0.10 | 0.08 | <0.00 | 0.07 | 0.06 | 0.02 | 0.02 | 0.03 | 0.07 |
| **Tb159** | 0.00 | 0.01 | 0.01 | 0.00 | 0.01 | <0.00 | 0.01 | 0.01 | 0.00 | 0.01 | 0.01 | <0.00 | <0.00 | 0.00 | 0.01 |
| **Dy163** | 0.01 | <0.00 | 0.02 | <0.00 | 0.01 | 0.01 | 0.01 | 0.02 | <0.034 | 0.02 | 0.04 | 0.02 | <0.00 | <0.022 | 0.04 |
| **Ho165** | <0.00 | <0.00 | <0.00 | 0.00 | <0.00 | 0.00 | 0.00 | 0.00 | <0.00 | <0.00 | 0.00 | 0.00 | <0.00 | <0.00 | <0.00 |
| **Er166** | <0.00 | 0.01 | <0.00 | <0.00 | <0.00 | 0.01 | <0.00 | <0.00 | 0.01 | 0.01 | 0.02 | <0.00 | <0.00 | 0.00 | 0.01 |
| **Tm169** | 0.00 | <0.00 | 0.00 | <0.00 | <0.00 | <0.00 | <0.00 | <0.00 | <0.00 | <0.00 | <0.00 | 0.00 | <0.00 | <0.00 | <0.00 |
| **Yb172** | <0.00 | <0.00 | 0.04 | <0.00 | <0.00 | <0.00 | 0.01 | <0.00 | <0.00 | <0.00 | 0.03 | <0.00 | <0.00 | <0.00 | 0.01 |
| **Lu175** | <0.00 | <0.00 | 0.00 | <0.00 | <0.00 | <0.00 | 0.00 | <0.00 | 0.00 | <0.00 | 0.00 | <0.00 | <0.00 | 0.00 | 0.00 |
| **Hf178** | 0.01 | 0.01 | 0.04 | 0.02 | 0.04 | 0.02 | 0.02 | 0.02 | 0.03 | 0.01 | 0.07 | <0.0185 | 0.01 | 0.04 | 0.01 |
| **Ta181** | 0.14 | 0.27 | 0.21 | 0.26 | 0.23 | 0.14 | 0.30 | 0.28 | 0.16 | 0.32 | 0.15 | 0.75 | 0.13 | 0.51 | 0.70 |
| **W182** | <0.00 | 0.01 | <0.00 | <0.00 | 0.01 | <0.00 | <0.00 | <0.0220 | <0.00 | <0.00 | <0.0130 | <0.00 | <0.00 | <0.00 | 0.02 |
| **Pb208** | 13.10 | 18.36 | 35.45 | 29.91 | 36.34 | 12.13 | 34.78 | 28.21 | 14.21 | 46.27 | 29.58 | 25.95 | 15.77 | 35.08 | 36.20 |
| **Bi209** | <0.030 | <0.034 | <0.035 | 0.03 | <0.0247 | <0.0247 | <0.0231 | <0.034 | <0.034 | <0.036 | <0.0150 | <0.023 | <0.034 | <0.0224 | <0.023 |
| **Th232** | 0.00 | <0.00 | 0.06 | <0.00 | 0.00 | <0.00 | 0.00 | 0.00 | <0.00 | <0.00 | 0.05 | 0.00 | 0.00 | 0.00 | 0.00 |
| **U238** | <0.00 | <0.00 | 0.02 | <0.00 | <0.00 | <0.00 | 0.00 | <0.00 | <0.00 | 0.00 | 0.35 | <0.00 | <0.00 | <0.00 | 0.00 |

| | Tur3 | |
|---|---|---|
| **EPMA Ref** | 52 | 54 |
| **Sample No.** | KYD-4(2) | KYD-4(2) |
| **Li7** | 50.94 | 14.70 |
| **Be9** | 20.83 | 1.89 |
| **P31** | 58.77 | 18.04 |
| **Cl35** | 1084.71 | 294.64 |
| **K39** | 390.56 | 172.33 |
| **Sc45** | 13.37 | 5.93 |
| **Ti48** | 106.93 | 179.15 |
| **Ti49** | 178.99 | 312.59 |
| **V51** | 0.12 | 0.62 |
| **Cr52** | 2.55 | <0.68 |
| **Mn55** | 1384.91 | 577.88 |
| **Co59** | 2.72 | 1.78 |
| **Ni60** | 1.29 | 2.42 |
| **Cu63** | 0.14 | 0.07 |
| **Zn66** | 2727.18 | 912.93 |
| **Ga71** | 77.05 | 26.51 |
| **Ge73** | 3.54 | 1.53 |
| **As75** | <0.99 | <0.36 |
| **Rb85** | <0.0219 | <0.0116 |
| **Sr88** | 0.62 | 2.98 |
| **Y89** | 0.02 | 0.02 |
| **Zr90** | 0.38 | 0.01 |
| **Nb93** | 2.40 | 0.34 |
| **Mo95** | <0.082 | <0.043 |

| | Tur3 | |
|---|---|---|
| **EPMA Ref** | 52 | 54 |
| **Sample No.** | KYD-4(2) | KYD-4(2) |
| **Cd111** | <0.196 | <0.085 |
| **Sn118** | 12.61 | 1.84 |
| **Cs133** | 0.02 | <0.00 |
| **Ba137** | 0.02 | 0.02 |
| **La139** | 0.43 | 1.49 |
| **Ce140** | 0.64 | 2.47 |
| **Pr141** | 0.04 | 0.19 |
| **Nd146** | 0.13 | 0.38 |
| **Sm147** | <0.00 | 0.07 |
| **Eu153** | 0.01 | 0.05 |
| **Gd157** | <0.00 | 0.03 |
| **Tb159** | 0.00 | <0.00 |
| **Dy163** | 0.01 | 0.00 |
| **Ho165** | 0.01 | <0.00 |
| **Er166** | <0.00 | <0.00 |
| **Tm169** | 0.00 | 0.00 |
| **Yb172** | 0.01 | <0.00 |
| **Lu175** | <0.00 | <0.00 |
| **Hf178** | 0.07 | <0.00 |
| **Ta181** | 6.63 | 0.16 |
| **W182** | <0.0189 | <0.00 |
| **Pb208** | 16.11 | 29.01 |
| **Bi209** | <0.027 | <0.0109 |
| **Th232** | 0.02 | <0.00 |
| **U238** | 0.00 | <0.00 |

**Table 20:** Boron isotopic compositions of three tourmaline types.

| | Tur1 | | | | | Tur2 | | | | | Tur3 | | | |
|---|---|---|---|---|---|---|---|---|---|---|---|---|---|---|
| | $^{11}B/^{10}B$ | 2 S.E. | $\delta^{11}B$ (‰) | 2 S.E. (‰) | | $^{11}B/^{10}B$ | 2 S.E. | $\delta^{11}B$ (‰) | 2 S.E. (‰) | | $^{11}B/^{10}B$ | 2 S.E. | $\delta^{11}B$ (‰) | 2 S.E. (‰) |
| **Sample** | | | | | **Sample** | | | | | **Sample** | | | | |
| BH-149-3 | 3.998 | 0.003 | -11.2 | 0.3 | D-4 | 3.991 | 0.002 | -13.1 | 0.6 | KYD-4-2 | 3.988 | 0.001 | -13.7 | 0.3 |
| BH-149-3 | 3.997 | 0.003 | -11.6 | 0.6 | D-4 | 3.992 | 0.003 | -12.8 | 0.7 | KYD-4-2 | 3.989 | 0.001 | -13.5 | 0.3 |
| BH-149-3 | 3.997 | 0.003 | -11.5 | 0.5 | D-4 | 3.994 | 0.003 | -12.2 | 0.7 | KYD-4-2 | 3.988 | 0.002 | -13.7 | 0.6 |
| BH-149-3 | 3.997 | 0.003 | -11.5 | 0.5 | D-4 | 3.990 | 0.002 | -13.2 | 0.6 | KYD-4-2 | 3.988 | 0.005 | -13.7 | 0.3 |
| BH-149-3 | 3.997 | 0.006 | -11.6 | 0.5 | D-4 | 3.991 | 0.002 | -13.1 | 0.6 | KYD-4-2 | 3.990 | 0.005 | -13.3 | 0.3 |
| BH-149-3 | 3.992 | 0.004 | -12.8 | 0.6 | D-4 | 3.992 | 0.003 | -12.8 | 0.7 | KYD-4-2 | 3.985 | 0.005 | -14.4 | 0.9 |
| BH-149-3 | 4.000 | 0.005 | -10.7 | 0.3 | D-4 | 3.994 | 0.003 | -12.2 | 0.7 | KYD-4-2 | 3.986 | 0.004 | -14.2 | 0.7 |
| BH-149-3 | 3.991 | 0.005 | -13.1 | 0.4 | D-4 | 3.990 | 0.002 | -13.2 | 0.6 | KYD-4-2 | 3.986 | 0.004 | -14.3 | 0.9 |
| BH-149-3 | 3.997 | 0.006 | -11.4 | 0.5 | D-4 | 3.988 | 0.007 | -13.7 | 0.6 | KYD-4-2 | 3.982 | 0.004 | -15.2 | 0.6 |
| BH-149-3 | 3.993 | 0.002 | -12.5 | 0.4 | D-4 | 3.989 | 0.007 | -13.4 | 0.7 | KYD-4-2 | 3.990 | 0.003 | -13.1 | 0.4 |
| BH-149-3 | 3.997 | 0.002 | -11.6 | 0.6 | ML 10-H | 3.996 | 0.007 | -11.9 | 0.6 | | | | | |
| KYD14-1 | 3.992 | 0.002 | -12.8 | 0.5 | ML 10-H | 3.992 | 0.006 | -12.7 | 0.4 | | | | | |
| KYD14-1 | 3.990 | 0.002 | -13.3 | 0.5 | ML 10-H | 3.993 | 0.006 | -12.5 | 0.5 | | | | | |
| KYD14-1 | 3.993 | 0.002 | -12.5 | 0.5 | ML 10-H | 3.987 | 0.006 | -14.0 | 0.7 | | | | | |
| KYD14-1 | 3.988 | 0.002 | -13.8 | 0.5 | ML 10-H | 3.993 | 0.004 | -12.6 | 0.3 | | | | | |
| KYD14-1 | 3.996 | 0.005 | -11.9 | 0.4 | ML 10-H | 3.992 | 0.004 | -12.7 | 0.3 | | | | | |
| KYD14-1 | 3.994 | 0.002 | -12.2 | 0.3 | ML 10-H | 3.987 | 0.006 | -13.9 | 0.6 | | | | | |
| KYD14-1 | 3.994 | 0.002 | -12.2 | 0.5 | ML 10-H | 3.990 | 0.004 | -13.4 | 0.3 | | | | | |
| KYD14-1 | 3.993 | 0.002 | -12.4 | 0.5 | ML 10-H | 3.989 | 0.006 | -13.5 | 0.5 | | | | | |
| KYD14-1 | 3.991 | 0.002 | -13.1 | 0.4 | ML 10-H | 3.986 | 0.005 | -14.3 | 0.5 | | | | | |
| KYD14-1 | 3.992 | 0.005 | -12.8 | 0.5 | ML 10-H | 3.989 | 0.005 | -13.6 | 0.6 | | | | | |
| KYD14-1 | 3.992 | 0.002 | -12.7 | 0.4 | ML 10-H | 3.990 | 0.005 | -13.3 | 0.5 | | | | | |
| KYD14-1 | 3.991 | 0.002 | -12.9 | 0.5 | ML 10-H | 3.987 | 0.005 | -14.0 | 0.6 | | | | | |